

**Document Version**

Final published version

**Citation (APA)**

Soto Garcia, J. (2026). *Quantum critical properties of rydberg arrays in and out of equilibrium*. [Dissertation (TU Delft), Delft University of Technology]. <https://doi.org/10.4233/uuid:293a05e3-a3db-4c0d-b4d8-9a6c4c36709e>

**Important note**

To cite this publication, please use the final published version (if applicable).  
Please check the document version above.

**Copyright**

In case the licence states “Dutch Copyright Act (Article 25fa)”, this publication was made available Green Open Access via the TU Delft Institutional Repository pursuant to Dutch Copyright Act (Article 25fa, the Taverne amendment). This provision does not affect copyright ownership.  
Unless copyright is transferred by contract or statute, it remains with the copyright holder.

**Sharing and reuse**

Other than for strictly personal use, it is not permitted to download, forward or distribute the text or part of it, without the consent of the author(s) and/or copyright holder(s), unless the work is under an open content license such as Creative Commons.

**Takedown policy**

Please contact us and provide details if you believe this document breaches copyrights.  
We will remove access to the work immediately and investigate your claim.



QUANTUM CRITICAL PROPERTIES  
OF RYDBERG ARRAYS IN AND OUT  
OF EQUILIBRIUM

José SOTO GARCÍA

**QUANTUM CRITICAL PROPERTIES OF RYDBERG  
ARRAYS IN AND OUT OF EQUILIBRIUM**



# **QUANTUM CRITICAL PROPERTIES OF RYDBERG ARRAYS IN AND OUT OF EQUILIBRIUM**

## **Dissertation**

for the purpose of obtaining the degree of doctor  
at Delft University of Technology  
by the authority of the Rector Magnificus, Prof. dr. ir. H. Bijl,  
chair of the Board for Doctorates  
to be defended publicly on  
Tuesday, 31 March 2026 at 10:00

by

**José SOTO GARCÍA**

This dissertation has been approved by the promotor.

Composition of the doctoral committee:

Rector Magnificus,	chairperson
Prof. dr. A. F. Otte,	Delft University of Technology, <i>promotor</i>
Dr. N. Chepiga,	Delft University of Technology, <i>promotor</i>

*Independent members:*

Prof. dr. Y. M. Blanter,	Delft University of Technology
Dr. A. R. Akhmerov,	Delft University of Technology
Dr. P. R. Corboz,	University of Amsterdam,
Prof. dr. C. de Morais Smith,	Utrecht University
Prof. dr. J. D. Pritchard,	University of Strathclyde,
Prof. dr. M. Blaauboer,	Delft University of Technology, reserve member



*Keywords:* Rydberg Atoms, Strongly Correlated Systems, Quantum Many-Body Physics, Quantum Phase Transitions, Critical Phenomena, Kibble–Zurek Mechanism, Non-equilibrium Dynamics, Tensor Network Methods, Density Matrix Renormalization Group

*Printed by:* Proefschriftenprinten.nl

*Cover by:* Proefschriftenprinten.nl

Copyright © 2026 by J. Soto García

ISBN 978-94-6384-932-6

An electronic copy of this dissertation is available at  
<https://repository.tudelft.nl/>.

*No man is an island,  
Entire of itself,  
Every man is a piece of the continent,  
A part of the main.*

John Donne



# CONTENTS

<b>Summary</b>	<b>xi</b>
<b>Samenvatting</b>	<b>xiii</b>
<b>1. Introduction</b>	<b>1</b>
1.1. Arrays of Rydberg atoms	3
1.2. Brief introduction to quantum phase transitions	6
1.2.1. Landau–Ginzburg theory of phase transitions	7
1.2.2. The renormalization group	9
1.2.3. Finite-size scaling	11
1.3. Kibble-Zurek Mechanism	12
1.3.1. Kibble–Zurek Scaling Across a Kosterlitz–Thouless Transition	14
1.4. Finite-Time Scaling	15
1.5. Tensor Networks	16
1.5.1. Mathematical Description	17
1.5.2. Graphical representation	19
1.5.3. Density-Matrix Renormalization Group	21
1.5.4. Time-evolution algorithms for one-dimensional systems	22
1.5.5. Truncation of Matrix Product States	25
1.5.6. Symmetries and Tensor Networks	25
<b>2. The quantum Kibble-Zurek mechanism: the role of boundary conditions, end-points and kink types</b>	<b>33</b>
2.1. Introduction	34
2.2. The Models	34
2.2.1. Transverse Field Ising Model	34
2.2.2. 1D Quantum 3-state Potts Model	35
2.3. Numerical Methods	36
2.3.1. Ground State Calculations	36
2.3.2. Simulation of dynamics	36
2.4. System Size	37
2.5. Types of kinks and the endpoint	38
2.6. Boundary Conditions	45
2.7. Discussion	48
<b>3. Resolving chiral transitions in Rydberg arrays with quantum Kibble–Zurek mechanism and finite-time scaling</b>	<b>55</b>
3.1. Introduction	56

3.2.	Numerical Methods . . . . .	57
3.2.1.	Blockade Model . . . . .	57
3.2.2.	Modeling the Rydberg model with $1/r^6$ interaction . . . . .	59
3.2.3.	Ground State Calculations . . . . .	60
3.2.4.	Simulation of dynamics . . . . .	60
3.2.5.	Kink operators . . . . .	62
3.2.6.	Order parameter . . . . .	64
3.3.	Results . . . . .	64
3.3.1.	Finite-size effects in Kibble-Zurek mechanism . . . . .	64
3.3.2.	Finite-size effect in the finite-time scaling . . . . .	64
3.3.3.	Dynamical signatures of the Floating Phase . . . . .	66
3.3.4.	Finite-Time Scaling . . . . .	69
3.3.5.	Combining KZ with FTS . . . . .	69
3.3.6.	Derived critical exponents . . . . .	69
3.3.7.	Results for the Rydberg model with $1/r^6$ interaction. . . . .	71
3.4.	Discussion . . . . .	73
4.	<b>Infinite randomness criticality and localization of the floating phase in arrays of Rydberg atoms trapped with non-perfect tweezers</b>	<b>81</b>
4.1.	Introduction . . . . .	81
4.2.	The Model . . . . .	82
4.3.	Methods . . . . .	83
4.3.1.	Estimation of the disorder strength . . . . .	83
4.3.2.	Ground state calculations . . . . .	84
4.3.3.	Simulation of dynamics . . . . .	84
4.3.4.	Kibble-Zurek mechanism protocol . . . . .	85
4.4.	Results . . . . .	86
4.4.1.	Impact of Disorder on Non-Equilibrium Phenomena . . . . .	86
4.4.2.	Localization of the floating phase . . . . .	88
4.5.	Discussion . . . . .	91
5.	<b>Numerical investigation of quantum phases and phase transitions in a two-leg ladder of Rydberg atoms</b>	<b>99</b>
5.1.	Introduction . . . . .	100
5.2.	Overview of the phase diagram . . . . .	101
5.3.	Methods . . . . .	104
5.3.1.	Ground-state calculations . . . . .	104
5.3.2.	Extraction of correlation length and wave-vector . . . . .	106
5.3.3.	Extraction of the central charge . . . . .	108
5.3.4.	Benchmark: Ising transition into checkerboard phase . . . . .	108
5.4.	Transitions into $\mathbb{Z}_2$ and $\mathbb{Z}_2 \otimes \tilde{\mathbb{Z}}_2$ phases . . . . .	110
5.4.1.	Ising transitions . . . . .	111
5.4.2.	Disorder to $\mathbb{Z}_2 \otimes \tilde{\mathbb{Z}}_2$ transition . . . . .	111
5.5.	Transitions into $\mathbb{Z}_3$ and $\mathbb{Z}_3 \otimes \tilde{\mathbb{Z}}_2$ phases . . . . .	115
5.5.1.	Disorder to $\mathbb{Z}_3$ transition . . . . .	116
5.5.2.	Ising transition between the $\mathbb{Z}_3$ and $\mathbb{Z}_3 \otimes \tilde{\mathbb{Z}}_2$ phases . . . . .	117

5.5.3. Disorder to $\mathbb{Z}_3 \otimes \tilde{\mathbb{Z}}_2$ transition . . . . .	117
5.6. Beyond $\mathbb{Z}_3 \otimes \tilde{\mathbb{Z}}_2$ . . . . .	119
5.7. Operator choice vs. $\xi$ and $q$ . . . . .	120
5.8. Central charge for the transition out of $\mathbb{Z}_2 \otimes \tilde{\mathbb{Z}}_2$ . . . . .	123
5.9. Discussion . . . . .	125
<b>6. Conclusion</b>	<b>131</b>
<b>A. Appendix</b>	<b>135</b>
A.1. Blockade Models . . . . .	135
A.1.1. Implementation Details . . . . .	135
A.1.2. Modified TEBD for the $r = 1$ Blockade . . . . .	135
A.1.3. Modified TEBD for the $r = 2$ Blockade . . . . .	137
<b>Acknowledgements</b>	<b>141</b>
<b>Curriculum Vitae</b>	<b>143</b>
<b>List of Publications</b>	<b>145</b>



# SUMMARY

Rydberg atoms trapped in optical tweezers have emerged as a powerful platform for exploring the physics of low-dimensional systems. Thanks to the precise control over the tweezers location, interatomic interactions, and couplings to external fields, these platforms have revealed a wide variety of critical phenomena.

This thesis numerically explores the quantum phases and phase transitions that can be engineered in quasi one-dimensional arrays of Rydberg atoms. It employs a combination of equilibrium and non-equilibrium approaches within the matrix product state framework.

We first studied the quantum Kibble–Zurek (KZ) mechanism in minimal one-dimensional models, showing how boundary conditions and quench endpoints affect scaling behavior. A refined definition of kinks was introduced, yielding robust results even away from the classical Hamiltonian. Building on this, we incorporated a blockade model into the time-evolving block decimation (TEBD) algorithm and combined KZ with finite-time scaling (FTS) to study Rydberg chains, establishing a protocol suitable for experiments. This approach distinguished the Kosterlitz–Thouless transition from the Huse–Fisher universality class, providing an alternative way to experimentally detect the floating phase, and allowed the precise location of conformal points as well as the extraction of critical exponents.

Motivated by optical tweezer imperfections, we then examined the effect of disorder on the critical phenomena observed in these chains. We found that disorder alters the nature of quantum criticality, driving the system toward the infinite-disorder universality class, and visibly changing the nature of the KZ scaling. It also localizes the algebraic correlations of the floating phase, destroying Friedel oscillations in the bulk of the chain and saturating the entanglement entropy at a finite value.

Finally, we extended the analysis to two-leg Rydberg ladders, where the phase diagram revealed new phases with resonant Rydberg states between the upper and lower chains. This geometry produced novel critical phenomena, including the merging of two Ising transitions into the Ashkin–Teller universality class and the more exotic merging of an Ising and Pokrovsky–Talapov transition.

The findings presented here provide a theoretical guidance for investigating critical dynamics, the impact of disorder, and the emergence of exotic critical phenomena in both one and quasi-two-dimensional Rydberg atom arrays.



# SAMENVATTING

Rydbergatomen die in optische pincetten worden gevangen, zijn uitgegroeid tot een krachtig platform voor het onderzoeken van de fysica van laag-dimensionale systemen. Dankzij de nauwkeurige controle over de positie van de pincetten, de interatomaire interacties en de koppelingen aan externe velden, hebben deze platforms een grote verscheidenheid aan kritische verschijnselen aan het licht gebracht.

Deze thesis onderzoekt numeriek de kwantumfasen en faseovergangen die kunnen worden gerealiseerd in quasi-eendimensionale arrays van Rydbergatomen. Hiervoor wordt een combinatie van evenwichts- en niet-evenwichtsbenaderingen gebruikt binnen het raamwerk van matrix-producttoestanden.

We bestudeerden eerst het kwantum Kibble–Zurek (KZ)-mechanisme in minimale eendimensionale modellen, waarbij we aantoonde hoe randvoorwaarden en quencheindpunten het schaalgedrag beïnvloeden. Een verfijnde definitie van *kinks* werd geïntroduceerd, wat robuuste resultaten opleverde, zelfs buiten het klassieke Hamiltoniaan. Hierop voortbouwend hebben we een blokademodel geïntegreerd in het *time-evolving block decimation* (TEBD)-algoritme en KZ gecombineerd met *finite-time scaling* (FTS) om Rydbergketens te bestuderen. Zo werd een protocol ontwikkeld dat geschikt is voor experimenten. Deze aanpak maakte het mogelijk om de Kosterlitz–Thouless-overgang te onderscheiden van de Huse–Fisher-universaliteitsklasse, bood een alternatieve manier om de zwevende fase experimenteel te detecteren, en maakte de precieze bepaling van conforme punten en kritische exponenten mogelijk.

Gemotiveerd door imperfecties in optische pincetten hebben we vervolgens het effect van wanorde onderzocht op de kritische verschijnselen die in deze ketens worden waargenomen. We vonden dat wanorde de aard van de kwantumkriticiteit verandert, waardoor het systeem wordt gedreven naar de *infinite-disorder*-universaliteitsklasse en het KZ-schaalgedrag zichtbaar wordt gewijzigd. Bovendien lokaliseert wanorde de algebraïsche correlaties van de zwevende fase, waardoor Friedel-oscillaties in het binnenste van de keten verdwijnen en de verstrengelingsentropie verzadigt op een eindige waarde.

Ten slotte hebben we de analyse uitgebreid naar tweeledige Rydberggladders, waarbij het fasediagram nieuwe fasen onthulde met resonante Rydbergtoestanden tussen de bovenste en onderste keten. Deze geometrie leidde tot nieuwe kritische verschijnselen, waaronder het samensmelten van twee Ising-overgangen tot de Ashkin–Teller-universaliteitsklasse en de meer exotische versmelting van een Ising- en een Pokrovsky–Talapov-overgang.

De resultaten die hier worden gepresenteerd bieden theoretische richtlijnen voor het onderzoeken van kritische dynamica, de invloed van wanorde en het ontstaan van exotische kritische verschijnselen in zowel één- als quasi-tweedimensionale arrays van Rydbergatomen.



# 1

## INTRODUCTION

Traditionally, phases of condensed-matter systems have been understood within two fundamental paradigms: Fermi-liquid theory for metals and Landau's theory of phase transitions [1]. Fermi-liquid theory provides a remarkably successful framework to describe the low energy spectrum of conventional metals. Within this picture, the elementary excitations are free quasiparticles that resemble electrons in terms of their quantum numbers (charge and spin) but the effective mass is renormalized due to the Coulomb interactions [2, 3]. This theory has been successful in explaining crucial physical concepts such as the transistor or the BCS theory of superconductivity. Complementarily, Landau's theory of phase transitions provides a powerful description of phase transitions by classifying them according to symmetry breaking [1].

However, many exotic phases and phase transitions lie beyond those two paradigms. Such phases typically emerge in systems of strongly correlated electrons, including quantum spin liquids, fractional quantum Hall states, and high-temperature superconductors [1, 4]. Models of strongly correlated electrons may be conceptually simple, but very difficult to solve. Only a few cases are analytically tractable, while straightforward numerical approaches are not sufficient due to the exponential growth of the Hilbert space with the system size [5].

Strongly correlated systems arise when electron-electron interactions become significant and can no longer be treated as a small perturbation. In regimes where the Coulomb repulsion dominates over the kinetic energy, conventional perturbation theory breaks down and the standard framework for three-dimensional electronic systems, Fermi-liquid theory, no longer applies [4]. These effects become especially pronounced in low-dimensional systems, where the motion of electrons is constrained [6].

As a starting point, one-dimensional systems provide a particularly powerful setting to study strongly correlated matter. In 1D, electron mobility is highly constrained, and individual quasiparticle excitations cease to exist. Instead, the excitations are inherently collective. The universal low-energy description is provided by the Luttinger liquid framework [3, 7]. Moreover, 1D systems are simple enough to allow for exact analytical treatments, highly efficient numerical simulations, and controlled experimental realizations, making them an ideal theoretical laboratory. A central goal of modern research in condensed matter physics is to understand how exotic phases emerge from quantum phase transitions and how they might be engineered in strongly correlated materials. To this

end, physicists employ a combination of advanced theoretical approaches and state-of-the-art numerical methods, complemented by experiments in highly tunable quantum systems [3, 8, 9].

From the theoretical side, despite the strong interactions between particles that prevents perturbative treatments, many theoretical techniques have been developed allowing for exact solutions in one-dimensional minimal models. These minimal models, although very simple, capture many of the essential properties observed in low-dimensional systems. The pioneering example is the Bethe ansatz [7, 10], introduced in 1931 for the 1D isotropic Heisenberg model and later extended to a wide variety of other one-dimensional models. These integrable systems, although not all of them are solvable by the Bethe ansatz, provide a valuable starting point for understanding strongly correlated physics in 1D. Beyond integrable models, field-theoretical approaches such as bosonization [3] and conformal field theory (CFT) [11] have proven remarkably successful in capturing the universal long-wavelength and low-energy behavior of one-dimensional systems, although their applicability remains restricted to this regime.

In parallel with these theoretical developments, a set of numerical methods have been developed for studying strongly correlated systems. Quantum Monte Carlo can be extremely powerful, but its applicability is severely limited by the sign problem in many fermionic and frustrated systems [12, 13]. Tensor network methods, with the development of the density matrix renormalization group (DMRG) and related algorithms, have therefore become the leading approach for one-dimensional systems, providing highly accurate access to ground states and low-lying excitations [14, 15]. Despite their success, tensor network methods have their own limitations. These systems are restricted to low-energy finite systems with a limited amount of entanglement [15, 16].

Together with the development of theoretical techniques, there has been an astonishingly fast advance in the control and manipulation of single atoms. This progress has enabled the emergence of a wide variety of experimental platforms that serve as playgrounds for studying low-dimensional quantum systems. These platforms include neutral atoms in optical lattices or optical tweezers [17, 18], trapped ions [19], quantum dots [20] and superconducting circuits [21] among others. The field is vast, and we do not attempt to review it in detail here; the interested reader is referred to comprehensive reviews on the topic [9, 22].

Many of these systems are also promising candidates for digital qubits in future universal quantum computers [23]. In the meantime, and perhaps more importantly for condensed matter physics, they function as analog quantum simulators that allow the experimental realization of well-defined Hamiltonians [9, 22].

Analog quantum simulators, however, face their own challenges. They are typically limited to relatively small system sizes and finite simulation times. Moreover, imperfections in the positioning of particles and in the control of their interactions introduce some degree of disorder [24]. Nevertheless, experimental capabilities are improving rapidly, with advances in coherence times, system sizes, and control over geometry in one, two, and even three dimensions. In particular, arrays of Rydberg atoms trapped in optical tweezers have recently emerged as one of the most promising platforms, combining high controllability with strong, long-range interactions, and are central to the developments discussed in this thesis [18, 25, 26].

The rest of this thesis is organized as follows. The remainder of this chapter introduces the theoretical background underlying the study, including the fundamentals of the Hamiltonian for interacting Rydberg atoms, the theory of renormalization and critical phenomena, and the tensor network modeling of quantum many-body systems in the framework of matrix product states. Chapter 2 examines the effect of boundary conditions and quench endpoints on the scaling of the Kibble–Zurek (KZ) mechanism. It also analyzes how different definitions of kinks influence the scaling behavior and their relation to the choice of endpoint. Chapter 3 employs non-equilibrium physics, combining the KZ mechanism with finite-time scaling (FTS) of the order parameter, to investigate critical phenomena in arrays of Rydberg atoms. Chapter 4 considers a more realistic scenario by studying the impact of optical tweezer imperfections on critical phenomena in Rydberg arrays. Chapter 5 extends the analysis to two-leg Rydberg ladders, exploring quantum phases and phase transitions in this richer geometry. Finally, Chapter 6 provides concluding remarks and offers an outlook for future directions.

## 1.1. ARRAYS OF RYDBERG ATOMS

Among the various experimental platforms introduced above, neutral atom arrays have emerged as particularly powerful for the study of strongly correlated quantum matter. Their key advantage lies in the combination of single-atom control, long coherence times, and the strong, tunable, long-range interactions characteristic of Rydberg states [18, 25, 26]. These properties make them uniquely suited for the realization of programmable quantum simulators.

Rydberg platforms have already been successfully employed to explore exotic phases of matter, not only in one dimension [24] and two dimensions [27, 28], but also in more unconventional geometries such as fractal lattices [29]. Their large variety of accessible energy levels supports multiple types of couplings, such as van der Waals and Förster resonances [25]. Combined with their long-range interactions, this feature has enabled researchers to realize striking phenomena, including incommensurate Luttinger liquids [30], commensurate–incommensurate phase transitions, topological phases of matter [31, 32], and non-equilibrium dynamics beyond the framework of equilibrium statistical mechanics [33]. In this thesis, however, we restrict our attention to systems governed by van der Waals interactions. For a more comprehensive review of Rydberg atoms and their broader range of applications, see [18, 34].

Our starting point is the Hamiltonian representing an array of neutral atoms interacting with each other and with external fields. These neutral atoms are treated as a two-level system with  $|g\rangle$  the ground state and  $|r\rangle$  a Rydberg state. This Hamiltonian, derived from the quantum optics framework [25, 35], is given by:

$$H = \frac{\Omega}{2} \sum_i (|g_i\rangle\langle r_i| + |r_i\rangle\langle g_i|) - \Delta \sum_i \hat{n}_i + \sum_{i<j} V_{ij} \hat{n}_i \hat{n}_j, \quad (1.1)$$

where  $\Omega$  represents the Rabi frequency characterizing the atom-light interaction,  $\Delta$  denotes the detuning of the driving field, and  $V_{ij}$  accounts for the interaction between excited states of atom pairs, with occupation numbers  $\hat{n}_i$ .

The first two terms of the Hamiltonian represent the interaction between atoms and an external coherent light field, modeled within the two-level approximation. This interaction can be described by:

$$H = \frac{\omega}{2}\sigma_z + \Omega\sigma_x \cos(\nu t), \quad (1.2)$$

where  $\omega$  is the atomic transition frequency,  $\nu$  is the frequency of the external light field, and  $\sigma_z$  and  $\sigma_x$  are the Pauli matrices in the  $z$  and  $x$  direction respectively.

To facilitate the application of perturbation theory, we move into an interaction picture using the transformation  $U = U_0 V$ , where  $U_0 = \exp(-i\frac{\eta}{2}\sigma_z t)$  and  $\eta$  is a real parameter to be determined [36]. The transformed Hamiltonian becomes:

$$\tilde{H} = U_0^\dagger H U_0 - iU_0^\dagger \dot{U}_0, \quad (1.3)$$

yielding

$$\tilde{H} = \frac{\omega - \eta}{2}\sigma_z + \frac{\Omega}{2}(\sigma_+ e^{i(\eta - \nu)t} + \sigma_- e^{-i(\eta - \nu)t}) + \frac{\Omega}{2}(\sigma_+ e^{i(\eta + \nu)t} + \sigma_- e^{-i(\eta + \nu)t}), \quad (1.4)$$

with  $\sigma_+$  and  $\sigma_-$  the creation and annihilation operators respectively.

Selecting  $\eta = \nu$  and applying the rotating wave approximation [35, 36], we eliminate rapidly oscillating terms, simplifying to:

$$\tilde{H} \approx \frac{\omega - \nu}{2}\sigma_z + \frac{\Omega}{2}\sigma_x. \quad (1.5)$$

Additionally, the dominant interaction between a pair of Rydberg atoms located at positions  $\mathbf{R}_1$  and  $\mathbf{R}_2$  is the dipole–dipole interaction, which can be described by:

$$V_{\text{ddi}} = \frac{1}{4\pi\epsilon_0} \frac{\mathbf{d}_1 \cdot \mathbf{d}_2 - 3(\mathbf{d}_1 \cdot \mathbf{r})(\mathbf{d}_2 \cdot \mathbf{r})}{R^3}, \quad (1.6)$$

where  $\mathbf{d}_1$  and  $\mathbf{d}_2$  are the dipole moments of the atoms,  $R = |\mathbf{R}_1 - \mathbf{R}_2|$  is the interatomic distance, and  $\mathbf{r} = (\mathbf{R}_1 - \mathbf{R}_2)/R$  is the unit vector pointing from one atom to the other.

The dipole–dipole expression is the starting point for describing the Rydberg–Rydberg interaction, but in the absence of permanent dipoles, as it happens when two atoms are in identical Rydberg state, the effective interaction is van der Waals, as shown next. Given that  $V_{\text{ddi}}$  is odd under parity and that the state  $|\alpha\alpha\rangle$  is symmetric with even parity, the first-order correction

$$\langle \alpha\alpha | V_{\text{ddi}} | \alpha\alpha \rangle \quad (1.7)$$

vanishes. Consequently, the leading contribution to the interaction energy arises from second-order perturbation theory. When both atoms occupy the same Rydberg state  $|\alpha\alpha\rangle$ , the pair state is non-degenerate, and the second-order energy shift is given by:

$$\Delta E_{\alpha\alpha} = \sum_{\beta,\gamma} \frac{|\langle \alpha\alpha | V_{\text{ddi}} | \beta\gamma \rangle|^2}{E_{\alpha\alpha} - E_{\beta\gamma}}, \quad (1.8)$$

where the sum runs over all intermediate states  $|\beta\gamma\rangle$  that are dipole-coupled to  $|\alpha\alpha\rangle$ .

The squared exponent of the numerator indicates that the van der Waals interaction decays as  $R^{-6}$ . Furthermore, the interaction is pairwise additive, and can be expressed as

$$V_{ij} = \sum_{i < j} \frac{V_0}{R_{ij}^6} \hat{n}_i \hat{n}_j, \quad (1.9)$$

where  $V_0$  is a constant that scales with the principal quantum number as  $n^{11}$  [25]<sup>1</sup>. This steep scaling with the principal quantum number is important because it allows a broad range of interacting strength, from almost negligible to extremely strong interactions, by exciting atoms into slightly higher Rydberg states.

Combining the last term of the Hamiltonian with the driving and detuning terms, the effective Hamiltonian takes the form:

$$H = \frac{\Omega}{2} \sum_i (|g_i\rangle\langle r_i| + |r_i\rangle\langle g_i|) - \Delta \sum_i \hat{n}_i + \sum_{i < j} \frac{V_0}{R_{ij}^6} \hat{n}_i \hat{n}_j. \quad (1.10)$$

The van der Waals repulsion between Rydberg states induces a blockade effect, which prevents two atoms within a distance smaller than a blockade radius  $R_b$  from being simultaneously excited to a Rydberg state, as sketched in Figure 1.1. The blockade radius is defined by the condition  $V(R_b) = \Omega$ . Introducing  $a$  as the interatomic distance, the dimensionless Rydberg blockade is given by

$$R_b/a = (V_0/\Omega)^{1/6}. \quad (1.11)$$

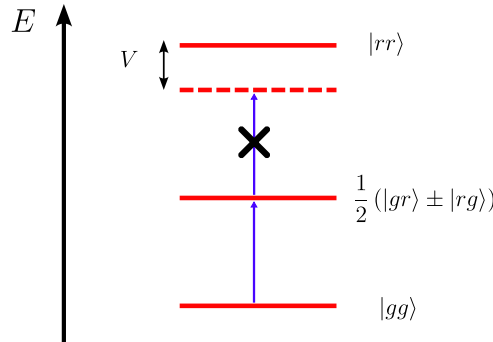


Figure 1.1.: Sketch of the Rydberg blockade. Two interacting atoms form a coupled quantum system with two relevant energy levels. A laser with Rabi frequency  $\Omega$  drives the excitation of one atom to the Rydberg state. However, when the van der Waals interaction  $V$  exceeds  $\Omega$ , the resulting energy shift prevents the simultaneous excitation of both atoms, giving rise to the blockade effect.

The formalism presented here provides the foundation for the theoretical and numerical analyses undertaken in this thesis, with parameters and specific interactions tailored according to experimental and computational considerations detailed in subsequent sections.

<sup>1</sup>Do not confuse the principal quantum number  $n$  with the occupation number  $\hat{n}$

## 1.2. BRIEF INTRODUCTION TO QUANTUM PHASE TRANSITIONS

Phase transitions are ubiquitous in nature, describing abrupt qualitative changes in macroscopic properties—for instance, the boiling of water, metal–insulator and superconducting transitions induced by temperature, structural rearrangements such as graphite to diamond, or the emergence of collective order like ferromagnetism [37, 38]. Even the Higgs mechanism, which endows elementary particles with mass in the Standard Model, is believed to have originated from a phase transition in the early universe [39, 40]. Classical phase transitions are driven by thermal fluctuations: as an external control parameter such as temperature  $T$ , pressure  $P$ , or magnetic field  $H$  is varied, thermal agitation destroys long-range order. By contrast, *quantum phase transitions* occur at absolute zero and are governed not by temperature but by quantum fluctuations arising from the Heisenberg uncertainty principle [41, 42]. As a non-thermal tuning parameter  $g$  (magnetic field, pressure, interaction strength) crosses a critical value  $g_c$ , the energy gap  $\Delta$  between the ground and first excited state closes, destabilizing the ordered phase. Such transitions are not merely theoretical, consequences of their existence have been observed in heavy-fermion metals, high- $T_c$  superconductors, and low-dimensional magnets [43–46], to cite some examples.

There are many ways to classify phase transitions. One common approach is by examining the behavior of the order parameter. Thus, in discontinuous (also called first order) phase transitions, the order parameter changes abruptly at the transition point. These transitions are characterized by coexistence of phases. A typical example is the melting of ice into liquid water. In contrast, continuous (also termed second-order) phase transitions show a smooth change on the order parameter across the transition, with no coexistence of phases. However, the first derivative of the order parameter with respect to the control parameter becomes discontinuous or divergent. A typical example is the emergence of ferromagnetism in metals when lowering the temperature.

While both classical and quantum transitions share unifying concepts such as order parameters, universality classes, and scaling laws, they differ fundamentally in the role of time. In classical systems, criticality is purely spatial: time enters only in the dynamics near criticality, characterized by a dynamical exponent  $z$ . This is because for a classical Hamiltonian of the form

$$H = H_{\text{kin}} + H_{\text{pot}},$$

the kinetic and potential terms commute,

$$[H_{\text{kin}}, H_{\text{pot}}] = 0,$$

so the partition function factorizes,

$$Z = \text{Tr} e^{-\beta H} = Z_{\text{kin}} Z_{\text{pot}}.$$

The kinetic part yields only analytic Gaussian integrals, so all singular behavior is encoded in  $Z_{\text{pot}}$ , which can be captured by a  $d$ -dimensional effective field theory (e.g. a Landau–Ginzburg functional or lattice model).

In quantum systems, however, statics and dynamics are inseparable:

$$[H_{\text{kin}}, H_{\text{pot}}] \neq 0,$$

and the partition function no longer factorizes. Instead, it can be written in the path integral formalism as

$$Z = \int \mathcal{D}[\phi(x, \tau)] e^{-S_E[\phi]}, \quad (1.12)$$

where  $\tau$  is the imaginary time,  $S_E[\phi]$  is the Euclidean action, and  $\phi$  is a coarse-grained field representing the order parameter. In this formulation, imaginary time  $\tau$  plays the role of an additional dimension, mapping the quantum problem to a classical statistical system in  $(d + 1)$  dimensions [41].

During this thesis, I employ various techniques to study critical phenomena in low-dimensional quantum many-body systems. As in many areas of theoretical physics, the deeper one goes, the more abstract the theory becomes, involving subtle and sophisticated concepts. We will not attempt to cover the full depth of these ideas here. After four years of a PhD, I still find many aspects of the underlying field theories challenging, especially when it comes to the subtle distinctions between quantum and classical systems.

Nevertheless, some basic concepts are both accessible and sufficient to develop an intuition for the techniques used in this work. With that in mind, I begin with a brief introduction to the Landau–Ginzburg theory of phase transitions. While this framework cannot provide quantitatively accurate critical exponents for low-dimensional systems, it offers a qualitative understanding of phase transitions and the behaviour of correlation functions near criticality. Moreover, it serves as a natural starting point for thinking about critical phenomena. Although the traditional formulation addresses classical systems undergoing temperature-driven transitions, one can extend the intuition to quantum systems at zero temperature by replacing temperature with an appropriate external control parameter.

### 1.2.1. LANDAU–GINZBURG THEORY OF PHASE TRANSITIONS

The Landau–Ginzburg (LG) framework provides a phenomenological description of continuous (second-order) phase transitions in terms of a coarse-grained order parameter  $m(x)$  that distinguishes between competing phases. It extends Landau's original mean-field theory by incorporating spatial variations of the order parameter, enabling the description of correlation functions and long-wavelength fluctuations [47].

The starting point is to write the free energy functional in the simplest form that captures the essential physics, namely as a polynomial in the order parameter  $m(x)$ . In the context of a ferromagnet,  $m(x)$  can be interpreted as the local magnetization. Since the system is symmetric under  $m \rightarrow -m$ , only even powers of  $m$  are allowed in the absence of an external field. An external field  $h(x)$ , conjugate to  $m(x)$ , breaks this symmetry and couples linearly to  $m(x)$ . To account for spatial variations, a gradient term is included, which penalizes differences in magnetization between neighbouring regions [48]:

$$F[m] = \int d^d x \left[ \frac{K}{2} (\nabla m(x))^2 + \frac{R(T)}{2} m^2(x) + \frac{U}{4} m^4(x) - h(x) m(x) \right], \quad (1.13)$$

where:

- $K > 0$  controls the energy cost of spatial variations in  $m(x)$ ,

- $R(T) \propto T - T_c$  changes sign at the critical temperature  $T_c$ ,
- $U > 0$  ensures stability ( $F \rightarrow +\infty$  for large  $|m|$ ),
- $h(x)$  is an external field conjugate to  $m(x)$ .

In the mean-field limit (neglecting the gradient term) and in the absence of an external field, the minima of  $F[m]$  are:

$$m_0 = \begin{cases} 0, & R > 0 \quad (T > T_c), \\ \pm \sqrt{|R|/U}, & R < 0 \quad (T < T_c). \end{cases}$$

Thus, the transition at  $T = T_c$  corresponds to the change from a single minimum ( $m_0 = 0$ ) to two degenerate minima ( $m_0 \neq 0$ ).

We now turn to the form of the two-point correlation function near the critical point:

$$\Gamma(x) = \langle m(0)m(x) \rangle - \langle m(0) \rangle \langle m(x) \rangle. \quad (1.14)$$

By adding a small localised field at the origin,  $h(x) = h\delta(x)$ , linear response theory gives:

$$\Gamma(x) = \frac{1}{\beta} \left. \frac{\partial \langle m(x) \rangle}{\partial h} \right|_{h=0}, \quad (1.15)$$

with  $\beta = 1/(k_B T)$  the inverse of the product of the Boltzmann's constant  $k_B$  and the temperature  $T$ . Within mean-field theory, the saddle-point equation for the configuration minimising  $F[m]$  is:

$$-K\nabla^2 m(x) + R m(x) + U m^3(x) - h\delta(x) = 0. \quad (1.16)$$

For small  $h$ , we write

$$m(x) = m_0 + h\varphi(x), \quad (1.17)$$

so that  $\Gamma(x) = \varphi(x)$ . Above  $T_c$  ( $m_0 = 0$ ), we obtain:

$$(-\nabla^2 + \xi^{-2})\Gamma(x) = \frac{1}{\beta K} \delta(x), \quad \text{where } \xi = \sqrt{\frac{K}{R}}. \quad (1.18)$$

For large distances, the solution of this equation has the universal asymptotic form

$$\Gamma_d(x) \sim \frac{e^{-x/\xi}}{x^{(d-1)/2}}, \quad (1.19)$$

with  $d$  denoting the system dimension. This form shows that, away from the critical point, correlations are short range and with a correlation length  $\xi$ .

At the critical point ( $R = 0$ ), the equation reduces to the Laplace equation:

$$-\nabla^2 \Gamma(x) = \frac{1}{\beta K} \delta(x), \quad (1.20)$$

whose mean-field solution is algebraic:

$$\Gamma(x) \propto \frac{1}{x^{d-2}}, \quad (d > 2). \quad (1.21)$$

Beyond mean-field theory, fluctuations modify the power law to:

$$\Gamma(x) \propto \frac{1}{x^{d-2+\eta}}, \quad (1.22)$$

where  $\eta$  is the anomalous dimension critical exponent.

More generally, the singular behavior near continuous phase transitions is captured by a set of critical exponents that describe how macroscopic observables scale as the critical temperature  $T_c$  is approached. Introducing the reduced temperature  $\varepsilon(T) = (T - T_c)/T_c$ , the order parameter  $m$  (e.g. the magnetization in a ferromagnet) vanishes as  $m \sim (-\varepsilon)^\beta$  for  $\varepsilon < 0$  in zero field, defining the exponent  $\beta$ . The susceptibility  $\chi = \partial m / \partial h|_{h=0}$  diverges as  $\chi \sim |\varepsilon|^{-\gamma}$ , with  $\gamma$  the susceptibility exponent, while the specific heat behaves as  $C \sim |\varepsilon|^{-\alpha}$ , where  $\alpha$  is the specific heat exponent. At the critical isotherm ( $\varepsilon = 0$ ), the order parameter scales with the external field as  $m \sim h^{1/\delta}$ , introducing the exponent  $\delta$ . The divergence of the correlation length  $\xi \sim |\varepsilon|^{-\nu}$  defines  $\nu$ , and at criticality the correlation function decays algebraically as  $\Gamma(x) \sim |x|^{-(d-2+\eta)}$ , where  $\eta$  is the anomalous dimension [37]. Within Landau–Ginzburg mean-field theory these exponents take the values

$$\alpha = 0, \quad \beta = \frac{1}{2}, \quad \gamma = 1, \quad \delta = 3, \quad \nu = \frac{1}{2}, \quad \eta = 0.$$

The LG model provides a valid coarse-grained description in any spatial dimension  $d$ , but its mean-field critical exponents are accurate only when fluctuations are negligible. The Ginzburg criterion shows that the upper critical dimension for this theory is  $d_c = 4$ . This means that for  $d > 4$  fluctuations are irrelevant and mean-field predictions are exact, while for  $d < 4$ , fluctuations become important near the critical point and modify the critical behavior, so the true exponents differ from the mean-field ones. In this case, it is necessary to employ other tools, such as renormalization group (RG) methods or numerical simulations to extract the critical exponents [2, 48].

### 1.2.2. THE RENORMALIZATION GROUP

In the vicinity of the critical point of a continuous phase transition, the correlation length  $\xi$  diverges, and this divergence governs the singular behavior of many measurable quantities (such as the susceptibility and specific heat) through universal critical exponents. These divergences originate from large fluctuations of the order parameter, which occur at all length scales. In other words, even when the system is coarse-grained, the fluctuations do not average out [49].

A classical example is the liquid–gas critical point of water. At this point, the densities of the liquid and vapor phases become indistinguishable, and the surface tension vanishes. Bubbles of steam and droplets of water coexist, intermixed at all size scales. This leads to strong light scattering, giving the liquid a characteristic white, opaque appearance [37].

Such scale-invariant fluctuations make the system intractable from a naive microscopic description because of the enormous number of interacting degrees of freedom. This challenge is not unique to phase transitions, it appears in diverse areas of physics such as turbulent fluid flows and quantum field theory. The key idea of the renormalization group (RG) is to integrate out fluctuations in a systematic, step-by-step manner,

starting from short length scales and moving toward larger ones. This can be done, for instance, by constructing block spins, integrating out modes with wavelengths shorter than a threshold  $\Lambda^{-1}$ , or, equivalently in momentum space, integrating out modes with wave vectors  $|k| > \Lambda$ . Non-analytic behavior emerges only after infinitely many such iterations [49].

The central concept of the RG is the behavior of the system near *fixed points*—points in parameter space that remain invariant under RG transformations [37]. Let  $K$  denote the set of couplings of the system. In the vicinity of a fixed point  $K^*$ , the RG transformation can be linearized:

$$K'_n = K_n^* + \delta K'_n, \quad (1.23)$$

$$\delta K'_n = \sum_m M_{nm} \delta K_m, \quad (1.24)$$

with

$$M_{nm} \equiv \left. \frac{\partial K'_n}{\partial K_m} \right|_{K=K^*}. \quad (1.25)$$

The eigenvalue problem

$$M_{nm}^{(\ell)} e_m^{(\sigma)} = \Lambda_\ell^{(\sigma)} e_n^{(\sigma)} \quad (1.26)$$

satisfies the semigroup property

$$\Lambda_\ell^{(\sigma)} \Lambda_{\ell'}^{(\sigma)} = \Lambda_{\ell\ell'}^{(\sigma)}, \quad (1.27)$$

implying the scaling form

$$\Lambda_\ell^{(\sigma)} = \ell^{y_\sigma}, \quad (1.28)$$

where  $y_\sigma$  is the scaling exponent associated with the eigenvector  $e^{(\sigma)}$  [37].

A direction is called *relevant* if  $y_\sigma > 0$ , since perturbations along it grow under coarse-graining and drive the system away from  $K^*$ . Directions with  $y_\sigma < 0$  are *irrelevant*, as they shrink and vanish upon approaching the critical fixed point. Marginal directions have  $y_\sigma = 0$  and require higher-order analysis [37].

Instead of the coupling-matrix formalism introduced above, the renormalization group can be formulated in terms of an action defined through a set of operators. In the operator language, the linearized RG corresponds to operator mixing near the fixed point. While the operator formalism is more general, for the sake of intuition we adopt the simpler matrix formulation. A comprehensive description of the operator approach can be found in [2].

As an example with two relevant variables—the reduced temperature  $\varepsilon$  and an external field  $h$ —the correlation length scales as

$$\xi(\varepsilon, h) = \ell \xi(\ell^{y_\varepsilon} \varepsilon, \ell^{y_h} h). \quad (1.29)$$

Choosing  $h = 0$  and  $\ell = \varepsilon^{-1/y_\varepsilon}$  gives

$$\xi(\varepsilon) = \varepsilon^{-1/y_\varepsilon} \xi(1). \quad (1.30)$$

Since  $\xi(\varepsilon) \propto \varepsilon^{-\nu}$ , we identify  $y_\varepsilon = 1/\nu$ .

Similarly, the singular part of the free energy density obeys

$$f(\varepsilon, h) = \ell^{-d} f(\ell^{y_\varepsilon} \varepsilon, \ell^{y_h} h). \quad (1.31)$$

Choosing  $\ell = \varepsilon^{-1/y_\varepsilon}$  yields the scaling form

$$f(\varepsilon, h) = \varepsilon^{d/y_\varepsilon} \tilde{f}(h/\varepsilon^{y_h/y_\varepsilon}). \quad (1.32)$$

From this we obtain the standard scaling relations:

$$\begin{aligned} 2 - \alpha &= d\nu = \frac{d}{y_\varepsilon}, \\ \Delta &= \frac{y_h}{y_\varepsilon}. \end{aligned} \quad (1.33)$$

Finally, an irrelevant coupling  $u$  with exponent  $y_u < 0$  transforms under coarse-graining as

$$u' = \ell^{y_u} u. \quad (1.34)$$

Using  $\ell = \varepsilon^{-1/y_\varepsilon}$  near criticality, this becomes

$$u' = u \varepsilon^{-y_u/y_\varepsilon} = u \varepsilon^{|y_u|/y_\varepsilon} \rightarrow 0 \quad \text{as } \varepsilon \rightarrow 0, \quad (1.35)$$

showing that irrelevant variables vanish in the scaling limit [37].

### 1.2.3. FINITE-SIZE SCALING

In a finite system, true continuous phase transitions do not occur, since singularities in thermodynamic quantities require the thermodynamic limit. Nevertheless, both simulations and experiments are necessarily performed on systems of finite linear size  $L$ . This naturally raises the question of whether it is still possible to observe and characterize the effects of a phase transition in a finite system.

One powerful approach is *finite-size scaling* (FSS), in which one studies how thermodynamic quantities, such as the order parameter, scale with the system size at or near criticality. As we will see, the order parameter at the critical point follows a power law in  $L$ , allowing the extraction of critical exponents from finite systems [37].

Near the fixed point of the renormalization group (RG), the singular part of the free energy density can be expressed in terms of the right eigenvectors of the linearized RG transformation:

$$f_s(\varepsilon, h, \dots, L^{-1}) = \ell^{-d} f_s(\varepsilon \ell^{y_\varepsilon}, h \ell^{y_h}, \dots, L^{-1} \ell). \quad (1.36)$$

Here,  $\varepsilon = (T - T_c)/T_c$  is the reduced temperature,  $h$  the external field, and  $L^{-1}$  appears as an additional scaling variable. The variable  $L^{-1}$  behaves as a relevant eigenvector with exponent  $y_L = 1$ , since rescaling lengths by a factor  $\ell$  transforms the system size as  $L \rightarrow L/\ell$ .

For simplicity, let us focus only on the dependence on  $\varepsilon$  and  $L$ . Choosing  $\ell = \varepsilon^{-1/y_\varepsilon}$ , we obtain:

$$f_s(\varepsilon, L^{-1}) = |\varepsilon|^{2-\alpha} F(L^{-1} |\varepsilon|^{-1/y_\varepsilon}). \quad (1.37)$$

This scaling form is exact for periodic boundary conditions, while for open boundaries additional surface scaling fields modify the scaling function [50].

Since  $|\varepsilon|^{-1/y_\varepsilon} = |\varepsilon|^{-\nu} = \xi_\infty$ , where  $\xi_\infty$  is the correlation length in the thermodynamic limit, the scaling variable can be interpreted as the ratio  $L/\xi_\infty$ . For finite  $L$ , all thermodynamic quantities remain finite—there are no true divergences. Rearranging the scaling form gives:

$$f_s(\varepsilon, L^{-1}) = L^{\frac{\alpha-2}{\nu}} \tilde{F}(\varepsilon L^{1/\nu}), \quad (1.38)$$

where  $\tilde{F}$  is an analytic scaling function for any finite  $L$ .

We now turn to the behavior of the order parameter at  $h = 0$ . By definition,

$$m(\varepsilon, L^{-1}) = \left. \frac{\partial f_s}{\partial h} \right|_{h=0} = \varepsilon^{\frac{d-y_h}{y_\varepsilon}} F_M(\varepsilon^{-\nu} L^{-1}) = L^{-d+y_h} \tilde{F}_M(\varepsilon L^{y_\varepsilon}), \quad (1.39)$$

where  $F_M$  and  $\tilde{F}_M$  are universal scaling functions. Using the standard definitions of the critical exponents,

$$\beta = \frac{d - y_h}{y_\varepsilon}, \quad \nu = \frac{1}{y_\varepsilon}, \quad (1.40)$$

we find that, at the critical point of the infinite system ( $t = 0$ ), the order parameter scales with system size as

$$m(0, L) \propto L^{-\beta/\nu}. \quad (1.41)$$

Thus, finite-size scaling at the critical point provides a direct way to extract the ratio  $\beta/\nu$  from numerical simulations or experiments, even in the absence of a true singularity.

### 1.3. KIBBLE-ZUREK MECHANISM

At the critical point of a continuous quantum phase transition, both the correlation length  $\xi$  and the relaxation time  $\tau$  diverge as power laws with respect to the distance from the critical point,  $|\varepsilon| = |g - g_c|/g$ , where  $g$  is some generic tuning parameter:

$$\xi \sim |\varepsilon|^{-\nu}, \quad (1.42)$$

$$\tau \sim |\varepsilon|^{-\nu z}, \quad (1.43)$$

with  $\nu$  and  $z$  being the correlation length and dynamical critical exponents, respectively.

If the system is driven linearly in time across the transition point with a constant rate  $s$ , the evolution ceases to be adiabatic when the rate of change  $|\dot{\varepsilon}/\varepsilon|$  becomes comparable to the energy gap  $\Delta \sim |\varepsilon|^{\nu z}$ . This breakdown of adiabaticity occurs at a characteristic time  $-\hat{t}$  given by

$$\hat{t} \sim s^{-\frac{\nu z}{1+\nu z}}. \quad (1.44)$$

This moment marks the onset of the impulse regime in the adiabatic-impulse-adiabatic approximation: the state effectively "freezes" and remains out of equilibrium until after  $+\hat{t}$ , when adiabatic evolution resumes, as illustrated in Figure 1.2. At the freeze-out time, the correlation length is

$$\hat{\xi} \sim s^{-\mu}, \quad (1.45)$$

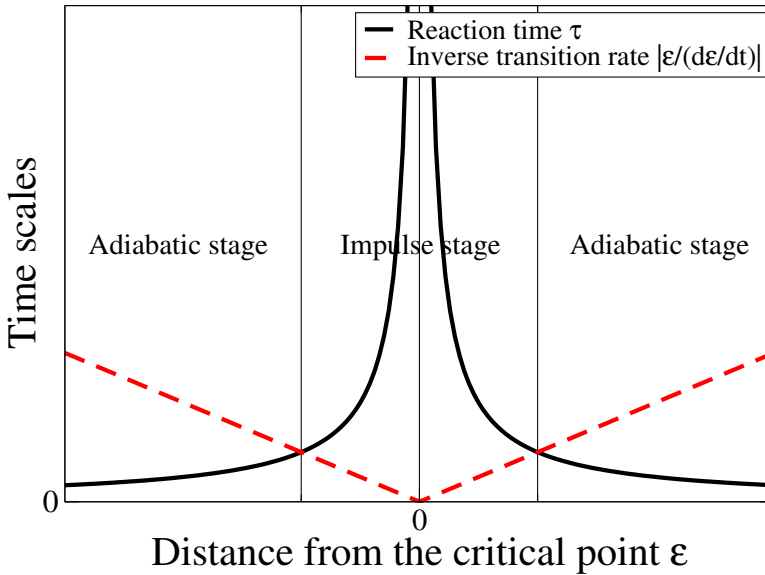


Figure 1.2.: Sketch of the reaction time  $\tau$  as a function of the distance to the dimensionless critical point  $\varepsilon$ . The red dash line the inverse transition rate for a linear quench. When reaction time equals the inverse transition rate the evolution enters the impulse regime. This figure was adapted from [51].

where the exponent  $\mu$  is defined as

$$\mu = \frac{\nu}{1 + \nu z}. \quad (1.46)$$

Once the system exits the non-adiabatic regime and enters the ordered phase, it "realizes" the symmetry has been spontaneously broken, and domains of size  $\hat{\xi}$  begin to form [52]. In one-dimensional systems, these domains are separated by defects—domain walls or kinks—whose density  $n_k$  scales inversely with the correlation length:

$$n_k \sim \hat{\xi}^{-1} \sim s^\mu. \quad (1.47)$$

Thus, for a *linear quench*, the scaling of defect density is uniquely determined by the critical exponents  $\nu$  and  $z$ , which are characteristic of the transition's universality class.

An illustrative example of kink formation in experiments is presented in Figure 1.3, adapted from [33]. The figure shows the state of an array of Rydberg atoms following a slow quench into a  $\mathbb{Z}_3$  symmetry-broken phase, crossing the critical point at  $(\Omega = 1, R_b/a = 2.16)$  in the upper panel and  $(\Omega = 1, R_b/a = 2.43)$  in the lower panel, where  $\Omega$  and  $R_b$  are the Rabi frequency and Rydberg blockade radius defined in 1.10 and 3.2b respectively, and  $a$  is the interatomic distance. Two distinct types of kinks can be observed: in the upper panel, kinks correspond to Rydberg atoms being brought closer together, whereas in the lower panel, kinks result in Rydberg atoms being spaced further

apart. A more detailed classification and discussion of kink types in one-dimensional Rydberg atom platforms is provided in chapters 2 and 3 of this thesis.

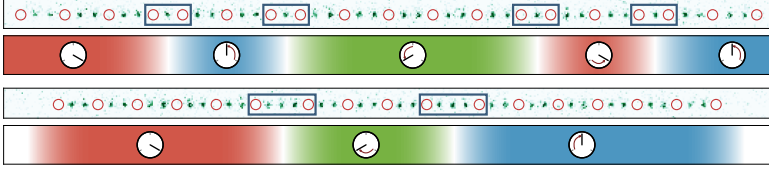


Figure 1.3.: Example of kink formation following a slow quench into the  $\mathbb{Z}_3$  symmetry-broken phase, adapted from [33]. The upper panel corresponds to parameters ( $\Omega = 1$ ,  $R_b/a = 2.16$ ), and the lower panel to ( $\Omega = 1$ ,  $R_b/a = 2.43$ ). Two types of kinks are visible: in the upper panel, kinks bring Rydberg atoms closer together, while in the lower panel, they increase their spacing. A detailed discussion of kink types in one-dimensional Rydberg platforms is provided in chapters 1 and 2.

### 1.3.1. KIBBLE–ZUREK SCALING ACROSS A KOSTERLITZ–THOULESS TRANSITION

The Kosterlitz-Thouless (KT) transition [53, 54] differs from conventional second-order phase transitions in that it exhibits an essential singularity rather than a power-law divergence in the correlation length and relaxation time. Near the critical point, the correlation length diverges as

$$\xi(\epsilon) = \xi_0 \exp\left(\frac{2a}{\sqrt{|\epsilon|}}\right), \quad (1.48)$$

where  $\epsilon$  is the distance to the critical point, and  $\xi_0$  and  $a$  are non-universal constants. The corresponding energy gap closes according to

$$\Delta(\epsilon) = \Delta_0 \exp\left(-\frac{2a}{\sqrt{|\epsilon|}}\right), \quad (1.49)$$

with  $\Delta_0$  another non-universal constant.

Under a linear quench  $\epsilon(t) = st$ , the Kibble–Zurek (KZ) mechanism predicts a breakdown of adiabatic evolution at a characteristic time  $\hat{t}$ , when the relaxation time  $\tau(\epsilon) \sim \Delta^{-1}(\epsilon)$  equals the inverse rate of change of the control parameter:

$$\tau(\hat{\epsilon}) = \frac{\hat{\epsilon}}{s}. \quad (1.50)$$

Solving this condition using the KT scaling form for  $\Delta(\epsilon)$ , one finds

$$\hat{t} = \frac{a^2/s}{\mathcal{W}^2(a\sqrt{\Delta_0/s})}, \quad (1.51)$$

where  $\mathcal{W}$  is the Lambert W function. The corresponding freeze-out value of the control parameter is

$$\hat{\epsilon} = \hat{t}s = \frac{a^2}{\mathcal{W}^2(a\sqrt{\Delta_0/s})}. \quad (1.52)$$

Evaluating the correlation length at this freeze-out scale gives

$$\hat{\xi} = \xi_0 \exp \left[ 2\mathcal{W} \left( a\sqrt{\Delta_0/s} \right) \right], \quad (1.53)$$

which grows faster than any power law in  $1/s$ , but slower than an exponential.

An alternative, approximate approach treats the KT transition as a conventional second-order transition with an effective correlation length exponent  $\nu \rightarrow \infty$ , leading to a scaling of the freeze-out length as  $\hat{\xi} \sim s^{-\mu}$  with  $\mu \rightarrow 1$ . While this power-law approximation captures the asymptotic behavior in the  $s \rightarrow 0$  limit, it becomes inaccurate at realistic quench rates. In practice, exponential and logarithmic corrections due to the essential singularity significantly reduce the effective exponent [55, 56].

## 1.4. FINITE-TIME SCALING

As previously mentioned, at the critical point of a continuous phase transition, the correlation length  $\xi$  and relaxation time  $\tau$  diverge. This poses a challenge for numerical simulations, which are inherently restricted to finite system sizes and finite timescales. We already showed that it is possible to extract universal information about critical phenomena from finite systems using finite-size scaling (FSS) [38]. The central assumption behind FSS is that when a system undergoes a renormalization-group (RG) transformation, its coupling constants flow in the same way as in the thermodynamic limit, even though the system size  $L$  is finite. As a result, critical exponents can be extracted by studying how observables scale with  $L$  [38].

An analogous concept holds in the time domain, known as finite-time scaling (FTS) [57]. FTS becomes relevant when a system is dynamically driven through a phase transition at a finite rate, for example by linearly changing a control parameter  $\epsilon(t) = st$ , where  $s$  is the rate of the quench. In such cases, the timescale set by the driving rate competes with the diverging relaxation time near criticality. When the quench is sufficiently fast, the driving rate  $s$  itself limits the growth of correlations, playing a similar role to the inverse system size in FSS [58, 59].

The FTS hypothesis assumes that even though  $\epsilon$  now depends on time, the order parameter  $M(t, \epsilon)$  obeys a dynamical scaling transformation consistent with RG theory. Under a rescaling by a factor  $b$ , time and the reduced coupling transform as [58, 59]:

$$M(t, \epsilon) = b^{-\beta/\nu} M(tb^{-z}, \epsilon b^{1/\nu}), \quad (1.54)$$

where  $z$  is the dynamical critical exponent. Since the control parameter varies linearly in time as  $\epsilon(t) = st$ , we can instead express the scaling in terms of a quench rate  $s$ :

$$M(t, s) = b^{-\beta/\nu} M(tb^{-z}, sb^{1/\nu}), \quad (1.55)$$

where  $\mu$  is the Kibble-Zurek critical exponent  $\mu = \nu/(1 + z\nu)$ .

Choosing the rescaling factor  $b = s^{-\mu}$  yields a scaling form that relates the order parameter to both the quench rate and the instantaneous value of the control parameter:

$$M(\epsilon, s) = s^{\beta\mu/\nu} m_2(\epsilon s^{-\mu/\nu}), \quad (1.56)$$

with  $m_2$  another universal function. This relation enables us to extract critical exponents by analyzing how observables behave as a function of the quench rate  $s$ . Two particularly useful consequences follow from this scaling form:

- Shift of the effective critical point: The value of  $\epsilon$  at which  $M = 0$ , denoted  $\epsilon_0(s)$ , shifts with the quench rate according to

$$\epsilon_0(s) = \epsilon_c + K s^{\mu/\nu}, \quad (1.57)$$

where  $K$  is a non-universal constant.

- Scaling of the order parameter at criticality: At  $\epsilon = \epsilon_c$ , the order parameter scales with the quench rate as

$$M(\epsilon_c, s) \propto s^{\beta\mu/\nu}. \quad (1.58)$$

FTS has proven to be a powerful tool for extracting critical properties from dynamic protocols, especially in quantum simulations or experiments where time, rather than system size, is the natural scale. It also offers a way to circumvent limitations imposed by equilibrium scaling, by accessing universal behavior through out-of-equilibrium dynamics [60].

## 1.5. TENSOR NETWORKS

The dimension of the Hilbert space of a quantum many body system increases exponentially with the number of particles in the system  $d^L$ , where  $d$  is the dimensionality of the single spin Hilbert space and  $L$  is the system size. For instance, the Hamiltonian describing a 100 spins 1/2 system has a dimension of  $2^{100}$ . Thus, storing a single eigenstate of that Hamiltonian would require around  $10^{21}$  Gb of storage memory, which is beyond the capabilities of today's computers. As a result, approximate methods are necessary for calculating the dynamics of quantum many-body systems.

Tensor Networks (TNs) [15, 61, 62] are a mathematical framework for modeling states in quantum many-body (QMB) systems. They provide a compact representation that encodes the entanglement structure among constituent particles. Beyond serving as a descriptive framework, TNs also function as a powerful approximation and compression technique, efficiently representing states with limited entanglement. Although originally developed for quantum many-body systems, their versatility has extended their use to diverse fields such as high-energy physics and machine learning [5]. In the QMB context, a many-body quantum state is represented by a network of tensors connected by entanglement bonds.

There are multiple TNs representations, i.e. MPS, PEP, MERA, etc [5, 63, 64]. The representation that best describes the system will depend on the system dimensions and the entanglement and correlation structure. Thus, the TN representation already gives

some clear and accessible information about the internal structure of the system. In the rest of this thesis we will focus on the widely used representations, MPS, which is most efficient for 1D and quasi 1D gapped systems, and it is a particular area where TNs are arguably the leading choice.

Typically, the relevant quantum many-body systems studied by physicists have local interactions. The ground state of gapped Hamiltonians with local interactions obeys the area law for entanglement entropy [5, 65]. This theorem states that the entanglement entropy of a system's region grows with the size of the region's boundary rather than with the region's size. This property is particularly relevant in one-dimensional (1D) systems, where the region's boundary, and therefore the entanglement entropy, are constant with the chain's length.

This property gives an extra advantage for TNs representation, since from the immense Hilbert space, only a tiny region satisfies the area Law, which corresponds to the low energy states, which commonly are the interesting states for physicists. It is precisely the states on the Area law region the ones that are targeted by TN algorithms [5].

### 1.5.1. MATHEMATICAL DESCRIPTION

At the core of any tensor network representation lies the *Singular Value Decomposition* (SVD). This linear algebraic tool is fundamental to the construction and understanding of matrix product states (MPS) in the context of quantum many-body systems [15].

Given an arbitrary rectangular matrix  $M$  of dimensions  $(a \times b)$ , the SVD allows us to decompose it as

$$M = USV^\dagger, \quad (1.59)$$

where  $U$  has orthogonal columns and  $V$  orthogonal rows, and  $S$  is a diagonal matrix with non-negative real numbers known as *singular values*.

In the context of quantum many-body physics, this decomposition plays a key role: it corresponds to the *Schmidt decomposition* of a bipartite quantum system. This connection becomes particularly powerful when we aim to transform a general pure quantum state into the MPS form.

Consider a generic pure quantum state on a one-dimensional lattice of  $L$  sites, each with local Hilbert space dimension  $d$ :

$$|\psi\rangle = \sum_{\sigma_1, \dots, \sigma_L} c_{\sigma_1, \dots, \sigma_L} |\sigma_1, \dots, \sigma_L\rangle, \quad (1.60)$$

where the total number of complex coefficients  $c_{\sigma_1, \dots, \sigma_L}$  is  $d^L$ , which grows exponentially with system size.

This state can be expressed as an MPS through *iterative* procedure based on successive applications of the SVD. First, the coefficient tensor  $c_{\sigma_1, \dots, \sigma_L}$  is reshaped into a matrix:

$$C_{\sigma_1, (\sigma_2 \dots \sigma_L)}, \quad (1.61)$$

treating  $\sigma_1$  as a row index and the remaining indices as a combined column index. We

then perform an SVD:

$$\begin{aligned}
 c_{\sigma_1, \dots, \sigma_L} &= C_{\sigma_1, (\sigma_2 \dots \sigma_L)} \\
 &= \sum_{a_1=1}^{r_1} U_{\sigma_1, a_1} S_{a_1, a_1} \left( V^\dagger \right)_{a_1, (\sigma_2 \dots \sigma_L)} \\
 &\equiv \sum_{a_1=1}^{r_1} A_{\sigma_1, a_1} C_{a_1, (\sigma_2 \dots \sigma_L)},
 \end{aligned} \tag{1.62}$$

where we define  $A_{\sigma_1, a_1} = U_{\sigma_1, a_1} S_{a_1, a_1}$  and  $C = SV^\dagger$ .

This process is repeated on  $C_{a_1, (\sigma_2 \dots \sigma_L)}$ , treating  $a_1 \sigma_2$  as a new row index, and again applying the SVD. Iterating this decomposition yields the MPS form:

$$c_{\sigma_1, \dots, \sigma_L} = A^{\sigma_1} A^{\sigma_2} \dots A^{\sigma_L}. \tag{1.63}$$

Thus, any quantum many-body state can be expressed as:

$$|\psi\rangle = \sum_{\sigma_1, \dots, \sigma_L} c_{\sigma_1, \dots, \sigma_L} |\sigma_1, \dots, \sigma_L\rangle = \sum_{a_1, \dots, a_{L-1}} \sum_{\sigma_1, \dots, \sigma_L} A_{a_1}^{\sigma_1} A_{a_1 a_2}^{\sigma_2} \dots A_{a_{L-1}}^{\sigma_L} |\sigma_1, \dots, \sigma_L\rangle. \tag{1.64}$$

Thanks to the orthogonal columns of  $U$  in the SVD, the matrices  $A$  satisfy the *left-normalized* condition:

$$\sum_{\sigma_\ell} (A^{\sigma_\ell})^\dagger A^{\sigma_\ell} = I. \tag{1.65}$$

Similarly, if the decomposition is performed from right to left, we obtain matrices  $B$  that are *right-normalized*:

$$\sum_{\sigma_\ell} B^{\sigma_\ell} (B^{\sigma_\ell})^\dagger = I, \tag{1.66}$$

due to the orthogonal rows of  $V^\dagger$ . A particularly useful form of an MPS is the *mixed-canonical form*, where the state is expressed as:

$$|\psi\rangle = \sum_{\sigma_1, \dots, \sigma_L} A^{\sigma_1} \dots A^{\sigma_\ell} S B^{\sigma_{\ell+1}} \dots B^{\sigma_L} |\sigma_1, \dots, \sigma_L\rangle, \tag{1.67}$$

with  $S$  the diagonal matrix of singular values from the SVD at bond  $\ell$ . In this form, the *Schmidt decomposition* of the state across the bipartition at site  $\ell$  is immediate:

$$|a_\ell\rangle_A = \sum_{\sigma_1, \dots, \sigma_\ell} A^{\sigma_1} \dots A^{\sigma_\ell} |\sigma_1, \dots, \sigma_\ell\rangle, \tag{1.68}$$

$$|a_\ell\rangle_B = \sum_{\sigma_{\ell+1}, \dots, \sigma_L} B^{\sigma_{\ell+1}} \dots B^{\sigma_L} |\sigma_{\ell+1}, \dots, \sigma_L\rangle. \tag{1.69}$$

The full state then takes the Schmidt form:

$$|\psi\rangle = \sum_a s_{a_\ell} |a_\ell\rangle_A |a_\ell\rangle_B. \tag{1.70}$$

This decomposition is only valid when both  $|a_\ell\rangle_A$  and  $|a_\ell\rangle_B$  are orthonormal. The mixed-canonical form ensures this through the canonical properties of the  $A$  and  $B$  tensors:

$$\langle a'_\ell |_A | a_\ell \rangle_A = \sum_{\sigma_1, \dots, \sigma_\ell} (A^{\sigma_\ell \dagger} \dots A^{\sigma_1 \dagger} A^{\sigma_1} \dots A^{\sigma_\ell})_{a'_\ell, a_\ell} = \delta_{a'_\ell, a_\ell}, \quad (1.71)$$

$$\langle a'_\ell |_B | a_\ell \rangle_B = \sum_{\sigma_{\ell+1}, \dots, \sigma_L} (B^{\sigma_{\ell+1}} \dots B^{\sigma_L} B^{\sigma_L \dagger} \dots B^{\sigma_{\ell+1} \dagger})_{a'_\ell, a_\ell} = \delta_{a'_\ell, a_\ell}. \quad (1.72)$$

The difference between both contractions is subtle, their distinction lies in the direction of the contraction. Equation (1.71) performs the contraction from the left boundary toward site  $\ell$ , whereas Eq. (1.72) performs it from the right boundary toward the same site.

The Schmidt decomposition also provides direct access to the *entanglement properties* of the state. If we write the state in bipartite form,

$$|\psi\rangle = \sum_{i,j} \Psi_{ij} |i\rangle_A |j\rangle_B = \sum_{a=1}^{\min(a,b)} s_a |a\rangle_A |a\rangle_B, \quad (1.73)$$

then the *reduced density matrix* of subsystem  $A$  is

$$\hat{\rho}_A = \sum_a s_a^2 |a\rangle_A \langle a|_A. \quad (1.74)$$

From this, we can compute the *von Neumann entanglement entropy* as

$$S_{A|B} = -\text{Tr} \hat{\rho}_A \log_2 \hat{\rho}_A = -\sum_{a=1}^r s_a^2 \log_2 s_a^2, \quad (1.75)$$

which quantifies the bipartite entanglement between subsystems  $A$  and  $B$ .

The dimensions of the matrices composing an MPS, known as the bond dimension, are directly related to the entanglement entropy of the system. In gaped systems, where the maximum entropy saturates and does not scale with the system size, an accurate approximation can be achieved by truncation the maximum bond dimension to a finite value  $D$ . This truncation drastically reduces the number of parameters required to describe the quantum state of a system of size  $L$  from  $d^L$  to a manageable  $LdD^2$ .

### 1.5.2. GRAPHICAL REPRESENTATION

TNs allow for a very natural and simple graphical representation of quantum many-body states. In this formalism, each tensor is represented by a node in a graph, and each index of the tensor corresponds to a line (or leg) emanating from the node. The number of legs in a node indicates the rank of the tensor. Some simple examples of the representation of tensors are depicted in Figure 1.4.

Connections between nodes, represented by lines joining two tensors, correspond to contracted indices. In contrast, lines that remain open, that is, which are not connected to any other tensor, correspond to the physical indices associated with the degree of freedom of the system, as depicted in Figure 1.5.

Although there is no strict convention governing the shapes used to represent tensors in these diagrams, several common practices have become widespread in the literature [66, 67]. Circles are typically used to represent generic tensors. Squares often denote specific types of operators, such as orthogonal or unitary matrices. Triangles are

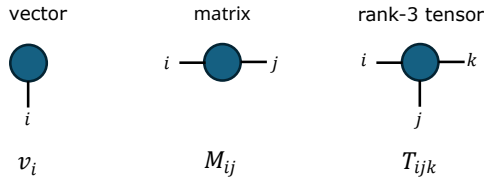


Figure 1.4.: Graphical representation of single tensors. A tensor is represented by a node, with the legs emanating from it corresponding to the indices of the tensor.

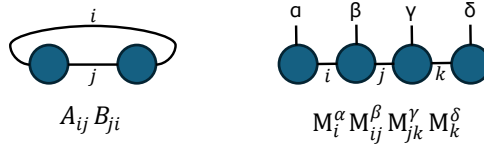


Figure 1.5.: Graphical example of basic tensor network contractions. Contracted indices are represented by lines joining two tensors.

commonly used for isometries, with the orientation of the triangle typically pointing toward the lower-dimensional space. Figure 1.6 shows the graphical representation of the transformation of a quantum many-body state from a naive basis into a TNs representation. This algorithm is rarely employed since we usually do not have the quantum state in its computational basis and we usually start directly with an MPS form, but it help us illustrate the mapping between computational and MPS basis.

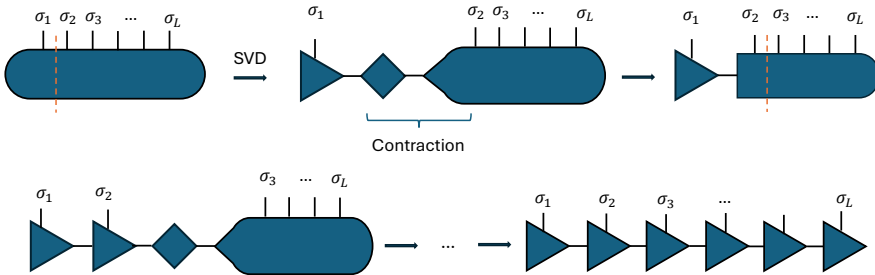


Figure 1.6.: Graphical representation of the conversion of a quantum many-body pure state into a matrix product state (MPS). The oval denotes the tensor corresponding to the computational basis of the quantum many-body state. By applying successive singular value decompositions, the state is expressed as a product of left-normalized tensors, represented by triangles pointing to the right, and singular value matrices, represented by diamonds. The tip of each triangle indicates the smaller dimension of the decomposition, excluding the physical index  $\sigma$ .

This graphical notation is also very useful for describing operations involving TNs. For instance, Figure 1.7 shows the graphical representation of the overlap between two quantum states,  $\langle\phi|\psi\rangle$ . It is important to note that although the result of a TN contraction is independent of the contraction order, the computational cost strongly depends on it. A naive contraction, where matrix indices are combined first followed by the physical indices, as depicted in Figure 1.7(a), requires on the order of  $O(d^L)$  multiplications. In contrast, performing the contraction as illustrated in Figure 1.7(b) reduces the cost to  $O(LD^3d)$ .

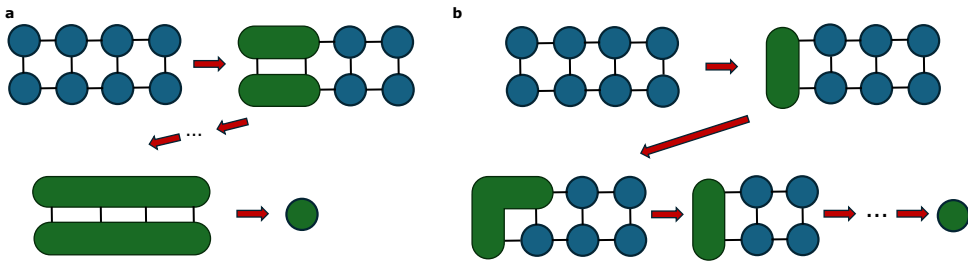


Figure 1.7.: Graphical representation of the overlap between two quantum states,  $\langle\phi|\psi\rangle$ . (a) A naive contraction scales as  $O(d^L)$ , while (b) an optimized contraction reduces the computational cost to  $O(LD^3d)$ .

After this brief introduction about TNs we are ready for an explanation of the basic algorithms used during this thesis.

### 1.5.3. DENSITY-MATRIX RENORMALIZATION GROUP

The density matrix renormalization group (DMRG) algorithm [14, 15, 68] is a variational algorithm for optimizing the MPS representation of a quantum state  $|\psi\rangle$  that minimizes the energy of a given quantum many-body Hamiltonian:

$$E = \frac{\langle\psi|\hat{H}|\psi\rangle}{\langle\psi|\psi\rangle}. \quad (1.76)$$

This problem can be solved using the Lagrange multipliers method:

$$\langle\psi|\hat{H}|\psi\rangle = \lambda\langle\psi|\psi\rangle. \quad (1.77)$$

This equation is non-linear, but can be solved iteratively in a very straightforward manner in the context of matrix product states. Expressing the quantum-states as MPS and the Hamiltonian as a MPO, the 2-sites DMRG looks for the pair of sites that minimizes Eq. (1.77). This minimization is done by keeping all matrices constant except the ones that are optimized:

$$\frac{\partial}{\partial(M_j^\dagger M_{j+1}^\dagger)} (\langle\psi|\hat{H}|\psi\rangle - \lambda\langle\psi|\psi\rangle) = 0. \quad (1.78)$$

Figure 1.8 shows the above equation in graphic notation. Considering systems with open

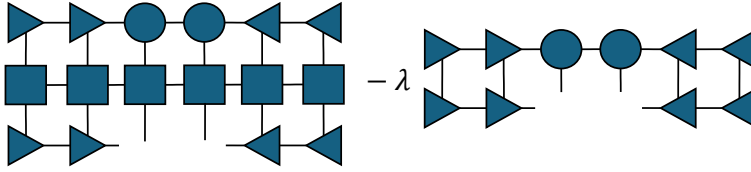


Figure 1.8.: Graphical notation of the eigenvalue equation in the two-sites Density-Matrix Renormalization Group algorithm. Right-pointing and left-pointing triangles denote left- and right-normalized MPS tensors, respectively. Circles represent MPS tensors that are not necessarily normalized, while squares denote single-site MPOs.

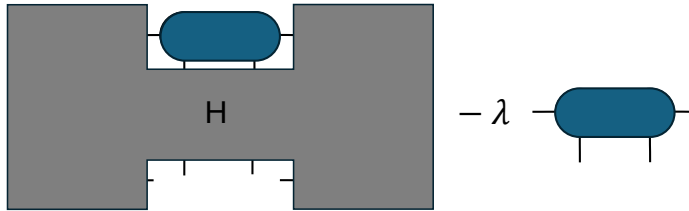


Figure 1.9.: Simplified form of the eigenvalue equation in the two-site Density-Matrix Renormalization Group (DMRG) algorithm. The operator  $H$  denotes the effective Hamiltonian obtained by contracting the entire tensor network except for the two sites being updated, whose joint tensor is represented by the oval shape.

boundary conditions only, the structure considered in Figure 1.8 can be simplified by applying left and right canonical contraction, as depicted in Figure 1.9. When the optimization problem transforms into a simple eigenvalue problem:

$$\hat{H}M - \lambda M = 0. \quad (1.79)$$

After finding the eigenvector for the smallest eigenvalue, the original form of the MPS is restored and the process is repeated with the next pair of matrices. This iteration process is repeated until the desired convergence in the energy or other observable of interest is obtained.

#### 1.5.4. TIME-EVOLUTION ALGORITHMS FOR ONE-DIMENSIONAL SYSTEMS

This project will use TN algorithms to study the time evolution of many-body systems. Up to date, several methods exist, each one has its advantages and disadvantages. The time-evolving block decimation algorithm (TEBD) [66, 69, 70] and the time-dependent variational principle (TDVP) [66, 71, 72] are two of the most commonly used algorithms. Both algorithms follow different principles.

### TIME-EVOLVING BLOCK DECIMATION

The time-evolving block decimation (TEBD) algorithm [66, 69, 70] was introduced in 2004 by G. Vidal et al. [70]. It approximates the time-evolution operator  $\hat{U}(\delta) = e^{-i\delta\hat{H}}$  as a product of local operators that are applied repeatedly to the quantum state to simulate the time evolution.

This method is more appropriate for Hamiltonians with short-range interactions, commonly referred to as local Hamiltonians. Local Hamiltonians can be written as:

$$\hat{H} = \sum_{j=0}^{N-1} \hat{h}_{j,j+1}. \quad (1.80)$$

If the Hamiltonian is split in even and odd summands, using the Baker-Campbell-Hausdorf formula to second order, the time-evolution operator can be written as:

$$\exp(-i\delta H) \approx \exp\left(-i\frac{\delta}{2}\hat{H}_{\text{even}}\right) \exp(-i\delta\hat{H}_{\text{odd}}) \exp\left(-i\frac{\delta}{2}\hat{H}_{\text{even}}\right). \quad (1.81)$$

Since the even and odd summands are internally commuting, each summand can be exponentiated individually:

$$\exp(-i\delta\hat{H}_{\text{even}}) = \exp\left(-i\delta \sum_{j \text{ even}} \hat{h}_{j,j+1}\right) = \prod_{j \text{ even}} \exp(-i\delta\hat{h}_{j,j+1}). \quad (1.82)$$

This approach can be generalized to more complicated divisions of the Hamiltonian into internally commuting parts.

Figure 1.10 shows an example of the application of a two-site interaction time evolution operator to a MPS in the TN graphical notation.

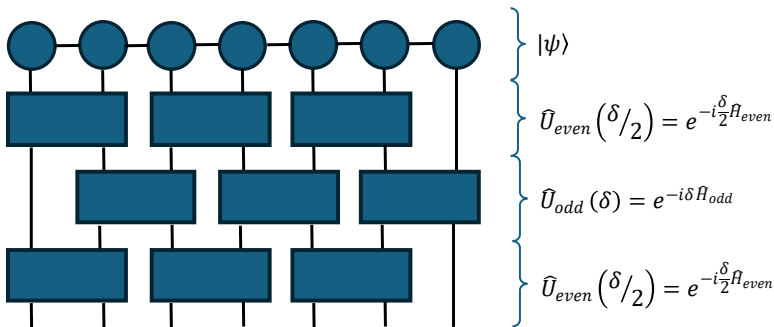


Figure 1.10.: Representation of a second-order time step for a two-site interaction Hamiltonian using the second-order TEBD algorithm. The time-evolution operator is decomposed into non-commuting even and odd terms. Each time step consists of three layers of gates applied sequentially.

Overall, TEBD is a fast and simple method for simulation the time-evolution of many-body systems, well-suited for short-range interactions.

## TIME-DEPENDENT VARIATIONAL PRINCIPLE

The time-dependent variational principle (TDVP) [66, 71, 72] is an algorithm for approximating the solution of the Schrödinger equation in a quantum system. Unlike the TEBD algorithm, TDVP does not explicitly construct the time-evolution operator but instead projects the Schrödinger equation onto the tangent space of the variational manifold, where the effective equations of motion are obtained and solved iteratively.

The algorithm closely resembles the density matrix renormalization group (DMRG) method. Time evolution can be carried out in two main ways: using a 1-site update (1-site TDVP) or a 2-site update (2-site TDVP). The 1-site formulation evolves strictly within the tangent space at fixed bond dimension, since the projection is taken with respect to each local tensor, as illustrated in Figure 1.11. By contrast, the 2-site formulation allows the bond dimension to increase dynamically, enabling exploration of additional symmetry sectors and a larger variational space. In this case, the procedure no longer corresponds to a strict tangent-space evolution, but the overall structure of the method remains essentially the same.

One advantage of this method that we will use to model Rydberg arrays is that it can handle exponentially decaying long-ranged interactions. However, it is generally slower and less efficient than TEBD, but it can be more robust and accurate in certain situations, as will be shown below.

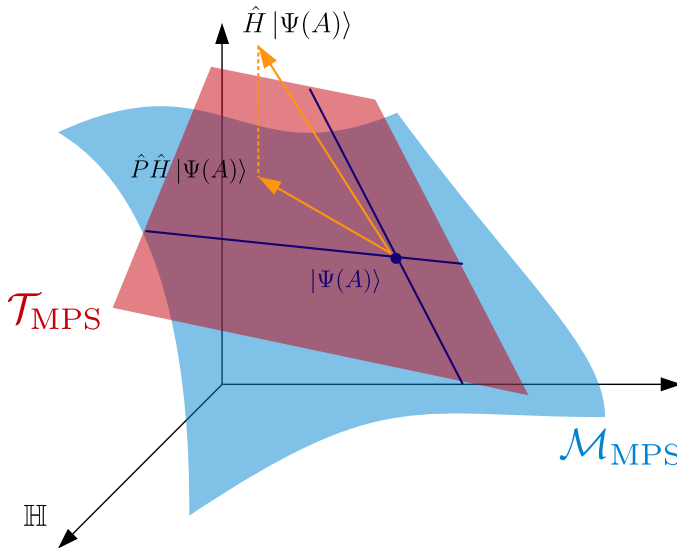


Figure 1.11.: Projection of  $\hat{H}|\Psi\rangle$  onto the tangent space of the MPS manifold. A quantum state  $|\Psi(A)\rangle$  in MPS form belongs to the manifold of MPS  $\mathcal{M}_{\text{MPS}}$  with fixed dimensions. The action of the Hamiltonian  $\hat{H}$  is projected onto the tangent space  $\mathcal{T}_{\text{MPS}}$  of MPS with one updated tensor. Figure adapted from [73].

### 1.5.5. TRUNCATION OF MATRIX PRODUCT STATES

When performing algorithms such as DMRG or TEBD, the bond dimensions of the matrices involved in the MPS representation can grow substantially. As a result, the computational cost increases rapidly, making it essential to develop methods for approximating quantum states while reducing the matrix sizes.

Several techniques exist to approximate a quantum many-body state using tensor network algorithms, while keeping the bond dimensions under control. In this thesis, we have employed only one of these methods: the compression of an MPS via the Singular Value Decomposition (SVD).

As discussed previously, when a system is represented in a mixed-canonical form, the singular value matrix  $S$  between the left- and right-canonical parts corresponds to the Schmidt coefficients, which are directly related to the von Neumann entanglement entropy. For ground states in gapped phases, these Schmidt values typically decay exponentially along the diagonal of the matrix.

Due to this exponential decay, the matrix  $S$  can be truncated, retaining only the largest  $\chi$  singular values, where  $\chi$  is a predefined cutoff. Along with this truncation, the corresponding columns of the left-canonical matrix and rows of the right-canonical matrix are also discarded. The result is a compressed MPS with reduced bond dimension.

One major advantage of this method is its practicality: as will be shown in the description of basic tensor network algorithms, such truncation can be carried out directly during the execution of the algorithm. However, this technique is not without drawbacks. The truncation is inherently *unbalanced*, as the size of each matrix depends on the truncation of the previous step. While this is typically not problematic for small truncation thresholds, it may introduce significant additional error when large truncations are applied.

If higher accuracy is required, the truncated MPS can serve as an initial guess for a more precise variational optimization. Although this thesis does not cover the variational approach in detail, readers interested in a comprehensive discussion are referred to the review by Schollwöck [15].

### 1.5.6. SYMMETRIES AND TENSOR NETWORKS

The implementation of symmetries in tensor networks (TNs) offers significant advantages. Any global symmetry of a many-body Hamiltonian is reflected in the local tensors that represent the system. If a quantum state is invariant under a global symmetry, then all local tensors describing that state transform trivially under the symmetry, and conversely, the invariance of all local tensors implies the global invariance of the states [74–78]. Symmetries can be exploited to impose constraints on the tensors, reducing their dimensionality. In the presence of a global symmetry, the local tensors in a TN representation can be brought into block-diagonal form, which reduces computational costs. This is because operations such as tensor contractions or singular value decompositions can be performed independently on the individual blocks, rather than on the full tensors [78].

Sometimes, local constraints can give rise to effective global symmetries, as in the case of the Rydberg blockade [79, 80]. In this model, strong short-range repulsion forbids the

simultaneous excitation of atoms within a blockade radius  $r$ , giving rise to the so-called  $r$ -site model. For  $r = 1$ , it reduces to the hard-core boson model [81]. The  $r = 1$  blockade respects the parity symmetry of the domain walls, which implies that domain walls can only be created or annihilated in pairs. For  $r = 2$ , domain walls appear in groups of three. As will be shown in Chapter 3 and further discussed in Appendix A, applying an appropriate transformation allows one to express the tensor network in a block-diagonal form that reflects this emergent symmetry.

Furthermore, certain quantum dimer and quantum loop models in ladders can be mapped to the hard-core boson model [82, 83]. Quantum dimer models serve as effective descriptions of spin- $\frac{1}{2}$  systems in the valence-bond basis, while quantum loop models can describe spin-1 chains. Both are widely used as toy models in quantum magnetism. These mappings illustrate how local constraints arise in diverse physical systems and how different models can be related mathematically—highlighting the versatility of TN algorithms for studying lattice Hamiltonians.

# BIBLIOGRAPHY

- [1] F. Alet, A. M. Walczak, and M. P. Fisher. “Exotic quantum phases and phase transitions in correlated matter”. In: *Physica A: Statistical Mechanics and its Applications* 369.1 (2006), pp. 122–142.
- [2] A. Altland and B. D. Simons. *Condensed matter field theory*. Cambridge university press, 2010.
- [3] T. Giamarchi. *Quantum physics in one dimension*. Internat. Ser. Mono. Phys. Oxford: Clarendon Press, 2004. DOI: [10.1093/acprof:oso/9780198525004.001.0001](https://doi.org/10.1093/acprof:oso/9780198525004.001.0001).
- [4] S. Paschen and Q. Si. “Quantum phases driven by strong correlations”. In: *Nature Reviews Physics* 3.1 (2021), pp. 9–26.
- [5] R. Orús. “A practical introduction to tensor networks: Matrix product states and projected entangled pair states”. In: *Annals of physics* 349 (2014), pp. 117–158.
- [6] A. J. James, R. M. Konik, P. Lecheminant, N. J. Robinson, and A. M. Tsvelik. “Non-perturbative methodologies for low-dimensional strongly-correlated systems: From non-abelian bosonization to truncated spectrum methods”. In: *Reports on Progress in Physics* 81.4 (2018), p. 046002.
- [7] M. A. Cazalilla, R. Citro, T. Giamarchi, E. Orignac, and M. Rigol. “One dimensional bosons: From condensed matter systems to ultracold gases”. In: *Reviews of Modern Physics* 83.4 (2011), pp. 1405–1466.
- [8] T. Giamarchi. “Theoretical framework for quasi-one dimensional systems”. In: *Chemical reviews* 104.11 (2004), pp. 5037–5056.
- [9] I. Buluta and F. Nori. “Quantum simulators”. In: *Science* 326.5949 (2009), pp. 108–111.
- [10] V. E. Korepin and F. H. Essler. *Exactly solvable models of strongly correlated electrons*. Vol. 18. World Scientific, 1994.
- [11] P. Francesco, P. Mathieu, and D. Sénéchal. *Conformal field theory*. Springer Science & Business Media, 2012.
- [12] W. M. Foulkes, L. Mitás, R. Needs, and G. Rajagopal. “Quantum Monte Carlo simulations of solids”. In: *Reviews of Modern Physics* 73.1 (2001), p. 33.
- [13] M. Troyer and U.-J. Wiese. “Computational Complexity and Fundamental Limitations to Fermionic Quantum Monte Carlo Simulations”. In: *Physical review letters* 94.17 (2005), p. 170201.
- [14] S. R. White. “Density matrix formulation for quantum renormalization groups”. In: *Physical review letters* 69.19 (1992), p. 2863.

- [15] U. Schollwöck. “The density-matrix renormalization group in the age of matrix product states”. In: *Annals of physics* 326.1 (2011), pp. 96–192.
- [16] J. Eisert, M. Cramer, and M. B. Plenio. “Colloquium: Area laws for the entanglement entropy”. In: *Reviews of modern physics* 82.1 (2010), pp. 277–306.
- [17] I. Bloch, J. Dalibard, and W. Zwerger. “Many-body physics with ultracold gases”. In: *Reviews of modern physics* 80.3 (2008), pp. 885–964.
- [18] A. Browaeys and T. Lahaye. “Many-body physics with individually controlled Rydberg atoms”. In: *Nature Physics* 16.2 (2020), pp. 132–142.
- [19] R. Blatt and C. F. Roos. “Quantum simulations with trapped ions”. In: *Nature Physics* 8.4 (2012), pp. 277–284.
- [20] R. Hanson, L. P. Kouwenhoven, J. R. Petta, S. Tarucha, and L. M. Vandersypen. “Spins in few-electron quantum dots”. In: *Reviews of modern physics* 79.4 (2007), pp. 1217–1265.
- [21] M. Kjaergaard, M. E. Schwartz, J. Braumüller, P. Krantz, J. I.-J. Wang, S. Gustavsson, and W. D. Oliver. “Superconducting qubits: Current state of play”. In: *Annual Review of Condensed Matter Physics* 11.1 (2020), pp. 369–395.
- [22] E. Altman, K. R. Brown, G. Carleo, L. D. Carr, E. Demler, C. Chin, B. DeMarco, S. E. Economou, M. A. Eriksson, K.-M. C. Fu, *et al.* “Quantum simulators: Architectures and opportunities”. In: *PRX quantum* 2.1 (2021), p. 017003.
- [23] I. M. Georgescu, S. Ashhab, and F. Nori. “Quantum simulation”. In: *Reviews of Modern Physics* 86.1 (2014), pp. 153–185.
- [24] H. Bernien, S. Schwartz, A. Keesling, H. Levine, A. Omran, H. Pichler, S. Choi, A. S. Zibrov, M. Endres, M. Greiner, *et al.* “Probing many-body dynamics on a 51-atom quantum simulator”. In: *Nature* 551.7682 (2017), pp. 579–584.
- [25] A. Browaeys, D. Barredo, and T. Lahaye. “Experimental investigations of dipole-dipole interactions between a few Rydberg atoms”. In: *Journal of Physics B: Atomic, Molecular and Optical Physics* 49.15 (2016), p. 152001.
- [26] J. B. Balewski, A. T. Krupp, A. Gaj, S. Hofferberth, R. Löw, and T. Pfau. “Rydberg dressing: understanding of collective many-body effects and implications for experiments”. In: *New Journal of Physics* 16.6 (2014), p. 063012.
- [27] S. Ebadi, T. T. Wang, H. Levine, A. Keesling, G. Semeghini, A. Omran, D. Bluvstein, R. Samajdar, H. Pichler, W. W. Ho, *et al.* “Quantum phases of matter on a 256-atom programmable quantum simulator”. In: *Nature* 595.7866 (2021), pp. 227–232.
- [28] C. Chen, G. Bornet, M. Bintz, G. Emperauger, L. Leclerc, V. S. Liu, P. Scholl, D. Barredo, J. Hauschild, S. Chatterjee, *et al.* “Continuous symmetry breaking in a two-dimensional Rydberg array”. In: *Nature* 616.7958 (2023), pp. 691–695.
- [29] N. E. Myerson-Jain, S. Yan, D. Weld, and C. Xu. “Construction of fractal order and phase transition with Rydberg atoms”. In: *Physical Review Letters* 128.1 (2022), p. 017601.

- [30] J. Zhang, S. H. Cantú, F. Liu, A. Bylinskii, B. Braverman, F. Huber, J. Amato-Grill, A. Lukin, N. Gemelke, A. Keesling, *et al.* “Probing quantum floating phases in Rydberg atom arrays”. In: *Nature Communications* 16.1 (2025), p. 712.
- [31] S. De Léséleuc, V. Lienhard, P. Scholl, D. Barredo, S. Weber, N. Lang, H. P. Büchler, T. Lahaye, and A. Browaeys. “Observation of a symmetry-protected topological phase of interacting bosons with Rydberg atoms”. In: *Science* 365.6455 (2019), pp. 775–780.
- [32] S. Kanungo, J. Whalen, Y. Lu, M. Yuan, S. Dasgupta, F. Dunning, K. Hazzard, and T. Killian. “Realizing topological edge states with Rydberg-atom synthetic dimensions”. In: *Nature communications* 13.1 (2022), p. 972.
- [33] A. Keesling, A. Omran, H. Levine, H. Bernien, H. Pichler, S. Choi, R. Samajdar, S. Schwartz, P. Silvi, S. Sachdev, *et al.* “Quantum Kibble–Zurek mechanism and critical dynamics on a programmable Rydberg simulator”. In: *Nature* 568.7751 (2019), pp. 207–211.
- [34] C. S. Adams, J. D. Pritchard, and J. P. Shaffer. “Rydberg atom quantum technologies”. In: *Journal of Physics B: Atomic, Molecular and Optical Physics* 53.1 (2019), p. 012002.
- [35] M. O. Scully and M. S. Zubairy. *Quantum optics*. Cambridge university press, 1997.
- [36] F. Mintert and M. Vanner. *Quantum Optics*. Lecture notes distributed in the course “Quantum Optics”, Imperial College London, 2020. Unpublished lecture notes. 2020.
- [37] N. Goldenfeld. *Lectures on phase transitions and the renormalization group*. CRC Press, 2018.
- [38] D. J. Amit and V. Martin-Mayor. *Field theory, the renormalization group, and critical phenomena: graphs to computers*. World Scientific Publishing Company, 2005.
- [39] P. W. Higgs. “Broken symmetries and the masses of gauge bosons”. In: *Physical review letters* 13.16 (1964), p. 508.
- [40] M. Laine and K. Rummukainen. “What’s new with the electroweak phase transition?” In: *Nuclear Physics B-Proceedings Supplements* 73.1-3 (1999), pp. 180–185.
- [41] S. Sachdev. “Quantum phase transitions”. In: *Physics world* 12.4 (1999), p. 33.
- [42] M. Vojta. “Quantum phase transitions”. In: *Reports on Progress in Physics* 66.12 (2003), p. 2069.
- [43] A. Millis. “Effect of a nonzero temperature on quantum critical points in itinerant fermion systems”. In: *Physical Review B* 48.10 (1993), p. 7183.
- [44] A. Schröder, G. Aeppli, R. Coldea, M. Adams, O. Stockert, H. Löhneysen, E. Bucher, R. Ramazashvili, and P. Coleman. “Onset of antiferromagnetism in heavy-fermion metals”. In: *Nature* 407.6802 (2000), pp. 351–355.
- [45] H. v. Löhneysen, A. Rosch, M. Vojta, and P. Wölfle. “Fermi-liquid instabilities at magnetic quantum phase transitions”. In: *Reviews of Modern Physics* 79.3 (2007), pp. 1015–1075.

- [46] P. Gegenwart, Q. Si, and F. Steglich. “Quantum criticality in heavy-fermion metals”. In: *nature physics* 4.3 (2008), pp. 186–197.
- [47] K. G. Wilson. “The renormalization group and critical phenomena”. In: *Reviews of Modern Physics* 55.3 (1983), p. 583.
- [48] J. Cardy. *Scaling and renormalization in statistical physics*. Vol. 5. Cambridge university press, 1996.
- [49] S.-k. Ma. “Introduction to the renormalization group”. In: *Reviews of Modern Physics* 45.4 (1973), p. 589.
- [50] M. Campostrini, A. Pelissetto, and E. Vicari. “Finite-size scaling at quantum transitions”. In: *Physical Review B* 89.9 (2014), p. 094516.
- [51] J. Dziarmaga. “Dynamics of a quantum phase transition and relaxation to a steady state”. In: *Advances in Physics* 59.6 (2010), pp. 1063–1189.
- [52] N. D. Antunes, P. Gandra, and R. J. Rivers. “Is domain formation decided before or after the transition?” In: *Physical Review D—Particles, Fields, Gravitation, and Cosmology* 73.12 (2006), p. 125003.
- [53] J. M. Kosterlitz and D. J. Thouless. “Ordering, metastability and phase transitions in two-dimensional systems”. In: *Journal of Physics C: Solid State Physics* 6.7 (1973), p. 1181.
- [54] J. M. Kosterlitz. “The critical properties of the two-dimensional xy model”. In: *Journal of Physics C: Solid State Physics* 7.6 (1974), p. 1046.
- [55] J. Dziarmaga and W. H. Zurek. “Quench in the 1D Bose-Hubbard model: Topological defects and excitations from the Kosterlitz-Thouless phase transition dynamics”. In: *Scientific reports* 4.1 (2014), p. 5950.
- [56] B. Gardas, J. Dziarmaga, and W. H. Zurek. “Dynamics of the quantum phase transition in the one-dimensional Bose-Hubbard model: Excitations and correlations induced by a quench”. In: *Physical Review B* 95.10 (2017), p. 104306.
- [57] F. Zhong. “Probing criticality with linearly varying external fields: Renormalization group theory of nonequilibrium critical dynamics under driving”. In: *Physical Review E* 73.4 (2006), p. 047102.
- [58] S. Gong, F. Zhong, X. Huang, and S. Fan. “Finite-time scaling via linear driving”. In: *New Journal of Physics* 12.4 (2010), p. 043036.
- [59] F. Zhong. “Finite-time scaling and its applications to continuous phase transitions”. In: *Applications of Monte Carlo Method in Science and Engineering*. Cite-seer, 2011.
- [60] R.-Z. Huang and S. Yin. “Nonequilibrium critical dynamics in the quantum chiral clock model”. In: *Physical Review B* 99.18 (2019), p. 184104.
- [61] S. Östlund and S. Rommer. “Thermodynamic limit of density matrix renormalization”. In: *Physical review letters* 75.19 (1995), p. 3537.
- [62] S. Rommer and S. Östlund. “Class of ansatz wave functions for one-dimensional spin systems and their relation to the density matrix renormalization group”. In: *Physical review b* 55.4 (1997), p. 2164.

- [63] F. Verstraete and J. I. Cirac. “Renormalization algorithms for quantum-many body systems in two and higher dimensions”. In: *arXiv preprint cond-mat/0407066* (2004).
- [64] G. Vidal. “Entanglement renormalization”. In: *Physical review letters* 99.22 (2007), p. 220405.
- [65] M. B. Hastings. “An area law for one-dimensional quantum systems”. In: *Journal of statistical mechanics: theory and experiment* 2007.08 (2007), P08024.
- [66] S. Paeckel, T. Köhler, A. Swoboda, S. R. Manmana, U. Schollwöck, and C. Hubig. “Time-evolution methods for matrix-product states”. In: *Annals of Physics* 411 (2019), p. 167998.
- [67] J. K. Taylor. “An introduction to graphical tensor notation for mechanistic interpretability”. In: *arXiv preprint arXiv:2402.01790* (2024).
- [68] S. R. White. “Density-matrix algorithms for quantum renormalization groups”. In: *Physical review b* 48.14 (1993), p. 10345.
- [69] F. Verstraete, J. J. Garcia-Ripoll, and J. I. Cirac. “Matrix product density operators: Simulation of finite-temperature and dissipative systems”. In: *Physical review letters* 93.20 (2004), p. 207204.
- [70] G. Vidal. “Efficient simulation of one-dimensional quantum many-body systems”. In: *Physical review letters* 93.4 (2004), p. 040502.
- [71] J. Haegeman, J. I. Cirac, T. J. Osborne, I. Pižorn, H. Verschelde, and F. Verstraete. “Time-dependent variational principle for quantum lattices”. In: *Physical review letters* 107.7 (2011), p. 070601.
- [72] J. Haegeman, C. Lubich, I. Oseledets, B. Vandereycken, and F. Verstraete. “Unifying time evolution and optimization with matrix product states”. In: *Physical Review B* 94.16 (2016), p. 165116.
- [73] L. Vanderstraeten, J. Haegeman, and F. Verstraete. “Tangent-space methods for uniform matrix product states”. In: *SciPost Physics Lecture Notes* (2019), p. 007.
- [74] S. Singh, R. N. Pfeifer, and G. Vidal. “Tensor network decompositions in the presence of a global symmetry”. In: *Physical Review A—Atomic, Molecular, and Optical Physics* 82.5 (2010), p. 050301.
- [75] S. Singh, R. N. Pfeifer, and G. Vidal. “Tensor network states and algorithms in the presence of a global U (1) symmetry”. In: *Physical Review B—Condensed Matter and Materials Physics* 83.11 (2011), p. 115125.
- [76] S. Singh and G. Vidal. “Tensor network states and algorithms in the presence of a global SU (2) symmetry”. In: *Physical Review B—Condensed Matter and Materials Physics* 86.19 (2012), p. 195114.
- [77] P. Schmoll, S. Singh, M. Rizzi, and R. Orús. “A programming guide for tensor networks with global SU (2) symmetry”. In: *Annals of Physics* 419 (2020), p. 168232.
- [78] J. I. Cirac, D. Perez-Garcia, N. Schuch, and F. Verstraete. “Matrix product states and projected entangled pair states: Concepts, symmetries, theorems”. In: *Reviews of Modern Physics* 93.4 (2021), p. 045003.

- [79] N. Chepiga and F. Mila. “Floating phase versus chiral transition in a 1D hard-boson model”. In: *Physical review letters* 122.1 (2019), p. 017205.
- [80] N. Chepiga and F. Mila. “Kibble-Zurek exponent and chiral transition of the period-4 phase of Rydberg chains”. In: *Nature Communications* 12.1 (2021), p. 414.
- [81] P. Fendley, K. Sengupta, and S. Sachdev. “Competing density-wave orders in a one-dimensional hard-boson model”. In: *Physical Review B* 69.7 (2004), p. 075106.
- [82] N. Chepiga and E. Mila. “DMRG investigation of constrained models: from quantum dimer and quantum loop ladders to hard-boson and Fibonacci anyon chains”. In: *SciPost Physics* 6.3 (2019), p. 033.
- [83] B. La Riviere and N. Chepiga. “ $\mathbb{Z}_4$  transitions in quantum loop models on a zig-zag ladder”. In: *SciPost Physics* 17.5 (2024), p. 144.

# 2

## THE QUANTUM KIBBLE-ZUREK MECHANISM: THE ROLE OF BOUNDARY CONDITIONS, ENDPOINTS AND KINK TYPES

*Quantum phase transitions are characterised by the universal scaling laws in the critical region surrounding the transitions. This universality is also manifested in the critical real-time dynamics through the quantum Kibble-Zurek mechanism. In recent experiments on a Rydberg atom quantum simulator, the Kibble-Zurek mechanism has been used to probe the nature of quantum phase transitions. In this chapter we analyze the caveats associated with this method and develop strategies to improve its accuracy. Focusing on two minimal models—transverse-field Ising and quantum three-state Potts, both in one dimension—we study the effect of boundary conditions, the location of the endpoints and some subtleties in the definition of the kink operators. In particular, we show that the critical scaling of the most intuitive types of kinks is extremely sensitive to the correct choice of endpoint, while more advanced types of kinks exhibit remarkably robust universal scaling. Furthermore, we show that when kinks are tracked over the entire chain, fixed boundary conditions improve the accuracy of the scaling. Surprisingly, the Kibble-Zurek critical scaling appears to be equally accurate whether the fixed boundary conditions are chosen to be symmetric or anti-symmetric. Finally, we show that the density of kinks extracted in the central part of long chains obeys the predicted universal scaling for all types of boundary conditions.*

---

Parts of this chapter have been published in *arXiv*, 2024, arXiv:2412.20186 [1].

## 2.1. INTRODUCTION

Quantum phase transitions have become a central topic in condensed matter physics [2], particularly with the rapid experimental progress in Rydberg atom platforms. These systems provide exceptional control over atomic positions and interactions, enabling the realization of exotic phases of matter and the observation of diverse critical phenomena [3].

While numerical studies traditionally focus on ground states near the critical point [4], this approach does not fully reflect experimental conditions. In Rydberg arrays, for instance, the system is prepared far from criticality and then driven adiabatically across the transition [3, 5]. As a result, the Kibble–Zurek (KZ) mechanism [5–9] is the relevant framework for exploring critical behavior.

This has motivated extensive numerical [10–15] and experimental [16–26] studies of the quantum KZ mechanism. However, while power-law scaling consistent with KZ predictions has been observed, the extracted critical exponents often deviate from theoretical expectations. These discrepancies are generally attributed to competing effects during the KZ protocol interfering with the universal behavior [27–29].

In our work, we address this discrepancy by systematically analyzing how the quench endpoint, boundary conditions, and the analyzed chain fragment affect the extraction of critical exponents in two minimal models in one dimension (1D): the transverse field Ising model (Ising) and the quantum 3-state Potts (Potts) model. Moreover, we introduce a refined definition of kinks that yields more robust results across varying conditions. We believe these findings provide important guidance for connecting theory, numerics, and experiments in the study of quantum critical phenomena.

The remainder of this chapter is organized as follows. In Section 2.2, we introduce the two models studied in this work. Section 2.3 provides a concise review of the Tensor Network algorithms used in our simulations, along with relevant technical details. In Section 2.4, we investigate the influence of system size on the Kibble–Zurek mechanism. Section 2.5 presents an alternative approach to counting kinks by focusing exclusively on isolated kinks, and we show that this method is more robust to changes in the final point of the sweep through the transition. In Section 2.6, we compare various boundary conditions, demonstrating that fixing the boundaries—either on the same or in different directions—yields more accurate results than leaving them free. Finally, Section 2.7 summarizes our findings and offers concluding remarks.

## 2.2. THE MODELS

### 2.2.1. TRANSVERSE FIELD ISING MODEL

The transverse field Ising model (for simplicity we will refer to it as Ising model) is defined by the following microscopic Hamiltonian:

$$H = J \sum_{i=1}^{L-1} \sigma_i^z \sigma_{i+1}^z - h \sum_{i=1}^L \sigma_i^x, \quad (2.1)$$

where  $\sigma^{z,x}$  represents the Pauli matrices,  $J$  is the nearest-neighbor Ising coupling, and  $h$  is an external magnetic field in the transverse direction. The model is ferromagnetic

when  $J < 0$  and antiferromagnetic when  $J > 0$ . In this chapter, we consider the latter case. The location of the critical point  $h/J = 1$  is known exactly due to the model being self dual [30], along with all relevant critical exponents:  $z = 1$ ,  $\nu = 1$ ,  $\mu = 1/2$  [31]. To control the boundary conditions we also included a magnetic field in the first and last lattice sites along the  $z$ -direction.

$$H = H_0 - (h_{z1}\sigma_1^z + h_{zL}\sigma_L^z). \quad (2.2)$$

The standard kink number operator is defined as

$$n_k = \frac{1}{2} \sum_{i=1}^{L-1} (1 \mp \langle \sigma_i^z \sigma_{i+1}^z \rangle), \quad (2.3)$$

with the upper (lower) sign corresponding to the ferromagnetic (antiferromagnetic) case. In the ferromagnetic case, the operator counts a kink whenever two neighboring spins are misaligned, while in the antiferromagnetic case it counts a kink whenever they fail to alternate, as depicted in Figure 2.1.

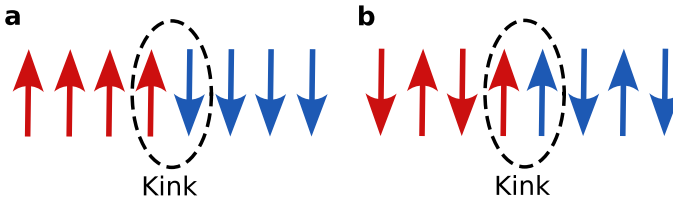


Figure 2.1.: Sketch of the standard definition of kinks for the (a) ferromagnetic and (b) antiferromagnetic Ising model. In the first case, a kink is when two spins antialign while in the second case, a kink is when two spins align.

### 2.2.2. 1D QUANTUM 3-STATE POTTS MODEL

The ferromagnetic quantum 3-state Potts model, to which we will refer as 3-state Potts model for simplicity, is a generalization of the ferromagnetic Ising model for the local Hilbert space of dimension three. The microscopic Hamiltonian is given by:

$$H = -J \sum_{i=1}^{L-1} \sum_{a=1}^3 P_i^a P_{i+1}^a - h \sum_{i=1}^L P_i, \quad (2.4)$$

where  $P_i^a = |a\rangle\langle a|_i - \frac{1}{3}\mathbb{1}$  is a traceless Hermitian operator derived from the projector onto the state  $|a\rangle$  at site  $i$ , and  $P_i = |\lambda_0\rangle\langle\lambda_0|_i - \frac{1}{3}\mathbb{1}$  is the traceless Hermitian operator associated with projection along the state  $|\lambda_0\rangle = \frac{1}{\sqrt{3}}\sum_a |a\rangle$ . The first term represents a ferromagnetic interaction, and the second term represents a generalized transverse field. The critical point is located at  $h/J = 1$  and has critical exponents  $\nu = 5/6$  and  $z = 1$ , and thus  $\mu \approx 0.454$ [31]. Similarly to the Ising model, boundaries can be polarized by adding an external longitudinal field:

$$H = H_0 - \sum_{a=1}^3 (h_{a1}P_1^a + h_{aL}P_L^a). \quad (2.5)$$

The kink operator has the form:

$$n_k = \sum_{i=1}^{L-1} \left( 1 - \langle \sum_a (|a\rangle \langle a|)_i (|a\rangle \langle a|)_{i+1} \rangle \right), \quad (2.6)$$

where  $(|a\rangle \langle a|)_i$  is the projector onto state  $|a\rangle$  at site  $i$ . Thus  $n_k$  counts a kink whenever two neighboring sites differ. For simplicity, we will refer to the three possible directions as  $A$ ,  $B$  and  $C$ . A schematic definition of the kink is shown in Figure 2.2 for clarity.



Figure 2.2.: Sketch of the kink definition for the 3-state Potts model. A kink is counted when two neighboring spins are not aligned in the same direction. For simplicity the 3 possible directions of the spin are labeled as  $A$ ,  $B$  and  $C$ .

## 2.3. NUMERICAL METHODS

### 2.3.1. GROUND STATE CALCULATIONS

The initial state defined at time  $t = 0$  is a ground state at a given starting point in the disordered phase sufficiently far from the transition. To ensure this point was in the adiabatic regime we set the starting point  $h_0 = 10 \cdot s^{1/(1+z\nu)}$ . The ground state was determined using the density matrix renormalization group (DMRG) algorithm [32, 33] in the matrix product state (MPS) formalism. Singular values smaller than  $10^{-6}$  were discarded, and maximal bond dimension was restricted to  $D = 300$ . Convergence of the ground state was assumed when the energy difference between two successive sweeps, including an increase in the bond dimension, divided by the system size was not exceeding  $10^{-8}$ .

### 2.3.2. SIMULATION OF DYNAMICS

Simulations of the time evolution for the Ising model with open boundary conditions and 3-state Potts model were conducted using a second-order time-evolving block decimation (TEBD) algorithm [34–36]. As noted in the Introduction, we propose an alternative definition of kink in this work; however, unless otherwise specified, kink counting follows the standard definitions given in Eqs. (2.3) and (2.6) for the Ising and 3-state Potts models, respectively.

In Figure 2.3, we compare two cutoff values for the minimum singular value,  $\chi = 10^{-6}$  and  $\chi = 10^{-7}$ , as well as two time step values,  $dt = 0.1$  and  $dt = 0.01$ . We observe no significant differences in the kink density across these parameters.

Figure 2.4 presents a comparison of various bond dimensions  $D$  for both the Ising model (Figure 2.4(a)) and the 3-state Potts model (Figure 2.4(b)). In both cases, the Kibble-Zurek exponent  $\mu$  remains stable for moderately large  $D$ , with noticeable deviations occurring only at very small bond dimensions. Based on these observations, we fixed the time step at  $dt = 0.1$ , set the maximum bond dimension to  $D = 300$ , and applied a singular value cutoff of  $\chi > 10^{-6}$  for the simulations presented in the main text.

For simulations employing periodic boundary conditions, the time-dependent variational principle (TDVP) [36–38] was used instead, while retaining the same values of  $D$  and  $\chi$  as in TEBD.

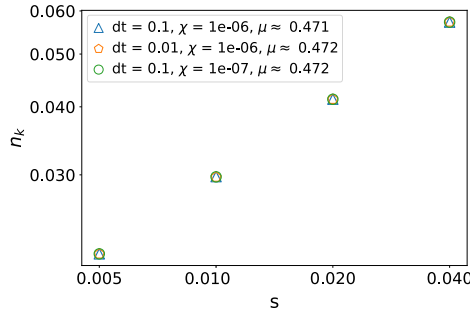


Figure 2.3.: Comparison of the kink density in the 3-state Potts model for system size  $L = 101$ , obtained using different numerical parameters. Results are shown for two singular value cutoffs ( $\chi = 10^{-6}$  and  $\chi = 10^{-7}$ ) and two time steps ( $dt = 0.1$  and  $0.01$ ). The negligible differences confirm the validity of the tensor network approximation against moderate variations in truncation threshold and time discretization.

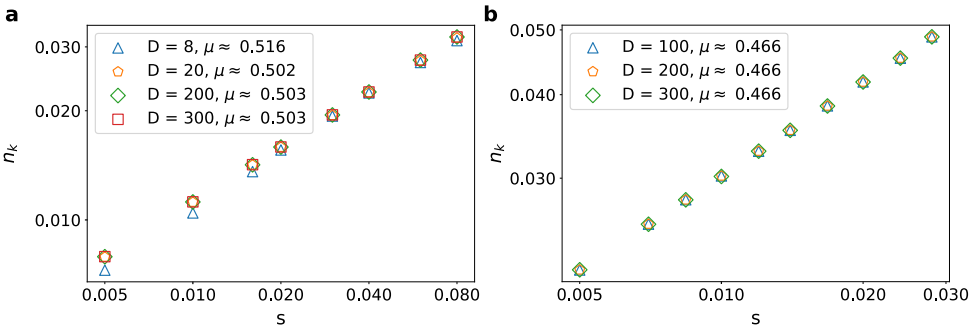


Figure 2.4.: Kibble-Zurek scaling of the density of kinks  $n_k$  as a function of the sweep rate for various bond dimensions  $D$  in (a) the 1D transverse-field Ising model and (b) the 1D quantum 3-state Potts model. In both cases,  $L = 201$  sites. Simulation of Kibble-Zurek dynamics requires relatively small bond dimension ( $D \lesssim 100$ ). For the rest of the simulations  $D = 300$  was used for both Ising Potts models.

## 2.4. SYSTEM SIZE

We first investigated the role of finite-size effects in the Kibble-Zurek (KZ) mechanism for both models. Figure 2.5(a) summarizes our findings for the Ising model, where we

explored a wide range of sweep rates  $s$  to capture the various dynamical regimes exhibited by the system. Three distinct regimes emerge clearly. For slow sweeps, the correlation length becomes comparable to the system size, and the system evolves adiabatically throughout the process. In this regime, the kink density remains near zero and is largely independent of the sweep rate [9, 39]. For fast sweeps, the evolution is fully non-adiabatic, and the kink density saturates at a maximum value determined by the final point of the quench [40, 41]. Between these two extremes lies the KZ scaling regime, characterized by a power-law dependence of the kink density on the sweep rate.<sup>1</sup>

For the Ising model, increasing the system size does not notably affect the exponent  $\mu$  associated with the KZ scaling—nearly all system sizes, except  $L = 30$ , yield the same  $\mu$ . However, the threshold sweep rate at which the slope is linear decreases as the system size grows, extending the interval over which the KZ mechanism can be observed.

A qualitatively similar picture is seen in the 3-state Potts model, as shown in Figure 2.5(b). However, in contrast to the Ising case, the KZ scaling exponent  $\mu$  exhibits noticeable finite-size effects. The slope of the scaling curve gradually approaches the theoretical value  $\mu = 5/11$  from above as the system size increases. The most likely reason for this tendency is that the range of  $s$  suitable for a reliable KZ fitting correspond to slower sweeps than those allowed by system sizes we can access. For  $L = 401$  sites, the numerically extracted exponent  $\mu \approx 0.463$  agrees with the theoretical prediction within 2%.

## 2.5. TYPES OF KINKS AND THE ENDPOINT

The standard experimental protocol for extracting the KZ exponent  $\mu$  consists of driving the system from the disordered phase into the ordered phase and counting the number of kinks after the transition for various sweep rates. In our simulations we evaluate the expectation value of the kink operator rather than sampling individual spin configurations.

As mentioned in the introduction, in a first approximation, the system freezes upon entering the non-adiabatic regime, and the correlation length (that in 1D is directly related to the density of kinks) remains fixed thereafter. However, it has been shown that this approximation is oversimplified: the system continues to evolve and correlations continue to spread even as it crosses the critical point [43–46]. In the Ising model, a more refined picture involves the creation of entangled kinks pairs with opposite momenta that spread correlations across the system.

Moreover, during the dynamics, quantum coarsening competes with the KZ mechanism, further increasing the correlation length [29]. As a result, the correlation length continues to increase even after the system has returned to the adiabatic regime. Finally, if the transverse field is not completely suppressed, there is a certain probability of a local spin flip. Thus not all the detected kinks arise from the KZ mechanism itself.

In this section, we analyze two factors that affect the calculation of the KZ critical exponent  $\mu$ : the endpoint where the dynamics terminate and the choice of a kink opera-

<sup>1</sup>At the boundaries between the KZ regime and the other two regimes, we observe a transient behavior in which the kink density increases more rapidly with the sweep rate than the KZ scaling would predict. The transient regime between the fast-quench and the KZ regime is the pre-saturated regime, which occurs when the initial point is in the adiabatic regime, but the ending point is inside the non-adiabatic regime [42]. The size of both transient regimes is model dependent.

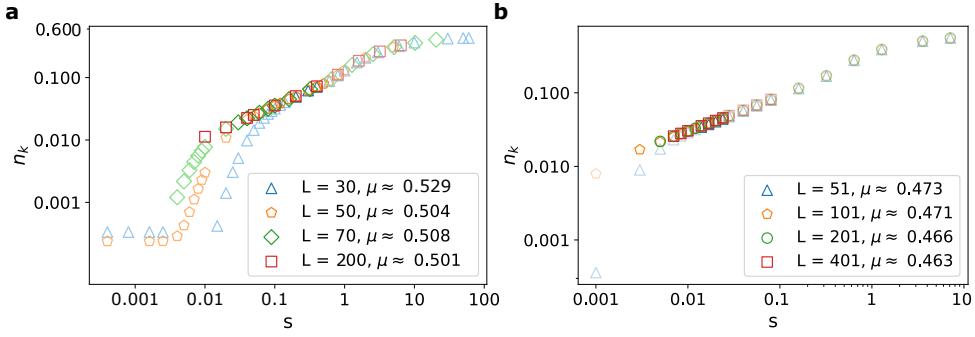


Figure 2.5.: Kibble–Zurek scaling of the kink density  $n_k$  as a function of the sweep rate  $s$  for different system sizes in (a) the Ising and (b) 3-state Potts models. In both panels, three distinct dynamical regimes are visible. At slow sweep rates, the system evolves adiabatically, and the kink density remains near zero. As the sweep rate increases, an intermediate regime emerges in which  $n_k$  exhibits universal power-law scaling with  $s$ . At high sweep rates, the dynamics become fully non-adiabatic, and the kink density saturates to a constant value. (a) For system sizes  $L \geq 50$ , the numerical results are in excellent agreement with the theoretical prediction  $\mu = 0.5$ . (b) A small finite-size effect leads to a slight overestimation of the critical exponent  $\mu$  in smaller systems. For  $L = 401$ , the extracted exponent agrees with the theoretical value  $\mu = 5/11$  within 2%. Data points not included in the KZ fits are shown in pale. All simulations were performed with a maximum bond dimension of  $D = 300$ .

tor. All results presented in this section were obtained with fixed boundary conditions, while the effect of various boundary conditions on the apparent KZ critical exponent will be discussed in detail in the next section. We consider two types of kink definitions as sketched in Figure 2.6, for the Ising model with antiferromagnetic (Figure 2.6(a)-(c)) and ferromagnetic (Figure 2.6(d)-(f)) interactions. In the standard definition, a kink is counted whenever the expected order is violated. For instance, in the ferromagnetic case, a kink is counted if any pair of neighboring spins are anti-aligned, while in the antiferromagnetic case, it is counted if they are aligned (see Figure 2.6(d) and (a) correspondingly).

Alternatively, one can count only isolated kinks, thus excluding configurations in which more than two consecutive spins deviate from the expected order. In the antiferromagnetic case, this means disregarding regions where three or more neighboring spins are aligned instead of alternating:

$$n_k = \sum_i \left( \langle P_{\uparrow i} \otimes P_{\downarrow i+1} \otimes P_{\downarrow i+2} \otimes P_{\uparrow i+3} \rangle + \langle P_{\downarrow i} \otimes P_{\uparrow i+1} \otimes P_{\uparrow i+2} \otimes P_{\downarrow i+3} \rangle \right), \quad (2.7)$$

with  $P_{\uparrow}$  and  $P_{\downarrow}$  are the projectors for spin up and down respectively, as shown in 2.6(b). In the ferromagnetic case, it entails excluding regions where three or more spins are anti-

aligned:

$$n_k = \sum_i (\langle P_{\uparrow i} \otimes P_{\uparrow i+1} \otimes P_{\uparrow i+2} \otimes P_{\uparrow i+3} \rangle + \langle P_{\downarrow i} \otimes P_{\downarrow i+1} \otimes P_{\downarrow i+2} \otimes P_{\downarrow i+3} \rangle), \quad (2.8)$$

as depicted in 2.6(e). Such scenarios are typical for a single-spin flip, as shown Figure 2.6(c) and (f). Under the conventional definition [9], such a single flip would count as two kinks. However, since a local flip is not a true domain wall but rather an impurity within a single domain, it should be excluded from the final count.

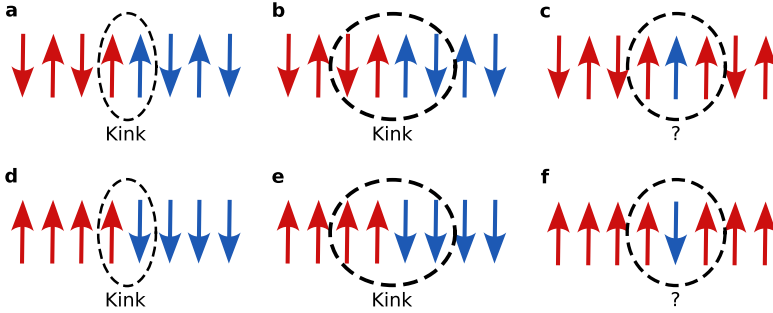


Figure 2.6.: Kinks and domain walls in the Ising model with (a)-(c) antiferromagnetic and (d)-(e) ferromagnetic interactions. Red and blue colors are assigned to each of the two ground-states. (a),(d) In the standard definition [9], a kink is counted whenever the expected ordering is violated. (b,e) In the "isolated kink" definition proposed in this work, kinks are identified over four consecutive spins, requiring that the domains on either side of the kink have a minimum length of two. (c,f) A single spin-flip is interpreted as a double kink under the standard definition, but is excluded in the isolated kink criterion, since it does not alter the nature of the surrounding domains. We argue that such isolated spin flips should not contribute to the kink count, as they do not correspond to genuine domain boundaries.

Figure 2.7(a) shows the critical scaling of the density of standard kinks with a sweep rate for three different endpoints:  $h_e = 0$  and  $h_e = \pm 0.2$ . While the KZ exponent extracted for the trajectory terminating at  $h_e = 0$  is in excellent agreement with the theory prediction for Ising criticality  $\mu = 0.5$ , critical exponents extracted for other endpoints deviate significantly. If instead we use an advanced definition of kinks where a single-spin flip is explicitly excluded from the kink counting, extremely accurate values of KZ exponents have been extracted from time-evolution to all three endpoints, as demonstrated in Figure 2.7(b). This means that local impurities, which are not real domain walls, do not play any role in the Kibble-Zurek dynamics and must generally be filtered out by a proper definition of the kink operators. Alternatively, one can terminate the dynamical evolution at the point where the quantum term responsible for the local spin flip is absent, and such impurities do not appear.

This logic of robust kinks can be extended beyond the trivial Ising model, as shown in Figure 2.8. However, for the 3-state Potts model, the definition of a robust kink is more

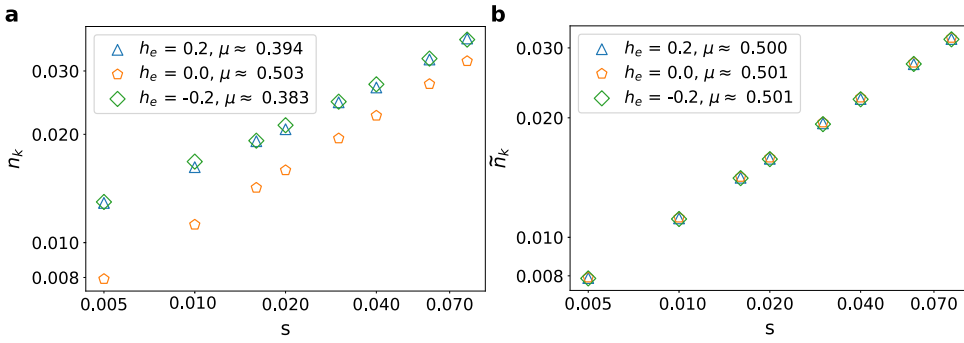


Figure 2.7.: Scaling of the density of kinks  $n_k$  with the sweep rate  $s$  for the Ising model for various final values of the transverse field  $h_e$  using (a) the standard kinks operator, (b) a kink operator that only counts isolated domain walls (i.e. excludes local spin flips). The Kibble-Zurek exponent  $\mu$  is extracted from the slope of the power law scaling. (a) Numerically extracted  $\mu$  using the standard kink operator agrees with the theory prediction  $\mu = 0.5$  only for  $h_e = 0$ , while the value of  $\mu$  extracted with other endpoints is significantly underestimated. (b) The scaling of isolated kinks provides accurate numerical estimates of the Kibble-Zurek critical exponent  $\mu$  for a wide range of final endpoints. In both cases, the system size is  $L = 201$ .

subtle, since the spin flip might or might not lead to a switch of domain walls, as shown in Figure 2.8(c)-(d). In this case, the advanced definition of kink discards spin flips inside a domain (Figure 2.8(c)), but treats a spin flip that bridges two different domains as a single kink (Figure 2.8(d)):

$$n_k = \sum_i \left( \sum_{a \neq b} \langle (|a\rangle \langle a|)_i (|a\rangle \langle a|)_{i+1} (|b\rangle \langle b|)_{i+2} (|b\rangle \langle b|)_{i+3} \right. \\ \left. + \sum_{\substack{a,b,c \\ a \neq b, b \neq c, a \neq c}} \langle (|a\rangle \langle a|)_i (|b\rangle \langle b|)_{i+1} (|c\rangle \langle c|)_{i+2} \right). \quad (2.9)$$

This method of counting kinks in the 3-state Potts model produces results comparable to those of the Ising model, as shown in Figure 2.9. When using the standard definition of a kink, the Kibble-Zurek exponent  $\mu$  is the closest to its theoretical value when the sweep ends at zero transverse field,  $h_e = 0$ , where the dynamical term vanishes. If the sweep terminates before or after this sweet spot,  $\mu$  is noticeably underestimated, as illustrated in Figure 2.9(a). In contrast, the advanced kink definition (Figure 2.9(b)) is more robust to the ending point, causing the three curves to overlap and yielding a more accurate  $\mu$ . In all cases, the density of kinks scales as a power law dependence on the sweep rate.

In Figure 2.10, we show the profiles of the local kink density for the Ising and 3-state Potts models at various endpoints of a single sweep rate. A direct comparison between standard and isolated kinks reveals that all profiles corresponding to the same sweep



Figure 2.8.: Domain wall characterization in the 3-state Potts model. (a) In the standard definition, a kink is counted whenever two consecutive sites occupy different local states. (b) In the "isolated kink" definition proposed in this work, a kink is only counted when two differing spins are also aligned with their nearest neighbors, ensuring that the adjacent domains have a minimum length of two. (c) A single spin-flip is interpreted as a double kink under the standard definition, but is excluded in the isolated kink definition, as it does not alter the structure of the surrounding domain. (d) A spin-flip occurring at the boundary between two genuine domains is counted as a double kink in the standard approach. In contrast, the isolated kink definition count it as a single kink, since only two true domains are present in the configuration.

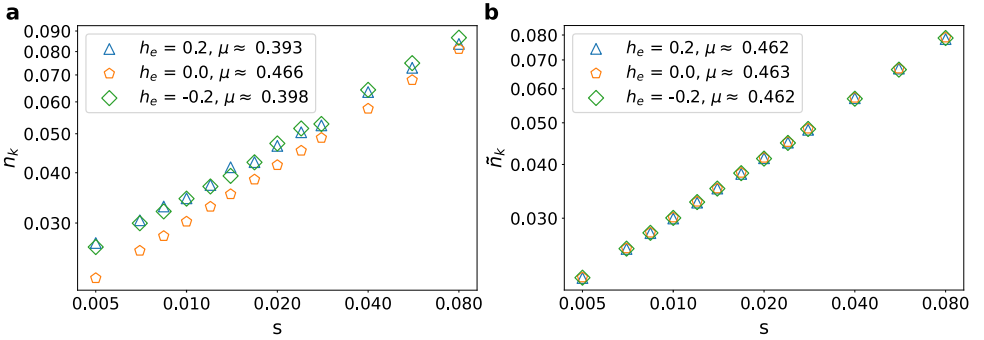


Figure 2.9.: Scaling of the density of kinks  $n_k$  with the sweep rate  $s$  for the 3-state Potts model for various final values of the transverse field using (a) the standard kinks operator, (b) a kink operator that only counts isolated domain walls. The Kibble-Zurek exponent  $\mu$  is extracted from the slope of the power law scaling. With the simple kink operator, only  $\mu$  extracted for the trajectory that ends at  $h_e = 0$  is reasonably close (within 3%) to the theoretical value  $\mu = 0.454$  for Potts, while other endpoints significantly reduce the the slope. When using the isolated kink operator, numerically extracted value agree within 2% with the theory prediction for a wide range of endpoints. In both presented cases the system size is  $L = 201$ .

rate and system size, but ending at different final fields, are nearly identical up to a constant vertical shift. This shift appears to result from single-spin-flip excitations, as it disappears entirely when considering isolated kinks: in that case, all curves collapse onto each other.

In the 3-state Potts model, we can also compare the local density of spin flips inside or between domains for  $h_e = 0$  and  $h_e \neq 0$ . Figure 2.11 illustrates these scenarios: panel (a) shows the local density profiles for both types of spin flips when  $h_e = 0$ , and panel

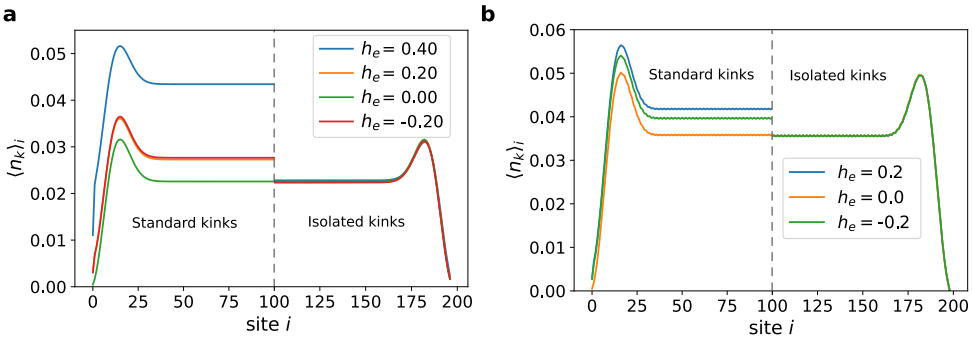


Figure 2.10.: Local density of kinks  $n_k$  along the chain for (a) the Ising and (b) the 3-state Potts models for various values of the final transverse field  $h_e$ . Each plot is split in two: in the left side, the kink operator is the standard domain wall operator, while in the right side only isolated kinks are measured. For both, Ising and Potts models, when  $h_e = 0$  the profiles of standard and isolated kinks coincide. However, for different end points the profile of standard kinks is shifted, while the profile for isolated kinks remains robust.

(b) shows them when  $h_e = 0.2$ . As expected from Figure 2.10, spin flips occur more frequently under nonzero  $h_e$ . Moreover, even though flipping a spin inside a domain costs twice as much energy as flipping one at a domain boundary, such “in-domain” flips are still more common. The apparent contradiction is resolved by noting that domain walls are relatively rare, making it statistically more likely for a random spin to be inside a domain rather than at its boundary.

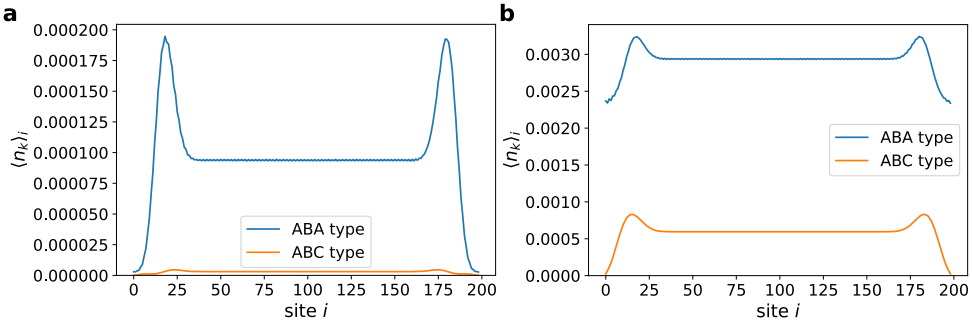


Figure 2.11.: Local density of two types of local kinks  $n_k$  in the 3-state Potts model, shown along the chain for (a)  $h_e = 0$  and (b)  $h_e = 0.2$ . The blue curve corresponds to spin flips inside a domain, and the orange curve to spin flips at a domain boundary. In both cases spin flips inside a domain are more abundant than at a domain boundary.

Finally, let us compare the evolution of the overall density of standard and isolated kinks in the whole quench protocol. The results for the Ising model are presented in

Figure 2.12. Let us carefully explain this figure. When  $h \rightarrow \infty$ , the ground state is

$$|\psi\rangle = |\dots + + + + \dots\rangle.$$

2

The density of kinks in this maximally disordered state is  $n_k \approx 0.5$  while isolated kinks is  $n_k \approx 0.125$ . This number can be easily obtained by counting the number of domain walls or isolated domain walls respectively in the perfectly disordered state (i.e. number of aligned pairs of spins or isolated aligned pairs of spins in the antiferromagnetic Ising model). As we approach the phase transition at  $h = 1$ , but still far from the non-adiabatic regime, the average number of kinks decreases, while the density of isolated kinks remains constant. Around the phase transition, the density of kinks drops sharply as ordered domains form separated by domain walls. The density of standard kinks reaches a minimum at  $h = 0$ , where quantum fluctuations are solely driven by the Kibble-Zurek mechanism, and increases for  $h > 0$ . In contrast, the density of isolated kinks attains its minimum before  $h = 0$  and remains nearly constant over a wide range of  $h$  values on both sides of the transition. This indicates that the isolated kink operator is robust against random quantum fluctuations and selectively detects domain walls generated by the KZ mechanism.

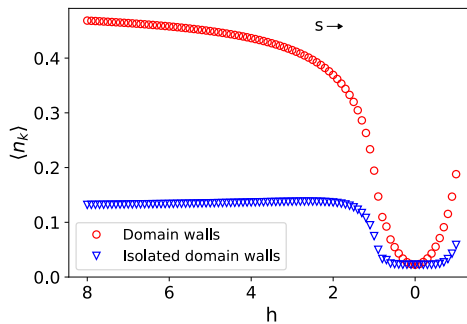


Figure 2.12.: Evolution of the kink density  $n_k$  during a constant-rate quench in the Ising model, comparing the standard kink-counting method (red circles) to counting only isolated kinks (blue triangles), where isolated means that single spin flips are not counted. Deep in the disordered phase ( $h \gg 1$ ), the density of kinks reaches its maximum ( $n_k = 0.5$  for the standard definition and  $n_k = 0.125$  for isolated kinks). As the system crosses the phase transition at  $h = 1$ , the emergence of large ordered regions leads to a sudden drop in the kink density. At  $h = 0$ , both counting methods yield the same minimal density, since any remaining kinks are solely due to domain wall creation as described by the KZ mechanism. Notably, while isolated kinks maintain their minimal density over a wide range of  $h$ , the standard kink definition only attains this minimal value at  $h = 0$ .

## 2.6. BOUNDARY CONDITIONS

The critical properties of a quantum system depend not only on the bulk Hamiltonian but also on its boundary conditions, and the same holds true for its dynamical behavior. Recently, the role of periodic and antiperiodic boundary conditions in the Kibble–Zurek mechanism was investigated in [47], where it was found that Kibble–Zurek scaling remains essentially unchanged whether the boundary conditions are periodic or antiperiodic. Since many experimental setups inherently involve different boundary conditions, we extend these results by performing a more comprehensive study covering a wider variety of boundary conditions. To investigate whether boundary conditions influence the apparent Kibble–Zurek exponent, we examined the scaling of kink densities for both the Ising and the 3-state Potts model under various boundary conditions. Our results for the two models are summarized in Figure 2.13 and Figure 2.14 correspondingly. For this, we evaluate the density of kinks in two different ways: over the entire chain including the edges, and over a small interval in the middle of the chain. In this section we present results obtained with  $L = 201$  and we use the standard definition of kinks (see previous section for details). We polarize boundary conditions by applying an external longitudinal magnetic field.

For the Ising model, we examine five different boundary conditions, as defined in Eq. (2.2): boundary conditions fixed at both edges of the chain in a symmetric  $h_{z1} = h_{zL} = 10$  or antisymmetric  $h_{z1} = -h_{zL} = 10$  way; weakly polarized boundary conditions with  $h_{z1} = h_{zL} = 0.1$ ; free boundary conditions ( $h_{z1} = h_{zL} = 0$ ); and the boundary condition fixed at one edge and free at another one  $h_{z1} = 0$  and  $h_{zL} = 10$ . Our results are summarized in Figure 2.13. When kinks are counted in the small central interval ( $\approx 10\%$  of the total length) of a long chain, the density of kinks evaluated for all five boundary conditions scales with a KZ critical exponent that agrees within 2% with the theory expectation  $\mu = 0.5$ . If instead, the density of kinks is evaluated over the entire chain (as it is often the case in experiments where available system sizes are limited) the critical exponent evaluated with the fixed boundary conditions turns out to be significantly more accurate. As a big surprise, we observe no difference in KZ dynamics with fixed symmetric and fixed antisymmetric boundary conditions, for which equilibrium properties are drastically different.

For the ferromagnetic 3-state Potts model, we also examine five different boundary conditions, as defined in Eq. (2.5): fixed boundary conditions favoring the same (A A) or different (A B) ferromagnetic state at each edge; free (0 0) and fixed-free (A 0) boundary conditions. These four boundary conditions are direct generalization of the boundary conditions considered for the Ising model. In addition, we also consider mixed boundary conditions (AB AB) obtained by applying positive longitudinal field in the C direction at each edge. The results obtained with these boundary conditions are summarized in Figure 2.14. Similar to the Ising model case, we see that when the KZ exponent is extracted from the total density of kinks, the results obtained with fixed boundary conditions are significantly more accurate than those obtained with other types of boundaries (see Figure 2.14(a)). If, however, the density of kinks is evaluated only in the central interval of a long enough chain, the boundary conditions become irrelevant, just like we have observed for the Ising model in Figure 2.13(b).

We also examine the scenario of periodic boundary conditions (PBC). In Figure 2.15,

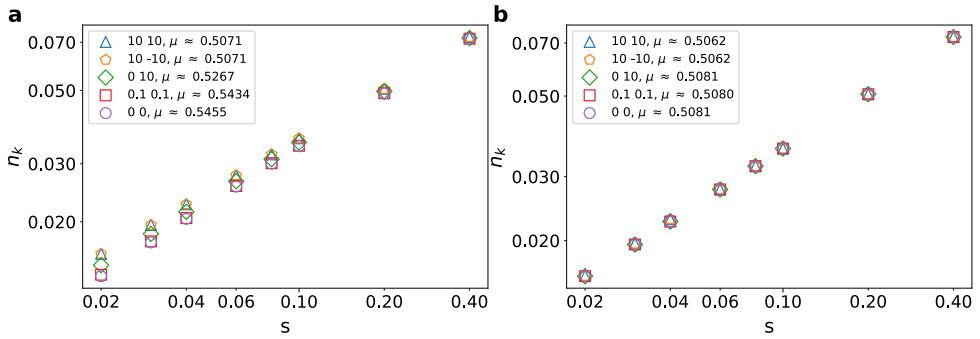


Figure 2.13.: Scaling of the density of kinks  $n_k$  with the sweep rate  $s$  for the Ising model for various boundary conditions when measuring the density of kinks (a) over the entire chain (b) over the central 10% of the chain. The boundary conditions were fixed with external longitudinal field applied at first and last site of the chain and indicated in the legends. The results evaluated in the central part of the chain always agree within 2% with the theory prediction  $\mu = 1/2$ , while the results evaluated over the entire chain provide more accurate estimate of the KZ exponent when the boundary conditions are fixed.

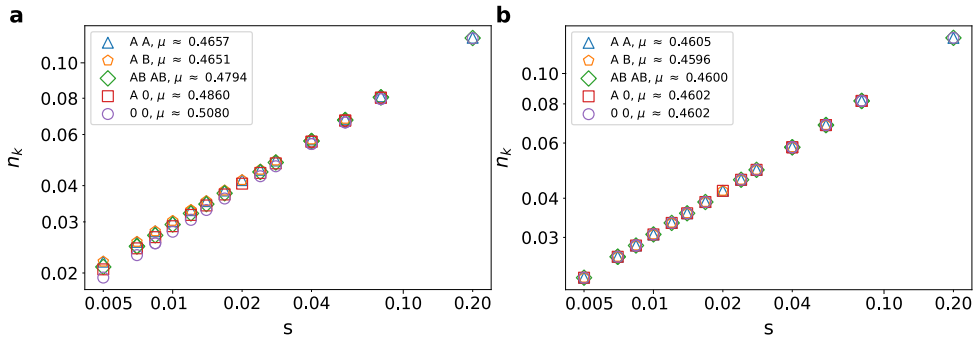


Figure 2.14.: Scaling of the density of kinks  $n_k$  with the sweep rate  $s$ , in the 3-state Potts model for various boundary conditions when the density of kinks is measured (a) over the whole chain, and (b) over the central 10% interval of the chain. Fixed boundary conditions are labeled with A or B, mixed with AB (not-C), free boundary is marked with 0. The results evaluated in the central part of the chain always agree within 2% with the theory prediction  $\mu = 5/11$ , while the results evaluated over the entire chain provide more accurate estimate of the KZ exponent when the boundary conditions are fixed.

we compare the scaling of the kink density for the antiferromagnetic Ising model under PBC for two system sizes,  $L = 200$  (the system size compatible with the periodicity of

the ground state) and  $L = 201$  (the system size non-compatible with the ground-state periodicity, often called anti-periodic boundary conditions in the field-theory context). We see that  $\mu$  is independent of this choice.

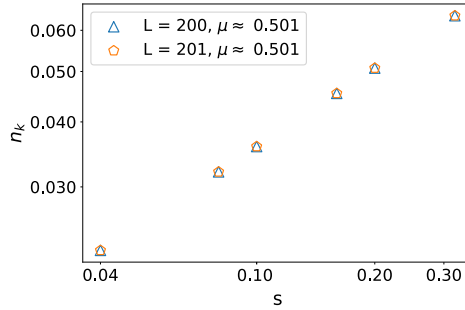


Figure 2.15.: Comparison of the kink density scaling for the antiferromagnetic Ising model under periodic boundary conditions (PBC) when the system size is compatible ( $L$ -even) and when it is incompatible ( $L$ -odd) with the periodicity of the ground state. Two data sets demonstrate a remarkable overlap.

In Figure 2.16, we present the local kink density along the chain under various boundary conditions for the Ising model (Figure 2.16(a)) and the 3-state Potts model (Figure 2.16(b)). Both models exhibit remarkably similar kink distribution profiles when identical boundary conditions are applied. For the periodic boundaries, the kink distribution, as expected, is uniform across the chain. For open and fixed boundaries—whether fixed in the same or opposite directions—kinks tend to accumulate near, but not directly adjacent to, the boundaries, reaching zero at the edges. The reason for this absence of kinks at the edges is that polarized boundaries reduce quantum fluctuations in their vicinity, preventing the formation of domain walls. Remarkably, the total number of kinks is the same for fixed and periodic boundary conditions, with only the distribution being affected.

When boundaries are open but free, the peak in the kink distribution observed for fixed boundaries disappears, although the kink density still decreases toward the boundaries. Under these conditions, the total number of kinks is reduced compared to the fixed boundary conditions.

Finally, for the mixed boundaries in the Potts model—where the degree of freedom is partially constrained at the edges, such that local state  $C$  is disfavored, while  $A$  and  $B$  can appear with equal probability—the peak in the kink distribution is smaller than in the fixed case. Here, the total number of kinks falls between those for free and fixed boundary conditions. And, as we have seen in Figure 2.14 the accuracy of the KZ exponent also lies in between the fixed and free cases.

The last question that we are going to explore is the optimal length of the central interval of the chain to evaluate the KZ exponent. Figure 2.17 provides the value of the KZ exponent  $\mu$  as a function of the relative discarded interval at each edge of the chain with  $L = 201$  sites while computing the density of kinks for various boundary conditions. Ising and 3-state Potts models show a similar behaviour. In both cases the  $\mu$  matches

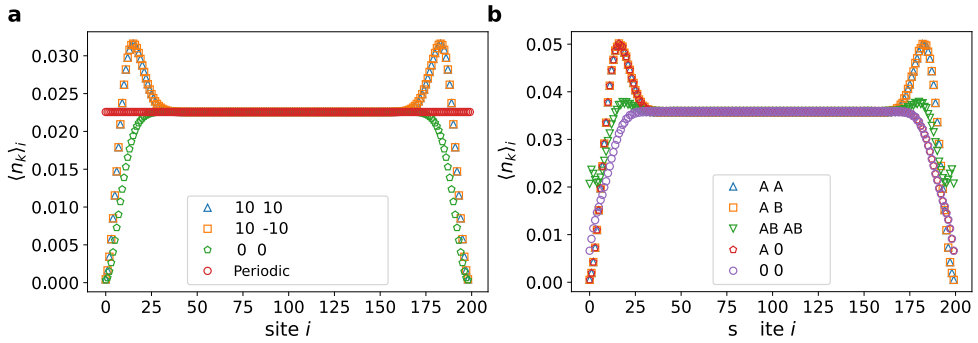


Figure 2.16.: Distribution of kinks along the chain for (a) the Ising and (b) the 3-state Potts model for various boundary conditions listed in the legend.

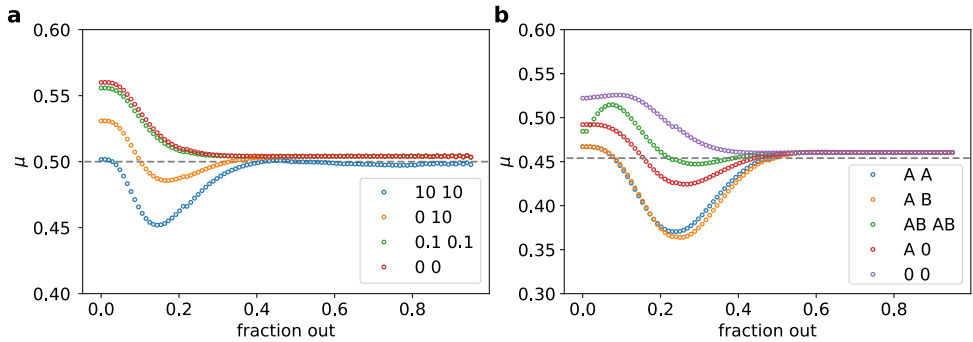


Figure 2.17.: Kibble-Zurek exponent as a function of the fraction of the edge discarded for density calculations for various boundary conditions for (a) The Ising and (b) the Potts model. Dashed lines indicate theory predictions  $\mu = 0.5$  for Ising and  $\mu = 5/11$  for Potts.

the theoretical value for the whole chain when boundaries are fixed. For all boundary conditions the edge effects seem to vanish after half of the considered chains (in other words, about 100 sites) are discarded. This interval is expected to depend on the specific model and the range of sweep rates considered, but already these simple examples provide us with a good indication that one has to discard many dozens of sites posting quite a significant lower bound on the total length of the chain.

## 2.7. DISCUSSION

In this chapter, we have studied the effect of boundary conditions and ending point in the Kibble-Zurek mechanism. Our main finding is that the accuracy of the Kibble-Zurek mechanism in the naive implementation is extremely sensitive to the location of the final point—the point where the time evolution terminates and the measurements are performed. Our data show that, for the two minimal models considered here, the best

choice of the final point would be the point where the transverse field responsible for quantum fluctuations vanishes. If the final measurement point deviates from this classical limit, whether it lies before or after the zero-transverse-field point, the observed critical exponent  $\mu$  deviates markedly from the theoretically predicted universal value

Interestingly enough, exactly the same type of fine-tuning to the classical end point has been realized in Rydberg simulators. In the experiment, after quenching through a quantum phase transition, the Rabi frequency  $\Omega$  responsible for quantum fluctuations of atoms between the ground-state and excited Rydberg state has to be turned off to perform the read-outs. The only difference between the two protocols is a path to reach this specific end point. In the minimal models considered above, we quenched the transverse field itself to the point when it vanishes. In experiments, one quenches either the laser detuning (this would correspond to an additional longitudinal field in the minimal models) or the combination of the detuning and Rabi frequency to an arbitrary point inside the ordered phase and then turns off the lasers responsible for the resonance. Importantly, in both protocols, the transition is crossed with a linear ramp. Numerical simulations that closely reproduce the experimental protocol demonstrate excellent agreement with the expected universal scaling at the Ising and Potts points[15].

Such fine-tuning of the final point is natural for experiments on Rydberg atoms, but may not be generic in other contexts. In this chapter, we present an alternative approach based on a more careful definition of the kink operator, which demonstrates a remarkable robustness to the location of the final endpoint.

It is worth noting that measuring kinks is not the only way of calculating the KZ critical exponent. Alternative methods, although less commonly used, can be advantageous for certain models. As mentioned earlier, the kink density is inversely related to the correlation length. Estimating the correlation length has the benefit of avoiding the ambiguities associated with the definition of kinks. However this approach also owns its own challenges. Extracting the correlation length requires fitting correlation functions, with it is often problematic. In our experience, after a quench, the correlation function typically fails to display a clean exponential decay making reliable fits difficult. Consequently, the extracted results tend to be highly sensitive to the choice of fitting window. Other approaches have also been explored, such as analyzing the scaling of the excitation energy relative to the ground state at the end point [48], or studying the dynamics of the entanglement entropy [49]. However, these methods are generally less accurate and less practical than kink counting. Moreover, similar to the kink density, they are also affected by the so-called end-point effect.

In our approach, the kink represents a domain wall between two *extended* domains, excluding, in particular, localized excitations within the domain of the same ground-state, like a single-spin flip. This definition requires some level of book-keeping but admits a conceptually straightforward generalization to other more complex models.

In addition, we investigated how different boundary conditions affect the accuracy of the critical scaling. For both minimal models considered, we find that the accuracy of the Kibble-Zurek critical exponent is systematically improved for fixed boundary conditions with respect to the free ones. Surprisingly, we observe no distinction in the critical dynamics obtained with symmetric and antisymmetric (in the conformal field theory sense) fixed boundary conditions, despite their drastic differences in equilibrium. In

equilibrium, the frustration induced by opposite boundary conditions has a strong impact on macroscopic quantities. The order parameter ceases to be well defined, reflecting the incompatibility between boundary constraints and bulk ordering. Furthermore, the entanglement entropy is enhanced, and its scaling may deviate from the standard area law expected in gapped phases. In effective models of Rydberg atoms, the presence of a longitudinal field (arising from laser detuning) partially fixes the boundary conditions by favoring the excitation of edge atoms into Rydberg states. Increasing the laser detuning at the edges can further reinforce these effective fixed boundary conditions. The lack of any difference between symmetric and anti-symmetric boundary conditions relaxes experimental constraints. Typically, arrays with a total size  $N = kp + 1$  with  $k \in \mathbb{Z}$  have been used to probe the transition into the period- $p$  phase. Our results suggest that the scaling should be universal for any values of  $N$  (of course,  $N$  has to be big enough to host the Kibble-Zurek regime).

We also report that, for sufficiently long chains, the universal Kibble-Zurek scaling can be accurately extracted by calculating the density of kinks in the central part of the chain, thus ignoring the effect of the boundaries. The size of the chain in this case must be substantially larger than the resulting correlation length after a quench, which naturally increases with decreasing sweep rate. For the minimal models and sweep rates considered here, the edge effects are significant over the first 30-40 sites, imposing a lower bound on the total chain length of at least  $N \gtrsim 100$  sites. These lengths are feasible but challenging in modern Rydberg experiments, so fixing the boundary conditions seems to be the best strategy for now.

# BIBLIOGRAPHY

- [1] J. Soto-Garcia and N. Chepiga. “Quantum Kibble-Zurek mechanism: The role of boundary conditions, endpoints, and kink types”. In: *Physical Review B* 113.8 (2026), p. 085430.
- [2] S. Sachdev. *Quantum Phase Transitions*. 2nd ed. Cambridge University Press, 2011.
- [3] H. Bernien, S. Schwartz, A. Keesling, H. Levine, A. Omran, H. Pichler, S. Choi, A. S. Zibrov, M. Endres, M. Greiner, *et al.* “Probing many-body dynamics on a 51-atom quantum simulator”. In: *Nature* 551.7682 (2017), pp. 579–584.
- [4] J. Cardy. *Scaling and renormalization in statistical physics*. Vol. 5. Cambridge university press, 1996.
- [5] A. Keesling, A. Omran, H. Levine, H. Bernien, H. Pichler, S. Choi, R. Samajdar, S. Schwartz, P. Silvi, S. Sachdev, *et al.* “Quantum Kibble–Zurek mechanism and critical dynamics on a programmable Rydberg simulator”. In: *Nature* 568.7751 (2019), pp. 207–211.
- [6] W. H. Zurek, U. Dorner, and P. Zoller. “Dynamics of a quantum phase transition”. In: *Physical review letters* 95.10 (2005), p. 105701.
- [7] A. Polkovnikov. “Universal adiabatic dynamics in the vicinity of a quantum critical point”. In: *Phys. Rev. B* 72 (16 Oct. 2005), p. 161201. DOI: [10.1103/PhysRevB.72.161201](https://doi.org/10.1103/PhysRevB.72.161201). URL: <https://link.aps.org/doi/10.1103/PhysRevB.72.161201>.
- [8] M. Uhlmann, R. Schützhold, and U. R. Fischer. “Vortex quantum creation and winding number scaling in a quenched spinor Bose gas”. In: *Physical review letters* 99.12 (2007), p. 120407.
- [9] J. Dziarmaga. “Dynamics of a quantum phase transition and relaxation to a steady state”. In: *Advances in Physics* 59.6 (2010), pp. 1063–1189.
- [10] P. Laguna and W. H. Zurek. “Density of kinks after a quench: When symmetry breaks, how big are the pieces?” In: *Physical Review Letters* 78.13 (1997), p. 2519.
- [11] H. Saito, Y. Kawaguchi, and M. Ueda. “Kibble-Zurek mechanism in a quenched ferromagnetic Bose-Einstein condensate”. In: *Physical Review A—Atomic, Molecular, and Optical Physics* 76.4 (2007), p. 043613.
- [12] G. De Chiara, A. Del Campo, G. Morigi, M. B. Plenio, and A. Retzker. “Spontaneous nucleation of structural defects in inhomogeneous ion chains”. In: *New Journal of Physics* 12.11 (2010), p. 115003.
- [13] A. Del Campo, G. De Chiara, G. Morigi, M. B. Plenio, and A. Retzker. “Structural Defects in Ion Chains by Quenching the External Potential: The Inhomogeneous Kibble-Zurek Mechanism”. In: *Physical review letters* 105.7 (2010), p. 075701.

- [14] D. Jaschke, K. Maeda, J. D. Whalen, M. L. Wall, and L. D. Carr. “Critical phenomena and Kibble–Zurek scaling in the long-range quantum Ising chain”. In: *New Journal of Physics* 19.3 (2017), p. 033032.
- [15] J. Soto Garcia and N. Chepiga. “Resolving chiral transitions in one-dimensional Rydberg arrays with quantum Kibble-Zurek mechanism and finite-time scaling”. In: *Physical Review B* 110.12 (2024), p. 125113.
- [16] C. N. Weiler, T. W. Neely, D. R. Scherer, A. S. Bradley, M. J. Davis, and B. P. Anderson. “Spontaneous vortices in the formation of Bose–Einstein condensates”. In: *Nature* 455.7215 (2008), pp. 948–951.
- [17] S. Griffin, M. Lilienblum, K. Delaney, Y. Kumagai, M. Fiebig, and N. Spaldin. “From multiferroics to cosmology: Scaling behaviour and beyond in the hexagonal manganites”. In: *arXiv preprint arXiv:1204.3785* (2012).
- [18] G. Lamporesi, S. Donadello, S. Serafini, F. Dalfovo, and G. Ferrari. “Spontaneous creation of Kibble–Zurek solitons in a Bose–Einstein condensate”. In: *Nature Physics* 9.10 (2013), pp. 656–660.
- [19] M. Mielenz, J. Brox, S. Kahra, G. Leschhorn, M. Albert, T. Schätz, H. Landa, and B. Reznik. “Trapping of topological-structural defects in Coulomb crystals”. In: *Physical review letters* 110.13 (2013), p. 133004.
- [20] K. Pyka, J. Keller, H. Partner, R. Nigmatullin, T. Burgermeister, D. Meier, K. Kuhlmann, A. Retzker, M. B. Plenio, W. Zurek, *et al.* “Topological defect formation and spontaneous symmetry breaking in ion Coulomb crystals”. In: *Nature communications* 4.1 (2013), p. 2291.
- [21] S. Ulm, J. Roßnagel, G. Jacob, C. Degünther, S. Dawkins, U. Poschinger, R. Nigmatullin, A. Retzker, M. Plenio, F. Schmidt-Kaler, *et al.* “Observation of the Kibble–Zurek scaling law for defect formation in ion crystals”. In: *Nature communications* 4.1 (2013), p. 2290.
- [22] J. Beugnon and N. Navon. “Exploring the Kibble–Zurek mechanism with homogeneous Bose gases”. In: *Journal of Physics B: Atomic, Molecular and Optical Physics* 50.2 (2017), p. 022002.
- [23] B. Ko, J. W. Park, and Y.-i. Shin. “Kibble–Zurek universality in a strongly interacting Fermi superfluid”. In: *Nature physics* 15.12 (2019), pp. 1227–1231.
- [24] J.-M. Cui, F. J. Gómez-Ruiz, Y.-F. Huang, C.-F. Li, G.-C. Guo, and A. del Campo. “Experimentally testing quantum critical dynamics beyond the Kibble–Zurek mechanism”. In: *Communications Physics* 3.1 (2020), p. 44.
- [25] Y. Bando, Y. Susa, H. Oshiyama, N. Shibata, M. Ohzeki, F. J. Gómez-Ruiz, D. A. Lidar, S. Suzuki, A. Del Campo, and H. Nishimori. “Probing the universality of topological defect formation in a quantum annealer: Kibble-Zurek mechanism and beyond”. In: *Physical Review Research* 2.3 (2020), p. 033369.
- [26] K. Lee, S. Kim, T. Kim, and Y. Shin. “Universal Kibble–Zurek scaling in an atomic Fermi superfluid”. In: *Nature Physics* 20.10 (2024), pp. 1570–1574.
- [27] M. Rigol, V. Dunjko, and M. Olshanii. “Thermalization and its mechanism for generic isolated quantum systems”. In: *Nature* 452.7189 (2008), pp. 854–858.

- [28] A. del Campo, F. J. Gómez-Ruiz, and H.-Q. Zhang. “Locality of spontaneous symmetry breaking and universal spacing distribution of topological defects formed across a phase transition”. In: *Physical Review B* 106.14 (2022), p. L140101.
- [29] R. Samajdar and D. A. Huse. “Quantum and classical coarsening and their interplay with the Kibble-Zurek mechanism”. In: *arXiv preprint arXiv:2401.15144* (2024).
- [30] G. B. Mbeng, A. Russomanno, and G. E. Santoro. “The quantum Ising chain for beginners”. In: *SciPost Physics Lecture Notes* (2024), p. 082.
- [31] P. Di Francesco, P. Mathieu, and D. Sénéchal. *Conformal Field Theory*. Graduate Texts in Contemporary Physics. New York: Springer, 1997. ISBN: 9780387947853. URL: <https://books.google.ch/books?id=keUrdME5rhIC>.
- [32] S. R. White. “Density matrix formulation for quantum renormalization groups”. In: *Physical review letters* 69.19 (1992), p. 2863.
- [33] U. Schollwöck. “The density-matrix renormalization group in the age of matrix product states”. In: *Annals of physics* 326.1 (2011), pp. 96–192.
- [34] G. Vidal. “Efficient simulation of one-dimensional quantum many-body systems”. In: *Physical review letters* 93.4 (2004), p. 040502.
- [35] F. Verstraete, J. J. Garcia-Ripoll, and J. I. Cirac. “Matrix product density operators: Simulation of finite-temperature and dissipative systems”. In: *Physical review letters* 93.20 (2004), p. 207204.
- [36] S. Paeckel, T. Köhler, A. Swoboda, S. R. Manmana, U. Schollwöck, and C. Hubig. “Time-evolution methods for matrix-product states”. In: *Annals of Physics* 411 (2019), p. 167998.
- [37] J. Haegeman, J. I. Cirac, T. J. Osborne, I. Pižorn, H. Verschelde, and F. Verstraete. “Time-dependent variational principle for quantum lattices”. In: *Physical review letters* 107.7 (2011), p. 070601.
- [38] J. Haegeman, C. Lubich, I. Oseledets, B. Vandereycken, and F. Verstraete. “Unifying time evolution and optimization with matrix product states”. In: *Physical Review B* 94.16 (2016), p. 165116.
- [39] J. Dziarmaga. “Dynamics of a quantum phase transition: Exact solution of the quantum Ising model”. In: *Physical review letters* 95.24 (2005), p. 245701.
- [40] C.-Y. Xia and H.-B. Zeng. “Kibble Zurek mechanism in rapidly quenched phase transition dynamics”. In: *arXiv preprint arXiv:2110.07969* (2021).
- [41] H.-B. Zeng, C.-Y. Xia, and A. Del Campo. “Universal breakdown of Kibble-Zurek scaling in fast quenches across a phase transition”. In: *Physical Review Letters* 130.6 (2023), p. 060402.
- [42] H.-C. Kou and P. Li. “Varying quench dynamics in the transverse Ising chain: The Kibble-Zurek, saturated, and presaturated regimes”. In: *Physical Review B* 108.21 (2023), p. 214307.
- [43] M. Kolodrubetz, B. K. Clark, and D. A. Huse. “Nonequilibrium dynamic critical scaling of the quantum Ising chain”. In: *Physical review letters* 109.1 (2012), p. 015701.

- [44] A. Chandran, A. Erez, S. S. Gubser, and S. L. Sondhi. “Kibble-Zurek problem: Universality and the scaling limit”. In: *Physical Review B—Condensed Matter and Materials Physics* 86.6 (2012), p. 064304.
- [45] A. Francuz, J. Dziarmaga, B. Gardas, and W. H. Zurek. “Space and time renormalization in phase transition dynamics”. In: *Physical Review B* 93.7 (2016), p. 075134.
- [46] D. Sadhukhan, A. Sinha, A. Francuz, J. Stefaniak, M. M. Rams, J. Dziarmaga, and W. H. Zurek. “Sonic horizons and causality in phase transition dynamics”. In: *Physical Review B* 101.14 (2020), p. 144429.
- [47] F. J. Gómez-Ruiz, D. Subires, and A. del Campo. “Role of boundary conditions in the full counting statistics of topological defects after crossing a continuous phase transition”. In: *Physical Review B* 106.13 (2022), p. 134302.
- [48] B. Gardas, J. Dziarmaga, and W. H. Zurek. “Dynamics of the quantum phase transition in the one-dimensional Bose-Hubbard model: Excitations and correlations induced by a quench”. In: *Physical Review B* 95.10 (2017), p. 104306.
- [49] L. Cincio, J. Dziarmaga, M. M. Rams, and W. H. Zurek. “Entropy of entanglement and correlations induced by a quench: Dynamics of a quantum phase transition in the quantum Ising model”. In: *Physical Review A—Atomic, Molecular, and Optical Physics* 75.5 (2007), p. 052321.

# 3

## RESOLVING CHIRAL TRANSITIONS IN RYDBERG ARRAYS WITH QUANTUM KIBBLE–ZUREK MECHANISM AND FINITE-TIME SCALING

*The experimental realization of the quantum Kibble-Zurek mechanism in arrays of trapped Rydberg atoms has brought the problem of commensurate-incommensurate transition back into the focus of active research. Relying on equilibrium simulations of finite intervals, direct chiral transitions at the boundary of the period-3 and period-4 phases have been predicted. In this chapter, we study how these chiral transitions can be diagnosed experimentally with critical dynamics. We demonstrate that chiral transitions can be distinguished from the floating phases by comparing Kibble-Zurek dynamics on arrays with different numbers of atoms. Furthermore, by sweeping in the opposite direction and keeping track of the order parameter, we identify the location of conformal points. Finally, combining forward and backward sweeps, we extract all critical exponents characterizing the transition and demonstrate that the chiral universality class is non-conformal, with a non-integer dynamical critical exponent  $z$ .*

---

Parts of this chapter have been published in Physical Review B, 2024, vol. 110, no 12, p. 125113 [1].

### 3.1. INTRODUCTION

The development of conformal field theory (CFT) [2, 3] has led to the discovery of many fascinating critical phenomena. However, by construction, CFT is restricted to quantum phase transitions with dynamical critical exponent  $z = 1$ . The latter implies, in particular, a quantum-classical correspondence, which opens a way to study QPT with models of classical statistical mechanics. However, many critical phenomena are characterized by  $z \neq 1$  and cannot be explained by CFT [4].

The construction of advanced entanglement-based numerical techniques such as tensor network algorithms [5–8] and recent progress in quantum simulating platforms have further stimulated the discovery of exotic critical phenomena, putting a focus onto quantum versions of phase transitions. The study of phase transitions beyond CFT, although extremely challenging, has been attracting a lot of attention in the past decades. One of the most intriguing and debated problem is a possibility of a direct chiral transition out of crystalline period-3 phase predicted by Huse and Fisher [9] in the context of adsorbed monolayers [10–14].

Recent experiments on Rydberg atoms have shed new light onto this originally classical problem, but now in the context of one-dimensional (1D) quantum chains [15–24]. In these experiments, Rydberg atoms are trapped with optical tweezers at a well-controlled inter-atomic distance. The effective model for an array of Rydberg atoms can be described by the Hamiltonian of hard core bosons:

$$H = \frac{\Omega}{2} \sum_i (d_i + d_i^\dagger) - \Delta \sum_i n_i + \sum_{i < j} V_{ij} n_i n_j, \quad (3.1)$$

where  $\Omega$  is the Rabi frequency bringing an atom to the Rydberg state,  $\Delta$  is laser detuning and  $V_{ij} \propto 1/r_{ij}^6$  is a van der Waals potential. Within the hard-core boson formalism, an atom excited to a Rydberg state is considered occupied ( $n_i = 1$ ), while an atom in the ground state is regarded as empty ( $n_i = 0$ ). The operators  $d_i^\dagger$  and  $d_i$  respectively create and annihilate a Rydberg excitation at site  $i$ . Competition between the laser detuning, favouring atoms to be in Rydberg states, and strong van der Waals repulsions between them leads to a rich phase diagram dominated by lobes with integer periodicities  $p = 2, 3, 4, \dots$  [15, 25].

Although quantum-classical correspondence does not hold for non-conformal criticality, many features of the transitions with  $z \neq 1$  appear to be qualitatively similar [9, 17, 18, 20, 26]. In particular, using Huse and Fisher's original criteria for chiral transitions and numerical simulations with state-of-the-art density matrix renormalization group algorithm [5–7], it has been shown that in Rydberg arrays, the transition out of  $p = 3$  phase changes its nature multiple times [17–19, 27]. At the point where chiral perturbations vanish, the transition is conformal in the three-state Potts universality class; away from this point but not too far from it the transition is direct in the Huse-Fisher universality class; further away the transition is a two-step process via conformal Kosterlitz-Thouless [28] and non-conformal Pokrovsky-Talapov [29] transitions, with a floating phase between the two. Quite surprisingly, numerical simulations revealed that the boundary of the  $p = 4$  phase undergoes a similar zoo of QPTs with a conformal Ashkin-Teller point, followed by the  $p = 4$  chiral transition, and then by the floating phase [18, 20].

The experimental data obtained with Rydberg atoms can be explained from the numerical predictions describing intervals of chiral transitions [17, 20, 23]. However, the numerical methods used to diagnose phase transitions differ greatly from the experimental techniques. Numerical simulations mainly rely on equilibrium physics and extracted critical exponents  $\nu$  of the correlation length,  $\bar{\beta}$  of the incommensurate wave vector, and  $\alpha$  of the specific heat. At the same time, the experiments are performed out of equilibrium, employing quantum Kibble-Zurek (KZ) mechanism [15, 30, 31], which tracks the number of domain walls (kinks) formed upon sweeping through a phase transition as a function of sweep rate. This chapter aims to fill the gap between the theoretical predictions for chiral transitions and experimentally accessible measurements to diagnose them.

With that purpose in mind, we employ a combination of two non-equilibrium methods. We use the KZ mechanism from the disordered to the ordered phase and the finite-time scaling of the order parameter from the ordered to the disordered phase. Both methods are very easy to implement experimentally and do not require fitting correlation functions or calculating structure factors, but only employ local operators.

The remaining of this chapter is organized as follows: Section 3.2 describes the numerical methods and technical details for the extraction of the critical exponents. Section 3.3 shows and compare our numerical calculations for the blockade model and the model with  $1/r^6$  interactions. Finally, we discuss our results in Section 3.4.

## 3.2. NUMERICAL METHODS

### 3.2.1. BLOCKADE MODEL

The strong van der Waals repulsion between Rydberg states induces an effective blockade at short distances. Owing to the rapid decay of the van der Waals interaction, it is reasonable to approximate the Hamiltonian in Eq. (3.1) by an  $r$ -site blockade model:

$$H = \sum_i -\frac{\Omega}{2}(d_i^\dagger + d_i) - \Delta n_i + V_{r+1} n_i n_{i+r+1} \quad (3.2a)$$

$$n_i (n_i - 1) = n_i n_{i+1} = \dots = n_i n_{i+r} = 0. \quad (3.2b)$$

All operators in Eq. (3.2a) are acting in the constrained Hilbert space defined by Eq. (3.2b), which implies that two atoms cannot be excited within a certain distance  $r$ . Only the next-to-blockade interaction is considered, and the rest of the decaying interaction tail is set to zero. Various blockade ranges give access to different slices of the phase diagram [20]: we will use  $r = 1$  blockade to probe chiral transition out of period-3 phase and  $r = 2$  for the period-4 case. The advantage of the blockade model is three-fold: *i*) it provides a good approximation to the van der Waals potential [17, 18, 20]; *ii*) tensor networks with explicitly implemented blockade have significantly lower computational costs [16, 20]; *iii*) for these models, the location and extent of chiral transitions are known with a high accuracy [17, 20].

To fully profit from the reduced Hilbert space, a new basis was taken, wherein each element of the new basis is composed of a pair of adjacent local basis elements, where the last element of each tensor overlaps with the first site on the following tensor. In

other words, we span the local physical degrees of freedom of each individual tensor over two consecutive atoms. Using the occupation of the atom shared between two nearest tensors as a quantum label of the auxiliary bond that connects them, we can bring the network into a block-diagonal form. The latter drastically reduces the computational complexity. Figure 3.1 illustrates how the  $r = 1$  blockade basis is constructed.

The bulk Hamiltonian in the new  $|h_i\rangle$  basis is:

$$h_i = -\frac{\Omega}{2} (\tilde{a}_i \tilde{b}_{i+1} + \text{h.c.}) - \Delta \tilde{q}_i + V_2 \tilde{q}_i \tilde{p}_{i+1}. \quad (3.3)$$

The term  $\tilde{a}_i \tilde{b}_{i+1} + \text{h.c.}$  represents the first term in Eq. (3.2a) of the main text. This term flips an atom between ground and Rydberg states. It comprises three local sites, with  $\tilde{a}|h_1\rangle = |h_2\rangle$ ,  $\tilde{b}|h_1\rangle = |h_3\rangle$ , and 0 otherwise. The operators  $\tilde{q}_i$  and  $\tilde{p}_i$  are local density operators for the left and right sites in each pair, returning non-zero values only for  $\tilde{q}|h_3\rangle = |h_3\rangle$  and  $\tilde{p}|h_2\rangle = |h_2\rangle$  correspondingly. As a result, the next-nearest-neighbor interaction  $V_2 n_i n_{i+2}$  transforms into a nearest-neighbor interaction  $V_2 \tilde{q}_i \tilde{p}_{i+1}$ .

In order to match the original Hamiltonian of Eq. (3.3), this effective model must be carefully adapted close to the boundary.

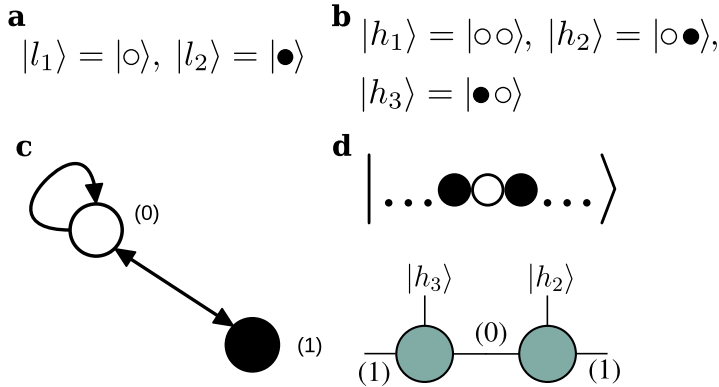


Figure 3.1.: Mapping of the  $r = 1$  blockade model onto a model preserving the block diagonal structure of tensors. (a) Local Hilbert space  $|l_i\rangle$  of the original model. (b) New local Hilbert space spanned over two consecutive sites. (c) Fusion graph for the recursive construction of the environment (both, left and right): starting with empty site (0), another empty site can always be added, ending up with label (0). Additionally, an occupied site can be added, leading to the label (1). On the other side, starting with label (1), only an empty site can be added, which results in label (0). (d) Example of the label assignment in MPS representation on two consecutive tensors written for the selected state.

The explicit implementation of  $r = 2$  blockade is conceptually very similar, as described in Figure 3.2. We span the local degrees of freedom over three consecutive atoms and use the quantum state of the two atoms shared by nearest tensors as quantum labels

for their common auxiliary leg. The bulk Hamiltonian has the form:

$$h_i = -\frac{\Omega}{2} (\tilde{a}_i \tilde{b}_{i+1} \tilde{c}_{i+2} + \text{h.c.}) - \Delta \tilde{p}_i + V_3 \tilde{q}_i \tilde{p}_{i+1}. \quad (3.4)$$

In this case, the term  $\tilde{a}_i \tilde{b}_{i+1} \tilde{c}_{i+2} + \text{h.c.}$  represents the first term in Eq. (3.2a) of the main text, which flips an atom between ground and Rydberg states. The only non-zero elements are  $\tilde{a} |h_1\rangle = |h_2\rangle$ ,  $\tilde{b} |h_1\rangle = |h_3\rangle$  and  $\tilde{c} |h_1\rangle = |h_4\rangle$ . The terms  $\tilde{q}_i$  and  $\tilde{p}_i$  represent the density of the local sites  $i$  and  $i+2$  correspondingly, with only a single non-zero entry  $\tilde{q} |h_4\rangle = |h_4\rangle$  and  $\tilde{p} |h_2\rangle = |h_2\rangle$ . The interaction  $V_3 n_i n_{i+3}$  transforms into a nearest-neighbor interaction  $V_2 \tilde{q}_i \tilde{p}_{i+1}$  under the new basis. Similarly to the  $r=1$  case, this Hamiltonian has to be adapted close to the edges to capture the boundary terms.

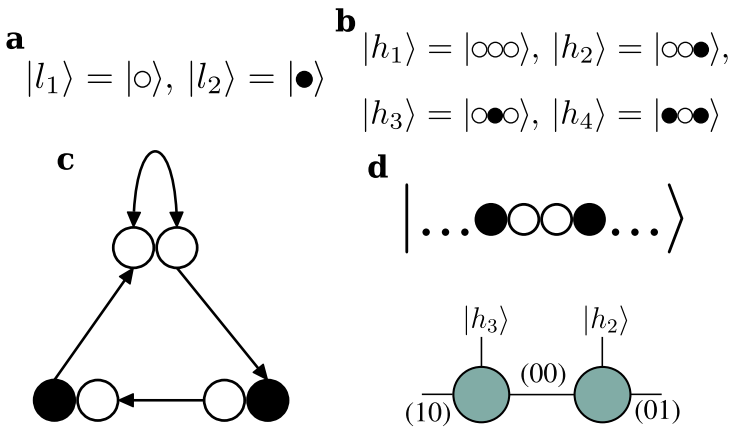


Figure 3.2.: Mapping of the  $r=2$  blockade model onto a model preserving the block diagonal structure of tensors. (a) Local Hilbert space of the original model  $|l_i\rangle$ . (b) New local Hilbert space spanned over three consecutive sites. (c) Fusion graph for the recursive construction of the left environment (for the right environment, the direction of arrows should be reverted). (d) Example of the label assignment in MPS representation on two consecutive tensors written for the selected state.

A more complete description of the algorithms are described in Appendix A.

### 3.2.2. MODELING THE RYDBERG MODEL WITH $1/r^6$ INTERACTION

An interaction written as a sum of exponentials can be incorporated without any approximation into a matrix product operator (MPO) representation. Specifically, an interaction of the form

$$c \sum_r \lambda^r \hat{n}_i \hat{n}_{i+r} \quad (3.5)$$

admits an exact implementation withing the bulk operator [7]:

$$\hat{W}_i = \begin{bmatrix} \hat{I} & 0 & 0 \\ \hat{n} & \lambda \hat{I} & 0 \\ 0 & c\lambda \hat{n} & \hat{I} \end{bmatrix}. \quad (3.6)$$

Thus, the decaying  $1/r^{-6}$  van der Waals interaction was expressed as a sum of 6 exponentials [7, 32], i.e.  $1/r^6 = \sum_{i=1}^6 c_i \lambda_i^r$ . The coefficients  $c_i$  and exponents  $\lambda_i$  were determined by minimizing the cost function defined as:

$$\sum_{r=1}^L \left| \frac{1}{r^6} - \sum_{i=1}^6 c_i \lambda_i^r \right|, \quad (3.7)$$

following the procedure described in Ref. [32]. This approximation reproduces the interaction with excellent accuracy up to a distance of approximately 20 atoms, yielding a cost-function error of about  $3.5 \times 10^{-18}$  for a system size  $L = 241$ .

### 3.2.3. GROUND STATE CALCULATIONS

The initial state defined at time  $t = 0$  is a ground state at a given point in the phase diagram sufficiently far from the transition. This point is located either in the disordered phase (corresponding to the starting point for the Kibble-Zurek mechanism) or in the ordered period-3 or period-4 phases (the starting points for the backward sweeps for the finite-time scaling of the order parameter).

For the blockade model, the ground state was determined with imaginary time-evolving block decimation (TEBD) for the two blockade models. We used second-order Trotter decomposition. Maximal bond dimension was kept at  $D = 300$ , and singular values below  $\chi > 10^{-6}$  were truncated. Convergence criteria were based on the order parameter, with calculations considered converged when the relative variation of the order parameter was smaller than  $10^{-9}$ . Deep inside the ordered phase, the correlation length is very small, and the energy cost of the domain wall formation is relatively cheap. Therefore, there are many low-lying excited states above the ground states. When the system is close to the classical limit, and the entanglement is low, the TEBD is often stuck at such states with multiple domain walls. To circumvent this issue, we took as a starting guess a classical state (with  $D = 1$ ) that resembles the expected pattern of occupied and empty sites.

For the model with the  $1/r^6$  interactions ground state was calculated using the two-sites density-matrix renormalization group (DMRG) algorithm [5–7]. To match the ordered phase and boundary conditions, the system sizes were chosen in the form  $L = Np + 1$ , where  $N$  is an integer, and  $p$  is the periodicity of the ordered phase. Ground-state convergence was assumed when the variation in total energy between two consecutive full sweeps satisfied  $\Delta E < 10^{-8}$ .

### 3.2.4. SIMULATION OF DYNAMICS

Simulations of dynamics in the blockade model were performed using a second-order time-evolving block decimation algorithm (TEBD). For the  $r = 1$  blockade, a two-site

Trotterization was applied, while for the  $r = 2$  blockade, a three-site Trotterization was used. The time step was maintained at  $\delta t = 0.1$ , and the maximum bond dimension and singular value cutoff were set to  $D = 300$  and  $\chi > 10^{-6}$  correspondingly.

Figure 3.3 shows convergence with respect to bond dimension for Kibble-Zurek(KZ) dynamics across transitions of various types. In Figure 3.3(a) and (b), we present the extracted density of kinks formed across the three-state Potts and for the Ashkin-Teller point correspondingly as a function of sweep rates for bond dimension ranging from  $D = 50$  to  $D = 300$ . It is clear from the figure that the finite-bond dimension effect is stronger for the Ashkin-Teller point, but in both cases, the results for the two largest bond dimensions are indistinguishable.

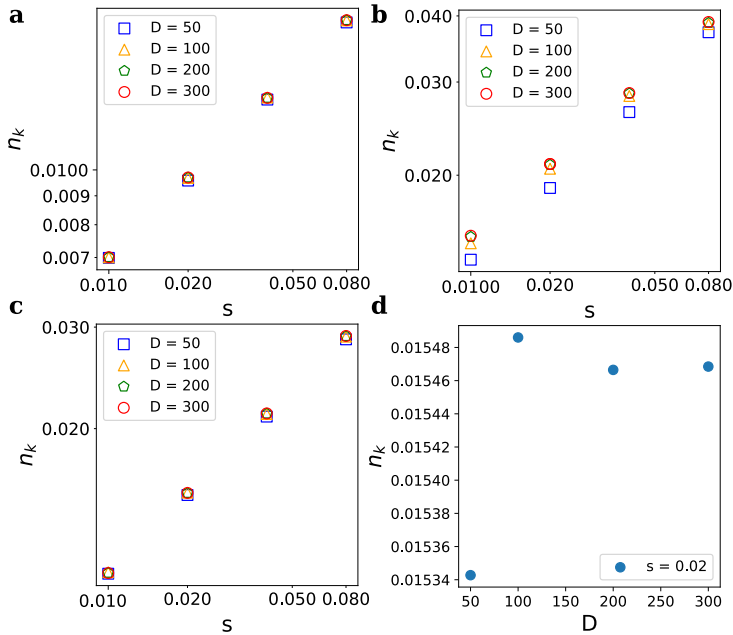


Figure 3.3.: Density of kinks as a function of sweep rate in a log–log scale for various maximal bond dimensions  $D$  measured after crossing (a) the three-state Potts transition; (b) the Ashkin-Teller transition; (c) the chiral transition. (d) Density of kinks formed across the chiral transition for a given sweep rate as a function of bond dimension  $D$ .

Figure 3.3(c) shows the density of kinks formed while crossing the  $p = 3$  chiral transition. Figure 3.3(d) shows the convergence of the extracted density of kinks for a given sweep rate  $s$  as a function of bond dimension  $D$ .

For the Rydberg model with  $1/r^6$  van der Waals interactions, time evolution was simulated using the Time-Dependent Variational Principle (TDVP) [33, 34]. The long-range interactions were approximated using a sum of 7 exponentials; the maximum error in this approximation was  $\sim 10^{-10}$ , with a cost function  $\sim 1.3 \times 10^{-19}$ . Different  $\delta t$  for various sweep rates and critical points were tested during 24h simulations. The values of

$\delta t$  that gave the fastest simulations were taken for surrounding sweep rates and critical points. Truncation criteria were maintained at  $\chi > 10^{-6}$ , and the maximum bond dimension was set to  $D = 400$ .

### 3.2.5. KINK OPERATORS

Kinks can be counted in two different ways. One way is counting the number of domain walls. Figure 3.4 depicts the types of domain walls that can appear in period-3 as described in Ref. [9]. An alternative method for counting kinks is using an operator that counts the absence of an ordered state. This *no-order* operator would be  $(1 - \bullet\circ\circ - \circ\circ\bullet - \circ\bullet\circ)$  in the period-3 case, and quantifies a kink every time the periodicity of the phase is not followed. These two methods of counting kinks are not always equivalent. For instance, the first method would count one kink in the state  $\bullet\circ\circ\bullet\circ\circ\bullet$ , while the second method would count two kinks. Additionally, the first method would not count any kink in the state  $\bullet\circ\circ\circ\circ\bullet$ , since the type of domain of the chain does not change, while the second method would count three kinks. A comprehensive analysis of domain-wall counting in the context of the KZ mechanism can be found in Chapter 2.

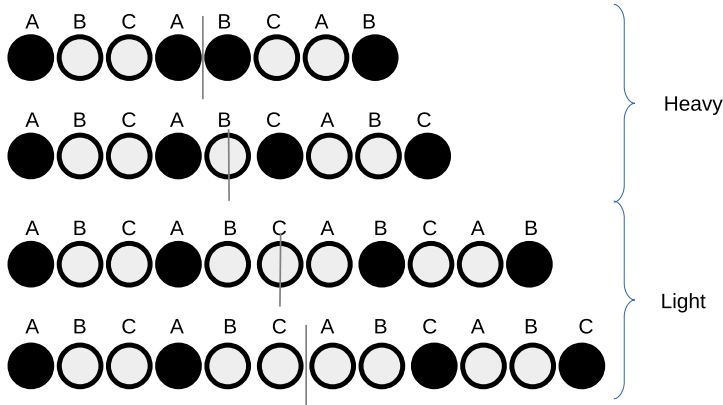


Figure 3.4.: Types of domain walls in the period 3 phase. There are three types of domains, depending on the label  $A$ ,  $B$  or  $C$  on top of the black dot.

In Figure 3.5, we compare the KZ scaling using the two abovementioned counting methods. Figure 3.5(a) compares two different cuts through the Potts point for a  $r = 1$  blockade, while Figure 3.5(b) compares two final distances from the AT point in the  $r = 2$  blockade model. In all cases, blue squares and green pentagons represent the density of kinks measured with the no-order operator while orange triangles and red circles represent the density of domain walls as described in Figure 3.4

For the  $r = 1$  blockade model, data points representing the density of domain walls for the two different cuts and the density kinks using the no-order operator for cut 2 overlap and are close to the theoretical value  $\mu \approx 0.454$ . In contrast, data points representing the density of kinks for the no-order operator are off and far from 0.454. However, for  $r = 2$

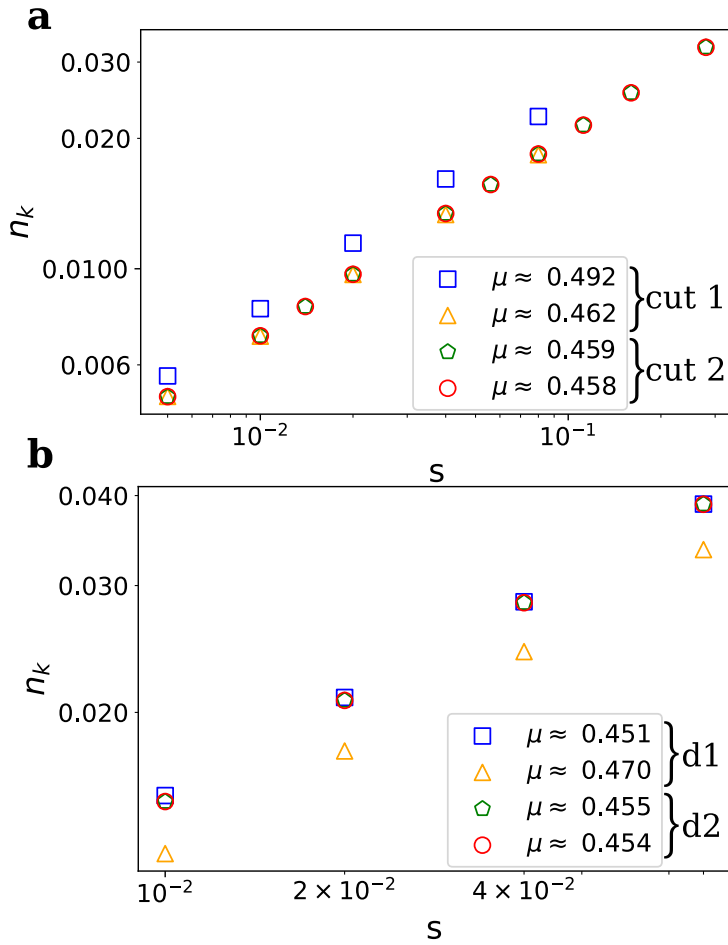


Figure 3.5.: KZ scaling for the density kinks measured as domain walls (orange triangles and red circles) or with a *no-order* operator (blue squares and green pentagons) for (a) two different cuts through the Potts point for the  $r = 1$  blockade model (b) two final distances from the AT points for the  $r = 2$  blockade model.

the opposite situation occurs. Data points representing the density of kinks measured with the no-order operator for the two different final distances d1 (short) and d2 (long) and the density of domain walls for d2 overlap and are close to the theoretical value  $\mu \approx 0.44$ , while the density of domain walls for d1 is off and far from 0.44. Similar effects were found for different cuts and final distances from the critical point, where convergence always occurred faster for the density of domain walls in the  $r = 1$  blockade and for the density of kinks calculated with the no-order operator for the  $r = 2$  blockade.

We believe that the discrepancy between the two methods comes from the rare ap-

pearance of unlikely events - the state  $\bullet\circ\circ\bullet\circ\circ\bullet$  is forbidden by the blockade, while the state  $\bullet\circ\circ\circ\circ\bullet$  is energetically more costly than any other type of domain walls sketched in Figure 3.4. However sweeping along certain trajectories, for example, those along which incommensurability is non-monotonous [17, 20] the probability of these events might increase. In our research we compared different trajectories, different start and end points and pick ups the kink operators that is the most robust: domain wall operators for period-3 and no-order operator for period-4.

## 3

### 3.2.6. ORDER PARAMETER

In this section, we define the order parameter associated with the gaped period-3 and period-4 phases with broken translation symmetry. As an order parameter, we use the local amplitude of the local density that we average over the whole finite-size chain. Explicitly, for the period-3 case, we use:

$$O = \frac{1}{L-2} \sum_{i=1}^{L-2} \max_i (|n_i - n_{i+1}|, |n_i - n_{i+2}|) \quad (3.8)$$

and for the period-4:

$$O = \frac{1}{L-3} \sum_{i=1}^{L-3} \max_i (|n_i - n_{i+1}|, |n_i - n_{i+2}|, |n_i - n_{i+3}|) \quad (3.9)$$

## 3.3. RESULTS

### 3.3.1. FINITE-SIZE EFFECTS IN KIBBLE-ZUREK MECHANISM

In the main text, we argue that in the Kibble-Zurek mechanism, the intermediate floating phase can be distinguished from the direct transition by tracking the finite-size effects in the density of kinks formed by sweeping through the criticality. Figure 3.6 shows the density of kinks as a function of the system size for the two cuts presented in Figure 3.9 of the main text. Figure 3.6(a) depicts a cut through the chiral transition. Through this cut, the density of kinks increases with the system size  $L$ . Figure 3.6(b) shows the cut through the floating phase, which is mainly governed by the Kosterlitz-Thouless (KT) transition between the disordered and the floating phases. In contrast to the direct transition, the density of kinks systematically decreases with the system size.

The Kibble-Zurek mechanism across the transitions into the period-4 phase with a  $r = 2$  blockade model shows qualitatively similar finite-size effects as in the period-3 case. The results for period-4 are summarized in Figure 3.7.

### 3.3.2. FINITE-SIZE EFFECT IN THE FINITE-TIME SCALING

Figure 3.8 compares the finite-time scaling (FTS) for two different system sizes. For both system sizes, direct transition (see Figure 3.8(a)) and sweep through a floating phase (see Figure 3.8(b)), we observe an almost perfect overlap except for the slowest sweep rates.

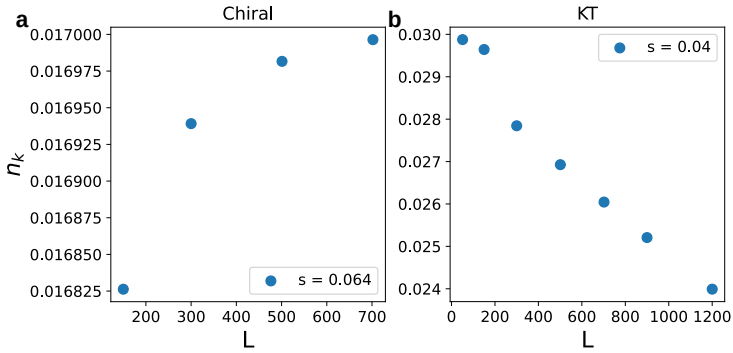


Figure 3.6.: Finite-size effect of the density of kinks formed by sweeping from the disordered phase to the period-3 phase across (a) the direct chiral transition and (b) the intermediate floating phase separated from the disordered phase by the Kosterlitz-Thouless (KT) transition. The value of sweep rate  $s$  is indicated at each panel.

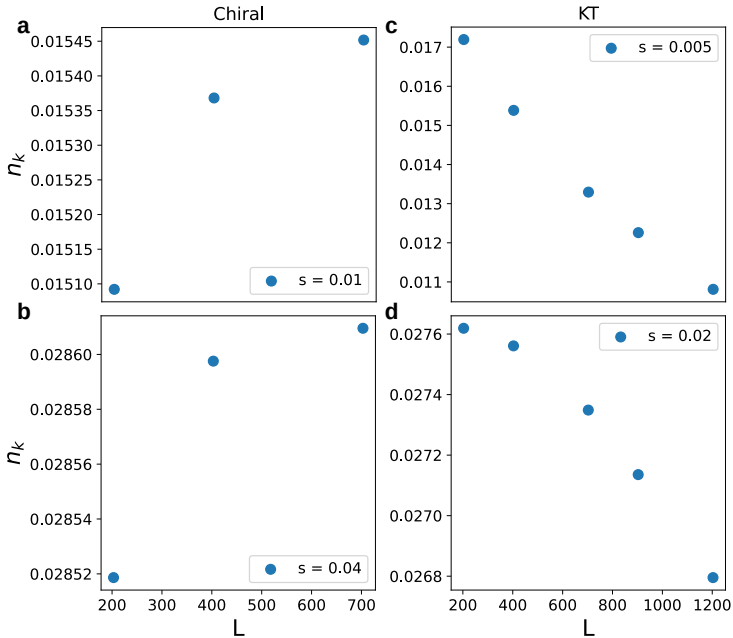


Figure 3.7.: Finite-size effect of the density of kinks formed by sweeping from the disordered phase to the period-4 phase across (a),(b) the direct chiral transition and (c),(d) the intermediate floating phase separated from a disordered phase by the Kosterlitz-Thouless (KT) transition. The trajectories for (a) and (b) and for (c) and (d) are identical.

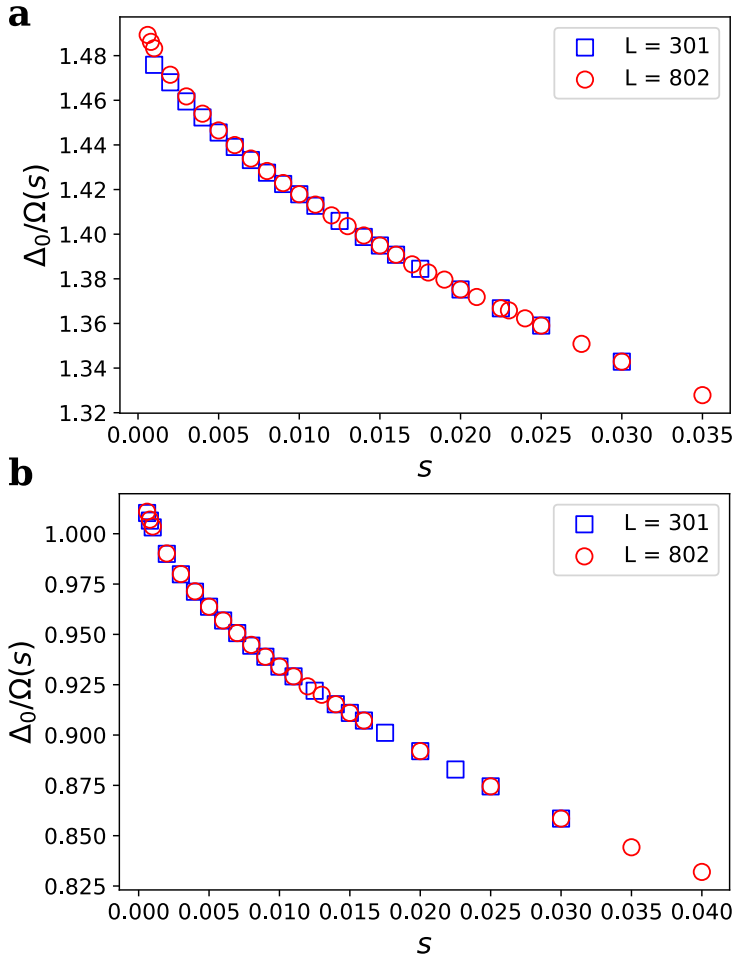


Figure 3.8.: Comparison of the system size effect in the finite-time scaling for (a) a direct transition and (b) an intermediate floating phase for two different system sizes. In both figures, the difference is visible only for very small sweep rates.

### 3.3.3. DYNAMICAL SIGNATURES OF THE FLOATING PHASE

Our first goal is to resolve the direct chiral transition from the intermediate critical phase. Upon approaching the floating phase from the disordered one, the correlation length  $\xi$  diverges as a stretch exponential due to Kosterlitz-Thouless transition [28]:

$$\xi(\epsilon) = \xi_0 \exp\left(\frac{2a}{\sqrt{|\epsilon|}}\right), \quad (3.10)$$

where  $\xi_0$  and  $a$  are non-universal constants. As already discussed in Chapter 2.1, this scaling leads to an effective exponent  $\nu_{\text{eff}} \rightarrow \infty$ , and consequently  $\mu_{\text{eff}} \rightarrow 1$ . Interestingly, this value is much larger than the one for the three-state Potts ( $\mu = 5/11$ ) or Ashkin-Teller

( $0.4 \leq \mu \leq 0.5$ ) transitions. But we rely on the fact that this scaling is only approached asymptotically and otherwise is affected by significant finite-size effects [35, 36].

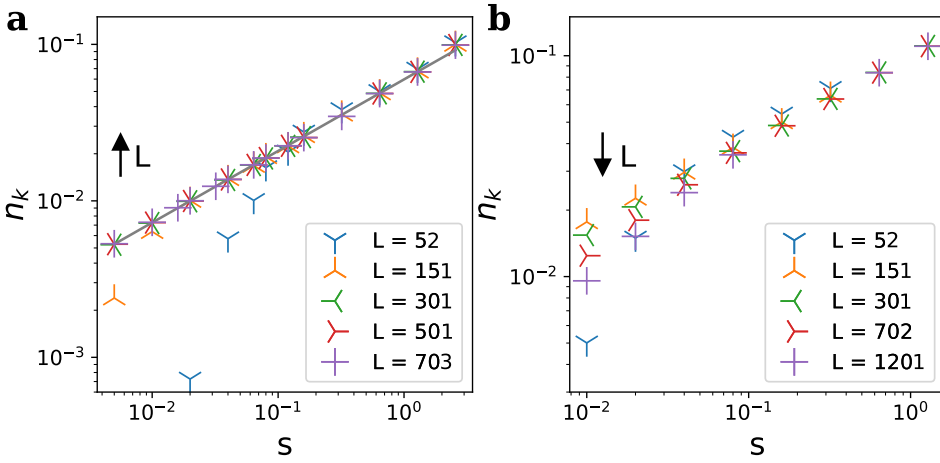


Figure 3.9.: Scaling of the density of kinks  $n_k$  with the sweep rate  $s$  through (a) the direct transition; and (b) the floating phase. Arrows show systematic finite-size effects that can be used to resolve the two critical regimes. The grey line is a linear fit in a log–log scale.

In Figure 3.9(a), we present the scaling of the density of kinks [37] formed by sweeping through the direct transitions for various system sizes. For a given size  $L$ , there is a certain range of sweep rates  $s$  where the scaling in log–log plot is linear, in agreement with the KZ mechanism. However, the curves turn down for small  $s$ , where the system dynamics approaches the adiabatic regime for a given  $L$ . A more detailed analysis is provided in Chapter 1, adapted from Ref.[38]. This is similar to when one underestimates a correlation length when it is comparable to or exceeds the chain length. The window of the universal KZ scaling can be increased by increasing the length  $L$ . In other words, comparing the density of kinks at low sweep rates for several system sizes, we see that it grows with  $L$  [37].

Across the floating phase, the finite-size effect is very different, as presented in Figure 3.9(b): the larger the system size, the closer to the asymptotic limit, and therefore the steeper the scaling is. Focusing again on low sweep rates, we see a systematic and fast decrease in kinks density with  $L$  [37]. However, the limitation of measurable density of kinks for very small system size  $L$  is still in place, as can be clearly seen for  $L = 52$ .

To summarize, for a set of sufficiently large system sizes, the density of kinks grows with the system size towards the universal KZ scaling when the system is driven through a direct transition and  $n_k$  decays significantly when sweeping through the floating phase.

#### CONFORMAL VS CHIRAL TRANSITIONS WITH KZ MECHANISM.

We have defined a protocol to distinguish the direct transition from the floating phase. Now let us see if with critical dynamics we could identify when the transition is conformal

mal. For this purpose, we systematically extract the KZ critical exponent  $\mu$  across various cuts into period-3 and period-4 phases. Our numerical results are summarized in Figure 3.10. For the model with  $r = 1$  blockade, there is only one conformal critical point, and its location is known exactly [27]. For the model with  $r = 2$  blockade, the location of the conformal point has been obtained numerically by tracking the commensurate line where chiral perturbations vanish [20].

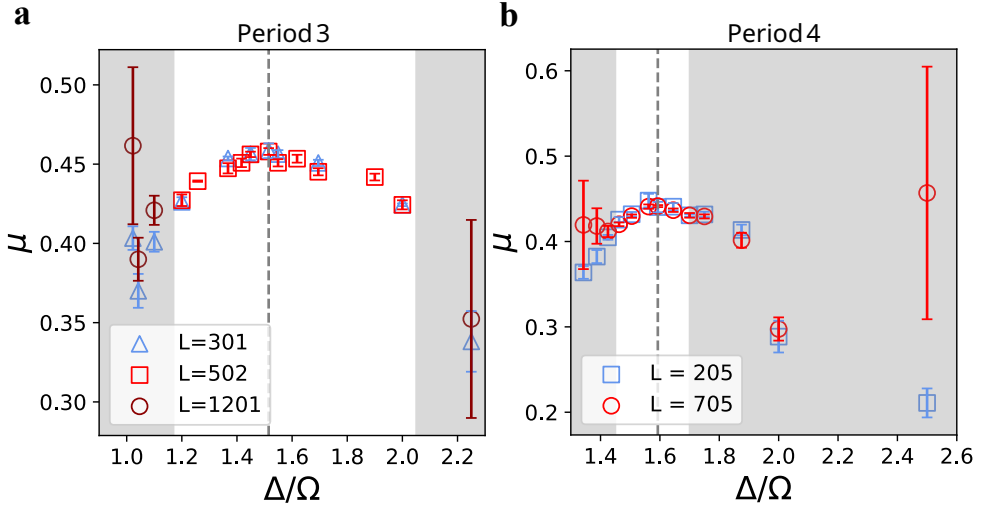


Figure 3.10.: Critical exponent  $\mu$  extracted with the Kibble-Zurek mechanism along various cuts through the transitions (a) into the period-3 phase with  $r = 1$  blockade and (b) into the period-4 phase with  $r = 2$  blockade. The vertical dashed line indicates the location of the conformal point. The shaded region states for the floating phase. In this area, the Kibble-Zurek mechanism is not defined, and our results should be taken only as  $\mu_{\text{eff}}$ . At the conformal points (dashed lines), the extracted values of  $\mu$  agree with theory predictions within 1%. The error bars represent uncertainties from the fitting procedure but do not account for errors arising from the finite bond dimension or the Trotter decomposition. For a more detailed discussion of these sources of error, see the Methods section.

For both transitions into period-3 and period-4 phases, the KZ critical exponent  $\mu$  measured for a set of consecutive cuts has a dome shape, taking maximal values at the cuts that go through the conformal points. Numerically obtained values  $\mu \approx 0.458$  for the three-state Potts and  $\mu \approx 0.442$  for the Ashkin-Teller point (with  $\nu \approx 0.78$  [20]) agree within 1% with the CFT predictions. Away from conformal points,  $\mu$  shows a slow decay. The dome-like shape we observe here is in excellent agreement with the experimental results [15], and has been overlooked in the previous numerical simulations of dynamics hidden by large numerical errors [15].

By looking at Figure 3.10 with marked conformal points, it is easy to associate them with maxima of  $\mu$ . However, if the location of these points were unknown (as is often the

case in experiments), then the problem would be quite challenging since the domes are relatively flat. As a solution, we propose performing a backward sweep.

### 3.3.4. FINITE-TIME SCALING

Sweeping from the ordered to the disordered phase—in the direction opposite to the KZ mechanism—allows to study a relaxation of the order. The faster is the sweeping rate the longer it takes for the order parameter [37] to disappear after crossing the transition, as illustrated by the inset of Figure 3.11(a). We extract the ratio  $\mu/\nu$  by fitting the location where the order parameter vanishes with Eq. (1.57), as shown in Figure 3.11(b). Furthermore, we extract  $\beta\mu/\nu$  in the inset by fitting the order parameter at the critical point with Eq. (1.58).

Combining the results from the two fits, we extract the critical exponent  $\beta$  along various cuts from period-3 and period-4 phases. The results are summarized in Figure 3.12(a) and (b) correspondingly. Similar to the Kibble-Zurek critical exponent  $\mu$ , we find that  $\beta$  takes its maximal values at the conformal points. However, the sharp peaks in  $\beta$  allow identifying the location of the critical point with significantly smaller uncertainty.

It is important to keep in mind that the critical exponent  $\beta$  is well understood only for the two conformal points. At the three-state Potts point, it takes the universal value  $\beta = 1/9$ . Our numerical result  $\beta \approx 0.112$  agrees within  $\sim 2\%$  with this value. As long as the transition to the disordered phase is direct and the order parameter goes to zero at the transition, the exponent  $\beta$  can be formally defined. However, its value is unknown and might be affected by the domain wall tension [9]. Indeed, what we observe is that  $\beta$  is not universal and varies along the chiral transition, decaying away from the conformal point. This fully agrees with previous numerical results on the chiral clock model where the exponent  $\beta$  for chiral transitions has been extracted [39].

Ashkin-Teller critical theory defines the family of universality classes with the exponents  $\frac{1}{12} \leq \beta \leq \frac{1}{8}$  and  $\frac{2}{3} \leq \nu \leq 1$  satisfying  $d = \beta/\nu = 1/8$  [40]. Our numerical result  $\beta \approx 0.1073$  belongs to the corresponding interval. Equilibrium simulations have reported an Ashkin-Teller point with  $\nu \approx 0.78$  [20], implying  $\beta \approx 0.098$ . This value agrees with our out-of-equilibrium result within 10%. Similar to the period-3 case, we see that the value of  $\beta$  is not universal along the  $p = 4$  chiral transition.

### 3.3.5. COMBINING KZ WITH FTS

Combination of forward and backwards sweeping opens a way to extract all critical exponents, including the dynamical critical exponent  $z$  presented in Figure 3.13(a) and (c): at the two conformal points our numerical results match the CFT value  $z = 1$ ; away from these points  $z$  increases, in agreement with previous studies [15, 20]. We also extract the critical exponent  $\alpha$ . Unlike other critical exponents,  $\alpha$  does not change significantly along the chiral transitions. This agrees with the idea that along chiral transitions,  $\alpha$  keeps the value it takes at the conformal point [41–43].

### 3.3.6. DERIVED CRITICAL EXPONENTS

In this section, we present additional results of the critical exponents that can be derived from the Kibble-Zurek mechanism and the finite-time scaling of the order parameter. In

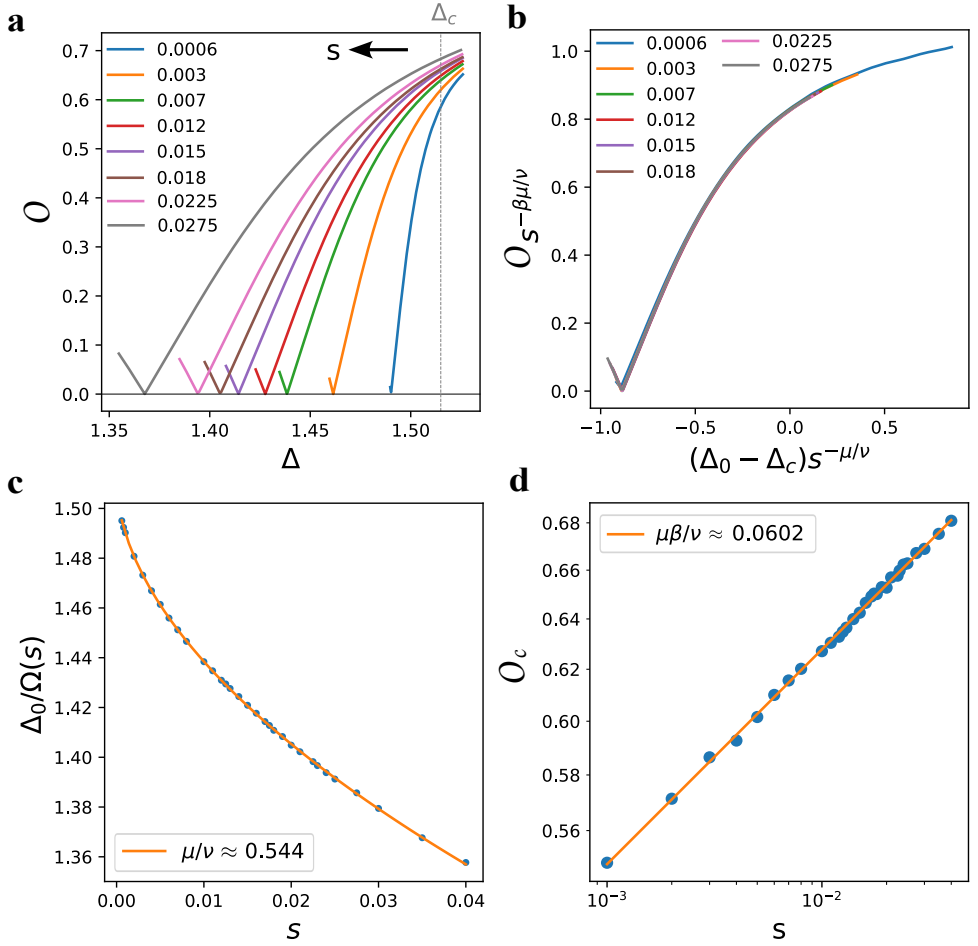


Figure 3.11.: Example of the finite-time scaling out of period-3 phase. (a) Order parameter as a function of the sweep rate before rescaling. (b) Same data as in (a), after rescaling according to the axes labels. (c) Scaling of the location of the point  $\Delta_0$ , where the order parameter vanishes as a function of sweep rate. (d) Scaling of the order parameter  $O$  at the critical point  $\Delta_c$  as a function of sweep rate  $s$ . Orange lines are fits with Eq. (1.57) and (1.58).

particular, we show the correlation length critical exponent  $\nu$  across various cuts into the period-3 (see Figure 3.14(a)) and into the period-4 (see Figure 3.14(c)) phases. In both cases, the critical exponent  $\nu$  of the chiral transition stays within  $\approx 5 - 6\%$  of the value at the corresponding conformal point. Our results for the period-3 case (see Figure 3.14(a)) agree with the results on the chiral clock model reporting the decrease of  $\nu$  away from the Potts point [39]. Curiously enough, for the period-4 case, we see that on one side of the transition,  $\nu$  might increase. It would be interesting to clarify the behaviour of  $\nu$  with

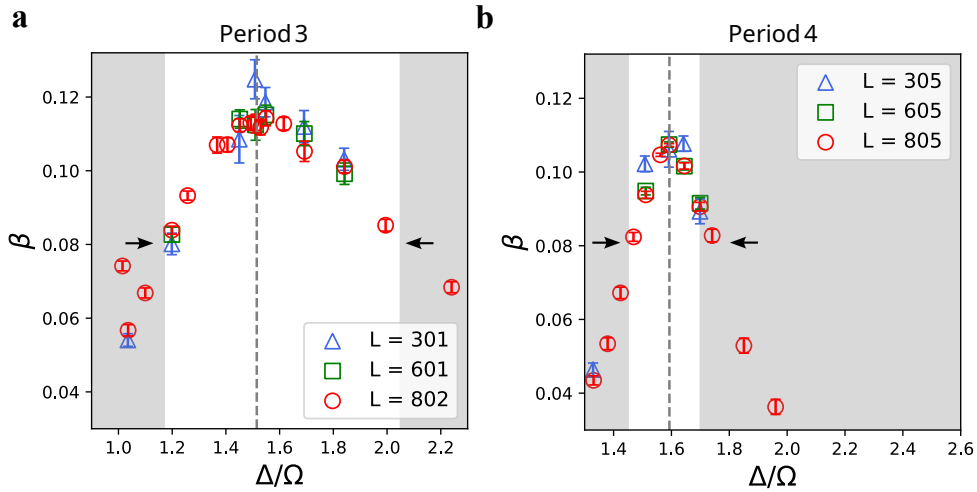


Figure 3.12.: Critical exponent  $\beta$  measured with finite-time scaling of the order parameter while sweeping from the ordered (a) period-3 and (b) period-4 phases to the disordered one. In both cases, the conformal points (dashed lines) correspond to the pronounced peaks in  $\beta$ . Shaded regions indicate the floating phases.

a more accurate systematic estimate of  $\nu$  across the period-4 transition.

In addition, we extract the scaling dimension  $d = \beta/\nu$  of the operator that defines the order parameter. These results are summarized in Figure 3.14(b),(d).

### 3.3.7. RESULTS FOR THE RYDBERG MODEL WITH $1/r^6$ INTERACTION.

Finally, we checked that our results on the blockade model can be extrapolated to the Rydberg model with the  $1/r^6$  van der Waals interaction.

#### ISING TRANSITION

We benchmark our method with Ising transition [15, 24] into period-2 phase for which there are theory predictions for all critical exponents ( $\nu = 1$ ,  $z = 1$ ,  $\mu = 0.5$ ).

Figure 3.15 show scaling of the density of kinks and extracted Kibble-Zurek critical exponent  $\mu$  for three different cuts across the Ising transition - the agreement is always within 2%.

#### CRITICAL EXPONENTS FOR THE PERIOD-3 PHASE

By sweeping from the disordered to the period-3 phase we extract the critical exponent  $\mu$  for various cuts along the transition. The results are summarized in 3.16(a). The point where the critical exponent  $\mu$  takes the maximal value is in good agreement with previously identified location of the three-state Potts point [18]. Interestingly, above the Potts

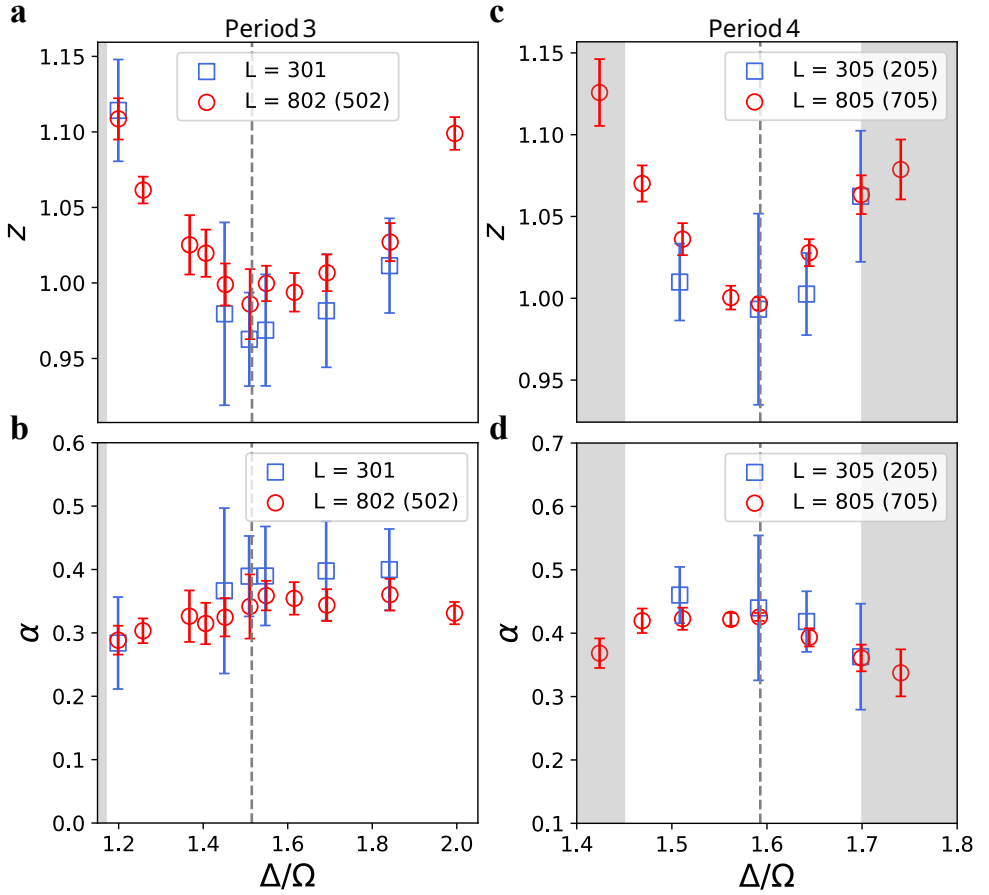


Figure 3.13.: Dynamical critical exponent  $z$  and specific heat critical exponent  $\alpha$  computed across various cuts across transitions to the (a)-(b) period-3 and (c)-(d) period-4 phases. (a),(c) Our results agree with  $z = 1$  at the two conformal points (dashed lines) and suggest that  $z > 1$  when the transitions are chiral. (b),(d) Numerically extracted values of  $\alpha$  are in good agreement with CFT predictions  $\alpha = 1/3$  for three-state Potts and  $\alpha \approx 0.44$  for the Ashkin-Teller point with  $\nu \approx 0.78$ . We show the results for small (blue) and large (red) system sizes; when  $L$  used in KZ and in finite-time scaling are different, the former is indicated in brackets. Shaded regions state for the floating phases.

point,  $\mu$  decays very slowly, in agreement with an extended interval of the chiral transition. However, although the qualitative shape of 3.16(a) is similar to the one of 3.10(a), the values of  $\mu$  seem to be above the theoretical ones, with a discrepancy of 5% for  $\mu$  on the Potts point respect to the CFT prediction  $\mu \approx 0.454$ .

We attribute this discrepancy to the small system sizes and fast sweep rates employed in the simulations due to numerical limitations. We expect that larger system sizes and

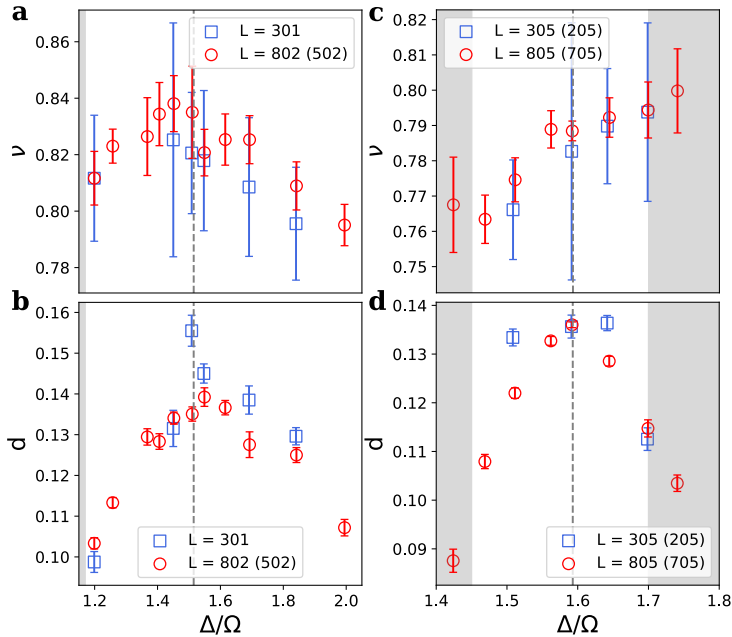


Figure 3.14.: Correlation length critical exponent  $\nu$  (a,c) and scaling dimension of the order parameter  $d = \beta/\nu$  (b,d) extracted by combining the Kibble-Zurek mechanism with finite-time scaling across the transition (a-b) into period-3 and (c-d) into period-4 phases.

slower sweep rates would enable a more accurate determination of the critical exponents and help distinguish the floating phase from the chiral transition.

Sweeping on the opposite direction—from the period-3 to the disordered phase—we perform a finite-time scaling and extract the critical exponent  $\beta$  by keeping track of the order parameter. Figure 3.16(b) depicts the numerically extracted values of  $\beta$  for various cuts across the transition. Similar to the blockade model, we see a sharp peak in  $\beta$  around the conformal point. At the three-state Potts point, the extracted value of  $\beta$  agrees with the theoretical prediction  $\beta = 1/9$  within 5%.

Combining the results from KZ and FTS we extract the critical exponent  $z$ . Figure 3.16(c) shows  $z$  for various cuts along the transition. As it happened in the blockade model,  $z$  has a minimum at the conformal point and increases with the chiral perturbation. The calculated value of  $z$  in the predicted Potts point is  $z \approx 1.01 \pm 0.05$ , in agreement with a conformal transition.

### 3.4. DISCUSSION

In this manuscript, we have shown that quantum phase transitions can be fully characterized using out-of-equilibrium physics—specifically, by combining the Kibble-Zurek (KZ) mechanism with finite-time scaling of the order parameter.

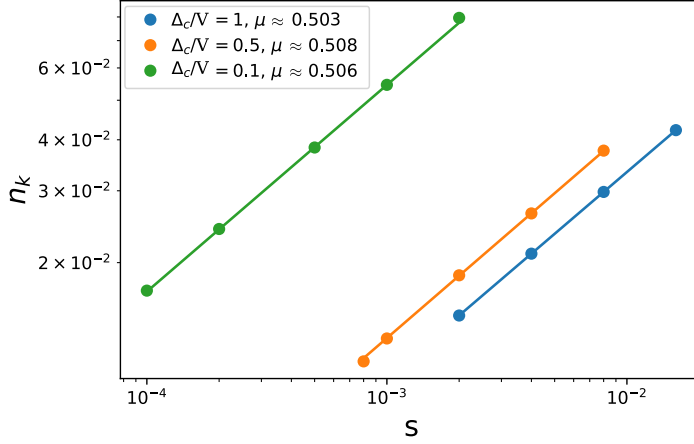


Figure 3.15.: Scaling of the density of kinks  $n_k$  with the sweep rate for a disordered to period  $p = 2$  phase transition in the Rydberg model at different critical values of detuning  $\Delta_c$ . The transition belongs to the Ising universality class characterized by a Kibble-Zurek exponent  $\mu = 0.5$ . The extracted value of  $\mu$  is in excellent agreement with theoretical predictions

We demonstrated that the emergence of an intermediate floating phase can be identified by comparing KZ dynamics in Rydberg atom arrays of varying system sizes. Our approach relies on the standard KZ protocol and, in contrast to previous proposals, does not require measurements of the correlation length, incommensurate wave vector [20], or structure factor [44] near or within the critical region.

We further showed that, by sweeping from the ordered to the disordered phase and monitoring the order parameter, the location of conformal points can be accurately determined from the distribution of values of the critical exponent  $\beta$ . The conformal point corresponds to the peak in  $\beta$ . Although this method involves multiple sweeps terminating at varying distances from the transition, the ordered phase is relatively robust to noise, and only a limited number of runs may be sufficient. To reliably prepare a high-fidelity ordered state and ensure identical initial conditions for all sweeps, one can employ the recently developed light-shift technique [45].

Finally, we have shown that when the transition is direct, the KZ mechanism can be combined with finite-time scaling of the order parameter to extract all critical exponents of the transition.

Our predictions for blockade models remain valid for the model with  $1/r^6$  van der Waals potential defined in Eq. (3.1). Performing a finite-time scaling of the period-3 order we observe a sharp peak in  $\beta$  [37] that agrees with previously identified location of the conformal point [18]. At the same point, the KZ exponent  $\mu$  takes its maximum, but the peak is not so pronounced.

The interval of the  $\mathbb{Z}_4$ -chiral transition in this model is very narrow [18], making it extremely challenging for dynamical studies. However, the protocols developed here are

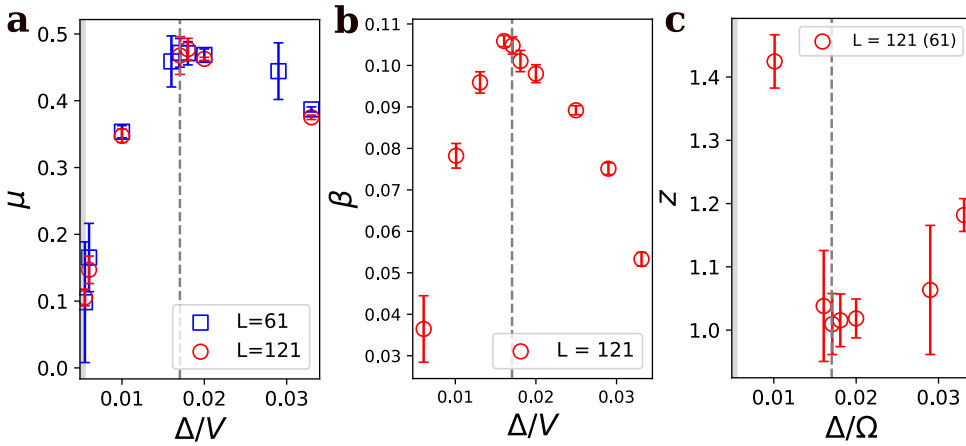


Figure 3.16.: Critical exponents (a)  $\mu$ , (b)  $\beta$  and (c)  $z$  computed across various cuts for the period-3 Rydberg model with  $1/r^6$  interaction using KZ, FTS, and combining both techniques, respectively. When combining KZ with FTS, the system size for KZ is in brackets. Both  $\mu$  and  $\beta$  have a dome shape that peaks at the conformal three-state Potts point. This peak is more pronounced for  $\beta$ , and agrees with theory prediction  $\beta = 1/9$  for the three-state Potts point within 5%.  $z$  has a minimum  $z \approx 1$  at the conformal point, which agrees with a conformal transition. Numerical results for  $\mu$  agree within 5% with CFT predictions  $\mu \approx 0.454$  for the three-state Potts point.

generic and can be applied to multi-component systems, where the extent of the chiral transition can be controlled [46]. A similar qualitative effect of the chiral perturbation on the value of the critical exponents  $\mu$ ,  $\beta$  and  $\nu$  has been previously reported in the chiral Potts [47] and chiral clock [48] models.

Our results, together with the previous numerical studies [17, 20, 23, 39] suggest that chiral transitions might belong to a weak universality class with critical exponents controlled by chiral perturbations. At the same time, when chiral perturbations become too strong, the chiral transitions are known to be unstable, and the floating phase opens.

Taking a closer look to the critical exponent  $\beta$  presented in Figure 3.12 we notice that its value at the point where the chiral transition terminates is roughly the same on both sides of the period-3 and period-4 conformal points. Given the uncertainties in our data and the imprecise location of the Lifshitz points, we cannot exclude the possibility that this is a merely coincidence. However, the possibility that chiral transition terminates once beta drops below a certain universal threshold warrants a more detailed and systematic investigation. We hope that our findings will stimulate further theoretical exploration into the universal properties of these exotic transitions.



# BIBLIOGRAPHY

- [1] J. Soto Garcia and N. Chepiga. “Resolving chiral transitions in one-dimensional Rydberg arrays with quantum Kibble-Zurek mechanism and finite-time scaling”. In: *Physical Review B* 110.12 (2024), p. 125113.
- [2] P. Di Francesco, P. Mathieu, and D. Sénéchal. *Conformal Field Theory*. Graduate Texts in Contemporary Physics. New York: Springer, 1997. ISBN: 9780387947853. URL: <https://books.google.ch/books?id=keUrdME5rhIC>.
- [3] A. M. Tselik. *Quantum Field Theory in Condensed Matter Physics*. 2nd ed. Cambridge University Press, 2003. DOI: [10.1017/CBO9780511615832](https://doi.org/10.1017/CBO9780511615832).
- [4] S. Sachdev. *Quantum Phase Transitions*. 2nd ed. Cambridge University Press, 2011.
- [5] S. R. White. “Density matrix formulation for quantum renormalization groups”. In: *Phys. Rev. Lett.* 69 (19 Nov. 1992), pp. 2863–2866. DOI: [10.1103/PhysRevLett.69.2863](https://doi.org/10.1103/PhysRevLett.69.2863). URL: <http://link.aps.org/doi/10.1103/PhysRevLett.69.2863>.
- [6] S. Östlund and S. Rommer. “Thermodynamic Limit of Density Matrix Renormalization”. In: *Phys. Rev. Lett.* 75 (19 Nov. 1995), pp. 3537–3540. DOI: [10.1103/PhysRevLett.75.3537](https://doi.org/10.1103/PhysRevLett.75.3537). URL: <http://link.aps.org/doi/10.1103/PhysRevLett.75.3537>.
- [7] U. Schollwöck. “The density-matrix renormalization group in the age of matrix product states”. In: *Annals of physics* 326.1 (2011), pp. 96–192.
- [8] S. Paeckel, T. Köhler, A. Swoboda, S. R. Manmana, U. Schollwöck, and C. Hubig. “Time-evolution methods for matrix-product states”. In: *Annals of Physics* 411 (2019), p. 167998. ISSN: 0003-4916. DOI: <https://doi.org/10.1016/j.aop.2019.167998>. URL: <https://www.sciencedirect.com/science/article/pii/S0003491619302532>.
- [9] D. A. Huse and M. E. Fisher. “Domain walls and the melting of commensurate surface phases”. In: *Physical Review Letters* 49.11 (1982), p. 793.
- [10] M. den Nijs. “The Domain Wall Theory of Two-dimensional Commensurate-Incommensurate Phase Transitions”. In: *Phase Transitions and Critical Phenomena* 12 (1988), p. 219.
- [11] J. Schreiner, K. Jacobi, and W. Selke. “Experimental evidence for chiral melting of the Ge(113) and Si(113) 3×1 surface phases”. In: *Phys. Rev. B* 49 (4 Jan. 1994), pp. 2706–2714. DOI: [10.1103/PhysRevB.49.2706](https://doi.org/10.1103/PhysRevB.49.2706). URL: <https://link.aps.org/doi/10.1103/PhysRevB.49.2706>.

- [12] D. L. Abernathy, S. Song, K. I. Blum, R. J. Birgeneau, and S. G. J. Mochrie. “Chiral melting of the Si(113) (3×1) reconstruction”. In: *Phys. Rev. B* 49 (4 Jan. 1994), pp. 2691–2705. DOI: [10.1103/PhysRevB.49.2691](https://doi.org/10.1103/PhysRevB.49.2691). URL: <https://link.aps.org/doi/10.1103/PhysRevB.49.2691>.
- [13] W. Selke and J. M. Yeomans. “A Monte Carlo study of the asymmetric clock or chiral Potts model in two dimensions”. In: *Zeitschrift für Physik B Condensed Matter* 46.4 (Dec. 1982), pp. 311–318. ISSN: 1431-584X. DOI: [10.1007/BF01307706](https://doi.org/10.1007/BF01307706). URL: <http://s://doi.org/10.1007/BF01307706>.
- [14] D. A. Huse and M. E. Fisher. “Commensurate melting, domain walls, and dislocations”. In: *Phys. Rev. B* 29 (1 Jan. 1984), pp. 239–270. DOI: [10.1103/PhysRevB.29.239](https://doi.org/10.1103/PhysRevB.29.239). URL: <https://link.aps.org/doi/10.1103/PhysRevB.29.239>.
- [15] A. Keesling, A. Omran, H. Levine, H. Bernien, H. Pichler, S. Choi, R. Samajdar, S. Schwartz, P. Silvi, S. Sachdev, *et al.* “Quantum Kibble–Zurek mechanism and critical dynamics on a programmable Rydberg simulator”. In: *Nature* 568.7751 (2019), pp. 207–211.
- [16] N. Chepiga and F. Mila. “DMRG investigation of constrained models: from quantum dimer and quantum loop ladders to hard-boson and Fibonacci anyon chains”. In: *SciPost Phys.* 6 (3 2019), p. 33. DOI: [10.21468/SciPostPhys.6.3.033](https://doi.org/10.21468/SciPostPhys.6.3.033). URL: <https://scipost.org/10.21468/SciPostPhys.6.3.033>.
- [17] N. Chepiga and F. Mila. “Floating phase versus chiral transition in a 1D hard-boson model”. In: *Physical review letters* 122.1 (2019), p. 017205.
- [18] I. A. Maceira, N. Chepiga, and F. Mila. “Conformal and chiral phase transitions in Rydberg chains”. In: *Physical Review Research* 4.4 (2022), p. 043102.
- [19] G. Giudici, A. Angelone, G. Magnifico, Z. Zeng, G. Giudice, T. Mendes-Santos, and M. Dalmonte. “Diagnosing Potts criticality and two-stage melting in one-dimensional hard-core boson models”. In: *Phys. Rev. B* 99 (9 Mar. 2019), p. 094434. DOI: [10.1103/PhysRevB.99.094434](https://doi.org/10.1103/PhysRevB.99.094434). URL: <https://link.aps.org/doi/10.1103/PhysRevB.99.094434>.
- [20] N. Chepiga and F. Mila. “Kibble-Zurek exponent and chiral transition of the period-4 phase of Rydberg chains”. In: *Nature Communications* 12.1 (2021), p. 414.
- [21] S. Whitsitt, R. Samajdar, and S. Sachdev. “Quantum field theory for the chiral clock transition in one spatial dimension”. In: *Phys. Rev. B* 98 (20 Nov. 2018), p. 205118. DOI: [10.1103/PhysRevB.98.205118](https://doi.org/10.1103/PhysRevB.98.205118). URL: <https://link.aps.org/doi/10.1103/PhysRevB.98.205118>.
- [22] N. Chepiga and F. Mila. “Lifshitz point at commensurate melting of chains of Rydberg atoms”. In: *Phys. Rev. Res.* 3 (2 Apr. 2021), p. 023049. DOI: [10.1103/PhysRevResearch.3.023049](https://doi.org/10.1103/PhysRevResearch.3.023049). URL: <https://link.aps.org/doi/10.1103/PhysRevResearch.3.023049>.
- [23] R. Samajdar, S. Choi, H. Pichler, M. D. Lukin, and S. Sachdev. “Numerical study of the chiral Z<sub>3</sub> quantum phase transition in one spatial dimension”. In: *Physical Review A* 98.2 (2018), p. 023614.

- [24] M. Rader and A. M. Läuchli. *Floating Phases in One-Dimensional Rydberg Ising Chains*. 2019. arXiv: [1908.02068](https://arxiv.org/abs/1908.02068) [[cond-mat.quant-gas](https://arxiv.org/abs/1908.02068)].
- [25] H. Bernien, S. Schwartz, A. Keesling, H. Levine, A. Omran, H. Pichler, S. Choi, A. S. Zibrov, M. Endres, M. Greiner, *et al.* “Probing many-body dynamics on a 51-atom quantum simulator”. In: *Nature* 551.7682 (2017), pp. 579–584.
- [26] B. E. Lüscher, F. Mila, and N. Chepiga. “Critical properties of the quantum Ashkin-Teller chain with chiral perturbations”. In: *Phys. Rev. B* 108 (18 Nov. 2023), p. 184425. DOI: [10.1103/PhysRevB.108.184425](https://doi.org/10.1103/PhysRevB.108.184425). URL: <https://link.aps.org/doi/10.1103/PhysRevB.108.184425>.
- [27] P. Fendley, K. Sengupta, and S. Sachdev. “Competing density-wave orders in a one-dimensional hard-boson model”. In: *Phys. Rev. B* 69 (7 Feb. 2004), p. 075106. DOI: [10.1103/PhysRevB.69.075106](https://doi.org/10.1103/PhysRevB.69.075106). URL: <https://link.aps.org/doi/10.1103/PhysRevB.69.075106>.
- [28] J. M. Kosterlitz and D. J. Thouless. “Ordering, metastability and phase transitions in two-dimensional systems”. In: *Journal of Physics C: Solid State Physics* 6.7 (1973), p. 1181. URL: <http://stacks.iop.org/0022-3719/6/i=7/a=010>.
- [29] V. L. Pokrovsky and A. L. Talapov. “Ground State, Spectrum, and Phase Diagram of Two-Dimensional Incommensurate Crystals”. In: *Phys. Rev. Lett.* 42 (1 Jan. 1979), pp. 65–67. DOI: [10.1103/PhysRevLett.42.65](https://doi.org/10.1103/PhysRevLett.42.65). URL: <https://link.aps.org/doi/10.1103/PhysRevLett.42.65>.
- [30] W. H. Zurek, U. Dorner, and P. Zoller. “Dynamics of a quantum phase transition”. In: *Physical review letters* 95.10 (2005), p. 105701.
- [31] J. Dziarmaga. “Dynamics of a quantum phase transition: Exact solution of the quantum Ising model”. In: *Physical review letters* 95.24 (2005), p. 245701.
- [32] B. Pirvu, V. Murg, J. I. Cirac, and F. Verstraete. “Matrix product operator representations”. In: *New Journal of Physics* 12.2 (2010), p. 025012.
- [33] J. Haegeman, J. I. Cirac, T. J. Osborne, I. Pižorn, H. Verschelde, and F. Verstraete. “Time-dependent variational principle for quantum lattices”. In: *Physical review letters* 107.7 (2011), p. 070601.
- [34] J. Haegeman, C. Lubich, I. Oseledets, B. Vandereycken, and F. Verstraete. “Unifying time evolution and optimization with matrix product states”. In: *Physical Review B* 94.16 (2016), p. 165116.
- [35] J. Dziarmaga and W. H. Zurek. “Quench in the 1D Bose-Hubbard model: Topological defects and excitations from the Kosterlitz-Thouless phase transition dynamics”. In: *Scientific reports* 4.1 (2014), p. 5950.
- [36] B. Gardas, J. Dziarmaga, and W. H. Zurek. “Dynamics of the quantum phase transition in the one-dimensional Bose-Hubbard model: Excitations and correlations induced by a quench”. In: *Physical Review B* 95.10 (2017), p. 104306.

- [37] See Supplemental Material, which includes Refs. [5–7, 15, 17, 18, 20, 24, 27, 32–34, 39], for implementation details on numerical algorithms for blockade models; technical details on simulation of ground-state and dynamics; discussion of the effect of finite sizes in Kibble-Zurek mechanism and on finite-time scaling; definition of the order parameter and of the kink operators; and for numerical results for the model with long-range van der Waals potential.
- [38] J. Soto-Garcia and N. Chepiga. “Quantum Kibble-Zurek mechanism: The role of boundary conditions, endpoints, and kink types”. In: *Physical Review B* 113.8 (2026), p. 085430.
- [39] R.-Z. Huang and S. Yin. “Nonequilibrium critical dynamics in the quantum chiral clock model”. In: *Physical Review B* 99.18 (2019), p. 184104.
- [40] J. C. Bridgeman, A. O’Brien, S. D. Bartlett, and A. C. Doherty. “Multiscale entanglement renormalization ansatz for spin chains with continuously varying criticality”. In: *Phys. Rev. B* 91 (16 Apr. 2015), p. 165129. DOI: [10.1103/PhysRevB.91.165129](https://doi.org/10.1103/PhysRevB.91.165129). URL: <https://link.aps.org/doi/10.1103/PhysRevB.91.165129>.
- [41] G. Albertini, B. M. McCoy, J. H. Perk, and S. Tang. “Excitation spectrum and order parameter for the integrable N-state chiral Potts model”. In: *Nuclear Physics B* 314.3 (1989), pp. 741–763. ISSN: 0550-3213. DOI: [https://doi.org/10.1016/0550-3213\(89\)90415-X](https://doi.org/10.1016/0550-3213(89)90415-X). URL: <http://www.sciencedirect.com/science/article/pii/055032138990415X>.
- [42] R. J. Baxter. “Superintegrable chiral Potts model: Thermodynamic properties, an “inverse” model, and a simple associated Hamiltonian”. In: *Journal of Statistical Physics* 57.1 (Oct. 1989), pp. 1–39. ISSN: 1572-9613. DOI: [10.1007/BF01023632](https://doi.org/10.1007/BF01023632). URL: <https://doi.org/10.1007/BF01023632>.
- [43] J. L. Cardy. “Critical exponents of the chiral Potts model from conformal field theory”. In: *Nuclear Physics B* 389.3 (1993), pp. 577–586. ISSN: 0550-3213. DOI: [https://doi.org/10.1016/0550-3213\(93\)90353-Q](https://doi.org/10.1016/0550-3213(93)90353-Q). URL: <http://www.sciencedirect.com/science/article/pii/055032139390353Q>.
- [44] J. Zhang, S. H. Cantú, F. Liu, A. Bylinskii, B. Braverman, F. Huber, J. Amato-Grill, A. Lukin, N. Gemelke, A. Keesling, *et al.* “Probing quantum floating phases in Rydberg atom arrays”. In: *arXiv preprint arXiv:2401.08087* (2024).
- [45] K.-L. Pham, T. F. Gallagher, P. Pillet, S. Lepoutre, and P. Cheinet. “Coherent light shift on alkaline-earth Rydberg atoms from isolated core excitation without autoionization”. In: *PRX Quantum* 3.2 (2022), p. 020327.
- [46] N. Chepiga. “Tunable Quantum Criticality in Multicomponent Rydberg Arrays”. In: *Physical review letters* 132.7 (2024), p. 076505.
- [47] Y. Huang, S. Yin, B. Feng, and F. Zhong. “Kibble-Zurek mechanism and finite-time scaling”. In: *Physical Review B* 90.13 (2014), p. 134108.
- [48] X.-J. Yu. “Dynamical phase transition and scaling in the chiral clock Potts chain”. In: *arXiv preprint arXiv:2309.03454* (2023).

# 4

## INFINITE RANDOMNESS CRITICALITY AND LOCALIZATION OF THE FLOATING PHASE IN ARRAYS OF RYDBERG ATOMS TRAPPED WITH NON-PERFECT TWEEZERS

*The success of Rydberg atoms arrays originates from the precise control of lattice geometries provided by optical tweezers, which allows access to a wide range of synthetic quantum phases. Experiments on one-dimensional arrays have stimulated tremendous progress in understanding quantum phase transitions into crystalline phases. However, the finite width of tweezers introduces small variations in interatomic distances, leading to quenched disorder in the interactions. In this letter, we numerically study how such disorder alters the nature of two critical regimes observed in experiments. Firstly, following experimental protocols, we analyze Kibble–Zurek dynamics and find a crossover from the clean Ising transition to the infinite-randomness fixed point as system size and disorder strength increase. Secondly, we show that the floating phase—an incommensurate Luttinger liquid phase emerging at stronger interactions—is localized by the disorder, yet preserves short-range incommensurate correlations with the same leading wave vector. Our results clearly reveal an additional technical challenge in the scalability of Rydberg-based quantum simulators.*

### 4.1. INTRODUCTION

A key advantage of Rydberg atoms platforms is the control over atomic positions and interaction strengths. In practice, however, fluctuations of atomic positions inside each

---

Parts of this chapter have been published in *arXiv*, 2025, arXiv:2506.11985 [1].

tweezer—especially along the axis perpendicular to the plane of the lattice—introduce an intrinsic level of spatial disorder (see, for instance, the appendix of Ref.[2]). While typically small, such distortions can qualitatively alter critical behavior [3, 4].

The paradigmatic example demonstrating the significant effect of disorder on quantum phase transitions in one dimension is infinite randomness criticality. It appears as a fixed point in the transverse-field Ising model in the presence of disorder—random distribution either in the interaction or in the transverse field or in both [5, 6]. It was shown that such disorder forms a relevant perturbation: even an infinitesimal width in the random distribution of coupling constants brings the system into a fundamentally different universality class in the thermodynamic limit. This regime is governed by extremely anisotropic scaling, with two distinct correlation length critical exponents  $\nu_{\text{typ}} = 1$  for typical and  $\nu_{\text{av}} = 2$  for average correlations, and an infinite dynamical critical exponent,  $z \rightarrow \infty$  [5–7], forming a striking contrast to the clean Ising transition with a single  $\nu = 1$  and  $z = 1$ . The crossover between these two universality classes—clean Ising and infinite randomness—is governed by system size, disorder strength, and proximity to criticality[6, 8–10].

These changes in universality class have profound consequences for the KZ mechanism. In clean Ising systems, the density of topological defects (kinks) scales with the sweep rate of the control parameter according to a universal power law  $\mu = 0.5$  [11]. In contrast, in the infinite-randomness criticality, this scaling is dramatically modified: the defect density no longer follows a power law, but exhibits a logarithmic dependence on the sweep rate [9, 10]. Interestingly, this anomalous scaling behavior only emerges at sufficiently slow sweeps, while faster ramps exhibit a crossover resembling the clean Ising regime [9, 10].

In this chapter, we study how disorder in the Rydberg interactions impacts two prominent physical phenomena recently highlighted in the literature: (i) the KZ probe of the Ising transition into the period-2 phase; and (ii) the equilibrium properties of the floating phase. Our focus on the Ising transition is motivated by the fact that, to date, it is the only case where the effects of disorder on both equilibrium and KZ scaling are theoretically well-understood [12], though the role of longer-range interactions is still debated [13–15]. By contrast, the effect of disorder on the chiral transitions appearing at the boundary of the period-3 and 4 lobes [16–21], to the best of our knowledge, remains unexplored. While we do not address this problem directly, we argue that disorder can explain systematic discrepancies between numerical simulations and experimental results[22]. Finally, we show that disorder has a dramatic effect on the floating phase: it destroys quantum criticality while preserving short-range incommensurate correlations with the same leading wave vector.

## 4.2. THE MODEL

We consider a finite one-dimensional chain of Rydberg atoms, described in terms of hard-core bosons with a disordered interaction potential:

$$\frac{H}{\hbar} = \frac{\Omega}{2} \sum_i (d_i + d_i^\dagger) - \Delta \sum_i n_i + \sum_{i < j} V_i \frac{n_i n_j}{(i-j)^6}, \quad (4.1)$$

where  $d_i^\dagger$  ( $d_i$ ) creates (annihilates) a Rydberg excitation at site  $i$ , and  $n_i = d_i^\dagger d_i$  is the corresponding number operator. The hard-core constraint enforces a single excitation per site, i.e.  $d_i^\dagger |1\rangle_i = 0$ .  $\Omega$  is the Rabi frequency and  $\Delta$  is the laser detuning of the coherent laser with respect to the resonant frequency. The blockade effect prevents simultaneous excitation of atoms within a certain distance, characterized by the blockade radius  $R_b/a = (V_0/\Omega)^{1/6}$ , with  $a$  being the interatomic distance.

We assume that tweezers form an evenly spaced lattice, while deviations in the atomic positions are introduced through a disorder in the interaction strength. Thus, the potential  $V_i$  is a quenched random variable with a uniform box distribution in the interval  $[1 - \delta V, 1 + \delta V]$ .

Based on the typical uncertainties on the position of the atoms [2], we study four values of disorder strength  $\delta V = 0.15, 0.25, 0.4$  and  $0.5$ . Further details can be found in Sec. 4.3. We also include the clean case  $\delta V = 0$  for the reference.

## 4.3. METHODS

### 4.3.1. ESTIMATION OF THE DISORDER STRENGTH

Atoms confined in optical tweezers exhibit positional fluctuations of approximately  $\delta x \approx 0.12, \mu\text{m}$  in the radial direction and  $\delta y \approx 0.6, \mu\text{m}$  along the longitudinal axis [2]. Such uncertainties can significantly affect the interaction strength between atoms.

To quantify this effect, we apply linear error propagation. For a general function  $f(x, y)$  with uncertainties  $\delta x$  and  $\delta y$ , the propagated uncertainty is

$$\delta f(x, y) = \sqrt{\left(\frac{\partial f}{\partial x}\right)^2 (\delta x)^2 + \left(\frac{\partial f}{\partial y}\right)^2 (\delta y)^2}. \quad (4.2)$$

In our case, the relevant dependence arises from the interatomic spacing  $a$  entering the van der Waals interaction:

$$V = \frac{V_0}{a^6} \sum_{i < j} \frac{1}{|i - j|^6} \hat{n}_i \hat{n}_j. \quad (4.3)$$

Propagating the uncertainty in  $a$  gives

$$\delta V = 6 \frac{V_0}{a^7} \delta a \sum_{i < j} \frac{1}{|i - j|^6} \hat{n}_i \hat{n}_j \Rightarrow \frac{\delta V}{V} = 6 \frac{\delta a}{a}. \quad (4.4)$$

To leading order, the uncertainty in the relative displacement is

$$\delta a = \Delta x = \sqrt{2} \delta x \approx 0.12 \sqrt{2} \mu\text{m}. \quad (4.5)$$

This estimate underestimates the true uncertainty in  $V(r)$ , as it neglects longitudinal fluctuations of the interatomic distance when evaluated at  $y = 0$ . Nonetheless, we adopt it as a conservative lower bound.

For completeness, including second-order perturbative corrections would yield

$$\delta a = \sqrt{(\Delta x)^2 + \frac{(\Delta y)^4}{2x^2}}. \quad (4.6)$$

Finally, we neglect fluctuations in the Rabi frequency  $\Omega$ , which would further increase the total uncertainty. Hence, the values reported here should be regarded as conservative lower bounds on the disorder strength in experiments.

Typical interatomic distances observed in experiments are [2]:

- $a \approx 8.7\text{--}4.3 \mu\text{m}$  for the period-2 phase,
- $a \approx 4.3\text{--}2.9 \mu\text{m}$  for the period-3 phase,
- $a \approx 2.9\text{--}2.2 \mu\text{m}$  for the period-4 phase.

Based on these ranges, we select four representative disorder strengths based on first order error propagation corresponding to characteristic points of the phase diagram:

- Ising transition ( $a \approx 5.74 \mu\text{m}$ ):  $\delta V \approx 0.17 V$ .
- Potts point in the period-3 phase [21] ( $a \approx 3.95 \mu\text{m}$ ):  $\delta V \approx 0.26 V$ .
- Ashkin–Teller point in the period-4 phase [21] ( $a \approx 2.7 \mu\text{m}$ ):  $\delta V \approx 0.38 V$ .
- Floating phase between periods 4 and 5: ( $a \approx 2.17 \mu\text{m}$ ):  $\delta V \approx 0.47 V$ .

In our simulations, we therefore consider four levels of disorder reflecting these estimates:  $\delta V = 0.15$ ,  $\delta V = 0.25$ ,  $\delta V = 0.40$ , and  $\delta V = 0.50$ .

### 4.3.2. GROUND STATE CALCULATIONS

The microscopic model of Rydberg atoms was simulated using two-sites Density Matrix Renormalization Group (DMRG) [23, 24] in the matrix product state (MPS) formalism [24]. The many-body system Hamiltonian was expressed as a matrix product operator (MPO) [25], and the algebraically decaying 2-site interactions were approximated by a sum of 6 exponentials [24, 26]  $1/r^6 = \sum_{i=1}^6 c_i \lambda_i^r$ , where  $c_i$  and  $\lambda_i$  are parameters determined by minimizing the cost function, defined as:

$$\sum_{r=1}^L \left| \frac{1}{r^6} - \sum_{i=1}^6 c_i \lambda_i^r \right|. \quad (4.7)$$

This approximation provides an almost perfect fitting for the interaction of  $\sim 20$  atoms distance and a cost function error of  $\sim 3.5 \times 10^{-18}$  for  $L = 241$ . The comparison between the  $1/r^6$  decaying interaction and our tensor product approximation is depicted in Figure 4.1. Ground state convergence was assumed when the variation in the total energy after two consecutive sweeps  $< 10^{-12}$ .

### 4.3.3. SIMULATION OF DYNAMICS

Time evolution was performed using a 2-site time-dependent variational algorithm (TDVP) [27–29]. In this case, the algebraically decaying 2-site interactions were approximated by a sum of 4 exponentials. This approximation provides almost perfect fitting for  $\sim 10$  atoms. For each time-step, convergence of the Lanczos algorithm was assumed when the difference on the energy after two consecutive iterations was  $< 10^{-7}$ .

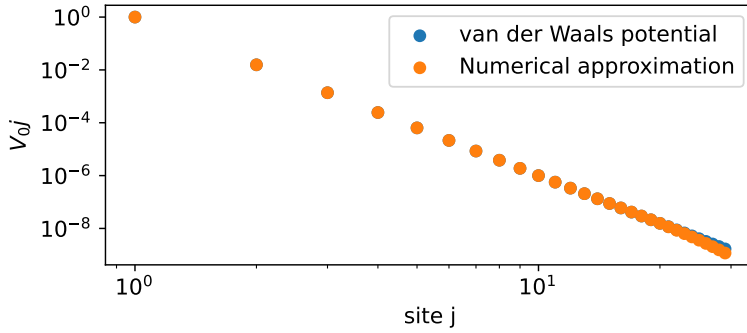


Figure 4.1.: Comparison between the exact van der Waals repulsion from the first atom in the chain to atoms at subsequent positions along the linearized lattice (blue dots), and a tensor product approximation of the interaction (orange dots). The approximation closely matches the exact interaction up to a distance of 10 lattice sites.

#### 4.3.4. KIBBLE-ZUREK MECHANISM PROTOCOL

Starting point for the Kibble-Zurek (KZ) mechanism was set at a distance of  $15 \times \sqrt{s}$  normalized by the interatomic strength constant  $V_0$  to ensure the system started in the adiabatic regime. This choice is motivated because for an Ising transition, adiabaticity breaks down when the distance to the critical point reaches  $|\varepsilon| \sim \sqrt{s}$ . The van der Waals interaction strength for each site was held fixed  $V_i = 1 \pm \delta V_i$  and  $\Delta$  and  $\Omega$  were swept around the phase transition in a direction perpendicular to the critical line identified in the phase diagram of Figure 1 (right) in Ref. [20]. The quench was terminated at  $\Omega = 0$ .

The number of kinks was quantified as the density of domain walls, following the definition proposed in Ref. [30]. Specifically, for a period-2 structure, two types of domains—A and B—can be distinguished based on whether the Rydberg excitation occupies odd or even lattice sites. A kink is then defined as a domain wall where the excitation pattern switches between domains A and B. Comparable results were obtained using the *non-order parameter* introduced in the same reference. In this alternative approach, a kink is identified through the local pattern  $(1 - \bullet \circ - \circ \bullet)$ . While both methods yield similar results, notable differences exist. For example, the configuration  $\bullet \circ \circ \bullet$  is not counted as a kink using the domain-wall method but is counted as two kinks under the non-order parameter definition. For a more detailed discussion of kink definitions and their influence on KZ scaling (see Chapter 2). All quench protocols crossed the critical point at  $(\Omega/V_0, \Delta/V_0) \approx (0.494, 1)$ , corresponding to the estimated transition point of the clean model [20].

For each sweep rate, the slow quench process was repeated between 20 and 300 times, depending on the specific sweep rate and system size, and the resulting kink densities were averaged. The uncertainty in the mean was estimated as  $1.96 \times$  the standard error, corresponding to a 95% confidence interval for the estimated mean.

## 4.4. RESULTS

### 4.4.1. IMPACT OF DISORDER ON NON-EQUILIBRIUM PHENOMENA

Let us first examine how the direct Ising transition in arrays of Rydberg atoms is influenced by uncertainties in the atomic positions, closely following the experimental protocol of Ref. [2] within the framework of the quantum Kibble–Zurek (KZ) mechanism. Specifically, we investigate the scaling of the kink density  $n_k$ —the density of domain walls formed after a slow quench across the Ising transition from the period-2 ordered phase—as a function of disorder strength  $\delta V$  and system size  $L$ . A microscopic definition of the kink operator employed in this study is provided in Sec. 4.3.

#### DEVIATION FROM THE POWER-LAW SCALING.

First, we demonstrate that disorder has a trackable impact on the critical Kibble-Zurek scaling. Figure 4.2 shows the scaling of the density of kinks  $n_k$  with the sweep rate  $s$  for various values of disorder strength  $\delta V$  and for a fixed system size  $L = 241$ . We present our results in a log-log scale, where the critical scaling in the clean case is linear (dashed line). As the disorder  $\delta V$  increases, the slope of the scaling  $\mu_{\text{eff}}$  decreases, deviating markedly from the clean power-law behavior. This deviation becomes even more evident in the inset, where we track an effective exponent  $\mu_{\text{eff}}$  from sets of three consecutive data points in Figure 4.2. Plotted against the first (leftmost) point in each set,  $\mu_{\text{eff}}$  decreases with decreasing sweep rate  $s$ . This trend becomes more pronounced as  $\delta V$  increases, leading to a systematic deviation of the measured exponent  $\mu$  from the theoretical predictions for the Ising transition.

We also compare how this deviation due to disorder is affected by the system size. In Figure 4.3 we present the scaling of the density of kinks  $n_k$  versus the sweep rate  $s$  for several system sizes at fixed disorder strength  $\delta V = 0.15$ . By contrast to the clean case,  $\mu$  decreases with system size, resulting in a stronger deviation from the clean Ising prediction. Such crossover between clean and disordered physics as a function of the system size is a documented feature in equilibrium [8, 31, 32]. The inset shows  $\mu_{\text{eff}}$ , extracted using the same method as in Figure 4.2, now plotted for each system size. As before,  $\mu_{\text{eff}}$  decreases with decreasing  $s$ , but the deviation is more pronounced for faster sweep rates and larger system sizes. A notable exception is the case  $L = 51$ , where  $\mu_{\text{eff}}$  increases instead. This is not unexpected: for small systems and sufficiently slow quenches, the finite energy gap at the critical point allows for an adiabatic evolution throughout the quench [11]. This may explain why the effect of disorder was not observed in recent experiments probing Ising transition with 51 Rydberg atoms [22].

#### DYNAMICAL SIGNATURES OF THE INFINITE RANDOMNESS

Previous studies have shown that in the infinite randomness universality class, the scaling of the density of kinks  $n_k$  with the sweep rate  $s$  follows a much weaker, logarithmic form, specifically  $n_k \sim [\log(s^{-1})]^{-2}$ , rather than a power law typical for the clean transitions [9, 10]. To test how well the KZ mechanism can capture infinite-randomness criticality on experimentally accessible system sizes, we plot  $1/n_k$  versus  $\log(1/s)$  on a log-log scale in Figure 4.4. The dashed line corresponds to the analytical prediction. As

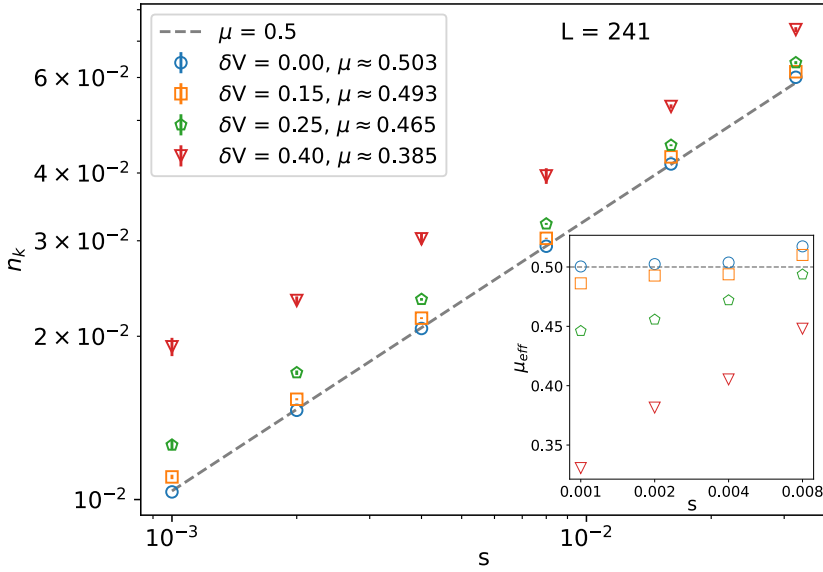


Figure 4.2.: Density of kinks  $n_k$  as a function of the sweep rate  $s$  for disorder strengths  $\delta V = 0.15, 0.25, 0.4$ , for a system size  $L = 241$ . The clean case (blue circles) is shown for reference. The dashed gray line indicates the theoretical prediction for the clean Ising transition. As disorder strength increases, the scaling of  $n_k$  progressively deviates from the clean power-law scaling. We averaged over up to 250-330 independent samples depending on the strength of the disorder. Inset: effective exponents  $\mu_{\text{eff}}$  extracted by fitting the slopes of sets of three consecutive points in the main panel. In the disordered case,  $\mu_{\text{eff}}$  decreases progressively for slow sweep rates.

$\delta V$  increases, the data increasingly conforms to this behavior, with the case  $\delta V = 0.4$  displaying an almost perfect match.

#### FINITE-SIZE EFFECTS OF KIBBLE-ZUREK MECHANISM IN THE PRESENCE OF DISORDER

We further discuss finite-size effects in the deviation from the clean Ising scaling in KZ dynamics. In Figure 4.5(a) we display the extracted values of  $\mu$  as a function of  $\delta V$  for various system sizes. The results confirm that the measurable KZ exponent  $\mu_{\text{eff}}$  decreases with increasing disorder and also with system size. Additionally, the error bars on the fitted exponents grow with  $\delta V$ , reflecting a growing deviation from simple power-law scaling.

To probe the dynamical fingerprints of the infinite-randomness critical point, we investigate how the kink-density distribution evolves with system size at a fixed sweep rate. As illustrated in Figure 4.5(b), the histogram of  $\log n_k$  remains centered on a clear average value, while its overall spread becomes progressively narrower for larger chains. A qualitatively similar trend was reported for disordered quantum Ising chains driven through the transition in the KZ regime (see Ref. [10]). The observed reduction of sample-to-

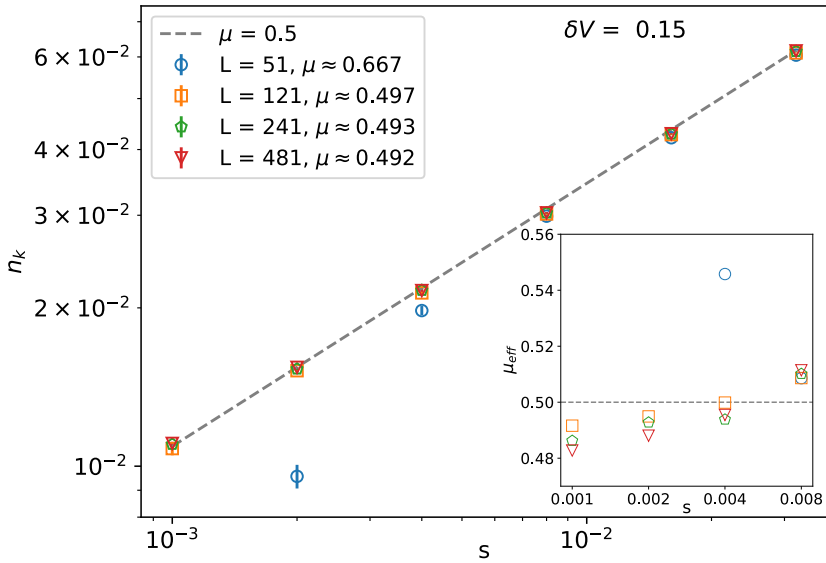


Figure 4.3.: Scaling of the kink density  $n_k$  with sweep rate  $s$  for disorder strength  $\delta V = 0.15$  and various system sizes. Results were averaged over up to 300 individual samples. Kibble-Zurek exponents obtained by fitting all shown points are listed in the legend. Inset: effective critical exponent  $\mu_{\text{eff}}$  extracted from sets of three consecutive points of the main panel. For slower sweep rates and larger system sizes the effect of disorder becomes more pronounced.

sample fluctuations yield a post-quench observable that is self-averaging even though equilibrium quantities at the underlying infinite-randomness fixed point itself remain non-self-averaging.

#### 4.4.2. LOCALIZATION OF THE FLOATING PHASE

We study the effect of disorder on the equilibrium floating phase, following the experimental approach of Ref. [33], and analyze the ground state using density matrix renormalization group (DMRG) simulations. In contrast to the Ising transition, whose critical point can be shifted by disorder, Rydberg arrays exhibit extended regions of floating phases. Here, we focus on a point deep inside one such region, between the period-4 and period-5 ordered lobes. We characterize the floating phase through three hallmarks: quasi-long-range incommensurate correlations, the structure factor, and the scaling of entanglement entropy.

#### FRIEDEL OSCILLATIONS

There are known examples in the literature of commensurate Luttinger liquids with repulsive interactions being localized by arbitrary weak disorder [34]. To probe this phenomenon in our setting, we analyze Friedel oscillations in the local density of Rydberg

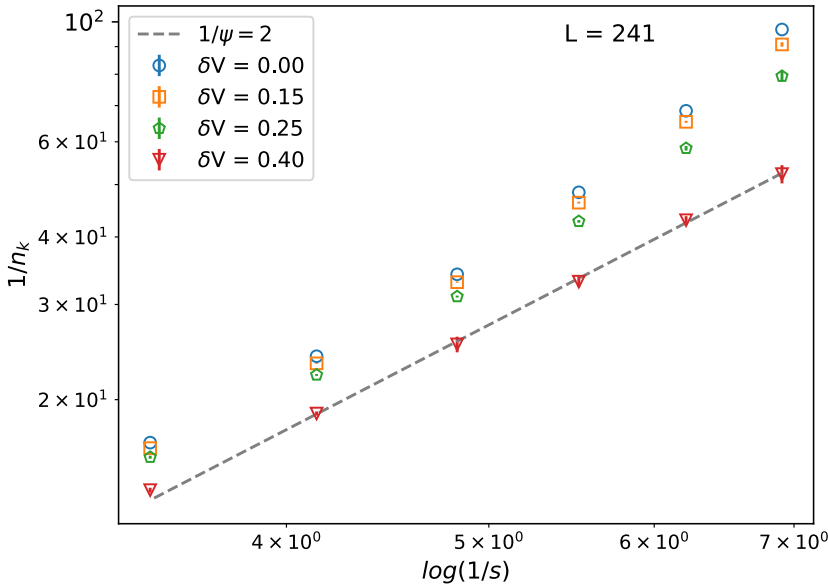


Figure 4.4.: Scaling of the inverse of the density of kinks  $n_k$  with the log of the inverse of the sweep rate  $s^{-1}$  for various disorder strengths on a log-log plot. The dashed gray line indicates theory prediction for infinite-randomness criticality  $1/n_k \sim \log^2(s^{-1})$ . Presented results were obtained for a chain with  $L = 241$  sites. As the disorder strength increases, the numerical results increasingly approach the predicted infinite-randomness scaling behavior.

excitations, which reveal the system's ability (or failure) to heal and screen impurities, here represented by the chain edges. In the critical floating phase, Friedel oscillations follow the predictions of boundary conformal field theory, exhibiting a slowly decaying profile, as illustrated for the clean case in Figure 4.6(a) (blue curve). By contrast, introducing disorder typical for this regime,  $\delta V = 0.5$  (see Sec. 4.3. for details), dramatically alters the oscillations: edge effects are almost entirely suppressed beyond  $\sim 30$  sites, indicating a finite localization length.

#### STRUCTURE FACTOR

An alternative approach that gives direct access to the incommensurability, both numerically and experimentally [33, 35], is to analyze the location of the first peak in the static structure factor:

$$S(q) = \frac{1}{L} \sum_{i,j} e^{iq(i-j)} C_{ij}, \quad (4.8)$$

with  $C_{ij} = \langle \hat{n}_i \hat{n}_j \rangle - \langle \hat{n}_i \rangle \langle \hat{n}_j \rangle$  being the density-density correlation function. In Figure 4.6(b), we compare the structure factor for clean and disordered systems for several system sizes. Remarkably, incommensurability is not destroyed by disorder, a phenomenon that

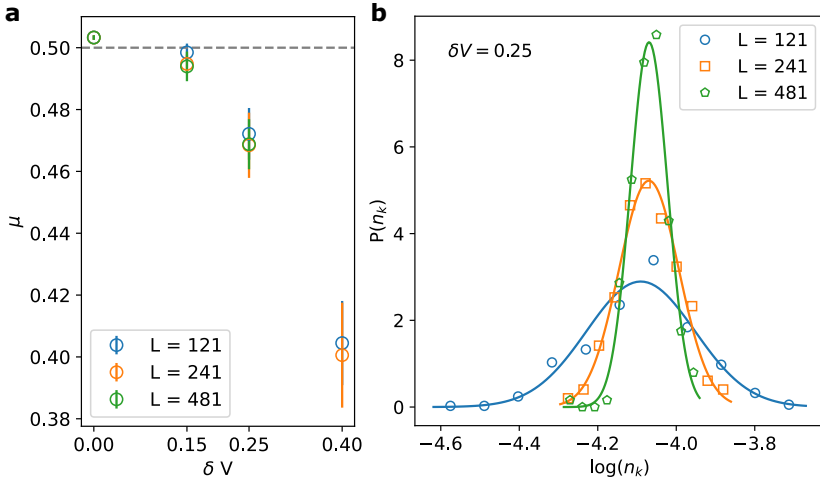


Figure 4.5.: Additional results on finite-size effects in Kibble-Zurek scaling. (a) The critical exponent  $\mu_{\text{eff}}$  is shown as a function of disorder strength  $\delta V$  for various system sizes. The effect of disorder slowly increases with system size, but due to large error bars it would be challenging to quantify the effect. (b) Probability distribution of kink density after a slow quench. We show the distribution of  $\log(n_k)$  for  $L = 121, 241, 481$  averaged over 430, 250, and 200 independent samples correspondingly. Histograms were computed using 11 fixed bins. As the system size increases, the distribution narrows, reflecting reduced fluctuations in larger systems. Solid lines correspond to a Gaussian fit.

has recently been reported in the context of Majorana wires [32]. Surprisingly, the leading wave-vector in the clean and disordered case deviates by no more than  $O(10^{-3})$ .

The main qualitative difference between the two cases is the height of the peak, which is directly related to the correlation length: large and rapidly growing with the system size inside the clean floating phase<sup>1</sup>, and small and stable in the presence of disorder (see Figure 4.6(c) for a quantitative comparison). For comparison we also include the results for a gapped disordered phase in the clean case.

#### ENTANGLEMENT ENTROPY

The localization of the floating phase is also reflected in the scaling of the entanglement entropy provided in Figure 4.7. In the clean case, the entanglement entropy follows the expected Calabrese-Cardy scaling relation [37]:

$$S_L(l) = \frac{c}{6} \log d(l) + s_1 + \log g, \quad (4.9)$$

where  $c$  is the central charge,  $d(l)$  is the conformal distance, and  $s_1$  and  $\log g$  are non-universal constants. In this case, the data are consistent with a Luttinger liquid, char-

<sup>1</sup>In a Luttinger liquid the peak of the structure factor follows the scaling relation  $S(L) \sim L^K$ , where  $K$  is the Luttinger liquid exponent [36]

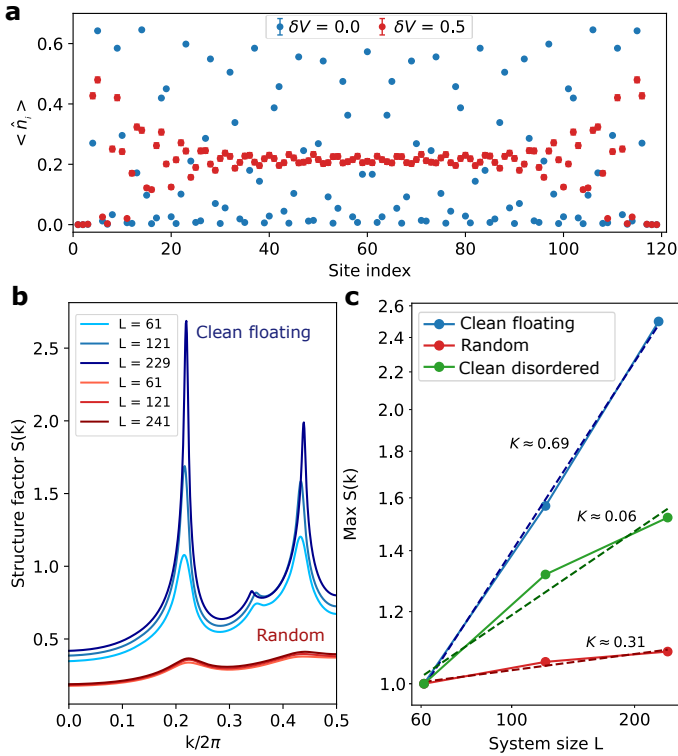


Figure 4.6.: Numerical evidence of localization of the floating phase. (a) Local density profile of a chain of Rydberg atoms for a disorder strength  $\delta V = 0.5$  (red) and for the clean case (blue) deep inside the floating phase for  $L = 121$ . In the disordered case, obtained by averaging over  $\sim 1700$  disorder configurations, the edge effects are localized at a distance about 30 lattice sites. We present the results for  $\Omega = 1$ ,  $\Delta = 3.5$ ,  $R_b/a = 4$  deep inside the floating phase. (b) Structure factor  $S$  for the clean (blue) and a disordered (red) system for the specified point. (c) Scaling of the peak height of the structure factor shown in (b). For a reference, we also include results for the clean case inside the disordered phase with incommensurate short-range correlations at  $\Delta = 2.5$  (green).

acterized by  $c = 1$ . By contrast, in the presence of disorder, the entanglement entropy saturates, showing no signatures of critical scaling.

## 4.5. DISCUSSION

We have demonstrated that the uncertainty in the atomic positions, which is an intrinsic feature of current experimental platforms based on Rydberg atoms, has a significant impact on the Kibble-Zurek (KZ) critical exponent  $\mu$ . Our results show that this effect be-

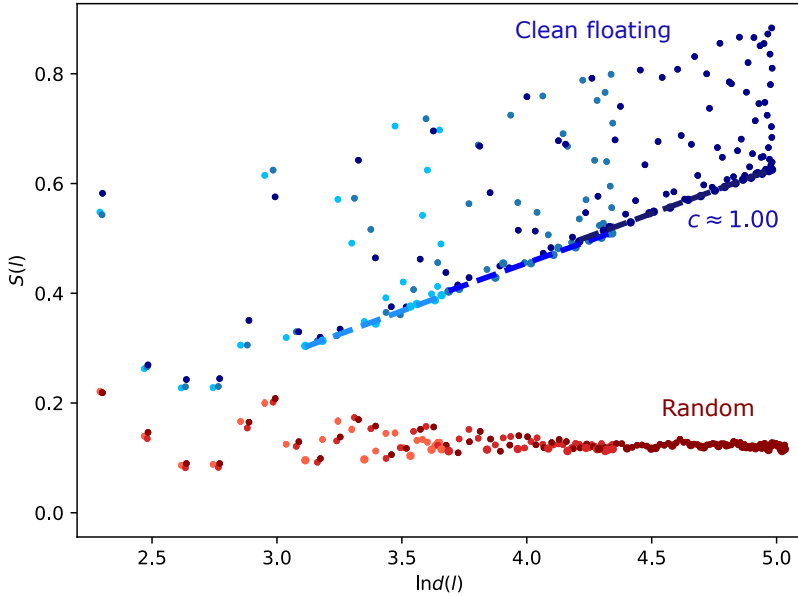


Figure 4.7.: Scaling of the entanglement entropy  $S$  as a function of the conformal distance  $d(l)$  for three system sizes for a clean system ( $\delta V = 0.0$ ) and a disordered system with  $\delta V = 0.5$  deep inside the floating phase. The clean system shows a semilog scaling of the entanglement entropy with the conformal distance, consistent with  $c = 1$ , indicating a floating phase, while the disordered case saturates to a constant value, indicating a gapped phase. The specific point in the phase diagram is  $\Omega = 1$ ,  $\Delta = 3.5$ ,  $R_b/a = 4$ .

comes more pronounced for larger system sizes and slower sweep rates, two regimes that are increasingly accessible in modern experiments. We have characterized the crossover from clean to disordered universality classes and identified the regimes in which the anomalous KZ scaling becomes observable. Our results shed new light on the robustness of dynamical critical phenomena in Rydberg platforms, raise a concern on the scalability of Rydberg-based quantum simulators, and provide a timely guidance for future experiments aiming to probe universal out-of-equilibrium behavior in the presence of disorder.

We expect that our numerical simulations underestimate the actual effect of disorder. This happens for two reasons. Firstly, for numerical efficiency we introduced the disorder in the coupling constant  $V_i$  that by construction underestimates the actual lattice distortion. Secondly, prior to measurement the trapping potential is typically turned off increasing the distortion in the lattice.

Our results provide important implications for future experimental studies of critical dynamics in Rydberg atom arrays. To date, the effects of disorder have not been systematically addressed during processing of experimental data obtained with quantum

Kibble-Zurek mechanism. The reported results for Ising transition obtained for arrays with about 51 atoms [2] were in a reasonable agreement with the clean theory. We argue that this is due to the chosen system size being sufficiently small compare to the large crossover length at weak disorder disorder strength typical for the period-2 phase. Moreover, at the slow sweep rates where disorder-induced deviations in  $\mu$  would be strongest, finite-size effects become dominant and obscure the underlying scaling behavior.

At the same time, previously reported experimental results for the period-3 and period-4 ordered phases [2] might already signal some signature of disorder. Experiments in these phases consistently report lower values of the critical exponent  $\mu$  than those obtained from numerical simulations [2]. As we have shown, strong disorder can significantly suppress  $\mu$  even in relatively small systems, providing a plausible explanation for this systematic discrepancy. Important that the difference between reported experimental and numerical values of  $\mu$  increases systematically with the periodicity of the phase: for period-2, simulations and experiments are in close agreement; for period-3, the gap widens; and for period-4, the discrepancy becomes substantial [2]. This trend is consistent with our findings and further supports the idea that disorder plays an increasingly important role as one moves to crystalline phases with higher periodicities.

We perform numerical simulations with long-range interactions and, remarkably, the results shown in Figure 4.4 are consistent with Fisher's infinite-randomness fixed point of the random Ising model with only nearest-neighbor interactions. In this regard, our findings differ from the predictions of strong-disorder renormalization group studies of Ising chains with random long-range interactions and random fields [14]. We hope this work will stimulate further theoretical progress in understanding the role of long-range couplings in disordered systems.

Furthermore, we have shown that the floating phase is highly sensitive to disorder and exhibits striking signatures of localization, including saturated entanglement entropy and a finite correlation length. At the same time, and quite unexpectedly, we find that the dominant wave vector  $q$  remains unchanged. This observation raises several fundamental questions, ranging from the robustness of the Huse–Fisher chiral transition against weak disorder to the possibility of commensurate–incommensurate transitions in random quantum chains. We hope that our results will stimulate further progress in the broader exploration of quantum critical phenomena.



# BIBLIOGRAPHY

- [1] J. Soto-Garcia and N. Chepiga. “Infinite Randomness Criticality and Localization of the Floating Phase in Arrays of Rydberg Atoms Trapped with Nonperfect Tweezers”. In: *Physical Review Letters* 136.5 (2026), p. 056502.
- [2] H. Bernien, S. Schwartz, A. Keesling, H. Levine, A. Omran, H. Pichler, S. Choi, A. S. Zibrov, M. Endres, M. Greiner, *et al.* “Probing many-body dynamics on a 51-atom quantum simulator”. In: *Nature* 551.7682 (2017), pp. 579–584.
- [3] H. Wang, C. Li, X. Li, Y. Gu, and S. Liu. “Lattice Defects in Rydberg Atom Arrays”. In: *arXiv preprint arXiv:2502.07886* (2025).
- [4] M. Prodius, A. S. Aramthottil, and J. Zakrzewski. “Interplay of localization and topology in disordered dimerized array of Rydberg atoms”. In: (2025). arXiv: [2505.07720](https://arxiv.org/abs/2505.07720).
- [5] D. S. Fisher. “Random transverse field Ising spin chains”. In: *Physical review letters* 69.3 (1992), p. 534.
- [6] D. S. Fisher. “Critical behavior of random transverse-field Ising spin chains”. In: *Physical review b* 51.10 (1995), p. 6411.
- [7] A. P. Young and H. Rieger. “Numerical study of the random transverse-field Ising spin chain”. In: *Physical Review B* 53.13 (1996), p. 8486.
- [8] N. Laflorencie, H. Rieger, A. W. Sandvik, and P. Henelius. “Crossover effects in the random-exchange spin- $\frac{1}{2}$  antiferromagnetic chain”. In: *Phys. Rev. B* 70 (5 Aug. 2004), p. 054430. DOI: [10.1103/PhysRevB.70.054430](https://doi.org/10.1103/PhysRevB.70.054430). URL: <https://link.aps.org/doi/10.1103/PhysRevB.70.054430>.
- [9] J. Dziarmaga. “Dynamics of a quantum phase transition in the random Ising model: Logarithmic dependence of the defect density on the transition rate”. In: *Physical Review B—Condensed Matter and Materials Physics* 74.6 (2006), p. 064416.
- [10] T. Caneva, R. Fazio, and G. E. Santoro. “Adiabatic quantum dynamics of a random Ising chain across its quantum critical point”. In: *Physical Review B—Condensed Matter and Materials Physics* 76.14 (2007), p. 144427.
- [11] W. H. Zurek, U. Dorner, and P. Zoller. “Dynamics of a quantum phase transition”. In: *Physical review letters* 95.10 (2005), p. 105701.
- [12] F. Iglói and C. Monthus. “Strong disorder RG approach of random systems”. In: *Physics reports* 412.5-6 (2005), pp. 277–431.
- [13] D. S. Fisher. “Phase transitions and singularities in random quantum systems”. In: *Physica A: Statistical Mechanics and its Applications* 263.1-4 (1999), pp. 222–233.

- [14] R. Juhász, I. A. Kovács, and F. Iglói. “Random transverse-field Ising chain with long-range interactions”. In: *Europhysics Letters* 107.4 (Aug. 2014), p. 47008. DOI: [10.1209/0295-5075/107/47008](https://doi.org/10.1209/0295-5075/107/47008). URL: <https://doi.org/10.1209/0295-5075/107/47008>.
- [15] H. Li, J. Wang, X.-J. Liu, and H. Hu. “Many-body localization in Ising models with random long-range interactions”. In: *Physical Review A* 94.6 (2016), p. 063625.
- [16] D. A. Huse and M. E. Fisher. “Domain walls and the melting of commensurate surface phases”. In: *Physical Review Letters* 49.11 (1982), p. 793.
- [17] D. A. Huse and M. E. Fisher. “Commensurate melting, domain walls, and dislocations”. In: *Phys. Rev. B* 29 (1 Jan. 1984), pp. 239–270. DOI: [10.1103/PhysRevB.29.239](https://doi.org/10.1103/PhysRevB.29.239). URL: <https://link.aps.org/doi/10.1103/PhysRevB.29.239>.
- [18] N. Chepiga and F. Mila. “Floating phase versus chiral transition in a 1D hard-boson model”. In: *Physical review letters* 122.1 (2019), p. 017205.
- [19] N. Chepiga and F. Mila. “Kibble-Zurek exponent and chiral transition of the period-4 phase of Rydberg chains”. In: *Nature Communications* 12.1 (2021), p. 414.
- [20] M. Rader and A. M. Läuchli. *Floating Phases in One-Dimensional Rydberg Ising Chains*. 2019. arXiv: [1908.02068](https://arxiv.org/abs/1908.02068) [[cond-mat.quant-gas](https://arxiv.org/abs/1908.02068)].
- [21] I. A. Maceira, N. Chepiga, and F. Mila. “Conformal and chiral phase transitions in Rydberg chains”. In: *Physical Review Research* 4.4 (2022), p. 043102.
- [22] A. Keesling, A. Omran, H. Levine, H. Bernien, H. Pichler, S. Choi, R. Samajdar, S. Schwartz, P. Silvi, S. Sachdev, *et al.* “Quantum Kibble–Zurek mechanism and critical dynamics on a programmable Rydberg simulator”. In: *Nature* 568.7751 (2019), pp. 207–211.
- [23] S. R. White. “Density matrix formulation for quantum renormalization groups”. In: *Physical review letters* 69.19 (1992), p. 2863.
- [24] U. Schollwöck. “The density-matrix renormalization group in the age of matrix product states”. In: *Annals of physics* 326.1 (2011), pp. 96–192.
- [25] F. Verstraete, J. J. Garcia-Ripoll, and J. I. Cirac. “Matrix product density operators: Simulation of finite-temperature and dissipative systems”. In: *Physical review letters* 93.20 (2004), p. 207204.
- [26] B. Pirvu, V. Murg, J. I. Cirac, and F. Verstraete. “Matrix product operator representations”. In: *New Journal of Physics* 12.2 (2010), p. 025012.
- [27] J. Haegeman, J. I. Cirac, T. J. Osborne, I. Pižorn, H. Verschelde, and F. Verstraete. “Time-dependent variational principle for quantum lattices”. In: *Physical review letters* 107.7 (2011), p. 070601.
- [28] J. Haegeman, C. Lubich, I. Oseledets, B. Vandereycken, and F. Verstraete. “Unifying time evolution and optimization with matrix product states”. In: *Physical Review B* 94.16 (2016), p. 165116.
- [29] S. Paeckel, T. Köhler, A. Swoboda, S. R. Manmana, U. Schollwöck, and C. Hubig. “Time-evolution methods for matrix-product states”. In: *Annals of Physics* 411 (2019), p. 167998.

- [30] J. Soto Garcia and N. Chepiga. “Resolving chiral transitions in one-dimensional Rydberg arrays with quantum Kibble-Zurek mechanism and finite-time scaling”. In: *Physical Review B* 110.12 (2024), p. 125113.
- [31] N. Laflorencie. “Entanglement Entropy and Localization in Disordered Quantum Chains”. In: *Entanglement in Spin Chains: From Theory to Quantum Technology Applications*. Ed. by A. Bayat, S. Bose, and H. Johannesson. Cham: Springer International Publishing, 2022, pp. 61–87. ISBN: 978-3-031-03998-0. DOI: [10.1007/978-3-031-03998-0\\_4](https://doi.org/10.1007/978-3-031-03998-0_4). URL: [https://doi.org/10.1007/978-3-031-03998-0\\_4](https://doi.org/10.1007/978-3-031-03998-0_4).
- [32] N. Chepiga and N. Laflorencie. “Resilient infinite randomness criticality for a disordered chain of interacting Majorana fermions”. In: *Physical review letters* 132.5 (2024), p. 056502.
- [33] J. Zhang, S. H. Cantú, F. Liu, A. Bylinskii, B. Braverman, F. Huber, J. Amato-Grill, A. Lukin, N. Gemelke, A. Keesling, *et al.* “Probing quantum floating phases in Rydberg atom arrays”. In: *Nature Communications* 16.1 (2025), p. 712.
- [34] T. Giamarchi. *Quantum physics in one dimension*. Vol. 121. Clarendon press, 2003.
- [35] J. Soto-Garcia and N. Chepiga. “Numerical investigation of quantum phases and phase transitions in a two-leg ladder of Rydberg atoms”. In: *Physical Review Research* 7.1 (2025), p. 013215.
- [36] P. Sengupta, A. W. Sandvik, and D. K. Campbell. “Bond-order-wave phase and quantum phase transitions in the one-dimensional extended Hubbard model”. In: *Physical Review B* 65.15 (2002), p. 155113.
- [37] P. Calabrese and J. Cardy. “Entanglement entropy and conformal field theory”. In: *Journal of physics a: mathematical and theoretical* 42.50 (2009), p. 504005.



# 5

## NUMERICAL INVESTIGATION OF QUANTUM PHASES AND PHASE TRANSITIONS IN A TWO-LEG LADDER OF RYDBERG ATOMS

*Given the rich critical phenomena observed in single arrays of Rydberg atoms, we present, as a natural extension, a quantitative ground-state phase diagram of Rydberg atoms arranged in a two-leg ladder geometry interacting via van der Waals potential. Using the Density Matrix Renormalization Group (DMRG) algorithm, we uncover a rich variety of crystalline  $\mathbb{Z}_k$  phases. Remarkably, except for the checkerboard phase, these  $\mathbb{Z}_k$  phases, appear in pairs characterized by the same pattern of occupied rungs but distinguishable by a spontaneously broken  $\tilde{\mathbb{Z}}_2$  symmetry between the two legs of the ladder. Within each pair, the two phases are separated by a continuous transition in the Ising universality class, which eventually fuses with the  $\mathbb{Z}_k$  transition, whose nature depends on  $k$ . We find that the transition into the  $\mathbb{Z}_2 \otimes \tilde{\mathbb{Z}}_2$  phase changes its nature multiple of times, including an Ashkin-Teller transition surprisingly stable over an extended interval, followed by the  $\mathbb{Z}_4$ -chiral transition and finally in a two step-process mediated melting via the floating phase. The transition into the  $\mathbb{Z}_3$  phase with resonant states on the rungs belongs to the three-state Potts universality class at the commensurate point, to the  $\mathbb{Z}_3$ -chiral Huse-Fisher universality class away from it, and eventually it is through an intermediate floating phase. The Ising transition between  $\mathbb{Z}_3$  and  $\mathbb{Z}_3 \otimes \tilde{\mathbb{Z}}_2$  phases, entering the floating phase, opens new possibility to realize lattice supersymmetry in Rydberg quantum simulators.*

---

Parts of this chapter have been published in Physical Review Research, 2025, vol. 7, no 1, p. 013215 [1].

## 5.1. INTRODUCTION

By now, it should be clear that quantum phase transitions play an essential role in the understanding and engineering of exotic phases of matter, and that Rydberg atoms trapped with optical tweezers are particularly attractive for quantum simulations due to their long life time, strong interactions and versatile geometries granted by an individual control over the atoms.

As we have previously explained, one of the fundamental problems brought forward by experiments on Rydberg atoms in 1D is the chiral melting [2] of the period- $p$  phases. One might expect that the transition out of phases with integer periodicity  $p$  can be effectively described in conformal field theory (CFT) [3] by the corresponding minimal models: Ising for  $p = 2$ , three-state Potts for  $p = 3$ , Ashkin-Teller for  $p = 4$ . However, due to long-range interactions between excited atoms, domain walls that bring particles closer to each other cost more energy than those sending particles further apart. This creates a chiral perturbation that, according to Huse and Fisher [2, 4], leads to a novel non-conformal transition for  $p = 3$ . Originally proposed in the 1980s in the context of 2+0D adsorbed monolayers, this exotic chiral transition remained an unsolved and intensely debated problem for several decades [2, 4–9]. Recently, large-scale DMRG simulations have fully resolved all critical regimes along the boundary of the period-3 phase: a single conformal point in the 3-state Potts universality class emerges where the chiral perturbation vanishes, followed by the Huse-Fisher chiral transitions up to the Lifshitz point, beyond which the chiral perturbation becomes too strong, leading to the emergence of a floating phase [10]—a critical Luttinger liquid phase characterized by quasi-long-range incommensurability [11–16]. Moreover, a similar sequence of quantum criticalities, including the conformal Ashkin-Teller point, the floating phase, and a novel  $\mathbb{Z}_4$ -chiral transition, has been numerically identified at the boundary of the period-4 phase [12, 17, 18]. This rich theoretical picture is in full agreement with experimental results reported for 1D arrays of Rydberg atoms [19].

The plethora of crystalline phases and an unprecedentedly rich critical behavior at the boundary of these phases motivate us to look beyond the simplest 1D chains of Rydberg atoms. Experimentally, recent technological advancements have enabled remarkable control over the positioning of tweezers, paving the way for the investigation of diverse lattice geometries beyond the single 1D chain [20–25] reporting, in particular, a realization of the floating phase in the rectangular two-leg ladder [26]. Theoretical investigations of Rydberg ladders, though still in their early stages, have already revealed a wealth of exotic quantum phenomena potentially realizable in current experimental platforms. For instance, two-leg ladders of Rydberg-dressed atoms with particle number conservation exhibit complicated ground-state phase diagrams, featuring supersymmetric criticality and various types of Luttinger liquid phases [27, 28]. Coupled Rydberg chains fine-tuned to their Ising critical point open a new route toward realizing spin liquid behavior [24, 29, 30], while triangular ladder geometries provide an alternative path for exotic dynamics [31]. Additionally, ladders with staggered detuning have been shown to exhibit an Ising transition driven by order-by-disorder mechanisms [32]. Effective blockade models of Rydberg atoms on a ladder have shown to host two different charge density wave phases with spontaneously broken  $\mathbb{Z}_3$  symmetry, as well as a transition in the Huse-Fisher chiral universality class, and an extended Ashkin-Teller transition

protected by integrability of the model [33]. The approximations introduced in these models—while necessary to make them tractable within specific analytical or numerical frameworks—can significantly alter the underlying physics and, in some cases, lead to contradictory predictions [26, 33], as discussed in more detail later in the text. Given this landscape, it is rather surprising that a fully quantitative study of a realistic Rydberg ladder model incorporating the van der Waals interactions is still lacking. In this work, we aim to fill this gap by performing state-of-the-art tensor network simulations of such system, providing a comprehensive characterization of its ground-state phase diagram.

We explore in detail the phase diagram of a realistic model of Rydberg atoms on a two-leg ladder bearing in mind two motivations. First, in quasi-1D systems, the competition between repulsive interactions along and across the legs enhances the symmetry of the problem. This increased symmetry might eventually lead to more complex synthetic phases, which cannot be realized within a single chain of Rydberg atoms, and to more exotic critical phenomena, including a wide variety of critical fusions. Second, we aim to resolve an open question on whether the chiral transitions observed in a single chain [11–13, 17, 34] appear in a two-leg ladder of Rydberg atoms. Previous results are controversial in this regard: in a toy model with a Rydberg blockade, only the chiral transition into  $\mathbb{Z}_3$  has been found, while the transition into period-4 phase has been identified as either conformal with central charge  $c = 1$  or first order [33]. By contrast, an opposite scenario featuring the chiral transition into  $\mathbb{Z}_4$  phase but lacking chiral transition into  $\mathbb{Z}_3$  phase, has been predicted for a rectangular Rydberg ladder with the inter-atomic distance along the legs being two times smaller than the distance between the legs [26]. In the present chapter, we focus on a realistic model with van der Waal interactions on a square ladder with equal inter-atomic distances along legs and rungs, and show a surprisingly rich phase diagram featuring an unusual pairwise appearance of the crystalline phases and—at least—two different chiral transitions.

The rest of the chapter is organized as follows: Section 5.2 introduces the lattice model of the two-leg Rydberg ladder along with an overview of the main phases and phase transitions. In section 5.3, we explain the numerical methods and the protocols used to extract the critical exponents, along with the benchmark on the Ising transition into the checkerboard phase. Sections 5.4 and 5.5 present a detailed study of the quantum phase transitions out of  $\mathbb{Z}_2$  and  $\mathbb{Z}_2 \otimes \tilde{\mathbb{Z}}_2$ , and out of  $\mathbb{Z}_3$  and  $\mathbb{Z}_3 \otimes \tilde{\mathbb{Z}}_2$  phases. Finally, we summarize our results and put them into perspective in Section 5.9.

## 5.2. OVERVIEW OF THE PHASE DIAGRAM

Let us remind you of the microscopic Hamiltonian of the Rydberg model defined in terms of hard-core bosons:

$$\frac{H}{\hbar} = \frac{\Omega}{2} \sum_i (d_i + d_i^\dagger) - \Delta \sum_i n_i + \sum_{i < j} V_{ij} n_i n_j, \quad (5.1)$$

where  $\Omega$  is the Rabi frequency and  $\Delta$  is the laser detuning of the coherent laser with respect to the resonant frequency. The stability of the Rydberg state is controlled by  $\Delta$ , which acts as a chemical potential. Atoms in a Rydberg state interact via a repulsive van der Waals potential  $V_{ij}$  that decreases with the distance  $|\vec{r}_{ij}|$  between the two excited

atoms as  $V_{ij} = V_0 |\vec{r}_{ij}|^{-6}$ , where  $V_0$  is a constant that depends on the chosen Rydberg level. The van der Waals repulsion between Rydberg states induces a blockade effect, which prevents two atoms within a distance smaller than the blockade radius  $R_b$ , from being simultaneously excited to a Rydberg state. This blockade is defined as  $V(R_b) \equiv \Omega$ , in other words  $R_b/a \equiv (V_0/\Omega)^{1/6}$ , where  $a$  is an interatomic distance.

For simplicity, we adopt the terminology of hard-core bosons, where atoms excited to a Rydberg state are referred to as “occupied” ( $n_i = 1$ ), and atoms in the ground state are termed “empty” ( $n_i = 0$ ). The creation (annihilation) operators are denoted by  $d_i^\dagger$  ( $d_i$ ), with the hard-core boson constraint forbidding multiple excitations, such that  $d_i^\dagger |1\rangle_i = 0$ .

Our main results are summarized in the phase diagram presented in Figure 5.1(a). The phase diagram features multiple lobes of crystalline phases, surrounded by a disordered phase. The disordered phase comprises two regions: one with commensurate density-density correlations (CD, gray area), and another with incommensurate correlations (ID, white area). Within the incommensurate region, the dominant wave-vector changes continuously, and eventually takes commensurate values. For instance, the dashed turquoise line in Figure 5.1(a), with  $q = 2\pi/3$ . Along this line, there are no chiral perturbations, and the transition to the corresponding  $\mathbb{Z}_3$  phase is conformal in the 3-state Potts universality class.

The lowest lobe corresponds to a checkerboard phase with one excited atom per rung, spontaneously breaking  $\tilde{\mathbb{Z}}_2$  symmetry between the two legs. Remarkably, at larger values of  $R_b/a$ , all ordered lobes appear in pairs. Within each pair, the two phases can be distinguished by a spontaneously broken  $\tilde{\mathbb{Z}}_2$  symmetry between the two legs. The phase appearing below spontaneously breaks  $\mathbb{Z}_k$  symmetry, forming a density wave phase along the chains. In the resonant phase, a single boson (excited Rydberg atom) occupies every  $k$ 's rung, and resonates between its two sites so that the local density profiles on both legs are identical. Naively, one would expect this phase to be fragile, but this resonant configuration appears to be a very stable one. The symmetry between the two legs is spontaneously broken in the lobe appearing just above, resulting in the phase with  $\mathbb{Z}_k \otimes \tilde{\mathbb{Z}}_2$  broken symmetry.

In Figure 5.2, we present the typical density profiles for each of the five ordered phases appearing in the phase diagram in Figure 5.1. For larger values of  $R_b/a$  we also see the emergence of  $\mathbb{Z}_4$  and  $\mathbb{Z}_4 \otimes \tilde{\mathbb{Z}}_2$  phases (see Figure 5.2 for examples of the density profiles) but due to growing computational costs we do not map out the accurate boundaries of these phases. In addition to the gaped ordered phases, we find a very thin floating phase surrounding the  $\mathbb{Z}_2 \otimes \tilde{\mathbb{Z}}_2$ ,  $\mathbb{Z}_3$  and  $\mathbb{Z}_2 \otimes \tilde{\mathbb{Z}}_2$  phases. The floating phase is critical Luttinger liquid phase with quasi-long-range order and algebraically decaying incommensurate correlations. This phase emerges due to the strong chiral perturbation produced by the long-range interactions.

Let us now briefly list all phase transitions appearing in the phase diagram in Figure 5.1.

- Disorder to  $\tilde{\mathbb{Z}}_2$  (checkerboard): Ising
- Disorder to  $\mathbb{Z}_2$  (period-2): Ising
- $\mathbb{Z}_2$  (period-2) to  $\mathbb{Z}_2 \otimes \tilde{\mathbb{Z}}_2$ : Ising

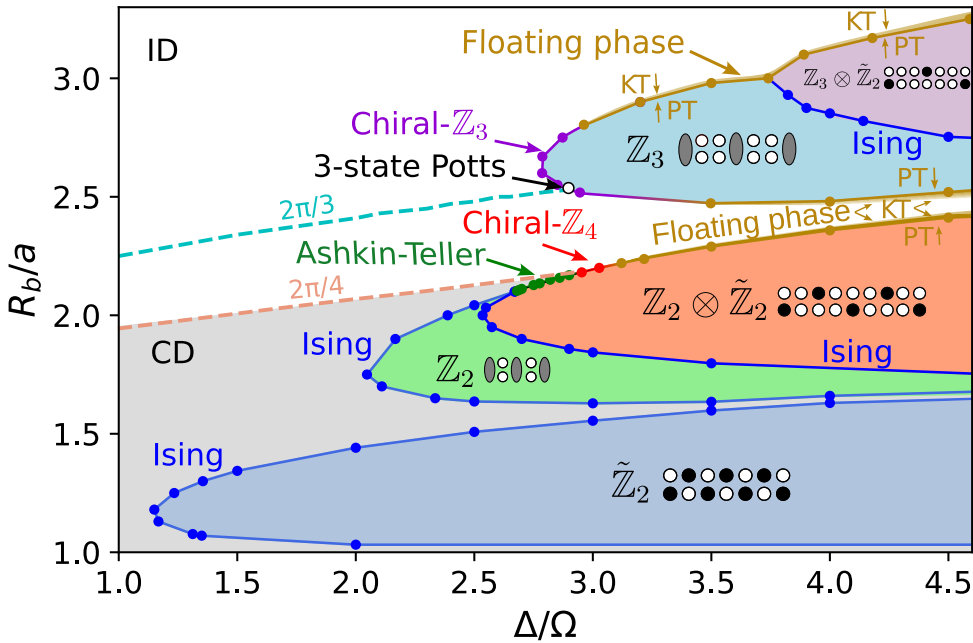


Figure 5.1.: The ground-state phase diagram of a square two-leg ladder of Rydberg atoms for the blockade radius  $R_b$  normalized to the interatomic distance  $a$  against the laser detuning  $\Delta$  normalized to the Rabi frequency  $\Omega$ . The blockade radius is defined as  $R_b/a \equiv (V/\Omega)^{1/6}$ . The diagram contains a disordered phase, five gaped phases with distinct crystalline structures and three narrow floating phases. The ordered phases are labeled according to their spontaneously broken symmetries. Floating phases are indicated by a dark yellow gradient line, reflecting the uncertainty in their precise extent. The sketches provide an intuitive visualization of one of the possible ground-states: filled circles state for the atoms in the excited Rydberg state, open circles for the atoms in the ground state, and gray ovals indicate a resonance state on a given rung. The disordered phase has a region with commensurate correlations (CD, gray) and incommensurate ones (ID, white). Dashed lines state for commensurate lines with  $q = 2\pi/4$  (orange) and  $q = 2\pi/3$  (cyan). There are four Ising transitions (blue). Transitions into  $Z_2 \otimes \tilde{Z}_2$  and into  $Z_3$  phases change its nature multiple times and, over a finite interval, fall within their corresponding chiral universality classes (red and purple).

- Disorder to  $Z_2 \otimes \tilde{Z}_2$ :
  - Commensurate region: Ashkin-Teller
  - Incommensurate region: Chiral/Floating Phase
- Disorder to  $Z_3$

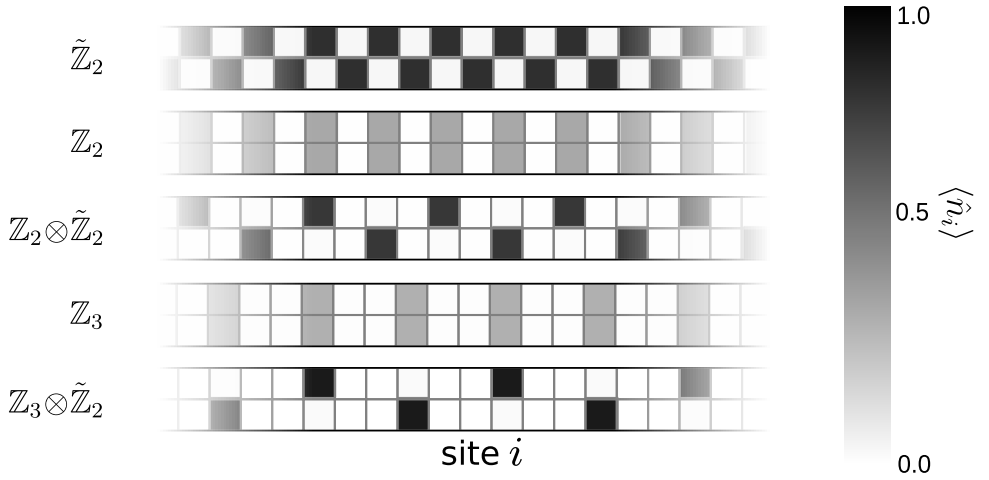


Figure 5.2.: Typical density profiles of the gaped phases discussed in the main text. Each square corresponds to a lattice site, with its color indicating the local density according to the color bar. We show profiles only for a central part of a long chain.

5

- Commensurate point: 3-state Potts
- Incommensurate region: Chiral/Floating Phase
- $\mathbb{Z}_3$  to  $\mathbb{Z}_3 \otimes \tilde{\mathbb{Z}}_2$ : Ising
- Disorder to  $\mathbb{Z}_3 \otimes \tilde{\mathbb{Z}}_2$ : Floating Phase
- In all cases, the transition from the disordered phase to the floating phase belongs to the Kosterlitz-Thouless [35] universality class, while the transition from the floating phase to the ordered gaped phase falls within the Pokrovsky-Talapov [36] universality class.

In the following sections, we discuss the details and present numerical evidences for all listed phase transitions.

## 5.3. METHODS

### 5.3.1. GROUND-STATE CALCULATIONS

#### APPROXIMATION OF ALGEBRAIC INTERACTIONS

The numerical simulations have been performed with a state-of-the art density matrix renormalization group (DMRG) algorithm in the form of variational matrix product states (MPS) [37, 38].

The matrix representing the pairwise algebraically decaying van der Waals interactions was approximated to a matrix product operator (MPO) using a modified incremental singular value decomposition method [39]. The algorithm exploits the upper-triangular

low-rank (UTLR) property of the pairwise interaction matrix. That is, the triangular portion of the matrix can be approximated as a low-rank matrix. As a result, the process of constructing an MPO representation of the interaction matrix is reformulated as a matrix completion problem. We restricted the bond dimension of the MPO to  $m = 11$ , keeping the tolerance to be  $10^{-9}$ . As a result, the error on the approximation of the Hamiltonian was always smaller than  $10^{-11}$ . In Figure 5.3, we show a comparison between the van der Waals potential scaling with the relative distance as  $1/r^6$  and the numerical approximation we used in our numerical simulations.

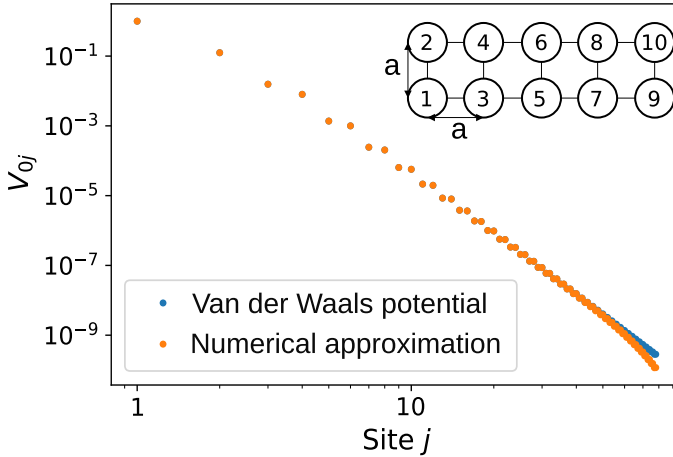


Figure 5.3.: Comparison of the van der Waals repulsion between the first atom in the chain and atoms at subsequent positions along the linearized lattice (blue dots) with a tensor product approximation of the interaction (orange dots). For the tensor product approximation, the matrix representing the pairwise algebraic interactions of the ladder was approximated to a matrix product operator using a modified incremental singular value decomposition method [39]. Note that the position on the lattice is not linearly proportional to the actual distance, as the atoms are arranged into a two-leg ladder.

#### TECHNICAL DETAILS.

We computed the ground states using the DMRG algorithm, keeping singular values above  $10^{-8}$ , and restricting the maximal bond dimension to 1200. Convergence of the ground state was assumed when the energy difference between two successive sweeps (including an increase in the bond dimension) was  $\leq 10^{-11}$ . The mentioned conditions allowed to reach convergence near criticality on systems with up to 700 rungs.

#### BOUNDARY CONDITIONS.

The number of rungs was always such that the ladder could accommodate the periodicity of the ordered phase. We applied fixed boundary conditions, but the way we fixed

boundaries varied depending on whether the phase or the transition under consideration broke the translational symmetry between two legs or not. When this  $\tilde{\mathbb{Z}}_2$  symmetry was preserved, we applied a large and equal on-site potential on each site in the first and last rung. When the  $\tilde{\mathbb{Z}}_2$  symmetry was spontaneously broken, we applied a strong on-site potential on the top site of the first and last rungs in a ladder with a number of rungs  $L = kn + 1$ , where  $n$  is some integer and  $k$  is periodicity of the  $\mathbb{Z}_k$  phase. Deep inside the ordered phases, the effect of fixed boundaries disappears at the distances exceeding the correlation length, thus the “wrong” choice of boundary conditions did not prevent us from seeing the correct ground-state of the bulk. In particular, and quite remarkably, favoring top or bottom sites at the edges does not destroy the resonant states deep in the bulk of the ladder. In the critical regions, however, appropriate boundary conditions are essential to ensure the correct critical scaling and to reduce possible crossover effects.

### 5.3.2. EXTRACTION OF CORRELATION LENGTH AND WAVE-VECTOR

Correlation length  $\xi$  and wave-vector  $q$  were extracted from fitting the density-density correlation function to the Ornstein-Zernike function [17, 40]:

$$C_{ij}^{\text{OZ}} \propto \frac{e^{-|i-j|/\xi}}{\sqrt{|i-j|}} \cos(q|i-j| + \varphi_0), \quad (5.2)$$

where  $\xi$  is the correlation length and  $q$  is the wave vector. Both parameters, along with an initial phase  $\varphi_0$ , were treated as fitting parameters.

We extracted the connected correlation function  $C_{ij} = \langle \hat{O}_i \hat{O}_j \rangle - \langle \hat{O}_i \rangle \langle \hat{O}_j \rangle$  numerically, where  $\hat{O}_i$  are various density operators. In particular, in order to compute density-density correlations along one leg of the ladder we used the operator  $\hat{t}_i$  ( $\hat{b}_i$ ), taking a value 1 if the top (bottom) site of the rung  $i$  is occupied and 0 otherwise. In addition, we used symmetric and anti-symmetric combinations of these two operators in order to capture the resonating states:

$$\begin{aligned} \hat{s}_i &= \hat{t}_i + \hat{b}_i \\ \hat{a}_i &= |\hat{t}_i - \hat{b}_i|. \end{aligned} \quad (5.3)$$

In general, the extracted values of  $\xi$  and  $q$  depend on the operator.

To extract  $\xi$ , oscillations were discarded and the slope of the decaying function was fitted in a semi-log scale with a linear function:

$$\ln C_{ij} \approx c - x/\xi - 1/2 \ln|i-j|. \quad (5.4)$$

An example of such a fit is presented in Figure 5.4(a), where correlations are calculated for operator  $\hat{s}$ .

In order to extract the wave-vector  $q$ , we removed the main slope of the exponential decay from the correlation function  $\tilde{C} = C_{ij} e^{c-x/\xi - 1/2 \ln|i-j|}$  and fit the rest with the oscillating cosine function:

$$\tilde{C} \approx A \cos(q|i-j| + \varphi_0), \quad (5.5)$$

as demonstrated in the Figure 5.4(b).

We noticed that, in the present case,  $q$  can alternatively be extracted from the location of the peak of the operator-operator structure factor recently used to analyze incommensurability in experiments [26]:

$$S(q) \propto \sum_{i,i'} e^{jq(i-i')} \langle \hat{s}_i \hat{s}_{i'} \rangle, \quad (5.6)$$

as presented in Figure 5.4(c)<sup>1</sup>.

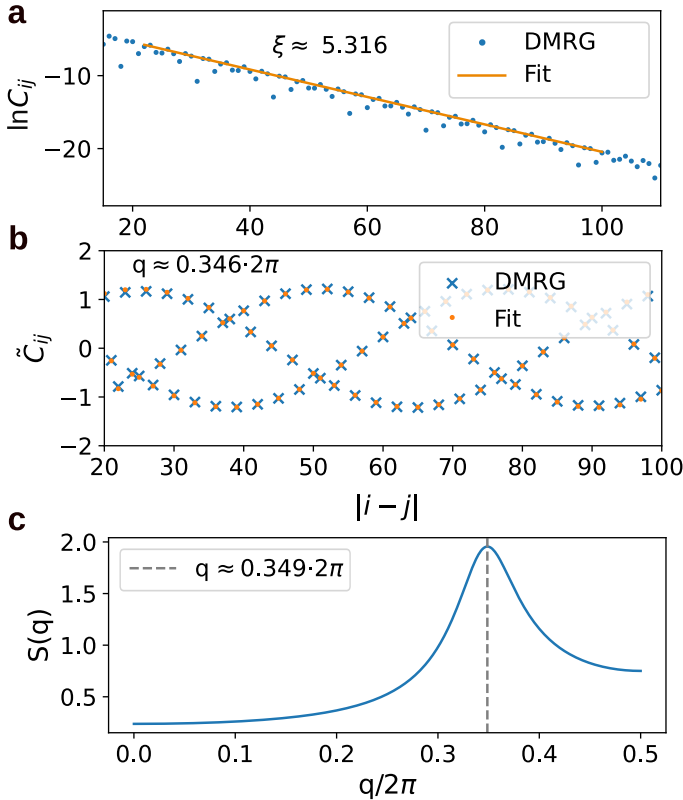


Figure 5.4.: Example of extraction of the correlation length and wave-vector  $q$ . (a) The correlation length is obtained by removing oscillations and fitting the correlation function on a semi-log plot. In this particular case, the operator for correlations is  $\hat{s}$ , defined in Eq. (5.3b) The wave-vector  $q$  is extracted by removing the slope and fitting the oscillations to a cosine function. (c) The structure factor shows a peak at the same value of  $q$  as the one obtained by fitting the oscillations. The data shown corresponds to  $\Delta/\Omega = 3.0$  and  $R_b/a = 2.4$ .

<sup>1</sup>Note that instead of  $\hat{s}_i$  one can use the operator  $\hat{a}_i$  leading to the same values of the dominant wave-vector  $q$ .

### 5.3.3. EXTRACTION OF THE CENTRAL CHARGE

According to conformal field theory (CFT), the entanglement entropy  $S$  in a finite-size chain with open boundary conditions scales with the block size of the bipartite chain as [41, 42]:

$$S_L(l) = \frac{c}{6} \ln d(l) + s_1 + \ln g \quad (5.7)$$

where  $c$  is the central charge,  $d(l) = \frac{2L}{\pi} \sin\left(\frac{\pi l}{L}\right)$  is the conformal distance,  $\ln g$  states for boundary entropy and  $s_1$  is a non-universal constant. When the boundaries are fixed, Friedel oscillations break translation symmetry and contribute to the entanglement. One can remove the dominant contribution from Friedel oscillations:

$$\tilde{S}_L(l) = S_L(l) + B(\langle \hat{t}_l \hat{t}_{l+1} \rangle + \langle \hat{b}_l \hat{b}_{l+1} \rangle), \quad (5.8)$$

where  $B$  takes some non-universal value. We present a typical scaling of entanglement entropy in Figure 5.5(a), shown before removing the Friedel oscillations, and in Figure 5.5(b), after removing them.

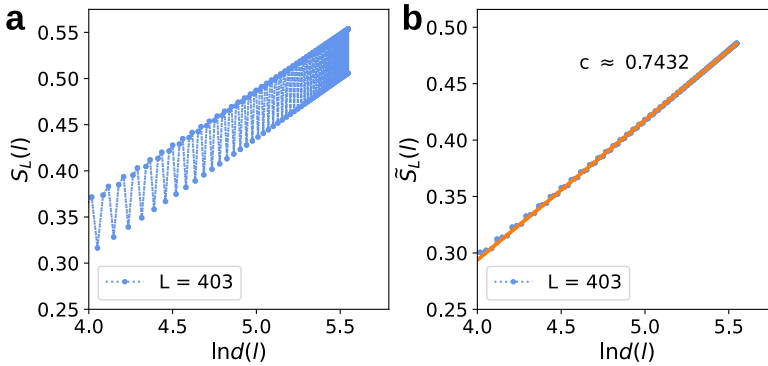


Figure 5.5.: Scaling of the entanglement entropy  $S$  with the conformal distance  $d(l)$ . (a) Oscillations in entanglement entropy are due to Friedel oscillations. (b) After removing the oscillations, the central charge can be extracted from a semi-log scaling. The data shown corresponds to  $\Delta/\Omega = 2.78594$  and  $R_b/a = 2.6$ .

### 5.3.4. BENCHMARK: ISING TRANSITION INTO CHECKERBOARD PHASE

Let us use the transition into the checkerboard phase as a benchmark to establish the method we will apply throughout the chapter for more complex transitions. The checkerboard phase spontaneously breaks  $\mathbb{Z}_2$  symmetry, and therefore, it is expected to belong to the Ising universality class. As an example, in Figure 5.6, we present numerical results along an horizontal cut at  $R_b/a = 1.25$ . In order to locate the transition, we look at the scaling dimension of the order parameter  $m \equiv \hat{a}_{L/2}$ . In the disordered phase,  $m$  vanishes with the system size, while in the ordered phase, it eventually converges to a finite value. We thus associate the critical point with a separatrix that scales linearly with the system size in the log-log scale, as shown in Figure 5.6(a). We locate the critical point at

$\Delta/\Omega = 1.2328$ ,  $R_b/a = 1.25$ . The slope of the separatrix gives the corresponding scaling dimension of the chosen operator. In the present case, the numerically extracted scaling dimension  $d \approx 0.125$  is in excellent agreement with the CFT prediction for the Ising transition [3]  $d = 1/8$ . At this critical point, we extract the central charge by fitting the entanglement entropy, as shown in Figure 5.6(b). Our results are in excellent agreement with the CFT prediction  $c = 1/2$ .

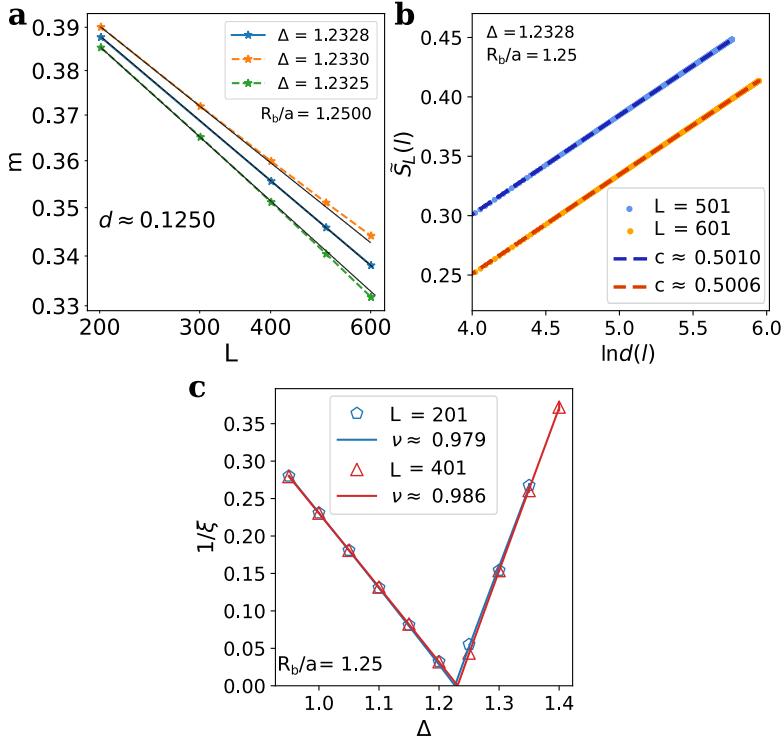


Figure 5.6.: Numerical extraction of the critical exponents for the transition out of the  $\bar{Z}_2$  phase. a) Finite-size scaling of the order parameter  $m = \hat{a}_i$  in the middle of a finite-size chain in a log-log scale. We identify the location of the critical point by the separatrix. To better highlight the curvature of the scaling curves, straight dashed lines are included as visual guides. The extracted scaling dimension  $d$  is in excellent agreement with the CFT prediction for Ising transition  $d = 1/8$ . b) Scaling of the entanglement entropy  $\hat{S}_L$  with the conformal distance  $d(l)$  after removing Friedel oscillations. Results for  $L = 601$  where shifted by  $-0.05$  for clarity. The slope agrees with the Ising central charge  $c = 1/2$ . c) Scaling of the inverse of the correlation length  $1/\xi$  in the vicinity of the transition, extracted from the density-density correlations of the operator  $\hat{a}$ . The extracted critical exponent  $\nu$  agrees with the theory prediction  $\nu = 1$ .

Finally, we extract the correlation length critical exponent  $\nu$ . To achieve this, we mea-

sure the correlation length on both sides of the transition and plot its inverse, as shown in Figure 5.6(c). We fit these data points on both sides of the transitions, assuming a single critical point and identical critical exponents in the ordered and disordered phases ( $\nu = \nu'$ ), while allowing for different non-universal pre-factors in each phase. The extracted critical exponent agrees within 2% of the CFT value  $\nu = 1$ .

#### 5.4. TRANSITIONS INTO $\mathbb{Z}_2$ AND $\mathbb{Z}_2 \otimes \tilde{\mathbb{Z}}_2$ PHASES

In this section, we focus on the pair of phases in which every other rung of the ladder is occupied by a boson. As mentioned earlier, there are two possible configurations: either a boson resonates between the top and bottom sites of the occupied rung, or it occupies one of the two sites, spontaneously breaking the symmetry between the two legs. The two symmetries,  $\mathbb{Z}_2$  and  $\tilde{\mathbb{Z}}_2$ , can be broken successively through two Ising transitions. From this perspective, the  $\mathbb{Z}_2$  phase appears as an intermediate phase between the disordered and  $\mathbb{Z}_2 \otimes \tilde{\mathbb{Z}}_2$  phases.

Interestingly, at larger values of  $R_b/a$ , the two symmetries are broken simultaneously, which leads to a unique sequence of exotic transitions: an interval of the Ashkin-Teller conformal transition is followed by an interval of the non-conformal chiral transition,

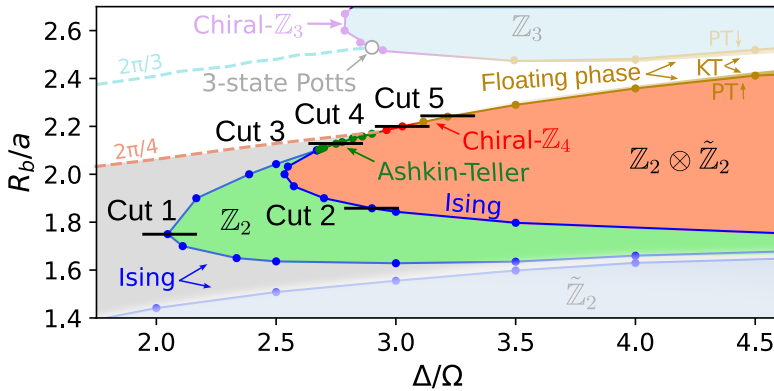


Figure 5.7.: Part of the phase diagram presented in Figure 5.1, zoomed around a pair of phases with spontaneously broken  $\mathbb{Z}_2$  symmetry, where, up to quantum fluctuations, every other rung of the ladder is occupied by a boson. The transition between the commensurate disordered phase (gray) and  $\mathbb{Z}_2 \otimes \tilde{\mathbb{Z}}_2$  phase occurs either through a pair of Ising transitions (blue), breaking  $\mathbb{Z}_2$  and  $\tilde{\mathbb{Z}}_2$  symmetries sequentially, or through an Ashkin-Teller transition (green). In the region where the disordered phase is incommensurate (white), the transition to the  $\mathbb{Z}_2 \otimes \tilde{\mathbb{Z}}_2$  phase is via a direct non-conformal  $\mathbb{Z}_4$ -chiral transition or through a floating phase—a narrow critical phase separated from the disordered and ordered phases by the Kosterlitz-Thouless (KT) and Pokrovsky-Talapov (PT) transitions, respectively. The location of the floating phase is indicated by a thick dark yellow gradient line, reflecting the uncertainty in the precise location of the KT transition.

and further along, a narrow intermediate floating phase emerges between the disordered and  $\mathbb{Z}_2 \otimes \tilde{\mathbb{Z}}_2$  phases. We provide numerical evidences for all these transitions, focusing in particular on the five cuts indicated in Figure 5.7.

### 5.4.1. ISING TRANSITIONS

Let us first discuss the pair of Ising transitions. The first Ising transition between the disordered and  $\mathbb{Z}_2$  phase spontaneously breaks translation symmetry by two rungs. We therefore define the order parameter as an amplitude of oscillations of total density on the rung  $m = |\hat{s}_i - \hat{s}_{i+1}|$ . In Figure 5.8(a), we perform a finite-size scaling of this operator to locate the critical line and to extract the scaling dimension  $d$ . At the identified critical point, we extract the central charge by fitting the scaling of the entanglement entropy, as shown in Figure 5.8(b). Finally we extract the correlation length critical exponent  $\nu$  by fitting the inverse of the correlation length on both sides of the transition. Numerically extracted values are in excellent agreement with the CFT predictions for an Ising transition [3]  $d = 1/8$ ,  $c = 1/2$  and  $\nu = 1$ .

We perform a similar analysis for the second Ising transition—between  $\mathbb{Z}_2$  and  $\mathbb{Z}_2 \otimes \tilde{\mathbb{Z}}_2$  phases. This transition is characterized by a spontaneously broken symmetry between upper and lower legs. Therefore, we identify the order parameter as the difference in local density taken on one rung  $m = \max(\hat{a}_i, \hat{a}_{i+1})$ . The maximum over two consecutive rungs is taken to select an occupied rung. As in the previous case, we extract the scaling dimension of the order parameter, the central charge, and the correlation length critical exponent. The extracted results are in excellent agreement with Ising predictions, and the examples of the scaling are presented in Figure 5.8(d)-(f).

### 5.4.2. DISORDER TO $\mathbb{Z}_2 \otimes \tilde{\mathbb{Z}}_2$ TRANSITION

Eventually, the two Ising transitions discussed above approach each other and fuse into a multicritical Ashkin-Teller point. Beyond this point, both symmetries,  $\mathbb{Z}_2$  and  $\tilde{\mathbb{Z}}_2$ , are broken simultaneously, and the nature of the transition undergoes multiple changes. As long as the disordered phase adjacent to the  $\mathbb{Z}_2 \otimes \tilde{\mathbb{Z}}_2$  is commensurate (gray area in Figure 5.7) the transition remains conformal in the Ashkin-Teller universality class. However, beyond a certain threshold, the disordered phase exhibits short-range incommensurability. The line where the wave-vector  $q$  starts to deviate from its commensurate value  $q = 2\pi/4$  is indicated in Figure 5.7 with an orange dashed line. Our results are consistent with the Ashkin-Teller conformal transition below this line, and the  $\mathbb{Z}_4$ -chiral transition is eventually replaced by the floating phase above it.

In order to distinguish the chiral transition from the conformal Ashkin-Teller, we use Huse-Fisher criterion [2]  $\Delta q \times \xi$ , where  $\Delta q$  measures the distance of the incommensurate wave-vector  $q$  to its commensurate value. In this particular case,  $\Delta q = |q - 2\pi/4|$ . The product  $\Delta q \times \xi$  is expected to vanish upon approaching the conformal transition, to take a finite value at the chiral transition, and to diverge at the Kosterlitz-Thouless transition into the floating phase. In Figure 5.9, we present the scaling of this product along the three cuts discussed in Figure 5.7, which go through different critical regimes. In 5.7, we provide further details on the operators that we used to extract  $q$  and  $\xi$  across various transitions.

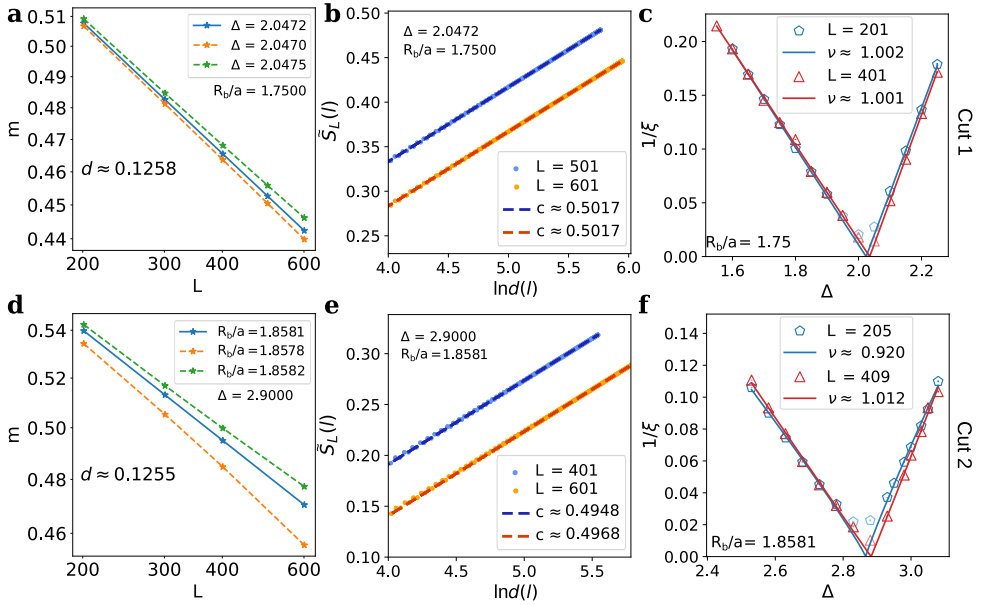


Figure 5.8.: Numerical evidence of the Ising transitions between (a)-(c) the disordered and  $\mathbb{Z}_2$  ordered phases; and (d)-(f) the  $\mathbb{Z}_2$  and  $\mathbb{Z}_2 \otimes \tilde{\mathbb{Z}}_2$  ordered phases. (a),(d) Finite-size scaling of the order parameter (a)  $m = |s_i - s_{i+1}|$  and (b)  $m = \max(\hat{a}_i, \hat{a}_{i+1})$  in a log-log scale. We identify the location of the critical point with the separatrix, its slope corresponds to the scaling dimension  $d$  of the order parameter. Numerical results are in excellent agreement with CFT predictions for Ising transition  $d = 1/8$ . (b),(e) Finite-size scaling of the reduced entanglement entropy. Numerically extracted values of the central charges are in excellent agreement with Ising transition  $c = 1/2$ . Results for  $L = 601$  were shifted by  $-0.05$  for clarity. (c),(f) Scaling of the inverse of the correlation length  $1/\xi$  on both sides of the transition extracted from the density-density correlations of the operator  $\hat{a}$ . In both cases the critical exponent  $\nu$  agree within 1% with the CFT prediction  $\nu = 1$ . Small shift in the location of the critical point is a typical finite-size effect [11, 12, 17].

The appearance of an extended interval of the Ashkin-Teller conformal transition is rather unusual. Previous studies of one-dimensional Rydberg arrays [12, 17] and ladders [26] featured a single Ashkin-Teller point appearing at the intersection of the critical and commensurate lines. In multi-component Rydberg array [43] and quantum loop ladder [44], where, similar to the present case, two Ising transitions fuse into a direct  $\mathbb{Z}_2 \otimes \tilde{\mathbb{Z}}_2$  transition, only the multicritical point was in the Ashkin-Teller universality class, followed by the chiral transition immediately after. Here, the extended interval of the Ashkin-Teller transition arises due to the fact that two Ising transitions fuse before the incommensurability develops.

To further support the evidence of an extended conformal Ashkin-Teller transition, we

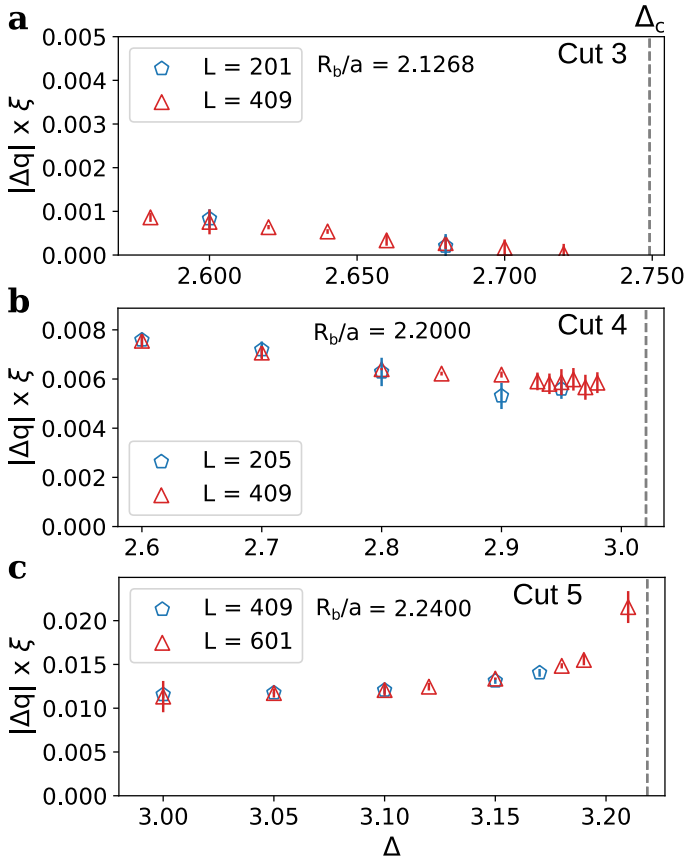


Figure 5.9.: Scaling of the product  $\Delta q \times \xi$  upon approaching (a) Ashkin-Teller; (b)  $\mathbb{Z}_4$ -chiral; and (c) the Kosterlitz-Thouless transitions. The correlation length  $\xi$  was extracted from the density-density correlations of the operator  $\hat{a}$ . The vertical dashed line indicates the location of the critical point. The scaling is performed along three horizontal cuts indicated in Figure 5.7. The error bars represent the 95% confidence interval for the point's location, obtained via error propagation, accounting for the uncertainties in the fitted parameters and their correlations.

present in Figure 5.10 the scaling behavior of three order parameters, defined as follows:

$$\begin{aligned}
 \hat{A} &= \max(\hat{a}_{L/2}, \hat{a}_{L/2+1}) \\
 \hat{B} &= \max(\hat{t}_{L/2-1}, \hat{t}_{L/2}, \hat{t}_{L/2+1}, \hat{t}_{L/2+2}) \\
 &\quad - \min(\hat{t}_{L/2-1}, \hat{t}_{L/2}, \hat{t}_{L/2+1}, \hat{t}_{L/2+2}) \\
 \hat{C} &= |\hat{s}_{L/2} - \hat{s}_{L/2+1}|.
 \end{aligned} \tag{5.9}$$

Operator  $\hat{A}$  measures a spontaneously broken symmetry between the two chains. It is

the same operator used to locate the Ising transition in Figure 5.8(b). Operator  $\hat{B}$  measures the amplitude of the local density over four consecutive sites along one chosen leg (here - top). This operator measures the spontaneously broken  $\mathbb{Z}_4$  symmetry—the result of simultaneously breaking  $\mathbb{Z}_2$  and  $\tilde{\mathbb{Z}}_2$ . Consequently, we expect this operator to have a scaling dimension  $d_{\hat{B}} = 1/8$ , corresponding to the Ashkin-Teller order parameter ( $\beta/\nu$  in Baxter’s notations for the eight-vertex model [45]). This operator corresponds to  $s_j$  in Eck and Fendley [33], where the emergence of the Ashkin-Teller transition over an extended interval was preserved by integrability of their model. Operator  $\hat{C}$  measures the amplitude of the total rung density, and therefore, reflects the order parameter associated with the spontaneously broken  $\mathbb{Z}_2$  translation symmetry. In Baxter’s solution for the eight-vertex model, its scaling dimension corresponds to  $\beta_e/\nu$  [45, 46]. This value is not universal but varies along the critical line, as we also observe in Figure 5.10. Returning to operator  $\hat{A}$ , its meaning is not clear in the Baxter’s theory for the eight-vertex model. However, it is reasonable to expect that if the order parameter associated with  $\mathbb{Z}_2$  symmetry is non-universal, then its counterpart—the order parameter of  $\tilde{\mathbb{Z}}_2$ —will also be non-universal, as we see in Figure 5.10. In Eck and Fendley [33], operator  $\hat{A}$  is referred to as  $(n_j^+ + n_j^-)$ , and its scaling dimension was also reported to vary along the critical line, consistent with our findings. In Figure 5.10(b), we provide an example of how the scaling dimension for all three operators was extracted.

5

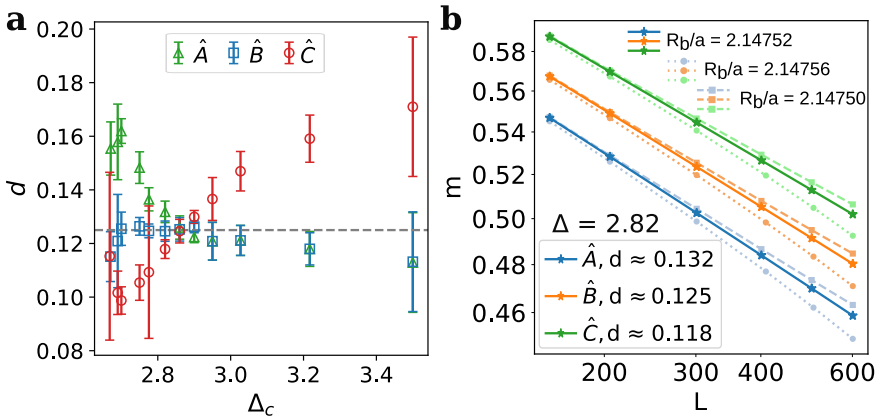


Figure 5.10.: Scaling dimension  $d$  calculated from the finite-size scaling of three different order parameters  $\hat{A}$ ,  $\hat{B}$  and  $\hat{C}$  defined by Eq. (5.9) and measured at the centre of the chain. (b) Example of the extraction of the critical exponent  $d_{\hat{A},\hat{B},\hat{C}}$  from the finite-size scaling of the order parameters. Error bars correspond to the 95% confidence interval for the fit, estimated as  $\pm 1.96$  times the standard error of the predicted values, obtained from the covariance matrix of the fit parameters.

Based on the extracted scaling dimension  $d_{\hat{B}}$ , we identify the interval of the Ashkin-Teller transition as  $2.7 \lesssim \Delta \lesssim 2.95$ . Within this interval, the numerically extracted central charge agrees with the CFT prediction  $c = 1$  within a 5% (see Section 5.8). Beyond  $\Delta \gtrsim 2.95$ , the transition is no longer conformal, and  $d_{\hat{B}} \neq 1/8$ . Before that, at  $2.67 \lesssim \Delta \lesssim 2.7$ ,

we see that  $d_{\hat{B}}$  deviates from this value, probably due to proximity to the multicritical point and possible crossover region. Note that  $d_{\hat{C}}$  takes values noticeably different from the value  $1/8$  that it takes at the Ising transition between disordered and  $\mathbb{Z}_2$  phases. This observation, combined with a large central charge in this region, allows us to confidently exclude the scenario in which the two Ising transitions continue up to  $\Delta_C \approx 2.95$ , with a single Ashkin-Teller point. Moreover, starting from  $\Delta = 2.75$ , the locations of the critical points identified by a separatrix for each of the three order parameters  $\hat{A}$ ,  $\hat{B}$  and  $\hat{C}$  is different by no more than  $O(10^{-5})$ .

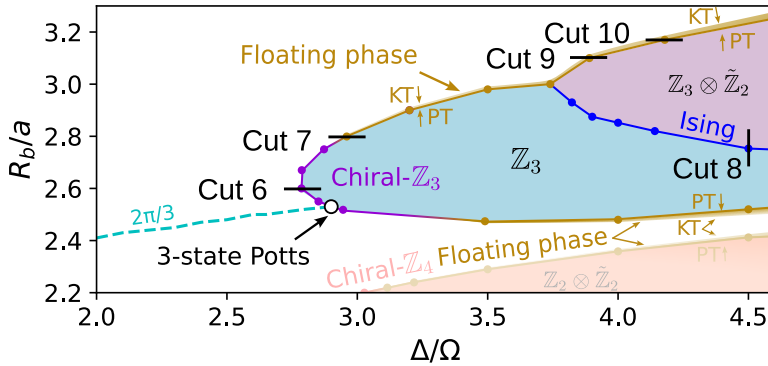


Figure 5.11.: Part of the phase diagram presented in Figure 5.1, zoomed around a pair of phases with spontaneously broken  $\mathbb{Z}_3$  symmetry, which, up to quantum fluctuations, corresponds to every third rung of the ladder being occupied. At the intersection of the commensurate line (dashed blue) with  $q = 2\pi/3$ , the transition into the  $\mathbb{Z}_3$  phase is in the three-state Potts universality class (open circle). Away from this point, but not too far, the transition falls within the Huse-Fisher  $\mathbb{Z}_3$ -chiral universality class, and further away, the transition is mediated by a narrow floating phase (gradient dark yellow) separated from the disordered phase by a Kosterlitz-Thouless (KT) and from the ordered phase by a Pokrovsky-Talapov (PT) transitions. The transition between the  $\mathbb{Z}_3$  and  $\mathbb{Z}_3 \otimes \tilde{\mathbb{Z}}_2$  phases is Ising (blue). The transition between the disordered and  $\mathbb{Z}_3 \otimes \tilde{\mathbb{Z}}_2$  phases is always through a floating phase. The gradient shading in the floating phase reflects the uncertainty in its precise boundaries.

## 5.5. TRANSITIONS INTO $\mathbb{Z}_3$ AND $\mathbb{Z}_3 \otimes \tilde{\mathbb{Z}}_2$ PHASES

Now, let us focus on the pair of phases where every third rung is occupied, illustrated in Figure 5.11. The bi-lobe structure consists of two phases:  $\mathbb{Z}_3$  and  $\mathbb{Z}_3 \otimes \tilde{\mathbb{Z}}_2$ , where, as in the previous case,  $\tilde{\mathbb{Z}}_2$  refers to a spontaneously broken symmetry between the two legs. In the limit of strong chiral perturbations, an intermediate floating phase is expected to emerge, separating each of the  $\mathbb{Z}_3$  phases from the disorder phase. Since the floating phase is an incommensurate Luttinger liquid phase with an emergent  $U(1)$  sym-

metry, we expect it to be separated from the crystalline  $\mathbb{Z}_3$  phases by a commensurate-incommensurate Pokrovsky-Talapov [36] transition and from the disordered phase by the Kosterlitz-Thouless [35] transition transparent for incommensurability. As we shall see below, the floating phase appearing at the boundary of the  $\mathbb{Z}_3$  lobes is very narrow, and we detect its appearance by a clear signature of the Kosterlitz-Thouless transition on one side of it.

### 5.5.1. DISORDER TO $\mathbb{Z}_3$ TRANSITION

When the symmetry between two legs is preserved, the nature of the transition into  $\mathbb{Z}_3$  phase is essentially identical to the one observed in the 1D chain of Rydberg atoms [11, 34]. Specifically, there is a single point where the commensurate line with  $q = 2\pi/3$  in the disordered phase intersects the critical line, resulting in a conformal transition within the three-state Potts universality class, as illustrated in Figure 5.11. Away from this point, but not too far, the transition is chiral in the Huse-Fisher universality class, and further away, the transition is a two-step process via Kosterlitz-Thouless and Pokrovsky-Talapov transitions, with an extremely narrow floating phase in between.

5

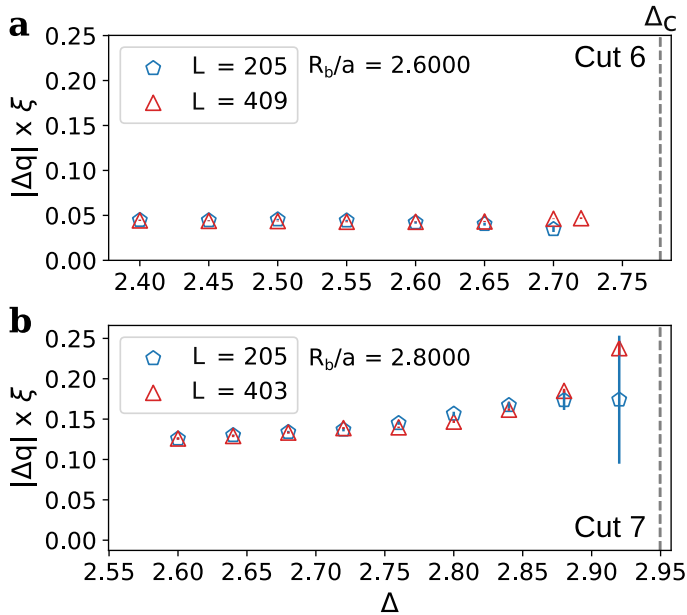


Figure 5.12.: Scaling of the product  $\Delta q \times \xi$  upon approaching (a) a chiral phase transition, and (b) a Kosterlitz-Talapov (KT) transition along Cuts 6 and 7 indicated in Figure 5.11. The correlation length  $\xi$  was extracted from the density-density correlations of the operator  $\hat{s}$ . The location of the transitions are marked with vertical dashed lines. The error bars show the 95% confidence interval for the point's location, incorporating fitting and error propagation.

To distinguish the chiral transition from the floating phase, we rely on the Huse-Fisher

criteria:  $\Delta q \times \xi$  remains finite upon approaching the chiral transition (see Figure 5.12(a)), but diverges when approaching the Kosterlitz-Thouless transition, as shown in Figure 5.12(b). This approach allows one to detect the floating phase even when its width is too small to study the scaling inside the floating phase.

### 5.5.2. ISING TRANSITION BETWEEN THE $\mathbb{Z}_3$ AND $\mathbb{Z}_3 \otimes \tilde{\mathbb{Z}}_2$ PHASES

Similar to the previous case, the symmetry between the two legs of the ladder is spontaneously broken, which leads to an Ising transition separating  $\mathbb{Z}_3$  and  $\mathbb{Z}_3 \otimes \tilde{\mathbb{Z}}_2$  phases, as indicated in Figure 5.11. In Figure 5.13, we provide numerical evidence of the Ising transition, including the numerically extracted scaling dimension of the order parameter  $m = \max(\hat{a}_i, \hat{a}_{i+1})$ , central charge, and correlation length critical exponent  $\nu$ . All numerical values are in excellent agreement with CFT predictions [3] for the Ising critical theory.

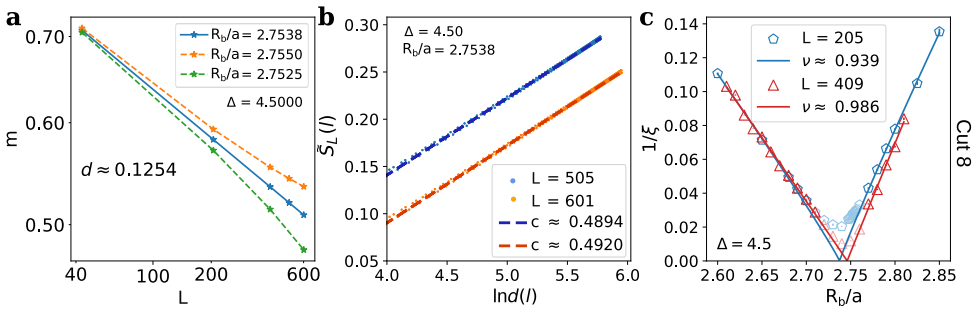


Figure 5.13.: Numerical evidences of the Ising transition between the  $\mathbb{Z}_3$  and  $\mathbb{Z}_3 \otimes \tilde{\mathbb{Z}}_2$  phases. (a) Finite-size scaling of the order parameter  $m = \max(\hat{a}_i, \hat{a}_{i+1})$ . The extracted scaling dimension  $d$  is in excellent agreement with CFT prediction  $d = 1/8$ . (b) Scaling of the entanglement entropy with the conformal distance. Results for  $L = 601$  are shifted by  $-0.05$  for better visualization. The slope is in excellent agreement with the Ising central charge  $c = 1/2$ . (c) Scaling of the inverse of the correlation length  $1/\xi$  in the vicinity of the transition extracted from the density-density correlations of the operator  $\hat{s}$ . The extracted critical exponent  $\nu$  agrees within 2% of the CFT value  $\nu = 1$ . Points that were not included in the fit are shown in pale.

### 5.5.3. DISORDER TO $\mathbb{Z}_3 \otimes \tilde{\mathbb{Z}}_2$ TRANSITION

The results for  $\Delta q \times \xi$  presented in Figure 5.14 suggest that the transition between the disordered phase and the  $\mathbb{Z}_3 \otimes \tilde{\mathbb{Z}}_2$  ordered phase is always mediated by a floating phase.

There are several possible scenarios, sketched in Figure 5.15, on how the floating phase coating the  $\mathbb{Z}_3$  transition might extend and encompass the  $\mathbb{Z}_3 \otimes \tilde{\mathbb{Z}}_2$  phase. In the simplest case, as depicted in Figure 5.15(a), the Ising and two Pokrovsky-Talapov transitions meet at a multicritical point. In this case, both the nature of this multicritical point and the

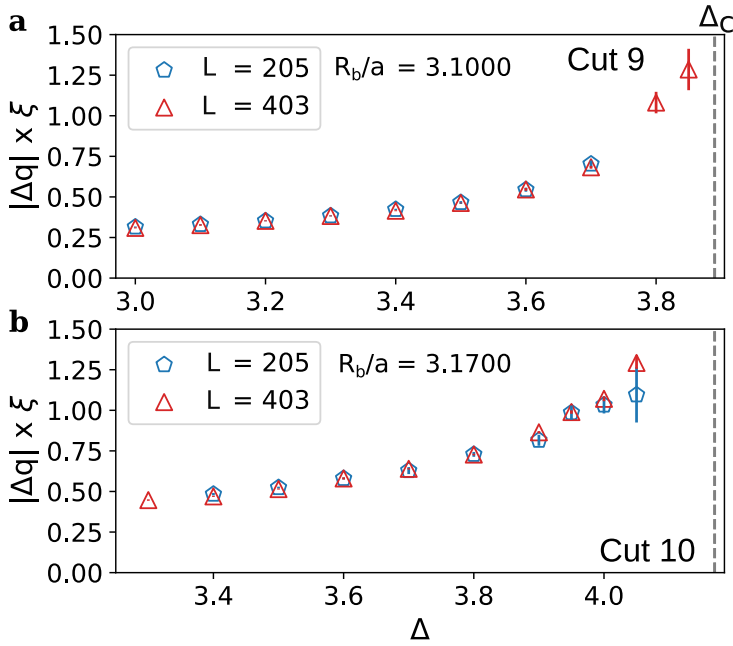


Figure 5.14.: Scaling of the product  $\Delta q \times \xi$  upon approaching (a) and (b) two Kosterlitz-Thouless transitions. The correlation length  $\xi$  was extracted from the density-density correlations of the operator  $\hat{s}$ . The scaling is performed along the horizontal cuts, Cut 9 and Cut 10, indicated in Figure 5.11. The error bars represent the 95% confidence interval for the point's location, incorporating fitting and error propagation.

renormalization group flows are not clear. In a more plausible scenario, the Ising transition continues through the floating phase and separates two Luttinger liquid phases, one of which has spontaneously broken  $\tilde{\mathbb{Z}}_2$  symmetry, as sketched in Figure 5.15(b). In this configuration, the Ising and Pokrovsky-Talapov transitions are expected to be independent, with the crossing point exhibiting either Ising or Pokrovsky-Talapov criticalities, depending on the measured order parameter. A similar scenario has been recently reported in the context of interacting Majorana fermions [47], although in that case, the Ising transition exited the floating phase via a Kosterlitz-Thouless transition. A third scenario, shown in Figure 5.15(c), is very similar to the previous case, but places the Ising transition higher in the energy spectrum, and therefore, not necessary present in the Luttinger liquid phase in the ground-state phase diagram. Finally, if both  $\mathbb{Z}_3$  and  $\tilde{\mathbb{Z}}_2$  symmetries are broken simultaneously, the most natural expectation is a first order transition out of the  $\mathbb{Z}_3 \otimes \tilde{\mathbb{Z}}_2$  phase. However, in this scenario, it is not clear how the floating phase, which gains a finite width by the time it reaches the Ising transition, terminates. We consider the scenario sketched in Figure 5.15(b) to be the most plausible. However, the extremely narrow extent of the floating phase in our model prevents numerical verification. It would be worthwhile, nonetheless, to explore the aforementioned scenarios

within simpler models, potentially with blockade constraints.

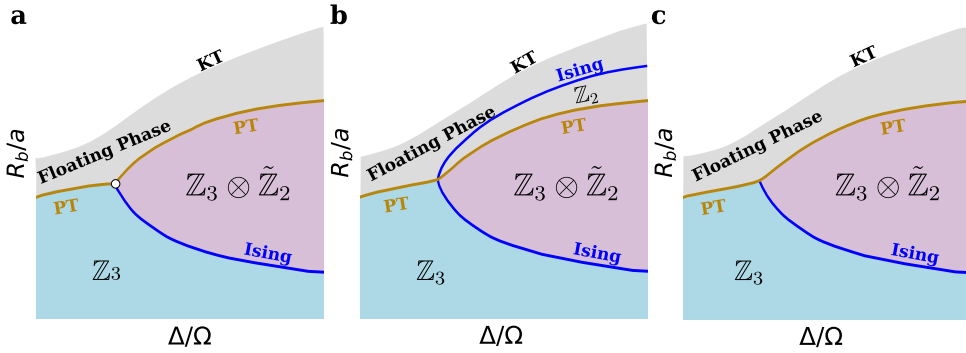


Figure 5.15.: Sketch of the three possible scenarios for the multicritical point where the floating,  $\mathbb{Z}_3$  and  $\mathbb{Z}_3 \otimes \tilde{\mathbb{Z}}_2$  phases meet. (a) The Ising and Pokrovsky-Talapov lines meet at a multicritical point, (b) The Ising critical line extends inside the floating phase as a higher-symmetry line separating two regions of the floating phase with spontaneously broken  $\tilde{\mathbb{Z}}_2$  symmetry in one of them, (c) the Ising transition takes place higher in the energy spectrum after crossing the Pokrovsky-Talapov transition.

### 5.6. BEYOND $\mathbb{Z}_3 \otimes \tilde{\mathbb{Z}}_2$

There are other crystalline phases above  $\mathbb{Z}_3 \otimes \tilde{\mathbb{Z}}_2$  that have not been studied in detail due to extremely slow convergence. In Figure 5.16 we present examples of the  $\mathbb{Z}_4$  and  $\mathbb{Z}_4 \otimes \tilde{\mathbb{Z}}_2$  phases, continuing the sequence of the bi-lobed structures.

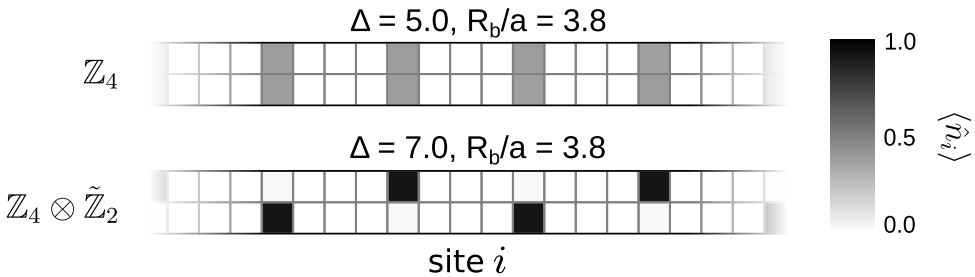


Figure 5.16.: Density profiles for other gaped phases not discussed in the main text. Specifically, the  $\mathbb{Z}_4$  phase was obtained for  $\Omega = 1$ ,  $\Delta = 5.0$  and  $R_b/a = 3.8$ , while the  $\mathbb{Z}_4 \otimes \tilde{\mathbb{Z}}_2$  phase was obtained for  $\Omega = 1$ ,  $\Delta = 7.0$  and  $R_b/a = 3.8$ . Each square corresponds to a lattice site, with its color indicating the local density according to the color bar. We show profiles only for the central part of a long chain.

## 5.7. INFLUENCE OF THE OPERATOR CHOICE ON THE EXTRACTED CORRELATION LENGTH $\xi$ AND WAVE VECTOR $q$

As discussed in the main body of this chapter, different operators exhibit distinct scaling behaviors near the critical points. These variations arise because each operator captures unique aspects of the broken symmetries associated to the phase transitions. In this section, we illustrate this phenomenon by comparing the scaling of the inverse correlation length  $1/\xi$  extracted from the density-density correlations for the three operators used in our calculations— $\hat{t}$ ,  $\hat{s}$  and  $\hat{a}$ —as defined in Eq. (5.3).

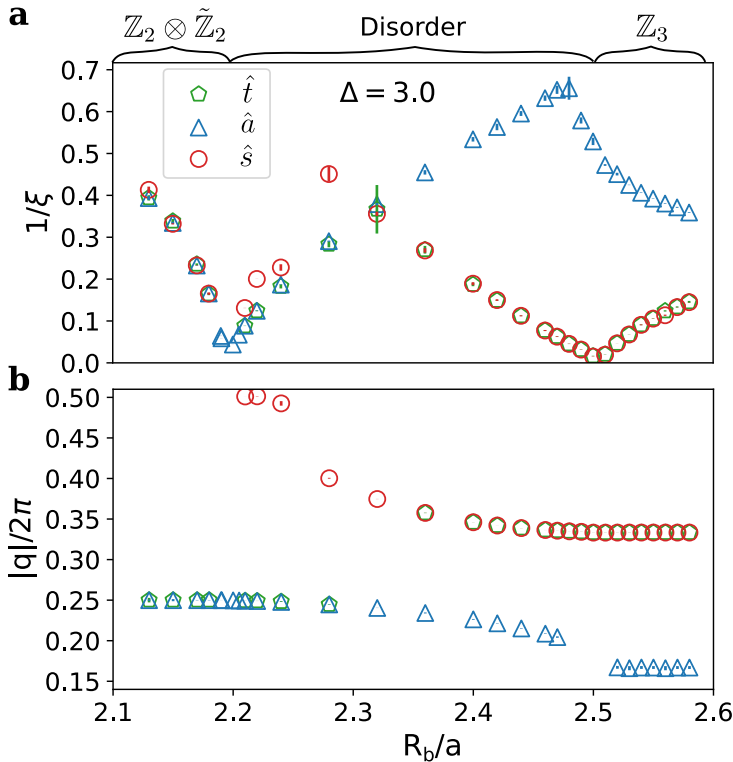


Figure 5.17.: Comparison of (a) the inverse of the correlation length  $1/\xi$  and (b) the wave-vector  $q$  calculated from the density-density correlation of the operators  $\hat{t}$ ,  $\hat{a}$  and  $\hat{s}$  for a vertical cut comprising phases  $\mathbb{Z}_2 \otimes \tilde{\mathbb{Z}}_2$ ,  $\mathbb{Z}_3$  and the disordered phase in between. The expressions for the operators  $\hat{t}$ ,  $\hat{a}$  and  $\hat{s}$  are described in Eq. (5.3). Error bars correspond to the 95% confidence interval for the fit, estimated as  $\pm 1.96$  times the standard error of the predicted values, obtained from the covariance matrix of the fit parameters.

Figure 5.17(a) presents the scaling of  $1/\xi$  for a vertical cut comprising the phases  $\mathbb{Z}_2 \otimes \tilde{\mathbb{Z}}_2$ ,  $\mathbb{Z}_3$  and the disordered phase in between. Within the  $\mathbb{Z}_2 \otimes \tilde{\mathbb{Z}}_2$ , phase the correlation

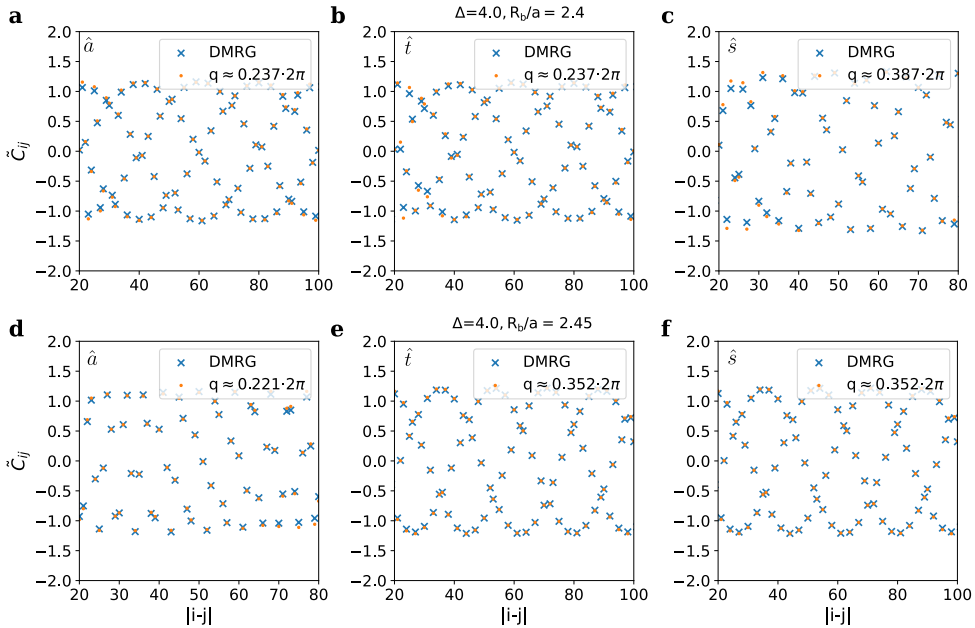


Figure 5.18.: Fitting of the wave-vector  $q$  to the oscillations of the correlation function, calculated for three distinct operators:  $\hat{a}$ ,  $\hat{t}$ , and  $\hat{s}$  defined in Eq. (5.3), in two different scenarios. (a) The operators  $\hat{a}$  and  $\hat{t}$  yield the same value for  $q$ , which differs from that obtained using  $\hat{s}$ . (b) The operators  $\hat{s}$  and  $\hat{t}$  produce the same value for  $q$ , distinct from the result obtained using  $\hat{a}$ . The definitions of the operators  $\hat{a}$ ,  $\hat{t}$ , and  $\hat{s}$  are provided in Eq. (5.3).

length is independent of the operator used. However, in the disordered phase, the correlation length associated with  $\hat{s}$  is slightly smaller than that of  $\hat{a}$  and  $\hat{t}$ , but our results are consistent with all correlation lengths diverging at the same critical point  $R_b/a$ , compatible with the direct transition between the disordered and  $\mathbb{Z}_2 \otimes \tilde{\mathbb{Z}}_2$  ordered phases.

The situation is drastically different upon entering the  $\mathbb{Z}_3$  phase: the correlation lengths associated with  $\hat{s}$  and  $\hat{t}$ , both susceptible to spontaneously broken symmetry in the  $\mathbb{Z}_3$  phase, diverge around  $R_b/a \approx 2.5$ . In contrast, the correlation length associated with  $\hat{a}$ , which tracks states with broken  $\tilde{\mathbb{Z}}_2$  symmetry, remains finite across the transition. Within the  $\mathbb{Z}_3$  phase, the correlation lengths calculated with  $\hat{t}$  and  $\hat{s}$  decrease with the distance to the transition, while the one extracted from  $\hat{a}$  increases as we move out of the transition.

The behavior of  $\xi$  seems to be closely related to that of the wave-vector  $q$ , as illustrated in Figure 5.17(b). Within the  $\mathbb{Z}_2 \otimes \tilde{\mathbb{Z}}_2$  phase, the values of  $q$  obtained from operators  $\hat{t}$  and  $\hat{a}$  are both  $q = 2\pi/4$ , which differ from  $q = 2\pi/2$  extracted from  $\hat{s}$ .

In the disordered phase,  $q$  derived from  $\hat{a}$  transitions from  $q = 2\pi/4$  in the vicinity of the  $\mathbb{Z}_2 \otimes \tilde{\mathbb{Z}}_2$  phase to  $q = 2\pi/6$ , at the  $\mathbb{Z}_3$  phase, while  $q$  goes from  $q = 2\pi/2$  near the  $\mathbb{Z}_2 \otimes \tilde{\mathbb{Z}}_2$  phase to  $q = 2\pi/3$  at the  $\mathbb{Z}_3$  phase. The behavior of  $q$  extracted from  $\hat{t}$  is more complex:

it matches that of  $\hat{a}$  near the  $\mathbb{Z}_2 \otimes \tilde{\mathbb{Z}}_2$  phase and aligns with  $\hat{s}$  closer to the  $\mathbb{Z}_3$  phase. A sudden change in  $q$  for  $\hat{t}$  occurs at the point where the values of  $\xi$  calculated for all three operators coincide ( $R_b/a \approx 2.32$ ). An example of the extraction of the  $q$  vector for the case when  $\hat{t}$  coincides with  $\hat{s}$  and when it coincides with  $\hat{a}$  is shown in Figure 5.18. As shown in Figure 5.19, this effect also occurs when  $q$  is extracted from the structure factor.

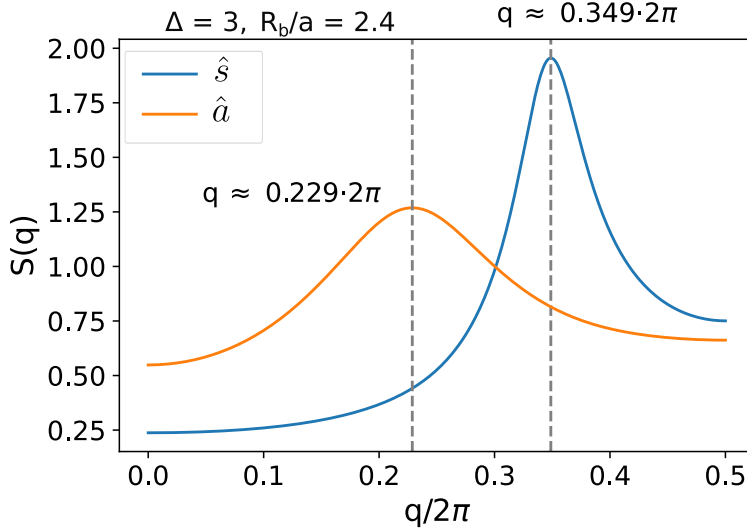


Figure 5.19.: Extraction of the wave-vector  $q$  from the peak of the two-particle correlation structure factor  $S(q)$ , computed for two different operators,  $\hat{s}$  and  $\hat{a}$ , at a specific point within the disordered phase between the  $\mathbb{Z}_2 \otimes \tilde{\mathbb{Z}}_2$  and  $\mathbb{Z}_3$  phases. The operator  $\hat{s}$  yields a value of  $q$  close to  $2\pi/3$ , corresponding to the occupancy level of the  $\mathbb{Z}_3$  phase, while the operator  $\hat{a}$  produces a value of  $q$  near  $2\pi/4$ , which aligns with the occupancy level of the  $\mathbb{Z}_2 \otimes \tilde{\mathbb{Z}}_2$  phase.

One would naively expect that the relative behavior between the three aforementioned operators observed near the  $\mathbb{Z}_2 \otimes \tilde{\mathbb{Z}}_2$  phase would also be observed near the  $\mathbb{Z}_3 \otimes \tilde{\mathbb{Z}}_2$  phase. However, this is not the case. As illustrated in Figure 5.20(a), within the  $\mathbb{Z}_3 \otimes \tilde{\mathbb{Z}}_2$  phase, the three operators give the same  $\xi$ . However, in contrast to the vicinity of the  $\mathbb{Z}_2 \otimes \tilde{\mathbb{Z}}_2$  phase, in the disordered phase close to the  $\mathbb{Z}_3 \otimes \tilde{\mathbb{Z}}_2$  phase, the correlation length associated with  $\hat{t}$  and  $\hat{s}$  are similar and compatible with the floating phase (approaching the transition with zero slope) and distinct from operator  $\hat{a}$ . This scenario suggests that the floating phase responsible for the spontaneously broken  $\mathbb{Z}_3$  symmetry is independent of the transition breaking  $\tilde{\mathbb{Z}}_2$ . In our numerical simulations, we cannot zoom closely enough to resolve the nature of the phase transition breaking  $\tilde{\mathbb{Z}}_2$ ; however, it could be either a first order transition or an Ising transition separating the two Luttinger liquids, as sketched in Figure 5.15(b). Wave-vector  $q$  presented in Figure 5.20(b) and extracted with  $\hat{t}$  and  $\hat{s}$  is compatible with commensurate-incommensurate transition (including the floating phase scenario).

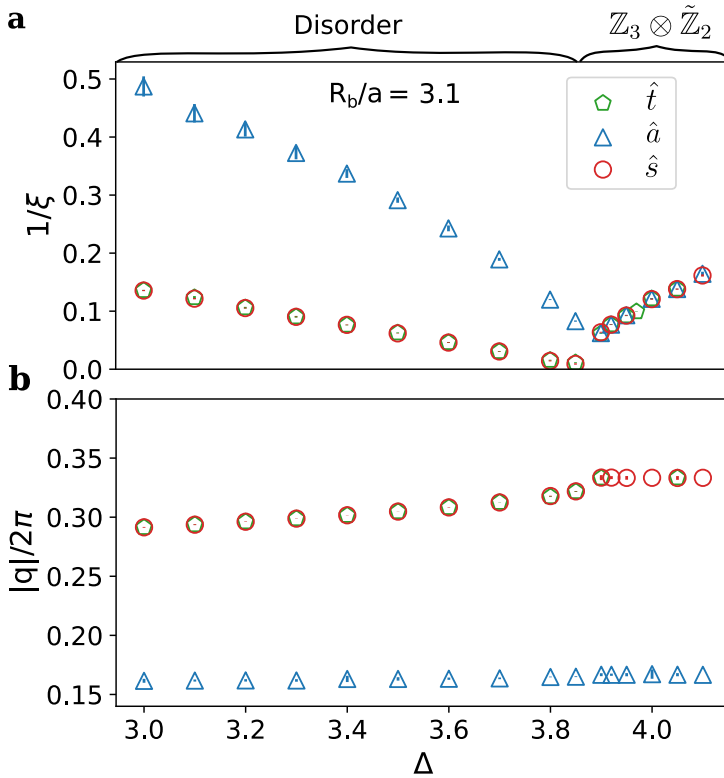


Figure 5.20.: Comparison of (a) the inverse of the correlation length  $1/\xi$  and (b) the wave-vector  $q$  calculated from the density-density correlations of operators  $\hat{t}$ ,  $\hat{a}$  and  $\hat{s}$  defined in Eq. (5.3), for an horizontal cut from the disordered to the  $\mathbb{Z}_3 \otimes \tilde{\mathbb{Z}}_2$  phase. The error bars depict the 95% confidence region for the values, estimated using  $\pm 1.96$  times the standard error of the predicted values

## 5.8. CENTRAL CHARGE FOR THE TRANSITION OUT OF $\mathbb{Z}_2 \otimes \tilde{\mathbb{Z}}_2$

In this section, we compute the central charge  $c$  along the critical line of the transition out of  $\mathbb{Z}_2 \otimes \tilde{\mathbb{Z}}_2$ . The location of the transition generally depends on the choice of the operator— $\hat{A}$ ,  $\hat{B}$  and  $\hat{C}$ —that we use to perform the finite-size scaling described in Eq. (5.9). We compare the central charge extracted at the critical points associates with each of the three operators with the best-fit value for  $c$ , determined as the value of  $c$  that shows minimal variation with the system size. Figure 5.21 summarizes our main results.

This figure reveals 4 distinct regimes, which coincide with the regimes observed for the finite-size scaling of the order parameter in Figure 5.10(a):

- $\Delta_c < 2.6$ . This range corresponds to the transition from  $\mathbb{Z}_2$  to  $\mathbb{Z}_2 \otimes \tilde{\mathbb{Z}}_2$ . Here, only operator  $\hat{A}$  effectively distinguishes the two phases. The central charge obtained with  $\hat{A}$  aligns with the best-fit value,  $c \approx 0.5$ , consistent with CFT predictions for the Ising universality class.

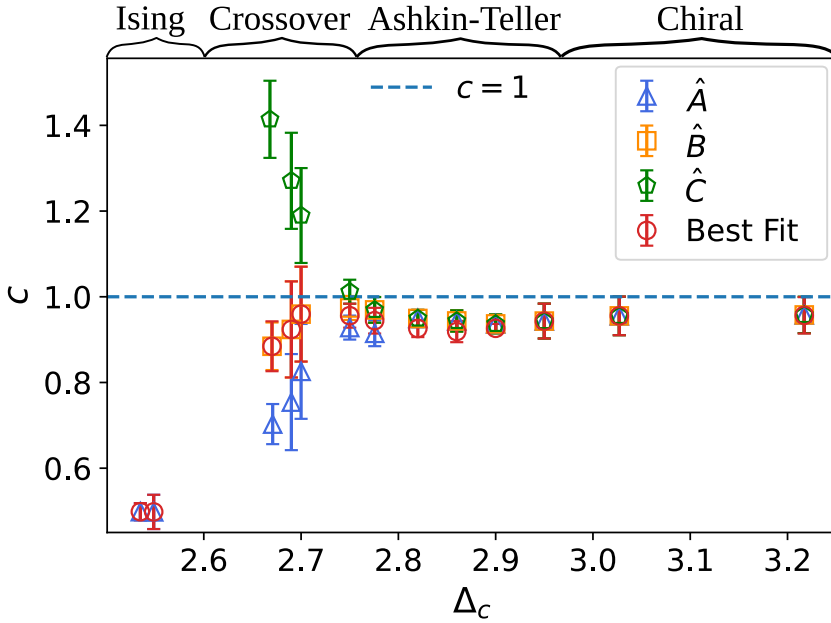


Figure 5.21.: Comparison of central charge  $c$  for various cuts along the upper critical line of the transition out of  $\mathbb{Z}_2 \otimes \mathbb{Z}_2$ , using critical point estimated from the scaling of the order parameters  $\hat{A}$ ,  $\hat{B}$  and  $\hat{C}$ , as defined in Eq. (5.9). These results are compared to the best-fit value of  $c$ , defined as the value of  $c$  that shows minimal variation with the system size ranging from 202 to 602 rungs.

- $2.6 < \Delta_c < 2.75$ . This region, located close to the critical point, appears to exhibit a crossover behavior between the Ising and Ashkin-Teller transitions. The location of the critical points differs slightly depending on the order parameter, which results in variations in the value of  $c$ . In this range, operator  $\hat{B}$  provides the closest match to the best-fit value of  $c$ . For this operator,  $c$  shows an intermediate value between the  $c = 0.5$  predicted for the Ising transition and  $c = 1$  predicted for the Ashkin-Teller transition. As we move further from the multicritical point into the Ashkin-Teller region,  $c$  approaches 1.
- $2.75 < \Delta_c < 2.95$ . This interval corresponds to the Ashkin-Teller region. Conformal field theory predicts  $c = 1$  for the Ashkin-Teller universality class. In this region, the choice of operator has minimal impact on the location of the critical point, and the computed values of  $c$  are nearly identical across all operators. However, the best-fit  $c$  is slightly lower than the values obtained from the operators, although all measurements remain close to 1, within 5% relative error. The small deviations from the theory prediction  $c = 1$  are likely due to finite size effects and are comparable with previously reported values for the Ashkin-Teller multicritical point in a related models [17].

- $2.95 < \Delta_c$ . Chiral transition. All operators identify the critical point at the same location, and the obtained effective central charge  $c$  is equal to the best-fit  $c$ . Chiral transition is not conformal, and the central charge is not defined.

## 5.9. DISCUSSION

To conclude, let us briefly compare our findings with previous literature on Rydberg chains and ladders. Similar to a 1D array of atoms, the phase diagram of the Rydberg ladder model consists of lobes of crystalline gaped phases surrounded by a disordered phase, a large fraction of which is incommensurate. Interestingly, except for the standing alone checkerboard lobe, all crystalline phases appear in pairs. These paired phases share the same periodicity in the rung density, but are distinguished by spontaneously broken symmetry between the two legs in one of the phases. This asymmetry gives rise to an Ising transition between each pair of ordered phases. The bi-lobed structure of the gaped phases has been overlooked in the previous experimental and numerical study of the Rydberg ladder [26]. It is possible, however, that larger inter-chain distance considered in Ref. [26] might affect the extent of each phase.

In contrast, the resonant phases—gaped phases preserving the symmetry between the two legs of the ladder—have been reported in the recent analytical study of a Rydberg blockade model on a ladder [33]. However, the phase diagram by Eck and Fendley [33] featured two different resonant  $\mathbb{Z}_3$  phases: a phase with a symmetric rung state  $\frac{1}{\sqrt{2}}(|10\rangle + |01\rangle)$ , called  $\mathbb{Z}_3^+$ , and one with antisymmetric rungs  $\frac{1}{\sqrt{2}}(|10\rangle - |01\rangle)$ , labeled  $\mathbb{Z}_3^-$ . The  $\mathbb{Z}_3$  phases in the present chapter corresponds to a symmetric  $\mathbb{Z}_3^+$  one in Eck and Fendley's notation. By contrast, its antisymmetric counterpart appears due to the hopping term  $d_{2i}d_{2i+1}^\dagger + \text{h.c.}$  introduced in Ref. [33] to keep the model integrable, but absent in the experimentally feasible model (5.1) that we consider here.

The complex bi-lobbed structure of the density-wave phases also leads to exotic critical behavior at their boundaries. In particular, we observed a fusion of two Ising transitions, resulting in an extended region with a conformal Ashkin-Teller transition, followed by a  $\mathbb{Z}_4$ -chiral transition. This suggests that, for some reason, the two symmetries  $\mathbb{Z}_2$  and  $\tilde{\mathbb{Z}}_2$  are simultaneously broken at the upper boundary of  $\mathbb{Z}_2 \otimes \tilde{\mathbb{Z}}_2$  phase. By contrast to the model proposed by Eck and Fendley [33], where an extended Ashkin-Teller criticality has been preserved by the integrability of the model, in the present case, the appearance of the finite interval of the conformal Ashkin-Teller transition is very surprising, as the model we consider is non-integrable. In our model, the conformal criticality is preserved by the lack of incommensurability surrounding the multicritical point where two Ising transitions fuse. Recently, the fusion of two Ising transition leading to a single Ashkin-Teller critical point immediately followed by the chiral transition has been predicted in the multi-component Rydberg array [43]. In that case, the disorder line separating a commensurate and incommensurate areas of the disordered phase hits the boundary of the crystalline phase at the multi-critical point. In the present case, this happens at a different point leaving a finite-interval with the Ashkin-Teller transition unperturbed by the chiral perturbations.

Another interesting opportunity is raised from the connection with multi-component Rydberg atoms, where the nature of the Ashkin-Teller criticality as well as the extent of

the chiral transition following it have been tuned continuously by the relative ratio of two Rabi frequencies [43]. In the two leg-ladder considered here, we observe a similar enhancement of symmetries, leading to a similar fusion of two Ising transitions. It is therefore natural to expect that a similar level of control over phases and phase transitions can be achieved by tuning the ratio of inter-atomic spacing within each chain and between them. It would be noteworthy to explore how the phase diagram in Figure 5.1 and the nature of the quantum phase transitions change with variations in the relative height of the ladder that can easily be controlled in experiment.

Furthermore, our study underscores the importance of the appropriate choice of the order parameter and operators in numerical and experimental studies of quantum phase transitions. In Figure 5.10, we demonstrated that the scaling dimension along the Ashkin-Teller ( $c = 1$ ) transition interval behaves differently for different operators, reflecting the complex nature of this critical line. For a given operator, its scaling dimension is related to its correlation length critical exponent. Since the nature of quantum phase transitions in Rydberg arrays is traditionally investigated using the quantum Kibble-Zurek mechanism, selecting the appropriate correlation function and kink operators [48, 49] is a key for experimental observation of this exotic transition.

Finally, there is another open question raised by our study—the nature of the multicritical point where the  $\tilde{\mathbb{Z}}_2$  Ising transition comes across the floating phase into  $\mathbb{Z}_3$  phase. In Figure 5.15, we already listed and briefly described several possible scenarios. We highlighted that the most plausible scenario is one where the Ising transition continues through the floating phase (see Figure 5.15(b)), which appears due to an emergent  $U(1)$  symmetry [50]. If our conjecture is correct, one can expect an emergent  $\mathcal{N} = (1, 1)$  supersymmetry [51, 52] along the line of Ising transition superposed with the  $U(1)$  symmetric Luttinger liquid phase. Due to the extremely narrow width of the floating phase and overall large complexity of calculations of the model with van der Waals potential, this problem cannot be resolved numerically within the current framework. We believe that the most promising approach would be to construct a related constrained model that allows for more accurate numerical simulations and, ideally, analytically solvable at least in certain limits or along the lines with higher symmetry. While this approach lies outside the immediate scope of our research, it represents an intriguing avenue for future investigation.

# BIBLIOGRAPHY

- [1] J. Soto-Garcia and N. Chepiga. “Numerical investigation of quantum phases and phase transitions in a two-leg ladder of Rydberg atoms”. In: *Physical Review Research* 7.1 (2025), p. 013215.
- [2] D. A. Huse and M. E. Fisher. “Domain walls and the melting of commensurate surface phases”. In: *Physical Review Letters* 49.11 (1982), p. 793.
- [3] P. Di Francesco, P. Mathieu, and D. Sénéchal. *Conformal Field Theory*. Graduate Texts in Contemporary Physics. New York: Springer, 1997. ISBN: 9780387947853. URL: <https://books.google.ch/books?id=keUrdME5rhIC>.
- [4] D. A. Huse and M. E. Fisher. “Commensurate melting, domain walls, and dislocations”. In: *Phys. Rev. B* 29 (1 Jan. 1984), pp. 239–270. DOI: [10.1103/PhysRevB.29.239](https://doi.org/10.1103/PhysRevB.29.239). URL: <https://link.aps.org/doi/10.1103/PhysRevB.29.239>.
- [5] H. J. Schulz. “Phase transitions in monolayers adsorbed on uniaxial substrates”. In: *Phys. Rev. B* 28 (5 Sept. 1983), pp. 2746–2749. DOI: [10.1103/PhysRevB.28.2746](https://doi.org/10.1103/PhysRevB.28.2746). URL: <https://link.aps.org/doi/10.1103/PhysRevB.28.2746>.
- [6] F. Haldane, P. Bak, and T. Bohr. “Phase diagrams of surface structures from Bethe-ansatz solutions of the quantum sine-Gordon model”. In: *Physical Review B* 28.5 (1983), p. 2743.
- [7] M. den Nijs. “The Domain Wall Theory of Two-dimensional Commensurate-Incommensurate Phase Transitions”. In: *Phase Transitions and Critical Phenomena* 12 (1988), p. 219.
- [8] J. Schreiner, K. Jacobi, and W. Selke. “Experimental evidence for chiral melting of the Ge (113) and Si (113)  $3 \times 1$  surface phases”. In: *Physical Review B* 49.4 (1994), p. 2706.
- [9] P. Fendley, K. Sengupta, and S. Sachdev. “Competing density-wave orders in a one-dimensional hard-boson model”. In: *Physical Review B* 69.7 (2004), p. 075106.
- [10] P. Bak. “Commensurate phases, incommensurate phases and the devil’s staircase”. In: *Reports on Progress in Physics* 45.6 (June 1982), p. 587. DOI: [10.1088/0034-4885/45/6/001](https://doi.org/10.1088/0034-4885/45/6/001). URL: <https://dx.doi.org/10.1088/0034-4885/45/6/001>.
- [11] N. Chepiga and F. Mila. “Floating phase versus chiral transition in a 1D hard-boson model”. In: *Physical review letters* 122.1 (2019), p. 017205.
- [12] I. A. Maceira, N. Chepiga, and F. Mila. “Conformal and chiral phase transitions in Rydberg chains”. In: *Phys. Rev. Res.* 4 (4 Nov. 2022), p. 043102. DOI: [10.1103/PhysRevResearch.4.043102](https://doi.org/10.1103/PhysRevResearch.4.043102). URL: <https://link.aps.org/doi/10.1103/PhysRevResearch.4.043102>.

- [13] R. Samajdar, S. Choi, H. Pichler, M. D. Lukin, and S. Sachdev. “Numerical study of the chiral  $\mathbb{Z}_3$  quantum phase transition in one spatial dimension”. In: *Phys. Rev. A* 98 (2 Aug. 2018), p. 023614. DOI: [10.1103/PhysRevA.98.023614](https://doi.org/10.1103/PhysRevA.98.023614). URL: <https://link.aps.org/doi/10.1103/PhysRevA.98.023614>.
- [14] G. Giudici, A. Angelone, G. Magnifico, Z. Zeng, G. Giudice, T. Mendes-Santos, and M. Dalmonte. “Diagnosing Potts criticality and two-stage melting in one-dimensional hard-core boson models”. In: *Phys. Rev. B* 99 (9 Mar. 2019), p. 094434. DOI: [10.1103/PhysRevB.99.094434](https://doi.org/10.1103/PhysRevB.99.094434). URL: <https://link.aps.org/doi/10.1103/PhysRevB.99.094434>.
- [15] R.-Z. Huang and S. Yin. “Nonequilibrium critical dynamics in the quantum chiral clock model”. In: *Physical Review B* 99.18 (2019), p. 184104.
- [16] J. Soto Garcia and N. Chepiga. “Resolving chiral transitions in one-dimensional Rydberg arrays with quantum Kibble-Zurek mechanism and finite-time scaling”. In: *Physical Review B* 110.12 (2024), p. 125113.
- [17] N. Chepiga and F. Mila. “Kibble-Zurek exponent and chiral transition of the period-4 phase of Rydberg chains”. In: *Nature Communications* 12.1 (2021), p. 414.
- [18] B. E. Lüscher, F. Mila, and N. Chepiga. “Critical properties of the quantum Ashkin-Teller chain with chiral perturbations”. In: *Phys. Rev. B* 108 (18 Nov. 2023), p. 184425. DOI: [10.1103/PhysRevB.108.184425](https://doi.org/10.1103/PhysRevB.108.184425). URL: <https://link.aps.org/doi/10.1103/PhysRevB.108.184425>.
- [19] H. Bernien, S. Schwartz, A. Keesling, H. Levine, A. Omran, H. Pichler, S. Choi, A. S. Zibrov, M. Endres, M. Greiner, *et al.* “Probing many-body dynamics on a 51-atom quantum simulator”. In: *Nature* 551.7682 (2017), pp. 579–584.
- [20] H. Labuhn, D. Barredo, S. Ravets, S. De Léséleuc, T. Macrì, T. Lahaye, and A. Browaeys. “Tunable two-dimensional arrays of single Rydberg atoms for realizing quantum Ising models”. In: *Nature* 534.7609 (2016), pp. 667–670.
- [21] S. De Léséleuc, V. Lienhard, P. Scholl, D. Barredo, S. Weber, N. Lang, H. P. Büchler, T. Lahaye, and A. Browaeys. “Observation of a symmetry-protected topological phase of interacting bosons with Rydberg atoms”. In: *Science* 365.6455 (2019), pp. 775–780.
- [22] S. Ebadi, T. T. Wang, H. Levine, A. Keesling, G. Semeghini, A. Omran, D. Bluvstein, R. Samajdar, H. Pichler, W. W. Ho, *et al.* “Quantum phases of matter on a 256-atom programmable quantum simulator”. In: *Nature* 595.7866 (2021), pp. 227–232.
- [23] P. Scholl, M. Schuler, H. J. Williams, A. A. Eberharter, D. Barredo, K.-N. Schymik, V. Lienhard, L.-P. Henry, T. C. Lang, T. Lahaye, *et al.* “Quantum simulation of 2D antiferromagnets with hundreds of Rydberg atoms”. In: *Nature* 595.7866 (2021), pp. 233–238.
- [24] G. Semeghini, H. Levine, A. Keesling, S. Ebadi, T. T. Wang, D. Bluvstein, R. Verresen, H. Pichler, M. Kalinowski, R. Samajdar, *et al.* “Probing topological spin liquids on a programmable quantum simulator”. In: *Science* 374.6572 (2021), pp. 1242–1247.

- [25] C. Chen, G. Bornet, M. Bintz, G. Emperauger, L. Leclerc, V. S. Liu, P. Scholl, D. Barredo, J. Hauschild, S. Chatterjee, *et al.* “Continuous symmetry breaking in a two-dimensional Rydberg array”. In: *Nature* 616.7958 (2023), pp. 691–695.
- [26] J. Zhang, S. H. Cantú, F. Liu, A. Bylinskii, B. Braverman, F. Huber, J. Amato-Grill, A. Lukin, N. Gemelke, A. Keesling, *et al.* “Probing quantum floating phases in Rydberg atom arrays”. In: *arXiv preprint arXiv:2401.08087* (2024).
- [27] P. Fromholz, M. Tsitsishvili, M. Votto, M. Dalmonte, A. Nersesyan, and T. Chanda. “Phase diagram of Rydberg-dressed atoms on two-leg triangular ladders”. In: *Physical Review B* 106.15 (2022), p. 155411.
- [28] M. Tsitsishvili, T. Chanda, M. Votto, P. Fromholz, M. Dalmonte, and A. Nersesyan. “Phase diagram of Rydberg-dressed atoms on two-leg square ladders: Coupling supersymmetric conformal field theories on the lattice”. In: *Physical Review B* 105.15 (2022), p. 155159.
- [29] R. Verresen, M. D. Lukin, and A. Vishwanath. “Prediction of toric code topological order from Rydberg blockade”. In: *Physical Review X* 11.3 (2021), p. 031005.
- [30] K. Slagle, Y. Liu, D. Aasen, H. Pichler, R. S. Mong, X. Chen, M. Endres, and J. Alicea. “Quantum spin liquids bootstrapped from Ising criticality in Rydberg arrays”. In: *Physical Review B* 106.11 (2022), p. 115122.
- [31] A. Kerschbaumer, M. Ljubotina, M. Serbyn, and J.-Y. Desaulles. “Quantum Many-Body Scars beyond the PXP model in Rydberg simulators”. In: (2024). arXiv: [2410.18913](https://arxiv.org/abs/2410.18913).
- [32] M. Sarkar, M. Pal, A. Sen, and K. Sengupta. “Quantum order-by-disorder induced phase transition in Rydberg ladders with staggered detuning”. In: *SciPost Physics* 14.1 (2023), p. 004.
- [33] L. Eck and P. Fendley. “Critical lines and ordered phases in a Rydberg-blockade ladder”. In: *Physical Review B* 108.12 (2023), p. 125135.
- [34] A. Keesling, A. Omran, H. Levine, H. Bernien, H. Pichler, S. Choi, R. Samajdar, S. Schwartz, P. Silvi, S. Sachdev, *et al.* “Quantum Kibble–Zurek mechanism and critical dynamics on a programmable Rydberg simulator”. In: *Nature* 568.7751 (2019), pp. 207–211.
- [35] J. M. Kosterlitz and D. J. Thouless. “Ordering, metastability and phase transitions in two-dimensional systems”. In: *Journal of Physics C: Solid State Physics* 6.7 (1973), p. 1181. URL: <http://stacks.iop.org/0022-3719/6/i=7/a=010>.
- [36] V. L. Pokrovsky and A. L. Talapov. “Ground State, Spectrum, and Phase Diagram of Two-Dimensional Incommensurate Crystals”. In: *Phys. Rev. Lett.* 42 (1 Jan. 1979), pp. 65–67. DOI: [10.1103/PhysRevLett.42.65](https://doi.org/10.1103/PhysRevLett.42.65). URL: <https://link.aps.org/doi/10.1103/PhysRevLett.42.65>.
- [37] S. R. White. “Density matrix formulation for quantum renormalization groups”. In: *Phys. Rev. Lett.* 69 (19 Nov. 1992), pp. 2863–2866. DOI: [10.1103/PhysRevLett.69.2863](https://doi.org/10.1103/PhysRevLett.69.2863). URL: <https://link.aps.org/doi/10.1103/PhysRevLett.69.2863>.

- [38] U. Schollwöck. “The density-matrix renormalization group in the age of matrix product states”. In: *Annals of physics* 326.1 (2011), pp. 96–192.
- [39] L. Lin and Y. Tong. “Low-rank representation of tensor network operators with long-range pairwise interactions”. In: *SIAM Journal on Scientific Computing* 43.1 (2021), A164–A192.
- [40] L. S. Ornstein. “Accidental deviations of density and opalescence at the critical point of a single substance”. In: *Proc. Akad. Sci.* 17 (1914), p. 793.
- [41] P. Calabrese and J. Cardy. “Entanglement entropy and conformal field theory”. In: *Journal of physics a: mathematical and theoretical* 42.50 (2009), p. 504005.
- [42] S. Capponi, P. Lecheminant, and M. Moliner. “Quantum phase transitions in multileg spin ladders with ring exchange”. In: *Physical Review B—Condensed Matter and Materials Physics* 88.7 (2013), p. 075132.
- [43] N. Chepiga. “Tunable Quantum Criticality in Multicomponent Rydberg Arrays”. In: *Physical review letters* 132.7 (2024), p. 076505.
- [44] B. La Riviere and N. Chepiga. “ $\mathbb{Z}_4$  transitions in quantum loop models on a zig-zag ladder”. In: *SciPost Physics* 17.5 (2024), p. 144.
- [45] R. J. Baxter. *Exactly solved models in statistical mechanics*. 1982. ISBN: 978-0-486-46271-4. DOI: [10.1142/9789814415255\\_0002](https://doi.org/10.1142/9789814415255_0002).
- [46] N. Chepiga and F. Mila. “Eight-vertex criticality in the interacting Kitaev chain”. In: *Phys. Rev. B* 107 (8 Feb. 2023), p. L081106. DOI: [10.1103/PhysRevB.107.L081106](https://doi.org/10.1103/PhysRevB.107.L081106). URL: <https://link.aps.org/doi/10.1103/PhysRevB.107.L081106>.
- [47] N. Chepiga and N. Laflorencie. “Topological and quantum critical properties of the interacting Majorana chain model”. In: *SciPost Phys.* 14 (2023), p. 152. DOI: [10.21468/SciPostPhys.14.6.152](https://doi.org/10.21468/SciPostPhys.14.6.152). URL: <https://scipost.org/10.21468/SciPostPhys.14.6.152>.
- [48] W. H. Zurek, U. Dorner, and P. Zoller. “Dynamics of a quantum phase transition”. In: *Physical review letters* 95.10 (2005), p. 105701.
- [49] J. Dziarmaga. “Dynamics of a quantum phase transition: Exact solution of the quantum Ising model”. In: *Physical review letters* 95.24 (2005), p. 245701.
- [50] R. Verresen, A. Vishwanath, and F. Pollmann. “Stable Luttinger liquids and emergent  $U(1)$  symmetry in constrained quantum chains”. In: (2019). arXiv: [1903.09179](https://arxiv.org/abs/1903.09179).
- [51] O. Foda. “A supersymmetric phase transition in Josephson-tunnel-junction arrays”. In: *Nuclear Physics B* 300 (1988), pp. 611–636. ISSN: 0550-3213. DOI: [https://doi.org/10.1016/0550-3213\(88\)90615-3](https://doi.org/10.1016/0550-3213(88)90615-3). URL: <https://www.science-direct.com/science/article/pii/0550321388906153>.
- [52] M. Sitte, A. Rosch, J. S. Meyer, K. A. Matveev, and M. Garst. “Emergent Lorentz Symmetry with Vanishing Velocity in a Critical Two-Subband Quantum Wire”. In: *Phys. Rev. Lett.* 102 (17 Apr. 2009), p. 176404. DOI: [10.1103/PhysRevLett.102.176404](https://doi.org/10.1103/PhysRevLett.102.176404). URL: <https://link.aps.org/doi/10.1103/PhysRevLett.102.176404>.

# 6

## CONCLUSION

In this thesis, we have investigated critical phenomena in chains of Rydberg atoms using both equilibrium and non-equilibrium approaches. The study relied on Tensor Network algorithms within the Matrix Product State (MPS) framework. New developments in the approximation of Matrix Product Operators for distance decaying long-range interactions beyond the well-established algebraic decay of Rydberg interactions made it possible to explore more complex geometries, such as the Rydberg ladder.

The motivation for studying these systems arises from the remarkable properties of Rydberg atoms. Their long-range decaying interactions give rise to a wide variety of critical phenomena. Moreover, they are highly tunable, allowing experimental realizations in one, two, and even three dimensions, with precise control over both interactions and atomic positions. These features make Rydberg platforms excellent candidates for analog quantum simulators.

Chapter 1 provided an introduction to the main theoretical concepts and numerical techniques that underpin the work. The presentation focused on equilibrium and non-equilibrium perspectives of critical phenomena, together with the foundations of tensor network algorithms in one dimension. The discussion was not meant to be comprehensive, but rather to provide the intuition necessary for understanding the results presented in subsequent chapters.

In Chapter 2, we analyzed the role of boundary conditions and of the final quench point on the quantum Kibble–Zurek (KZ) mechanism. Two well-known minimal models in one dimension were used for this purpose: the transverse-field Ising model and the transverse-field three-state Potts model. Regarding boundary conditions, we showed that for free boundaries, accurate results are obtained only when discarding the edges and focusing on the bulk of the chain. By contrast, with fixed boundaries accurate results can be achieved regardless of whether the edges are included, even when the fixed boundaries do not respect the local order. This is surprising, since in ground-state methods such boundaries typically induce frustration, thereby destroying local order and spoiling observables such as correlation functions, the order parameter, and entanglement entropy. Concerning the quench endpoint, we showed that with the standard definition of kinks, accurate results are obtained only when the process ends at the classical Hamiltonian. Ending away from this point underestimates the critical exponent. To address this issue, we proposed a refined definition of kinks that discards simple spin flips

from the counting. This definition yields accurate results over a broader region around the classical Hamiltonian endpoint, thereby making the analysis more robust.

These findings served as the foundation for Chapter 3, where we combined the quantum KZ mechanism with the finite-time scaling (FTS) of the order parameter to study critical behavior in Rydberg atom chains. The aim was to establish a protocol that can be readily implemented in experiments. By employing a blockade model, we were able to simulate larger system sizes and slower quench rates. Using the KZ scaling, we determined the onset of the floating phase and demonstrated that this method can clearly separate the Huse–Fisher universality class from the Kosterlitz–Thouless (KT) transition, due to their markedly different scaling behavior. With FTS, we were able to locate the conformal point for periods three and four, showing that it coincides with the maximum value of the critical exponent  $\beta\mu/\nu$  obtained with FTS and the exponent  $\mu$  extracted from KZ scaling. Notably, the peak in FTS was sharper, allowing for more precise identification of the critical point. Finally, by sweeping in both directions and combining KZ and FTS, we extracted the main critical exponents characterizing the transition.

In Chapter 4, we considered a more realistic scenario by including disorder in the system, motivated by the imperfect trapping of atoms in optical tweezers. The finite width of the tweezers introduces uncertainty in the radial and vertical positions of atoms, which propagates into the Rydberg interactions and modifies the critical behavior. The relative error depends on the interatomic distance, being smaller for low periodicities (where atoms are further apart) and larger for higher periodicities. For the Ising transitions, we observed that disorder leads to deviations from the linear scaling of kink density with the quench rate. The deviations become stronger at lower sweep rates and increase with disorder strength. Comparisons with the infinite-disorder universality class showed that the transition gradually approaches this class, and for disorder levels around  $\delta V = 0.4V$  the scaling fully overlaps with the infinite-disorder prediction. We also studied the effect of disorder on the floating phase and showed that for realistic experimental levels of positional uncertainty, the floating phase is destroyed. The system exhibits localized interactions and a saturation of entanglement entropy, consistent with a gapped phase.

Finally, in Chapter 5, we extended the analysis beyond one-dimensional arrays to a two-leg Rydberg ladder. The phase diagram was found to share similarities with the one-dimensional case, but with a richer variety of critical phenomena. Several lobes with different longitudinal periodicities were identified, as in one dimension, but in this case they split into phases distinguished by whether transverse translational symmetry is preserved or broken into a  $Z_2$  symmetry. This geometry revealed the merging of Ising transitions with other universality classes. In particular, the longitudinal  $Z_2$  phase showed the merging of two Ising transitions into the Ashkin–Teller universality class. Meanwhile, the longitudinal  $Z_3$  phase exhibited the more exotic scenario of a merging between a  $Z_2$  Ising transition and a Pokrovsky–Talapov transition. These results highlight the potential of ladder geometries as a platform for studying the interplay between Ising transitions and more complex universality classes.

This thesis has addressed only a small fraction of the rich physical possibilities offered by Rydberg atom arrays. The results presented here highlight intriguing phenomena and point toward many exciting directions for future research. Regarding Rydberg

ladders, it remains an open question what happens when the Ising transition intersects the Pokrovsky–Talapov universality class and enters the floating phase. As previously stated, this might lead to the engineering of supersymmetric states; however, identifying the effective fermionic and bosonic degrees of freedom in this case might be challenging. Furthermore, the computational power required to fully resolve this region of the phase diagram exceeds the capabilities of current hardware. Using a blockade model, as was done for the 1D chain, could substantially reduce the computational cost. Another promising direction is the study of different geometries. The rapid improvement of experimental set-ups now makes it possible to realize 3D configurations with great precision [1]. This enables investigations of how algebraically decaying Rydberg interactions affect the breaking of symmetries. For example, can a quantum chiral transition also occur in 2D or 3D quantum many-body systems? In addition, this work has only considered van der Waals interactions. Exploring different Rydberg levels and even mixtures of Rydberg species provides virtually unlimited opportunities to realize diverse many-body quantum Hamiltonians, from Förster resonances to regimes with attractive interactions. The finite size of optical tweezer arrays also offers a natural framework to explore the interplay between disorder and commensurate–incommensurate phase transitions. By tuning the Rydberg level and interatomic distances, it becomes possible to study a wide range of disorder strengths and to determine, for instance, how the chiral transition is influenced by disorder. In conclusion, the work in this thesis shows that Rydberg atoms provide an exceptional platform for testing theories of quantum many-body physics. While it is still debated whether digital quantum computers have reached quantum advantage, or when they will be able to tackle useful problems, analog quantum simulators based on Rydberg atoms have already surpassed classical algorithms in a variety of meaningful quantum physics applications.



# A

## APPENDIX

### A.1. BLOCKADE MODELS

#### A.1.1. IMPLEMENTATION DETAILS

Chapter 3 introduced a blockade model designed to reduce the computational complexity of simulating Rydberg atom systems. In this section, we describe in greater detail how the blockade model is implemented within the time-evolving block decimation (TEBD) algorithm. Specifically, we discuss the adaptations required for the  $r = 1$  and  $r = 2$  effective blockade Hamiltonians introduced in that chapter.

#### A.1.2. MODIFIED TEBD FOR THE $r = 1$ BLOCKADE

The bulk Hamiltonian expressed in the blockade basis was previously defined in Chapter 3 as

$$h_i = -\frac{\Omega}{2} (\tilde{a}_i \tilde{b}_{i+1} + \text{h.c.}) - \Delta \tilde{q}_i + V_2 \tilde{q}_i \tilde{p}_{i+1}. \quad (\text{A.1})$$

Using the two-atom basis introduced in Figure 3.1(b),  $\{|h_1\rangle, |h_2\rangle, |h_3\rangle\}$ , the operators in the first term of the blockade Hamiltonian act as

$$\tilde{a}|h_1\rangle = |h_2\rangle, \quad (\text{A.2})$$

$$\tilde{b}|h_1\rangle = |h_3\rangle, \quad (\text{A.3})$$

and annihilate all other states. The local density operators  $\tilde{q}_i$  and  $\tilde{p}_i$  act on the left and right atoms of each pair, respectively, and yield non-zero contributions only for

$$\tilde{q}|h_3\rangle = |h_3\rangle, \quad (\text{A.4})$$

$$\tilde{p}|h_2\rangle = |h_2\rangle. \quad (\text{A.5})$$

To incorporate the Rydberg blockade constraint into the TEBD algorithm, we developed a modified scheme applicable to both ground-state searches and real-time evolution under a nearest-neighbour blockade ( $r = 1$ ). This adaptation enforces the blockade condition by restricting the accessible Hilbert space and by modifying the structure of the two-site gates used in the Trotter decomposition. The resulting algorithm ensures

that configurations violating the blockade constraint are excluded throughout the simulation, thereby improving both numerical efficiency and physical consistency.

The two-site gates are decomposed into a basis containing only the allowed configurations under the blockade condition. The matrix representation of each gate is block-diagonal, with non-zero elements only for the following basis states:

$$O^{(0x0)(0x0)}, O^{(001)(001)}, O^{(100)(100)}, O^{(101)(101)}. \quad (\text{A.6})$$

where the indexes are expressed in the local density matrix and index  $x$  indicates an unconstrained spin configuration. Among these,  $O^{(0x0)(0x0)}$  corresponds to a  $2 \times 2$  subblock, while the remaining entries are  $1 \times 1$  scalar elements.

The algorithm proceeds by treating each of these matrix blocks independently. When contracting tensors, each block is processed according to its configuration, preserving the underlying structure imposed by the blockade constraint. In the transformed basis  $\{h\}$ , the tensor at each lattice site is decomposed into a set of matrices that reflect the restricted structure imposed by the blockade condition. Specifically, instead of a single tensor per site, we represent each local tensor by three separate matrices:

$$M_{\alpha\beta}^{00}, M_{\alpha\beta'}^{01}, M_{\alpha'\beta}^{10}, \quad (\text{A.7})$$

where the superscript  $ij$  indicates the relevant local physical configuration, and the Greek indices  $\alpha, \beta, \alpha', \beta'$  label the bond dimensions of the matrix.

Unlike conventional Matrix Product State (MPS) representations used in standard tensor network algorithms—where each local tensor has a fixed shape and uniform bond dimensions—the presence of the blockade constraint leads to a situation where different physical configurations are associated with matrices of different dimensions. This is reflected in our notation by adding a prime (') to the indices of matrices that connect to subspaces of different size.

For instance,  $M_{\alpha\beta'}^{01}$  has the same left bond dimension as  $M_{\alpha\beta}^{00}$ , but a different right bond dimension, indicated by the primed index  $\beta'$ . This non-uniform structure arises naturally from the fact that certain transitions are forbidden due to the blockade, effectively removing parts of the Hilbert space and leading to a block-sparse MPS representation. For zip contraction from right-canonical to left-canonical configuration, tensors are combined as:

$$\begin{aligned} M_{\alpha\beta}^{00} B_{\beta\gamma}^{00} &= M_{\alpha\gamma}^{000} \\ M_{\alpha\beta}^{00} B_{\beta\gamma'}^{01} &= M_{\alpha\gamma'}^{001} \\ M_{\alpha\beta'}^{01} B_{\beta'\gamma}^{10} &= M_{\alpha\gamma}^{010} \\ M_{\alpha'\beta}^{10} B_{\beta\gamma}^{00} &= M_{\alpha'\gamma}^{100} \\ M_{\alpha'\beta}^{10} B_{\beta\gamma'}^{01} &= M_{\alpha'\gamma'}^{101} \end{aligned} \quad (\text{A.8})$$

After these contractions, the resulting tensors are associated with the appropriate  $O$  blocks and grouped into a larger block-diagonal matrix:

$$\begin{pmatrix} M_{\alpha\gamma}^{000} & M_{\alpha\gamma'}^{001} & 0 \\ M_{\alpha'\gamma}^{100} & M_{\alpha'\gamma'}^{101} & 0 \\ 0 & 0 & M_{\alpha\gamma}^{010} \end{pmatrix} \quad (\text{A.9})$$

Each block is then independently subjected to singular value decomposition (SVD), allowing the retrieval of updated canonical tensors. For the upper  $2 \times 2$  block, we have:

$$\begin{pmatrix} M_{\alpha\gamma}^{000} & M_{\alpha\gamma'}^{001} \\ M_{\alpha\gamma}^{100} & M_{\alpha'\gamma'}^{101} \end{pmatrix} \xrightarrow{\text{SVD}} U_{(\alpha+\alpha')d} S_{dd} V_{d(\gamma+\gamma')} \quad (\text{A.10})$$

and for the  $1 \times 1$  block:

$$M_{\alpha\gamma}^{010} \xrightarrow{\text{SVD}} U_{\alpha d'} S_{d'd'} V_{d'\gamma} \quad (\text{A.11})$$

The resulting left-canonical tensors are extracted as:

$$U_{(\alpha+\alpha')d} = \begin{pmatrix} A_{\alpha d}^{00} \\ A_{\alpha' d}^{10} \end{pmatrix} \quad (\text{A.12})$$

$$U_{\alpha d'} = A_{\alpha d'}^{10} \quad (\text{A.13})$$

Similarly, the right-hand side matrices are reconstructed from the remaining SVD components:

$$S_{dd} V_{d(\gamma+\gamma')} = \begin{pmatrix} M_{d\gamma}^{00} & M_{d\gamma'}^{01} \end{pmatrix} \quad (\text{A.14})$$

$$S_{d'd'} V_{d'\gamma} = M_{d'\gamma}^{10} \quad (\text{A.15})$$

This construction ensures that the TEBD algorithm respects the blockade constraint at all stages of evolution or ground state preparation, while efficiently exploiting the structure of the restricted Hilbert space.

### A.1.3. MODIFIED TEBD FOR THE $r = 2$ BLOCKADE

The bulk Hamiltonian for the  $r = 2$  blockade model was introduced in Chapter 3 and is given by

$$h_i = -\frac{\Omega}{2} (\tilde{a}_i \tilde{b}_{i+1} \tilde{c}_{i+2} + \text{h.c.}) - \Delta \tilde{p}_i + V_3 \tilde{q}_i \tilde{p}_{i+1}. \quad (\text{A.16})$$

This Hamiltonian is defined in the three-atom basis  $\{|h_1\rangle, |h_2\rangle, |h_3\rangle, |h_4\rangle\}$  introduced in Figure 3.2 (b). The term  $\tilde{a}_i \tilde{b}_{i+1} \tilde{c}_{i+2} + \text{h.c.}$  flips an atom between its ground and Rydberg states. The only non-zero operator actions are

$$\tilde{a} |h_1\rangle = |h_2\rangle, \quad (\text{A.17})$$

$$\tilde{b} |h_1\rangle = |h_3\rangle, \quad (\text{A.18})$$

$$\tilde{c} |h_1\rangle = |h_4\rangle. \quad (\text{A.19})$$

The operators  $\tilde{q}_i$  and  $\tilde{p}_i$  represent the local densities at sites  $i$  and  $i + 2$ , respectively, with non-zero matrix elements

$$\tilde{q} |h_4\rangle = |h_4\rangle, \quad (\text{A.20})$$

$$\tilde{p} |h_2\rangle = |h_2\rangle. \quad (\text{A.21})$$

The tensor network algorithm for the  $r = 2$  Rydberg blockade follows the same general approach as the  $r = 1$  implementation, but it involves additional complexity due to the

longer blockade range. The Trotter decomposition now requires the use of three-body effective gates, and the tensor structure must be adapted to accommodate a larger variety of configurations within the constrained Hilbert space. This modification ensures that all unphysical states—those violating the  $r = 2$  blockade condition—are consistently excluded during the simulation, while maintaining numerical stability and computational efficiency.

The three-site gates are represented in a block-diagonal matrix form, with non-zero entries only for the configurations allowed by the  $r = 2$  blockade. These include:

$$\begin{aligned} &O^{(00x00)(00x00)}, O^{(00001)(00001)}, O^{(00010)(00010)}, \\ &O^{(01000)(01000)}, O^{(01000)(01000)}, O^{(01001)(01001)}, \\ &O^{(10000)(10000)}, O^{(10001)(10001)}, O^{(10010)(10010)}, \end{aligned} \quad (\text{A.22})$$

where the superscripts are expressed in the local density basis and  $x$  indicates a spin that is not fixed. Among these,  $O^{(00x00)(00x00)}$  corresponds to a  $2 \times 2$  block, while all others are scalar  $1 \times 1$  elements.

In the new basis that enforces the blockade constraint, each tensor is split into four distinct matrices corresponding to the allowable configurations:

$$M_{\alpha\beta}^{000}, \quad M_{\alpha\beta'}^{001}, \quad M_{\alpha'\beta''}^{010}, \quad M_{\alpha''\beta}^{100}, \quad (\text{A.23})$$

with different bond dimensions indicated by primes on the indices ( $\beta'$ ,  $\beta''$ , etc.) to reflect the non-uniform structure of the constrained Hilbert space.

The contraction process and singular value decomposition (SVD) are applied block-by-block. The contraction from a right-canonical to a left-canonical configuration yields a block-structured tensor of the form:

$$\begin{pmatrix} M_{\alpha\gamma}^{00000} & M_{\alpha\gamma'}^{00001} & M_{\alpha\gamma''}^{00010} & 0 & 0 & 0 \\ M_{\alpha''\gamma}^{10000} & M_{\alpha''\gamma'}^{10001} & M_{\alpha''\gamma''}^{10010} & 0 & 0 & 0 \\ 0 & 0 & 0 & M_{\alpha\gamma}^{00100} & 0 & 0 \\ 0 & 0 & 0 & 0 & M_{\alpha'\gamma}^{01000} & M_{\alpha'\gamma'}^{01001} \end{pmatrix} \quad (\text{A.24})$$

This block structure is first split into submatrices and each is processed via SVD independently:

$$\begin{pmatrix} M_{\alpha\gamma}^{00000} & M_{\alpha\gamma'}^{00001} & M_{\alpha\gamma''}^{00010} \\ M_{\alpha''\gamma}^{10000} & M_{\alpha''\gamma'}^{10001} & M_{\alpha''\gamma''}^{10010} \end{pmatrix} \xrightarrow{\text{SVD}} U_{(\alpha+\alpha'')} S_{d,d} V_{d(\gamma+\gamma'+\gamma'')} \quad (\text{A.25})$$

$$M_{\alpha\gamma}^{00100} \xrightarrow{\text{SVD}} U_{\alpha d'} S_{d'd'} V_{d'\gamma} \quad (\text{A.26})$$

$$\begin{pmatrix} M_{\alpha'\gamma}^{01000} & M_{\alpha'\gamma'}^{01001} \end{pmatrix} \xrightarrow{\text{SVD}} U_{\alpha' d''} S_{d'' d''} V_{d''(\gamma+\gamma')} \quad (\text{A.27})$$

$$(\text{A.28})$$

The resulting left-canonical tensors are extracted from the  $U$  matrices:

$$U_{(\alpha+\alpha'')d} = \begin{pmatrix} A_{\alpha d}^{000} \\ A_{\alpha'' d}^{100} \end{pmatrix} \quad (\text{A.29})$$

$$U_{\alpha d'} = A_{\alpha d'}^{001} \quad (\text{A.30})$$

$$U_{\alpha' d''} = A_{\alpha' d''}^{010}. \quad (\text{A.31})$$

The right-hand side matrices are reconstructed by contracting the singular values with the  $V$  matrices:

$$S_{dd} V_{d(\gamma+\gamma'+\gamma'')} = \begin{pmatrix} M_{d\beta}^{0000} & M_{d\beta'}^{0001} & M_{d\beta''}^{0010} \end{pmatrix} \quad (\text{A.32})$$

$$S_{d'd'} V_{d'\gamma} = M_{d'\gamma}^{0100} \quad (\text{A.33})$$

$$S_{d''d''} V_{d''(\gamma+\gamma')} = \begin{pmatrix} M_{d''\beta}^{1000} & M_{d''\beta'}^{1001} \end{pmatrix} \quad (\text{A.34})$$

At this stage, the blocks are reorganized to prepare for another SVD step:

$$\begin{pmatrix} M_{d\beta}^{0000} & M_{d\beta'}^{0001} & 0 & 0 \\ M_{d''\beta}^{1000} & M_{d''\beta'}^{1001} & 0 & 0 \\ 0 & 0 & M_{d\beta''}^{0010} & 0 \\ 0 & 0 & 0 & M_{d'\gamma}^{0100} \end{pmatrix} \quad (\text{A.35})$$

This second SVD step proceeds similarly to the previous one, producing updated  $A$  tensors and new right-hand side matrices  $M$ , thereby completing the update of the MPS tensors under the  $r = 2$  blockade constraint.

This two-step contraction and decomposition process ensures that the TEBD algorithm consistently respects the extended blockade condition, while maintaining the efficiency of local updates and leveraging the sparse structure of the restricted Hilbert space.



# ACKNOWLEDGEMENTS

No man is an island, and I would not be finalizing my thesis without the help and support of many people around me.

First of all, I want to thank my supervisor, Natalia Chepiga, for her guidance and advice throughout my PhD. Her energy and enthusiasm have been a constant source of inspiration, and her ideas have helped shape the content of this thesis.

I am also grateful to my promotor, Sander Otter, who has been an important figure I could always rely on whenever I needed help or advice. I would like to thank the secretariat for their tireless efforts and for making my journey as smooth as possible, even in situations that went beyond their duties.

I am grateful to my research group, Bowy, Pietro, and Julien, for creating, together with Klaiv, our office mate, a fun and relaxed environment both in and out of the office. Their company and good humor made coming to work each day a pleasure.

My thanks also go to Eliska's team, who warmly welcomed me when I first arrived in Delft and have supported me ever since.

I want to thank Luciano, Xiayi, Nahual, Guille, and Alberto, my dear friends, who have given me sound advice and reassurance in moments of doubt, providing the strength I needed to continue my research.

I am grateful to my book club crew for the intense and thought-provoking debates that have helped shape my thinking and communication skills. Many of the ideas presented in the propositions derive from those enjoyable discussions.

I would also like to thank my high school math teacher, Daniel, whose structured teaching style and dry sense of humor played a decisive role in my decision to study physics.

I want to thank my family, especially my parents and sister, for being a fundamental pillar in my life and for encouraging me to pursue my career.

Finally, I want to thank my girlfriend, Nina, for her love and support throughout these four years. Despite the distance, her joyful personality and kindness have been a constant source of strength and comfort.

Lastly, I extend my gratitude to all those people I have not named, but who have contributed to shaping who I am today.



# CURRICULUM VITÆ

## José SOTO GARCÍA

23-07-1991      Born in Almeria, Spain.

### EDUCATION

2009–2015      Degree in Pharmacy  
Universidad de Granada

2015–2020      Bachelor degree in Physics  
Universidad de Granada

2020–2021      Maser in Physics  
Imperial College London  
*Thesis:*          In search of Majorana Fermions  
*Promotor:*      Dr. D. Lee

2021              PhD. Physics  
Delft University of Technology  
*Thesis:*          Quantum Critical Properties of Rydberg Arrays in and  
out of Equilibrium  
*Supervisor:*    Dr. N. Chepiga  
*Promotor:*      Prof. dr. A. F. Otte

### AWARDS

2023              Best Poster Award



# LIST OF PUBLICATIONS

4. J. Soto-Garcia and N. Chepiga. “Infinite Randomness Criticality and Localization of the Floating Phase in Arrays of Rydberg Atoms Trapped with Nonperfect Tweezers”. In: *Physical Review Letters* 136.5 (2026), p. 056502
3. J. Soto-Garcia and N. Chepiga. “Quantum Kibble-Zurek mechanism: The role of boundary conditions, endpoints, and kink types”. In: *Physical Review B* 113.8 (2026), p. 085430
2. J. Soto-Garcia and N. Chepiga. “Numerical investigation of quantum phases and phase transitions in a two-leg ladder of Rydberg atoms”. In: *Physical Review Research* 7.1 (2025), p. 013215
1. J. Soto Garcia and N. Chepiga. “Resolving chiral transitions in one-dimensional Rydberg arrays with quantum Kibble-Zurek mechanism and finite-time scaling”. In: *Physical Review B* 110.12 (2024), p. 125113

